

SEARCHING FOR SUPERSYMMETRY IN BOOSTED
FULLY-HADRONIC FINAL STATES WITH B-JETS AND
CALIBRATING B-JET IDENTIFICATION USING SPATIALLY
MATCHED MUONS AT THE ATLAS DETECTOR

Rachael Ann Creager

A DISSERTATION

in

Physics and Astronomy

Presented to the Faculties of The University of Pennsylvania
in Partial Fulfillment of the Requirements for the Degree of Doctor of Philosophy
2020

I. Joseph Kroll, Professor, Physics and Astronomy
Supervisor of Dissertation

Joshua Klein, Edmund J. and Louise W. Kahn Professor, Physics and Astronomy
Graduate Group Chairperson

Dissertation Committee

Evelyn Thomson, Associate Professor, Physics and Astronomy
Adam Lidz, Associate Professor, Physics and Astronomy
Elliot Lipeles, Associate Professor, Physics and Astronomy
Jonathan Heckman, Assistant Professor, Physics and Astronomy
I. Joseph Kroll, Professor, Physics and Astronomy

SEARCHING FOR SUPERSYMMETRY IN BOOSTED
FULLY-HADRONIC FINAL STATES WITH B-JETS AND
CALIBRATING B-JET IDENTIFICATION USING SPATIALLY
MATCHED MUONS AT THE ATLAS DETECTOR

COPYRIGHT
2020
Rachael Ann Creager

All rights reserved.

Acknowledgements

This document represents five and a half years of work; this is the single largest academic accomplishment of my life. I could not have completed it without a village of support around me, and I'd like to acknowledge those supporters here.

First off, I'd like to thank my mom, Karen. Mom, I cannot thank you enough for advocating on my behalf from my earliest days, both in school and in daily life. You have always taken my education seriously and made me feel that women belong in STEM. Thank you for listening to me, for giving me good advice, and for taking care of me when I need it.

I'd also like to thank my little sister, Jessica. Jessica, you're my best friend; you are a better sister than I deserve. I love chatting with you, sharing memes, and Skyping for hours on end. I'm glad at least one of us decided to become a "real" doctor!

My father, Steve, has been a great source of support during my time at Penn. Dad, thanks for giving me great advice in navigating department politics. Your passion for university life is evident to everybody, especially me. Now we are both officially Dr. Creager!

Joe, thank you for serving as my advisor for the past years. I admire your discipline, your principles, and how you treat your students fairly and with respect. Thank you for giving me the freedom to pursue my own research interests while still guiding me towards success. Somebody once told me that your choice of advisor is the single biggest determining factor in your grad school happiness. Working with you has made my graduate school experience a happy one!

I'd like to thank all my CERN colleagues who have supported me throughout the years. First off, thank you to Ingo, who helped me understand p_T^{rel} back when I was a useless noob. Bing, you are a font of ideas and bring such a positive energy to your work. Valentina, thank you for your hard work and funny messages; I had a lot of fun prepping the snack box for you and Bing! Shion, thank you for your support in SUSY analysis and for being a supportive and understanding analysis

leader. James and Leigh, thanks for being such great office-mates; chatting with you was one of my favorite ways to relax. Finally, I'd like to thank all my colleagues for flavor-tagging and derivation software. Running the world's biggest scientific experiment with you was a privilege.

I'd also like to thank my entire graduate school cohort. You all have become great friends to me, and I'm immensely grateful for the time we spent together at Penn. Thank you Shannon, Robert, David, Chris K, Chris L, Analisa, Lia, Saul, Charlotte, Paul, Eric, Elodie, Christian, Tatyana, and Ashley. Meeting you all was the first time I felt that I could be a physics PhD and still be relatively "normal". I'll always remember the parties we threw together fondly!

Finally, I'd like to thank Tony. I will always be grateful to Penn for bringing us together, and I cannot image my life without you. I love you so much and am grateful that I get to build my life with you.

*"There is nothing more admirable than when two people who see eye to eye keep house
as man and wife, confounding their enemies and delighting their friends."*

— Homer, *The Odyssey*

ABSTRACT

SEARCHING FOR SUPERSYMMETRY IN BOOSTED FULLY-HADRONIC FINAL STATES WITH B-JETS AND CALIBRATING B-JET IDENTIFICATION USING SPATIALLY MATCHED MUONS AT THE ATLAS DETECTOR

Rachael Ann Creager

J. Kroll

This thesis presents two analyses that involve the identification of hadronic jets produced by the fragmentation of b -quarks or “ b -jets”. The identification exploits the hard fragmentation of b -quarks and relatively long lifetime of B hadrons. The first analysis is the calibration of the efficiency of the $MV2c10$ b -jet identification algorithm using a sample of b -jets with muons from B hadron decays and a kinematic property of these jets known as “ p_T^{rel} ”, which is constructed from the muons. This analysis was performed using 68 fb^{-1} of data collected at $\sqrt{s} = 13 \text{ TeV}$ with the ATLAS detector during Run 2 of the Large Hadron Collider. Improvements in the methods of this calibration have led to a reduction by more than an order of magnitude in the uncertainty of earlier measurements of b -jet tagging efficiency using this approach. This work included substantial contributions to the software and computing framework used to study the identification of jets produced by heavy flavor decay; these contributions are described herein. The second analysis is a search for electroweakly-produced supersymmetric partners of the gauge bosons or “gauginos”. This search uses 140 fb^{-1} of data collected at $\sqrt{s} = 13 \text{ TeV}$ with the ATLAS detector during Run 2 of the Large Hadron Collider. My work focused on developing a new signal region that targeted final states specifically containing two b -jets and two light-quark jets. As part of this optimization, I examined different supersymmetric scenarios and explored alternative techniques for estimating the Standard Model backgrounds. Based on preliminary results, in the wino-bino scenario, this search is expected to provide sensitivity to charginos with masses up to $\sim 1 \text{ TeV}$. For a scenario in the general-gauge-mediation model (where higgsino becomes the next-lightest SUSY particle), this search will

provide sensitivity for higgsinos with masses up to 600 GeV (discovery) or 800 GeV (exclusion) for most of the possible Z/h branching ratios. Finally, the sensitivity to the scenarios where higgsino is next-lightest and bino is the lightest SUSY particle has been studied, on which no explicit exclusion has been reported yet by the searches in LHC.

Contents

Acknowledgements	iii
Abstract	vi
Contents	vii
List of Tables	xii
List of Figures	xiv
1 Overview	1
2 Theoretical Framework	5
2.1 Lagrangians in Quantum Field Theories	5
2.1.1 Lagrangian Field Theory	5
2.1.2 Invariance and the Standard Model	6
2.2 Introduction to the Standard Model	7
2.2.1 Electroweak Unification	9
2.2.1.1 $U(1)$ & Electromagnetism	10
2.2.1.2 Unifying the Electromagnetic and Weak Forces	11
2.2.2 Motivating the Higgs Boson	12
2.2.3 What is the Higgs Boson?	13
2.2.4 Theory of Flavor Physics	15
2.2.4.1 Calculating Heavy Flavor Hadron Lifetime	16
2.2.5 Properties of Heavy Flavor Hadrons	19

2.3	Open Problems in the Standard Model	21
2.4	Cosmology and the Standard Model	22
2.4.1	Observing Dark Matter through Galactic Velocity Curves	23
2.4.2	The Expanding Universe	23
2.4.3	Thermal History of the Universe	25
2.4.4	Dark Matter Properties	27
2.5	Introduction to Supersymmetry	27
2.5.1	What is SUSY?	28
2.5.2	Terminology in SUSY	29
2.5.3	R-Parity	31
2.5.4	Electroweakly-Produced SUSY Scenarios	31
3	The LHC, ATLAS, and Data Simulation and Collection	34
3.1	Introduction to Collider Physics	34
3.1.1	Luminosity and Cross Section	34
3.2	The Large Hadron Collider	35
3.2.1	LHC Rings	36
3.2.2	Detectors	37
3.3	The ATLAS Detector	38
3.3.1	Coordinate System	39
3.3.2	The Inner Detector	40
3.3.3	Calorimeters	40
3.3.4	Muon Spectrometer	42
3.4	Data Collection	43
3.4.1	Trigger System	43
3.4.1.1	Level-1 Hardware Trigger	45
3.4.1.2	High-Level Trigger	45
3.4.1.3	Trigger Prescales	46
3.5	Reconstruction and Simulation	46
3.5.1	Object Reconstruction	46
3.5.2	Monte Carlo Simulation	51
3.6	Data Processing and Management	53
3.6.1	The Worldwide LHC Computing Grid	53

3.6.2	Distributed Analysis in ATLAS	55
3.6.3	The ATLAS Data Model	56
3.6.4	Distributed Data Management in ATLAS	57
3.6.5	Flavor Tagging Derivation Software	58
3.6.6	ATLAS Derivation Software	58
3.6.7	Flavor-Tagging Derivation Software	59
4	p_T^{rel} Calibration	63
4.1	Introduction to p_T^{rel}	63
4.2	Datasets and Samples	66
4.2.1	Trigger Selection	67
4.2.2	MC Samples	67
4.3	Object and Event-Level Selections	70
4.3.1	Jet selections	70
4.3.2	Muon selections	70
4.3.3	Event Selections: $b\bar{b}$ - and Light-Enhanced Regions	71
4.4	Method	72
4.4.1	b and c Templates	73
4.4.1.1	Bottom Template	73
4.4.1.2	Charm template	74
4.4.2	Light Template	75
4.4.3	Template fit	75
4.4.4	Efficiency Extraction	77
4.5	Upgrading the Calibration	77
4.5.1	MC Validation	80
4.5.2	Trigger Turn-on Curves	81
4.5.3	Studying the Lowest- p_T Muon-In-Jet Trigger	85
4.5.3.1	Jet p_T Reweighting	87
4.5.3.2	Trigger Emulation	88
4.6	Additional Studies	89
4.6.1	Extrapolation from Semileptonic to Inclusive b -Decays	89
4.6.2	Gluon-Splitting Studies	92
4.7	Systematic Uncertainties	96

4.7.1	Detector and Calibration Uncertainties	97
4.7.2	Modeling Uncertainties	99
4.7.2.1	Muon Uncertainties	99
4.7.2.2	Jet and Hadron Uncertainties	100
4.7.3	MC Statistical Uncertainties	100
4.7.4	Template Selection Uncertainties	101
4.8	Results	102
4.9	Future Work	104
5	Fully-Hadronic Electroweak SUSY	108
5.1	Signal Signature	108
5.1.1	SUSY Production Cross-Sections	108
5.1.2	Target Signatures	109
5.1.3	2B2Q Analysis Strategy	115
5.2	Datasets and Samples	116
5.2.1	Derivations	116
5.2.2	Data Samples	116
5.2.3	MC Samples	116
5.2.3.1	SM Backgrounds	116
5.2.3.2	SUSY Signals	117
5.3	Object and Event-Level Selections	118
5.3.1	Object Definitions	118
5.4	Signal Region Definition	125
5.4.1	Event-Level Selection Criteria	125
5.4.1.1	Preselection	125
5.4.1.2	Triggers	126
5.4.1.3	Event Cleaning	126
5.4.1.4	Non-Collision Background Veto	128
5.4.2	Discriminating Variables	131
5.4.3	Boosted 2B2Q Signal Region	132
5.5	Overview of Backgrounds	136
5.5.1	Background Estimation	137
5.5.1.1	ABCD Results	144

5.5.1.2	Signal Contamination in non-SR Regions	148
5.6	Higgsino Reinterpretation Studies	153
5.7	Future Work	154
6	Conclusion	161
A	Appendix	163
A.1	Motivating the Higgs Boson: Calculation Details	164
A.2	Up-to-date Systematic Uncertainty Tables for p_T^{rel}	166
A.3	p_T^{rel} Fit Results	171
A.3.1	Post-fit p_T^{rel} Plots for 60% WP	171
A.3.2	Post-fit p_T^{rel} plots for 70% WP	174
A.3.3	Post-fit p_T^{rel} plots for 77% WP	177
A.3.4	Post-fit p_T^{rel} plots for 85% WP	180
A.4	Correlation Study Plots for ABCD Method	183
A.4.1	Wh Selection	184
A.4.2	WZ Selection	187
A.4.3	Zh Selection	190
A.4.4	ZZ Selection	193
	Bibliography	196
	Glossary	209

List of Tables

2.1	Summary of all known elementary particles [10]	9
2.2	Summary of the four fundamental forces of nature [9] [7]	9
2.3	Summary of the major decay modes of the Higgs boson	14
4.1	Summary of p_T^{jet} bins and the thresholds applied in the corresponding triggers.	68
4.2	Unfiltered MC Samples Summary	69
4.3	Muon-Filtered MC Samples Summary	69
4.4	Relative b , c , and light fractions minimal (left) and variable (right) muon p_T cuts. . . .	71
4.5	List of selection criteria for muon-in-jet samples	71
4.6	Systematic uncertainties for the $MV2c10$ tagging algorithm at 85% nominal b -tagging efficiency	101
4.7	Systematic uncertainties for the $MV2c10$ tagging algorithm at 77% nominal b -tagging efficiency	102
4.8	Systematic uncertainties for the $MV2c10$ tagging algorithm at 70% nominal b -tagging efficiency	102
4.9	Systematic uncertainties for the $MV2c10$ tagging algorithm at 60% nominal b -tagging efficiency	102
4.10	Fractions of b -hadrons as produced in simulated Z^0 -decays, inclusive measurements performed at CDF [128], and compared to the average provided by the HFAG [127].	106
5.1	Summary of object definitions.	120
5.2	Summary of the boosted preselection. $n_{b-\text{jet}}^{\text{trk}}(\text{outside J})$ is the number of $R = 0.2$ track b -jets outside cone of any of the large- R jets with $\Delta R > 0.8$	126
5.5	Object multiplicity and kinematic variables used in the boosted category selection. . . .	132
5.6	Signal region definition for boosted 2B2Q analysis. $n_{W \rightarrow qq}$, $n_{Z \rightarrow qq}$ and $n_{W \text{ or } Z \rightarrow qq}$ are number of large- R jets passing the W -tag, Z -tag and W or Z tag, respectively. SRVZ is the logical OR of SRWZ and SRZZ, SRVh is the OR of SRWh and SRZh	135
5.7	Cutflow showing the cumulative effect of the SR selections on signal and bkg yields for Wh wino-bino signal (800 GeV NLSP, 200 GeV LSP). Errors shown are purely statistical.	136
5.8	Cutflow showing the cumulative effect of the SR selections on signal and bkg yields for WZ wino-bino signal (700 GeV NLSP, 100 GeV LSP). Errors shown are purely statistical.	136
5.9	Cutflow showing the cumulative effect of the SR selections on signal and bkg yields for Zh GGM higgsino signal (500 GeV NLSP, 0 GeV LSP). Errors shown are purely statistical.	136

5.10	Cutflow showing the cumulative effect of the SR selections on signal and bkg yields for ZZ GGM higgsino signal (500 GeV NLSP, 0 GeV LSP). Errors shown are purely statistical.	137
A.1	Systematic uncertainties for the $MV2c10$ tagging algorithm at 85% nominal b -tagging efficiency	167
A.2	Systematic uncertainties for the $MV2c10$ tagging algorithm at 77% nominal b -tagging efficiency	168
A.3	Systematic uncertainties for the $MV2c10$ tagging algorithm at 70% nominal b -tagging efficiency	169
A.4	Systematic uncertainties for the $MV2c10$ tagging algorithm at 60% nominal b -tagging efficiency	170

List of Figures

2.1	Nuclear Beta Decay of a neutron into a proton.	9
2.2	Visualizing the Higgs potential when $\mu^2 < 0$ [14]	14
2.3	Weak decay of the b -quark	18
2.4	A qualitative picture of the hadronization process [7]	20
2.5	Comparison of Fragmentation Function Shapes for b and c quarks. [21]	20
2.6	An artistic representation of Grand Unification Theory [25]	22
2.7	Galactic rotational velocity curve for NGC 6503. For comparison, the expected curves due to the gas, disk, and dark matter halos are shown as dotted lines [28]	24
2.8	All-sky image of the Cosmic Microwave Background. Structures are an artifact of early Universe anisotropies. [31]	26
2.9	Fermionic loop correction to the Higgs mass	28
2.10	A table showing a MSSM extension to the SM. The red boxes show the superpartnership between the neutral SM bosons and the charged Higgsinos and winos. The blue boxes show the superpartnership between the charged SM bosons and the neutral Higgsinos, neutral wino, and bino.	30
2.11	Electroweakino mass spectra in target physics scenarios. (a) Wino heavy states / higgsino light states: (\tilde{W}, \tilde{H}) (b) higgsino heavy states / wino light states: (\tilde{H}, \tilde{W}) (c)(d) wino or higgsino heavy states / bino light state: $(\tilde{W}/\tilde{H}, \tilde{B})$. To resolve the tension with DM relic abundance in bino LSP scenario, (c) mixes the bino LSP with a $20 \sim 100$ GeV heavier wino or higgsino. This mass splitting can be as large as $100 \sim 700$ GeV in (d), which is a special case of (c) where the bino mass is about half the Z or Higgs mass. Figure credit to Dr. Shion Chen.	33
3.1	Cartoon illustrating the LHC relative to local borders and geography [55]	36
3.2	Rendered cut-away view of the ATLAS detector, with two humans shown on the left in red for size reference. [59]	38
3.3	Cross-sectional slice of the ATLAS detector, showing what types of particles can be measured in each layer [61]	39
3.4	Rendered image of the ID [62]	41
3.5	Rendered image of the calorimeters [64]	42
3.6	Rendered image of the MS [65]	43

3.7	Plot of the recorded luminosity as a function of pileup for 2015-2018 data collected at ATLAS [70]	44
3.8	Cartoon showing the calculation of impact parameter d_0 for a track associated to a jet [82]	50
3.9	Flowchart of the ATLAS MC Simulation Process [87]	52
3.10	Map of all major LHC Grid sites [92]	54
3.11	Total CPU delivered by the LHC grid per month during Run 2, broken down by per-experiment usage [92] [97]	56
4.1	p^* distributions of final state muons from semileptonically decaying B^0 , B_s^0 , D^0 mesons and Λ_b^0 baryons in red, green, purple and blue, respectively. Due to the lower D^0 -mass the respective final state muon has less energy and hence a smaller p^* . Only muons from direct b -hadron decays are included. Figure credit to Dr. Bingxuan Liu.	64
4.2	Schematic drawing showing a jet cone in black with a b -hadron in the jet, decaying semileptonically at a secondary vertex shown in green. The final state muon is shown in green as well as the projection of its momentum transverse to the jet+muon axis, the p_T^{rel}	65
4.3	The dependence of the p_T^{rel} b -template shape on the p_T^{jet} and the decision of the b -tagging algorithm are shown on the in plots (a) and (b), respectively. In (a), the b -jet template is shown for three different p_T^{jet} -bins in green, red and blue with the statistical uncertainties depicted as error bars. A clear dependence on p_T^{jet} is observed. In (b), the b -jet template passing the 85% and 60% $MV2c10$ working points are compared to show the small dependence on tagger decision. Figure credit to Dr. Valentina Vecchio.	73
4.4	Distribution of p_T^{rel} for muons coming from direct and cascade decay of a B -hadron in three different p_T^{jet} bins. Figure credit to Dr. Valentina Vecchio.	74
4.5	Charm jets templates in different p_T^{jet} bins. Figure credit to Dr. Valentina Vecchio.	75
4.6	Muon p_T^{rel} spectra for the b -, c - and light-jet templates in yellow, blue and red, respectively. The heavy flavor templates are generated from simulation, while the light-jet template is extracted in a data-driven approach. Figure credit to Dr. Valentina Vecchio.	76
4.7	Prefit p_T^{rel} distributions. The distribution on the top is b -tagged by $MV2c10$ at $\varepsilon_b^{\text{nom}} = 85\%$, while the distribution on the bottom is untagged. The data is shown in black, while the templates are shown as a stack.	78
4.8	Postfit p_T^{rel} distributions. The distribution on the top is b -tagged by $MV2c10$ at $\varepsilon_b^{\text{nom}} = 85\%$, while the distribution on the bottom is untagged. The data is shown in black, while the templates are shown as a stack.	79
4.9	Falling p_T^{jet} spectra for the Run 1 (top) and Run 2 (bottom) MC. The Run 2 MC uses a different internal reweighting scheme, so the spectrum is sliced differently than in Run 1.	81
4.10	Falling p_T^{jet} spectra for the Run 1 (top) and Run 2 (bottom) MC, filtered to only include b -jets. The Run 2 MC uses a different internal reweighting scheme, so the spectrum is sliced differently than in Run 1.	82
4.11	Falling p_T^{jet} spectra for the Run 1 (top) and Run 2 (bottom) MC, filtered to only include light-flavor jets. The Run 2 MC uses a different internal reweighting scheme, so the spectrum is sliced differently than in Run 1.	83
4.12	p_T^{jet} distribution for samples of jets passing mu4j25 or (mu4j35 and mu4j25) triggers. The turn-on curve can be seen in the ratio plot at the bottom	84
4.13	ΔR distribution for samples of jets passing mu4j35 triggers with (red) and without (blue) spatial matching. The turn-on curve can be seen in the ratio plot at the bottom	86
4.14	ΔZ distribution for samples of jets passing mu4j35 triggers with (red) and without (blue) spatial matching. The turn-on curve can be seen in the ratio plot at the bottom	86

4.15	Comparison of the p_T^{jet} spectrum in $[20, 60]$ p_T bin between data and MC. Figure credit to Dr. Bingxuan Liu.	87
4.16	Scale factors applied to correct p_T^{jet} in MC in p_T^{jet} reweighting method of trigger correction. Figure credit to Dr. Bingxuan Liu.	88
4.17	Simulated b -tagging efficiency as a function of p_T^{jet} of jets containing muons (red curve), jets not containing muons (green curve) and their ratio (black curve). The semileptonic correction to p_T^{jet} applied in the bottom plot. Figure credit to Dr. Valentina Vecchio. . .	90
4.18	b -tagging efficiency in data and simulation as a function of p_T^{jet} for jet containing muons (top) and jets without muons (bottom). Figure credit to Dr. Valentina Vecchio.	92
4.19	Ratio between the b -tagging efficiency scale factor of jets with and without muons for the 77% working point as a function of p_T^{jet} . Figure credit to Dr. Valentina Vecchio. . .	93
4.20	Fraction of b -jets which are also $g \rightarrow b\bar{b}$ jets as a function of p_T^{jet} . Figure credit to Dr. Valentina Vecchio.	94
4.21	b -template comparison between inclusive b -jets (yellow curve) and gluon-splitting b -jets (blue curve). Top plot shows the p_T^{jet} bin between 30 and 40 GeV. Bottom plot shows the p_T^{jet} bin between 110 and 140 GeV. Figure credit to Dr. Valentina Vecchio.	95
4.22	p_T^{rel} distribution in data and MC after the template fit. The b -template here has the nominal amount of gluon-splitting as predicted by the unfiltered di-jet MC. Top plot shows the p_T^{jet} bin between 30 and 40 GeV. Bottom plot shows the p_T^{jet} bin between 110 and 140 GeV.	96
4.23	b -template comparison with nominal gluon-splitting (red) and 2.5-times enhanced gluon-splitting (blue). Top plot shows the p_T^{jet} bin between 30 and 40 GeV. Bottom plot shows the p_T^{jet} bin between 110 and 140 GeV. Figure credit to Dr. Valentina Vecchio.	97
4.24	p_T^{rel} distribution in data and MC after the template fit. The b -template here has 2.5 times the nominal amount of gluon-splitting as predicted by the unfiltered di-jet MC. Top plot shows the p_T^{jet} bin between 30 and 40 GeV. Bottom plot shows the p_T^{jet} bin between 110 and 140 GeV.	98
4.25	p_T^{jet} -dependent efficiencies (left) and scale factors (right) measured by the p_T^{rel} method for the <i>MV2c10</i> algorithm for the nominal efficiency of $\varepsilon_b^{\text{nom}} = 85\%, 77\%, 70\%$, and 60% (top to bottom). MC predictions are shown in gray while the data is depicted in black dots. The statistical and systematic uncertainties are shown in the green error bands. .	103
4.26	p_T^{jet} -dependent efficiencies (left) and scale factors (right) measured by the likelihood-based (top) and tag-and-probe (bottom) $t\bar{t}$ methods for the <i>MV2c10</i> algorithm for the nominal efficiency of $\varepsilon_b^{\text{nom}} = 70\%$. MC predictions are shown in red while the data is depicted in black dots. The statistical and systematic uncertainties are shown in the error bands. [81]	105
5.1	Cross-section plots for various SUSY production modes as a function of SUSY particle mass [129]	109
5.2	Exclusion results from ATLAS for stop pair-production as a function of stop mass and LSP mass for a few simplified SUSY models [139]	110
5.3	Exclusion results from ATLAS for gluino pair-production as a function of stop mass and LSP mass for a few simplified SUSY models [139]	110
5.4	Exclusion results from ATLAS for sbottom pair-production as a function of stop mass and LSP mass for a few simplified SUSY models [139]	111
5.5	Exclusion results from ATLAS for $C1N2$ electroweakino pair-production in WZ final states [139]	111
5.6	Exclusion results from ATLAS for $C1N2$ electroweakino pair-production in Wh final states [139]	112

5.7	Exclusion results from ATLAS for higgsino pair-production [139]	112
5.8	Exclusion results from ATLAS on a general gauge mediation model [139]	113
5.9	WW/WZ/Wh benchmark models with wino-dominant chargino-neutralino pair production decaying into bino-dominant LSP.	114
5.10	Neutralino-neutralino higgsino production model.	115
5.11	Reweighting the helicity angle of $\tilde{\chi}_1^\pm \tilde{\chi}_2^0 \rightarrow WZ \rightarrow qq\bar{q}\bar{q}$ signals with $(m_{\tilde{\chi}_1^\pm}, m_{\tilde{\chi}_2^0}) = (1000, 200)$ GeV. The black solid line is the nominal sample distribution. The blue dotted line is the distribution from MADSPIN interfaced between MADGRAPH and PYTHIA. The red solid line shows the distribution with both production and decay generated by MADGRAPH. Both the red and blue lines take boson polarization into account during decay chain simulation. The pink dotted line is the nominal sample after helicity angle reweighting: $w = 3 \sin^2 \theta^*/4$. (a) Helicity angle distribution for $Z \rightarrow q\bar{q}$. (b) Leading large- R mass and (c) D_2 (i.e. “2-prongedness”) distribution. Figure credit to Dr. Shion Chen.	119
5.12	Acceptance rate for events with exactly zero baseline-leptons (after overlap removal and $E_T^{\text{miss}} > 200$ GeV preselection) for various baseline lepton definitions. The acceptance is normalized to the ‘default’ setup, where electrons/muons pass $p_T > 6/5$ GeV, $ \eta < 2.47/2.5$ respectively as well as the Medium ID working point. The x-axis labels indicate the difference with respect to the ‘default’ setup. Figure credit to Dr. Shion Chen. . . .	121
5.13	The jet mass resolution as a function of p_T^{jet} for jets produced from a boosted W boson. Three different jet mass reconstruction algorithms are displayed: the calo-jet mass (m^{calo}), the track-assisted mass (m^{TA}), and the combined TA+calo mass (m^{comb}). [167]	122
5.14	Data-MC comparison of the mass (a) and D_2 (b) of large- R jets in a $t\bar{t}$ -enriched sample containing many W bosons. [172]	125
5.15	The combined L1 and HLT efficiency of the missing transverse energy trigger HLT_xe110_pu-fit_xe70_L1XE50 (primary chain in the beginning of 2018) and HLT_xe110_puFit_xe65_L1XE50 (primary chain since May 12th) as well as the efficiency of the corresponding L1 trigger L1_XE50 are shown as a function of the Z boson transverse momentum ($Z \rightarrow \mu\mu$ data was used to produce these plots). [177]	127
5.16	$\phi(E_T^{\text{miss}})$ before (black) and after (red) applying the dead tile jet veto. The boosted preselection is applied. Figure credit to Yuta Okazaki.	128
5.17	$\phi(E_T^{\text{miss}})$ before (black) and after (red) applying the dead tile jet veto. The boosted preselection with tightened $\min \Delta\phi(j, E_T^{\text{miss}})$ selection ($\min \Delta\phi(j, E_T^{\text{miss}}) > 0.4$) is applied. Figure credit to Yuta Okazaki.	129
5.18	Kinematic variables between data and MC in the boosted preselection region. Figure credit to Yuta Okazaki.	130
5.19	Non-collision background veto variables ($E_{T,\text{track}}^{\text{miss}}, \Delta\phi(E_T^{\text{miss}}, E_{T,\text{track}}^{\text{miss}})$) in (a,b) the boosted preselection region with $\min \Delta\phi(j, E_T^{\text{miss}}) > 0.4$, and (c,d) the boosted-preselection region with the $\min \Delta\phi(j, E_T^{\text{miss}}) > 2.9$, i.e. the non-collision-background-enhanced region. MC16a/d normalized to 80 fb^{-1} is used and overlaid with 2015-17 data. Figure credit to Dr. Shion Chen.	131
5.20	Plots of various kinematics at preselection level. Linear scale at left, log scale on right.	133
5.21	Illustration of the exclusive SRs in (a) 4Q and (b) 2B2Q category as function of reconstructed boson mass. The pink arrows represent the (approximate) mass window selection applied for reconstructed $W/Z/h$ -bosons. Overlap arises in the borders between SR bins involving $W \rightarrow q\bar{q}$ and $Z \rightarrow q\bar{q}$. Figure credit to Dr. Shion Chen.	135

5.22	$N - 1$ plots for 2B2Q boosted Wh SR. Wino-bino signal mass point (800 GeV NLSP, 200 GeV LSP) shown in grey. The plots on the right show the Z_n sensitivity as a function of selection criteria value.	138
5.23	$N - 1$ plots for 2B2Q boosted WZ SR. Wino-bino signal mass point (700 GeV NLSP, 100 GeV LSP) shown in grey. The plots on the right show the Z_n sensitivity as a function of selection criteria value.	139
5.24	$N - 1$ plots for 2B2Q boosted Zh SR. GGM higgsino signal mass point (500 GeV NLSP, 0 GeV LSP) shown in grey. The plots on the right show the Z_n sensitivity as a function of selection criteria value.	140
5.25	$N - 1$ plots for 2B2Q boosted ZZ SR. GGM higgsino signal mass point (500 GeV NLSP, 0 GeV LSP) shown in grey. The plots on the right show the Z_n sensitivity as a function of selection criteria value.	141
5.26	The expected sensitivity for Wh wino-bino signal search. Signal and background yields are estimated from simulation. Points inside the solid red curve have at least 3σ sensitivity, and points inside the dashed red curve have at least $ZN = 1.64$ (exclusion). Previously observed limits are shown in purple.	142
5.27	The expected sensitivity for WZ wino-bino signal search. Signal and background yields are estimated from simulation. Points inside the solid red curve have at least 5σ sensitivity, and points inside the dashed red curve have at least $ZN = 1.64$ (exclusion). Previously observed limits are shown in purple and orange.	143
5.28	The expected sensitivity for $Wh + WZ$ higgsino-bino signal search. Signal and background yields are estimated from simulation. Points inside the solid red curve have at least 3σ sensitivity, and points inside the dashed red curve have at least $ZN = 1.64$ (exclusion). Previously observed limits are shown in purple.	144
5.29	The expected sensitivity for the $Zh + ZZ$ GGM higgsino signal search as a function of gravitino mass (x-axis) versus branching ratio to the SM higgs (y-axis). Signal and background yields are estimated from simulation. Points inside the solid red curve have at least 5σ sensitivity, and points inside the dashed red curve have at least $ZN = 1.64$ (exclusion). Previously observed limits are shown in purple and teal.	145
5.30	An image to illustrate the basics of the ABCD method	146
5.31	A summary of the cuts used in each ABCD region	146
5.32	Basic ABCD results for Wh signal. Upper left: ABCD background yields. Upper right: background composition in regions A, B, C, D as piecharts. Lower left: checking the independence in $m_{T2}^{100}(J_1, J_2)$. Lower right: checking the independence in boson-cut variable.	147
5.33	Basic ABCD results for WZ signal. Upper left: ABCD background yields. Upper right: background composition in regions A, B, C, D as piecharts. Lower left: checking the independence in $m_{T2}^{100}(J_1, J_2)$. Lower right: checking the independence in boson-cut variable.	148
5.34	Basic ABCD results for Zh signal. Upper left: ABCD background yields. Upper right: background composition in regions A, B, C, D as piecharts. Lower left: checking the independence in $m_{T2}^{100}(J_1, J_2)$. Lower right: checking the independence in boson-cut variable.	149
5.35	Basic ABCD results for ZZ signal. Upper left: ABCD background yields. Upper right: background composition in regions A, B, C, D as piecharts. Lower left: checking the independence in $m_{T2}^{100}(J_1, J_2)$. Lower right: checking the independence in boson-cut variable.	150

5.36	Signal Contamination as a percentage of background yield in Wh ABCD non-SR Regions. Region A on top, B in center, C on the bottom. Previously excluded points are contained within the purple curve.	151
5.37	Signal Contamination as a percentage of background yield in WZ ABCD non-SR Regions. Region A on top, B in center, C on the bottom. Previously excluded points are contained within the orange and purple curves.	152
5.38	Estimated bias of background estimate in Wh region D due to signal presence in regions A, B, and C as a percentage of non-contaminated D background yield estimate	156
5.39	Estimated bias of background estimate in WZ region D due to signal presence in regions A, B, and C as a percentage of non-contaminated D background yield estimate	157
A.1	Lowest-order Feynman diagram for $\nu\bar{\nu} \rightarrow W^+W^-$	165
A.2	Tagged (left) and untagged (right) p_T^{rel} distributions for 20-30 GeV (top), 30-40 GeV (middle), and 40-50 GeV (bottom) p_T^{jet} bins using flavor fractions obtained by the log-likelihood fit.	171
A.3	Tagged (left) and untagged (right) p_T^{rel} distributions for 50-70 GeV (top), 70-90 GeV (middle), and 90-110 GeV (bottom) p_T^{jet} bins using flavor fractions obtained by the log-likelihood fit.	172
A.4	Tagged (left) and untagged (right) p_T^{rel} distributions for 110-140 GeV (top), 140-170 GeV (middle), and 170-200 GeV (bottom) p_T^{jet} bins using flavor fractions obtained by the log-likelihood fit.	173
A.5	Tagged (left) and untagged (right) p_T^{rel} distributions for 20-30 GeV (top), 30-40 GeV (middle), and 40-50 GeV (bottom) p_T^{jet} bins using flavor fractions obtained by the log-likelihood fit.	174
A.6	Tagged (left) and untagged (right) p_T^{rel} distributions for 50-70 GeV (top), 70-90 GeV (middle), and 90-110 GeV (bottom) p_T^{jet} bins using flavor fractions obtained by the log-likelihood fit.	175
A.7	Tagged (left) and untagged (right) p_T^{rel} distributions for 110-140 GeV (top), 140-170 GeV (middle), and 170-200 GeV (bottom) p_T^{jet} bins using flavor fractions obtained by the log-likelihood fit.	176
A.8	Tagged (left) and untagged (right) p_T^{rel} distributions for 20-30 GeV (top), 30-40 GeV (middle), and 40-50 GeV (bottom) p_T^{jet} bins using flavor fractions obtained by the log-likelihood fit.	177
A.9	Tagged (left) and untagged (right) p_T^{rel} distributions for 50-70 GeV (top), 70-90 GeV (middle), and 90-110 GeV (bottom) p_T^{jet} bins using flavor fractions obtained by the log-likelihood fit.	178
A.10	Tagged (left) and untagged (right) p_T^{rel} distributions for 110-140 GeV (top), 140-170 GeV (middle), and 170-200 GeV (bottom) p_T^{jet} bins using flavor fractions obtained by the log-likelihood fit.	179
A.11	Tagged (left) and untagged (right) p_T^{rel} distributions for 20-30 GeV (top), 30-40 GeV (middle), and 40-50 GeV (bottom) p_T^{jet} bins using flavor fractions obtained by the log-likelihood fit.	180
A.12	Tagged (left) and untagged (right) p_T^{rel} distributions for 50-70 GeV (top), 70-90 GeV (middle), and 90-110 GeV (bottom) p_T^{jet} bins using flavor fractions obtained by the log-likelihood fit.	181

A.13 Tagged (left) and untagged (right) p_T^{rel} distributions for 110-140 GeV (top), 140-170 GeV (middle), and 170-200 GeV (bottom) p_T^{jet} bins using flavor fractions obtained by the log-likelihood fit.	182
A.14 Background distribution without $\min \Delta\phi(j, E_T^{\text{miss}})$ cuts for regions A, B, C, and D (from left to right) in $\min \Delta\phi(j, E_T^{\text{miss}})$ (x-axis) versus boson-tagging cut decision (y-axis) . .	184
A.15 Signal distribution without $\min \Delta\phi(j, E_T^{\text{miss}})$ cuts for regions A, B, C, and D (from left to right) in $\min \Delta\phi(j, E_T^{\text{miss}})$ (x-axis) versus boson-tagging cut decision (y-axis)	184
A.16 Background distribution with $\min \Delta\phi(j, E_T^{\text{miss}})$ cuts for regions A, B, C, and D (from left to right) in $\min \Delta\phi(j, E_T^{\text{miss}})$ (x-axis) versus boson-tagging cut decision (y-axis) . .	184
A.17 Signal distribution with $\min \Delta\phi(j, E_T^{\text{miss}})$ cuts for regions A, B, C, and D (from left to right) in $\min \Delta\phi(j, E_T^{\text{miss}})$ (x-axis) versus boson-tagging cut decision (y-axis)	184
A.18 Background distribution without $\min \Delta\phi(j, E_T^{\text{miss}})$ cuts for regions A, B, C, and D (from left to right) in $\min \Delta\phi(j, E_T^{\text{miss}})$ (x-axis) versus $m_{T2}^{100}(J_1, J_2)$ (y-axis)	185
A.19 Signal distribution without $\min \Delta\phi(j, E_T^{\text{miss}})$ cuts for regions A, B, C, and D (from left to right) in $\min \Delta\phi(j, E_T^{\text{miss}})$ (x-axis) versus $m_{T2}^{100}(J_1, J_2)$ (y-axis)	185
A.20 Background distribution with $\min \Delta\phi(j, E_T^{\text{miss}})$ cuts for regions A, B, C, and D (from left to right) in $\min \Delta\phi(j, E_T^{\text{miss}})$ (x-axis) versus $m_{T2}^{100}(J_1, J_2)$ (y-axis)	185
A.21 Signal distribution with $\min \Delta\phi(j, E_T^{\text{miss}})$ cuts for regions A, B, C, and D (from left to right) in $\min \Delta\phi(j, E_T^{\text{miss}})$ (x-axis) versus $m_{T2}^{100}(J_1, J_2)$ (y-axis)	185
A.22 Background (colors) and signal (black) $\min \Delta\phi(j, E_T^{\text{miss}})$ distributions without $\min \Delta\phi(j, E_T^{\text{miss}})$ cuts for regions A, B, C, and D (from left to right)	186
A.23 Background (colors) and signal (black) $m_{T2}^{100}(J_1, J_2)$ distributions without $\min \Delta\phi(j, E_T^{\text{miss}})$ cuts for regions A, B, C, and D (from left to right)	186
A.24 Background (colors) and signal (black) $\min \Delta\phi(j, E_T^{\text{miss}})$ distributions with $\min \Delta\phi(j, E_T^{\text{miss}})$ cuts for regions A, B, C, and D (from left to right)	186
A.25 Background (colors) and signal (black) $m_{T2}^{100}(J_1, J_2)$ distributions with $\min \Delta\phi(j, E_T^{\text{miss}})$ cuts for regions A, B, C, and D (from left to right)	186
A.26 Background distribution without $\min \Delta\phi(j, E_T^{\text{miss}})$ cuts for regions A, B, C, and D (from left to right) in $\min \Delta\phi(j, E_T^{\text{miss}})$ (x-axis) versus boson-tagging cut decision (y-axis) . .	187
A.27 Signal distribution without $\min \Delta\phi(j, E_T^{\text{miss}})$ cuts for regions A, B, C, and D (from left to right) in $\min \Delta\phi(j, E_T^{\text{miss}})$ (x-axis) versus boson-tagging cut decision (y-axis)	187
A.28 Background distribution with $\min \Delta\phi(j, E_T^{\text{miss}})$ cuts for regions A, B, C, and D (from left to right) in $\min \Delta\phi(j, E_T^{\text{miss}})$ (x-axis) versus boson-tagging cut decision (y-axis) . .	187
A.29 Signal distribution with $\min \Delta\phi(j, E_T^{\text{miss}})$ cuts for regions A, B, C, and D (from left to right) in $\min \Delta\phi(j, E_T^{\text{miss}})$ (x-axis) versus boson-tagging cut decision (y-axis)	187
A.30 Background distribution without $\min \Delta\phi(j, E_T^{\text{miss}})$ cuts for regions A, B, C, and D (from left to right) in $\min \Delta\phi(j, E_T^{\text{miss}})$ (x-axis) versus $m_{T2}^{100}(J_1, J_2)$ (y-axis)	188
A.31 Signal distribution without $\min \Delta\phi(j, E_T^{\text{miss}})$ cuts for regions A, B, C, and D (from left to right) in $\min \Delta\phi(j, E_T^{\text{miss}})$ (x-axis) versus $m_{T2}^{100}(J_1, J_2)$ (y-axis)	188
A.32 Background distribution with $\min \Delta\phi(j, E_T^{\text{miss}})$ cuts for regions A, B, C, and D (from left to right) in $\min \Delta\phi(j, E_T^{\text{miss}})$ (x-axis) versus $m_{T2}^{100}(J_1, J_2)$ (y-axis)	188
A.33 Signal distribution with $\min \Delta\phi(j, E_T^{\text{miss}})$ cuts for regions A, B, C, and D (from left to right) in $\min \Delta\phi(j, E_T^{\text{miss}})$ (x-axis) versus $m_{T2}^{100}(J_1, J_2)$ (y-axis)	188
A.34 Background (colors) and signal (black) $\min \Delta\phi(j, E_T^{\text{miss}})$ distributions without $\min \Delta\phi(j, E_T^{\text{miss}})$ cuts for regions A, B, C, and D (from left to right)	189
A.35 Background (colors) and signal (black) $m_{T2}^{100}(J_1, J_2)$ distributions without $\min \Delta\phi(j, E_T^{\text{miss}})$ cuts for regions A, B, C, and D (from left to right)	189

[illegible]

A.60 Background (colors) and signal (black) $\min \Delta\phi(j, E_T^{\text{miss}})$ distributions with $\min \Delta\phi(j, E_T^{\text{miss}})$ cuts for regions A, B, C, and D (from left to right)	195
A.61 Background (colors) and signal (black) $m_{T2}^{100}(J_1, J_2)$ distributions with $\min \Delta\phi(j, E_T^{\text{miss}})$ cuts for regions A, B, C, and D (from left to right)	195

CHAPTER 1

Overview

“The future came and went in the mildly discouraging way that futures do.”

— Neil Gaiman, *The Nice and Accurate Prophecies of Agnes Nutter, Witch* [1]

I started at the University of Pennsylvania in August 2014. My first year was spent entirely on coursework; I began working on research in the summer of 2015, which I spent at CERN. The rest of my PhD was spent on physics analysis, with the majority of my time being spent on p_T^{rel} . I spent time on several “dead-end” projects, which I shall not describe. The following is a brief chronological description of my role in various projects during my PhD.

p_T^{rel} Analysis

I joined the p_T^{rel} analysis team (at the time consisting only of Ingo Burmeister, a doctoral student at TU Dortmund) in the summer of 2015 for my ATLAS authorship qualification task. My initial tasks were to validate the muon-filtered di-jet MC, produce muon-in-jet trigger turn-on curves (described in Section 4.5.2), and document the p_T^{rel} calibration. In the fall of 2015, an unfortunate discovery was made: the muon-in-jet triggers used to collect data for p_T^{rel} were improperly configured (specifically, the spatial ΔZ match between muons and the primary vertex was done incorrectly), so no useful muon-in-jet trigger data was collected for 2015. We attempted to use single-jet trigger data instead; the combined effect of the large single-jet trigger prescales and the low cross-section for muon-in-jet production in single-jet events resulted in insufficient statistics for the p_T^{rel} calibration. Nevertheless, we moved forward in the fall and winter of 2015, using the time to make software improvements and ensure that the analysis pipeline was working. In 2016, the ΔZ trigger problem was fixed and data was collected, allowing me to validate the muon-in-jet triggers and run the entire p_T^{rel} analysis pipeline. Bingxuan (Bing) Liu, a postdoc at Argonne, joined the p_T^{rel} team in 2016 as well; his

initial task was to implement p_T^{rel} in the ATLAS fast physics monitoring framework TADA [2]¹. Ingo graduated in 2017 using the p_T^{rel} results from 2016 data, and the p_T^{rel} team attempted to publish an internal ATLAS note documenting these results, spending a few months “cleaning up” details from the analysis skipped initially to expedite Ingo’s graduation. In the meantime, however, ATLAS had switched major software releases (from Release 20.7 to Release 21²); because the p_T^{rel} analysis was implemented in Release 20.7, it was eventually considered too old for publication. The Release 20.7 p_T^{rel} analysis framework was also built on and used many features from ROOT Version 5; many of these features, such as symbolic linking to precompiled libraries, were extremely unwieldy and system-dependent, slowing down the production of results.

In the fall of 2017, the p_T^{rel} team was contacted by Valentina Vecchio and her advisor, Giuseppe Salamanna³. Valentina wished to measure the fraction $\frac{t \rightarrow bW}{t \rightarrow qW}$; measuring the deviation of this value from 1 (i.e. measuring the value of $|V_{tb}|$) is a probe of SM top physics. This measurement requires a very precise measurement of the flavor-tagging efficiency in data *without* assuming that $\frac{t \rightarrow bW}{t \rightarrow qW} = 1$ (as most flavor-tagging calibrations do); p_T^{rel} is $b\bar{b}$ -based, making it the perfect candidate. We decided as a team to abandon Release 20.7 publication plans and focus on revamping the analysis for this measurement in Release 21. I worked closely with Valentina and Bing to re-implement the p_T^{rel} analysis framework for Release 21 and ROOT Version 6, making the analysis more reliable and easier to run. Using my experience with flavor-tagging derivation software, I also assisted Valentina in truth-level hadronization studies to better understand the effect of gluon-splitting on our p_T^{rel} templates. In the spring of 2018, we prepared an internal ATLAS note using the Release 21 results; however, the analysis had changed dramatically between Release 20.7 and Release 21 to reduce the uncertainty on our scale factors, requiring a corresponding improvement in our previous systematic uncertainty evaluation methods. We worked to re-evaluate the systematic uncertainties to our conveners’ satisfaction, but were unable to complete the analysis in time for Valentina’s defense.

As of writing, the Release 21 p_T^{rel} analysis results have still not been released, as there are still a few systematic uncertainties left to be evaluated (described in Section 4.9). Valentina (who is now a postdoc at University of Manchester) and Bing shall finalize this analysis in ~ 2020 , possibly making preparations for LHC Run 3 as well. In October 2019, Valentina began working with a qualification student at Manchester on p_T^{rel} MC; Bing and Valentina hope to have the result out within a year or so.

¹This proved to be impossible due to technical limitations of the TADA framework.

²Don’t ask why they’re named as they are – I have no idea!

³Both from Roma Tre.

Flavor-Tagging Derivation Software

I began to work on flavor-tagging derivations (see Section 3.6.5) initially as a part of my work on p_T^{rel} muon-in-jet triggers (see Section 4.5.2); I had to make several changes to the designated p_T^{rel} DAODs in order to complete the trigger studies. I served as the flavor-tagging derivation software contact from October 2016 to December 2018. In general, my tasks as derivation software contact were to maintain and improve the flavor-tagging derivation software and request derivation production through the official ATLAS pipeline whenever flavor-tagging users needed new derivation samples. In addition to supporting flavor-tagging users, I assisted in several major changes to ATLAS software (listed approximately in chronological order):

- ATLAS changed internal software releases, from Release 20.7 to Release 21. This also involved a brand new way of setting up derivation tasks, using the multi-process version of the ATLAS reconstruction software called [Athena Multi-Process \(AthenaMP\)](#) [3].
- ATLAS switched our version control software from SVN to git/Gitlab. At the same time, ATLAS implemented a continuous-integration development practice based on the Jenkins pipeline tool.
- Due to success in data-taking in Run 2, ATLAS implemented a policy of removing old/unused datasets and set stricter size caps on derivation sizes.
- The actual flavor-tagging of jets was moved from xAOD production to DAOD production

These tasks are discussed in-depth in Section 3.6.7.

Fully-Hadronic Electroweak SUSY

I joined the FH EWK SUSY search in January of 2019 at the suggestion of Joana Miguens, a postdoc here at Penn. Shion Chen, another Penn postdoc, had already been selected as the co-convenor for this analysis, so he guided my decision-making when choosing projects. In the spring of 2019, I studied the wino-bino to higgsino-bino reinterpretation (Section 5.6) and began developing the boosted 2B2Q signal regions (Section 5.4). In August 2019, I began studying the ABCD method of background estimation; at the same time, physicists from other groups in the fully-hadronic electroweak SUSY team began to investigate other background estimation methods using 1-lepton or 2-lepton regions. In October 2019, I finalized my SR definition and ABCD method results. During

this time, Joe Mullin (another graduate student at Penn) has worked on truth-level MC studies of $t\bar{t}$ backgrounds. He and Shion will continue to work on this search after my graduation.

Figure Credits

There are several figures produced during the course of my research for this thesis for which I cannot take credit. Rather than recreate or copy these figures from scratch, I want to credit the physicists responsible for this work. Dr. Shion Chen (Penn) created Figures 2.11, 5.11, 5.12, 5.19, and 5.21. Dr. Valentina Vecchio (Manchester) created Figures 4.3, 4.4, 4.5, 4.6, 4.17, 4.18, 4.19, 4.20, 4.21, and 4.23. Dr. Bingxuan Liu (Argonne) created Figures 4.1, 4.15, and 4.16. Yuta Okazaki (Kyoto) created Figures 5.16, 5.17, and 5.18.

CHAPTER 2

Theoretical Framework

*“My mind now turns to stories of bodies changed
Into new forms. O Gods, inspire my beginnings
(For you changed them too) and spin a poem that extends
From the world’s first origins down to my own time.”*

— Ovid, *Metamorphoses* [4]

This chapter introduces the theoretical framework used throughout this thesis. First, the Standard Model of particle physics is outlined, then the physics of b -quark and B -hadrons is detailed. After listing some of the deficiencies of the Standard Model, a potential solution is presented: the theory of supersymmetry.

2.1 Lagrangians in Quantum Field Theories

Before discussing particle physics, we need to begin with some mathematical formalism.

2.1.1 Lagrangian Field Theory

The [action](#) is a fundamental quantity of a system from which one can recover the equations of motion [5]. The action (denoted S) can always be written as an integral of a function we shall call the [Lagrangian](#), denoted L . The Lagrangian can be written as a spatial integral of a Lagrangian density, denoted \mathcal{L} . The action of a field ϕ can be written in terms of ϕ and its derivatives $\partial_\mu\phi$ like so:

$$S = \int L dt = \int \mathcal{L}(\phi, \partial_\mu\phi) d^4x \quad (2.1)$$

For the rest of this thesis, the term “Lagrangian” shall refer to the Lagrangian density \mathcal{L} . When a system evolves from one configuration at time t_0 to another at time t_1 , it does so along the “path”

in configuration space for which S is a stationary point (usually a minimum). This is called the *principle of least action*, written formally like so:

$$0 = \delta S \quad (2.2)$$

If our system is a field ϕ , then we can use the above condition to derive the *Euler-Lagrange Field Equation* to constrain our set of possible Lagrangians [6]⁴:

$$\frac{\partial \mathcal{L}}{\partial \phi} - \frac{\partial}{\partial x} \left(\frac{\partial \mathcal{L}}{\partial (\partial \phi / \partial x)} \right) - \frac{\partial}{\partial t} \left(\frac{\partial \mathcal{L}}{\partial \dot{\phi}} \right) = 0 \quad (2.3)$$

The study of fields and physical systems is intrinsically tied to the study of Lagrangians.

2.1.2 Invariance and the Standard Model

Having expressed the physical laws of fields in terms of a Lagrangian, we want to consider what happens when we apply mathematical transformations to those fields⁵. A system of fields in which the physical laws do not change after applying a transformation is said to be *invariant* or *symmetric* under that transformation. We can classify all transformations as either *global* (same transformation carried out at all space-time points) or *local* (transformation differs across space-time points) [6]. Sometimes a system of fields is invariant under a *group* of local transformations; we call this group a *gauge group*. We often describe the symmetries of a Lagrangian in terms of gauge groups.

If a Lagrangian is invariant under a continuous local transformation of its field $\phi(x)$ ⁶:

$$\phi(x) \rightarrow \phi'(x) = \phi(x) + \alpha \Delta \phi(x) \quad (2.4)$$

then by Noether's theorem [5], it has an associated charge/current which remains constant in time. In simpler terms, this means that every invariance/symmetry of a system has an associated conserved current.

This thesis shall describe the physics of matter and energy in terms of the “Standard Model” (Standard Model of particle physics (SM)) Lagrangian. This Lagrangian is invariant under gauge group $SU(3) \times SU(2) \times U(1)$. The “meaning” of each of these subgroups and their associated conserved currents will be discussed in Section 2.2.

⁴I've written the one-dimensional equation here, but one can easily generalize to three dimensions.

⁵A very simply example of a transformation is a change of coordinate system (e.g. translating the origin, rotation) in classical mechanics.

⁶where α is an infinitesimal parameter and $\Delta \phi$ is a deformation of the field

2.2 Introduction to the Standard Model

Particle physicists seek to explain the relationship between matter and energy in order to better understand the physical world. This relationship is best understood in terms of interactions between [elementary particles](#) via fundamental forces.

The elementary particles can be divided into four major classes (quarks, leptons, force carriers, and the Higgs boson) [7]:

- Quarks:
 - Up-type quarks (charge⁷=2/3): up, charm, top.
 - Down-type quarks (charge=-1/3): down, strange, bottom.
- Leptons:
 - Charged leptons: electron, muon, and tau.
 - Neutral leptons (neutrinos): ν_e , ν_μ , and ν_τ .
- Force Carriers: W^\pm , Z , photon, and gluon.
- Higgs boson (excitation of Higgs field).

The force carriers and Higgs have [spin](#) +1 and 0, respectively, and are known as [bosons](#). The leptons and quarks have half-integer spin and are called [fermions](#). The fermions can also be listed in terms of “generations”; Table 2.1⁸ lists all known elementary particles in this way. In addition to the particles listed, each quark and lepton has a matching [antiparticle](#) with the same mass but opposite charge.

All other particles are formed by combining elementary particles. Particles made of two or more quarks are called [hadrons](#). Specifically, particles formed from three quarks are called [baryons](#) and particles formed from two quarks are called [mesons](#). For example, a proton is a baryon formed by two up quarks and a down quarks (total charge +1) and a negative pion (π^-) is a meson formed by a down quark and an anti-up quark (total charge -1).

The interactions between elementary particles can be summarized in the [SM](#) of particle physics, a theory describing three of the four fundamental forces of nature ([electromagnetic](#), [weak](#), and [strong](#) forces, but not the gravitational force). Each of the three forces in the SM is described by a

⁷Note that in this thesis “charge” will always refer to electrical charge unless otherwise specified.

⁸Top quark mass from direct measurements.

Quantum Field Theory (QFT) involving the exchange of a spin-1 boson (called a gauge boson) [7]. The electromagnetic force is carried by the photon (γ), the weak force is carried by the W^\pm and Z bosons, and the strong force is carried by gluons (g). The distance scales and relative strength of these forces are summarized in Table 2.2⁹.

The electromagnetic force (also known as the Lorentz force) is the force exerted on a charged particle moving through a magnetic and/or electric field. It has no effect on chargeless particles. The electromagnetic force is mediated by photons, which are chargeless and massless.

The strong force binds hadrons together [8]. It is called “strong” because it is the strongest of the four fundamental forces. The strong force is mediated by gluons, which are chargeless and massless. This force only effects particles with **color charge**; whereas electromagnetic charge involves a single conserved charge quantity, color charge consist of *three* conserved quantities (“red”, “green”, and “blue” charge). Instead of calling these charges “positive” and “negative”, we call them “color” and “anticolor”. Every quark has a color charge, and every gluon is a mixture of two colors and/or anticolors. Leptons do not have any color and do not experience the strong force. Baryons and mesons must be color-neutral. For example, when a π^- is formed from a down and anti-up quark, these quarks must be red-antired, green-antigreen, or blue-antiblue. A baryon (antibaryon) is color-neutral when its **partons** are red-green-blue (antired-antigreen-antiblue).

The weak force provides the mechanism of interaction by which nuclear beta occurs, as shown in Figure 2.1 [9]. It also the only force which allows for “flavor changing”, interactions where a quark changes into a different type of quark via a W^\pm boson. Just as the electromagnetic force conserves charge and the strong force conserves color, the weak force conserves a value called **weak isospin**. The weak force is mediated by W^+ , W^- , and Z bosons. All three are massive, but the W^+ and W^- are charged whereas the Z is neutral.

The final SM particle, the Higgs boson, is incorporated to fix several theoretical problems with the SM, one of which will be highlighted by working through the example of $\nu_e + \bar{\nu}_e \rightarrow W^+ + W^-$ in Section 2.2.2. Before jumping into the Higgs mechanism, however, we must first discuss **electroweak unification**.

⁹Strengths given relative to strong force. Of course, the “strength” of a force depends on the nature of and distance from the source. These are just “ballpark” numbers. The weak and electromagnetic forces can be unified into a single field with $SU(2) \times U(1)$ gauge group.

	Quarks					Leptons			
	particle	charge	spin	mass [GeV/c ²]		particle	charge	spin	mass [GeV/c ²]
Gen. I	up	+2/3	1/2	0.0022	+0.0005 -0.0004	electron	-1	1/2	0.0005109989461 ±0.0000000000031
	down	-1/3	1/2	0.0047	+0.0005 -0.0003	electron neutrino	0	1/2	< 2 × 10 ⁻⁹
Gen. II	charm	+2/3	1/2	1.275	+0.025 -0.035	muon	-1	1/2	0.1056583745 ±0.0000000024
	strange	-1/3	1/2	0.095	+0.009 -0.003	muon neutrino	0	1/2	< 2 × 10 ⁻⁹
Gen. III	top	+2/3	1/2	173.0	±0.4	tau	-1	1/2	1.77686 ±0.00012
	bottom	-1/3	1/2	4.18	+0.04 -0.03	tau neutrino	0	1/2	< 2 × 10 ⁻⁹

		Force Carriers		
Electromagnetic	particle	charge	spin	mass [GeV/c ²]
	photon	0	1	0
Weak	W ⁺ boson	+1	1	80.379 ±0.012
	W ⁻ boson	-1	1	80.379 ±0.012
	Z boson	0	1	91.1876 ±0.0021
Strong	gluon	0	1	0

		Higgs		
Higgs	particle	charge	spin	mass [GeV/c ²]
	Higgs boson	0	0	125.18 ±0.16

Table 2.1: Summary of all known elementary particles [10]

Force	Force Carrier	Range	Strength	Gauge Group
Electromagnetic	photon	infinite	10 ⁻²	U(1)
Weak	W ⁺ , W ⁻ , and Z bosons	10 ⁻¹⁸ m	10 ⁻¹³	SU(2)
Strong	gluon	10 ⁻¹⁵ m	10	SU(3)
Gravity (not in SM)	graviton (theorized)	infinite	10 ⁻⁴²	none

Table 2.2: Summary of the four fundamental forces of nature [9] [7]

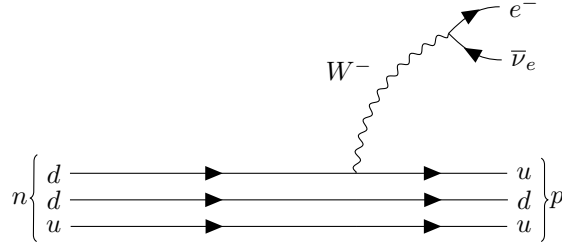


Figure 2.1: Nuclear Beta Decay of a neutron into a proton.

2.2.1 Electroweak Unification

Let's turn our attention back to the gauge groups of the SM, i.e groups of local transformations under which the SM Lagrangian is invariant. As mentioned in Section 2.1, the gauge group of the SM is $SU(3) \times SU(2) \times U(1)$. We will focus on the *electroweak* component of this group: $SU(2) \times U(1)$; a derivation of the $SU(3)$ symmetry of the strong gauge group can be found in Ref [7].

2.2.1.1 $U(1)$ & Electromagnetism

To understand the gauge group and boson of the EM field, let's work through a basic derivation of its Lagrangian. We know the Dirac field is *fermionic*, i.e. it obeys Fermi-Dirac statistics and its quanta are fermions. Therefore, let's start with the Lagrangian of a free Dirac fermion:

$$\mathcal{L}_{\text{Dirac}} = \bar{\psi}(i\gamma^\mu \partial_\mu - m)\psi \quad (2.5)$$

$\mathcal{L}_{\text{Dirac}}$ is invariant under a global transformation:

$$\psi(x) \rightarrow \exp[-i\alpha]\psi(x) \quad (2.6)$$

where α is some real constant. Applying this transformation multiple times in succession ($\psi \rightarrow \psi' \rightarrow \psi''$) returns a transformation in the same form:

$$\psi'' = \exp[-i\beta]\psi', \psi' = \exp[-i\alpha]\psi \implies \psi'' = \exp[-i(\alpha + \beta)]\psi = \exp[-i(\delta)]\psi \quad (2.7)$$

where $\delta = \alpha + \beta$. This property is called [unitarity](#), and the group of all such 1-dimensional transformations is called $U(1)$.

If, however, we try a *local* transformation (i.e. $\alpha = \alpha(x)$), then the free Dirac Lagrangian is no longer invariant [\[11\]](#):

$$\partial_\mu \psi(x) \rightarrow \exp[-i\alpha(x)](\partial_\mu - i\partial_\mu \alpha(x))\psi(x) \quad (2.8)$$

To fix this, we'll introduce a new spin-1 field $A_\mu(x)$:

$$A_\mu(x) \rightarrow A'_\mu(x) \equiv A_\mu(x) - \frac{1}{e}\partial_\mu \alpha(x) \quad (2.9)$$

and define the covariant derivative:

$$D_\mu \psi(x) \equiv \partial_\mu + ieA_\mu \quad (2.10)$$

If we substitute D_μ instead of ∂_μ into Equation (2.5), our Lagrangian is now invariant under a local $U(1)$ symmetry:

$$\mathcal{L} = \bar{\psi}(i\gamma^\mu D_\mu - m)\psi = \mathcal{L}_{\text{Dirac}} - e\bar{\psi}i\gamma^\mu A_\mu\psi \quad (2.11)$$

This Lagrangian described interactions between a Dirac spinor and a gauge field A_μ .

The only term missing to make this Lagrangian complete is a gauge-invariant kinetic term:

$$\mathcal{L}_{\text{Kin}} = -\frac{1}{4}F_{\mu\nu}(x)F^{\mu\nu}(x) \quad (2.12)$$

where $F_{\mu\nu} \equiv \partial_\mu A_\nu - \partial_\nu A_\mu$ is the electromagnetic field strength tensor [6]. Therefore, our [Quantum Electrodynamics \(QED\)](#) Lagrangian is:

$$\mathcal{L}_{\text{QED}} = \mathcal{L}_{\text{Dirac}} - e\bar{\psi}\gamma^\mu A_\mu\psi + \mathcal{L}_{\text{Kin}} \quad (2.13)$$

\mathcal{L}_{QED} is preserved under the group $U(1)$ of local 1-dimensional gauge transformations. As mentioned in Section 2.1, this implies that there is a conserved current associated with this invariance. For QED, the associated conserved current is:

$$J_\mu = \bar{\psi}\gamma^\mu\psi \quad (2.14)$$

2.2.1.2 Unifying the Electromagnetic and Weak Forces

Following similar arguments, one can show that the gauge group of the weak force must be $SU(2)$ [7], with local invariance under the following transformation:

$$\psi(x) \rightarrow \exp[ig_W\alpha(x) \cdot \mathbf{T}]\psi(x) \quad (2.15)$$

where $\mathbf{T} = \frac{1}{2}\boldsymbol{\sigma}$ are the three generators of the $SU(2)$ group, written in terms of Pauli spin matrices $\boldsymbol{\sigma}$. These generators $\boldsymbol{\sigma}\boldsymbol{\sigma}$ are 2×2 spin-matrices; therefore, the wavefunction $\psi(x)$ must be written as a two-component “weak isospin doublet”. This results in three associated gauge fields, $W^{(1)}$, $W^{(2)}$, and $W^{(3)}$.

The charged-current weak interaction (i.e. interactions mediated by W^\pm bosons) only couples to left-handed particle [chiral](#) states (or right-handed antiparticle chiral states). Keeping this constraint in mind, we can write the three associated weak currents like so:

$$j_1^\mu = \frac{g_W}{2}\bar{\psi}_L\gamma^\mu\sigma_1\psi_L, \quad j_2^\mu = \frac{g_W}{2}\bar{\psi}_L\gamma^\mu\sigma_2\psi_L, \quad j_3^\mu = \frac{g_W}{2}\bar{\psi}_L\gamma^\mu\sigma_3\psi_L \quad (2.16)$$

where ψ_L is a left-handed spinor (e.g. $(\begin{smallmatrix} \nu_L \\ e_L \end{smallmatrix})$) and $\bar{\psi}_L$ is a left-handed chiral adjoint spinor (e.g. $(\begin{smallmatrix} \bar{\nu}_L \\ \bar{e}_L \end{smallmatrix})$). In fact, we can identify the physical W^\pm bosons and their associated currents with linear combinations of $W^{(k)}$ and j_k^μ ($k = 1, 2, 3$):

$$W_\mu^\pm = \frac{1}{\sqrt{2}}(W_\mu^{(1)} \mp iW_\mu^{(2)}), \quad j_\pm^\mu = \frac{g_W}{\sqrt{2}}\bar{\psi}_L\gamma^\mu\sigma_\pm\psi_L \quad (2.17)$$

where $\sigma_\pm = \frac{1}{2}(\sigma_1 \pm i\sigma_2)$ are the weak isospin raising and lowering operators.

It's very tempting to identify the third conserved current, j_3^μ with the Z -boson; we know, however, that the Z boson couples to both left- and right-handed chiral states, whereas this current only couples to left-handed particles and right-handed antiparticles. Instead, let's follow a clever leap to

the electroweak model of Glashow, Salam, and Weinberg (GSW). We'll start by re-identifying the local gauge symmetry of electromagnetism, changing from $U(1)$ to $U(1)_Y$:

$$\psi(x) \rightarrow \exp[i g' \frac{Y}{2} \zeta(x)] \psi(x) \quad (2.18)$$

resulting in a new gauge field B_μ and a new conserved charge Y with associated current j_Y^μ . We can associate the Z -boson gauge field Z_μ to electromagnetic gauge field A_μ from our previous derivation to B_μ and $W^{(3)}$ via the weak mixing angle θ_W :

$$A_\mu = +B_\mu \cos\theta_W + W_\mu^{(3)} \sin\theta_W, \quad Z_\mu = -B_\mu \sin\theta_W + W_\mu^{(3)} \cos\theta_W \quad (2.19)$$

We can also write their associated currents as a linear combination of j_Y^μ and j_3^μ :

$$j_{em}^\mu = j_Y^\mu \cos\theta_W + j_3^\mu \sin\theta_W, \quad j_Z^\mu = -j_Y^\mu \sin\theta_W + j_3^\mu \cos\theta_W \quad (2.20)$$

By unifying our descriptions of the electromagnetic and weak gauge groups into $U(1)_Y \times SU(2)_L$, we can now write down gauge fields and conserved currents for all four electroweak bosons. We can associate the electromagnetic coupling strength g' and the weak coupling strength g_W using θ_W like so:

$$g_W \sin\theta_W = g' \cos\theta_W \quad (2.21)$$

An astute reader may have noticed a small problem with this result: the fields Z_μ , $W^{(1)}$, $W^{(2)}$, and $W^{(3)}$ don't have any mechanism to provide them with mass! We *know* experimentally that the weak bosons are massive and the photon is massless; how can we couple the electromagnetic and weak forces, but only give mass to the weak bosons? Our solution lies in the Higgs boson: after electroweak symmetry breaking (discussed in the next section), some of the fields associated with the Higgs can be “eaten” by the W^\pm and Z bosons to give them mass. The photon does not “eat” a field associated to the Higgs and stays massless. In this way, electroweak symmetry breaking and the Higgs boson fix one of the biggest theoretical problems in the SM by providing a mechanism to generate the weak boson masses. The next section shall provide another motivation for the Higgs boson's existence and describe electroweak symmetry breaking in qualitative terms.

2.2.2 Motivating the Higgs Boson

The Higgs boson was postulated in 1964 and incorporated into the SM in 1967 [12]. The addition of the Higgs solved many known problems in the SM. In the previous section, we showed that one can describe the W^\pm and Z bosons by unifying the electromagnetic and weak forces, but that

something else (i.e. the Higgs mechanism) is needed to provide them with mass. Similarly, without a Higgs boson, one can show that the cross-section for $\nu_e + \bar{\nu}_e \rightarrow W^+ + W^-$ scattering grows with the momenta s of the incoming particles. An in-depth derivation of this result at first-order can be found in Appendix A.1; adding the second-order terms makes the problem even worse, with the cross-section growing as s^2 . Adding the Higgs boson introduces additional diagrams which will cancel out these divergences¹⁰. The next section shall describe how electroweak symmetry is spontaneously broken by the Higgs mechanism.

2.2.3 What is the Higgs Boson?

Prior to its discovery in 2012, physicists knew that the Higgs mechanism (or something similar) must exist because the weak force propagators (W^\pm and Z bosons) need a mechanism to provide their masses and to cancel certain divergent scattering cross-sections, such as $\nu_e + \bar{\nu}_e \rightarrow W^+ + W^-$. This section will begin with a brief explanation of how particles acquire mass through interactions with the Higgs boson (electroweak symmetry breaking) and conclude with a description of properties of the Higgs boson.

First, in order to understand spontaneous symmetry breaking, let's consider a complex scalar field [7]:

$$\phi = \frac{1}{\sqrt{2}}(\phi_1 + i\phi_2) \quad (2.22)$$

The corresponding Lagrangian is:

$$\mathcal{L} = (\partial_\mu \phi)^* (\partial^\mu \phi) - V(\phi), \text{ with } V(\phi) = \mu^2(\phi^* \phi) + \lambda(\phi^* \phi)^2 \quad (2.23)$$

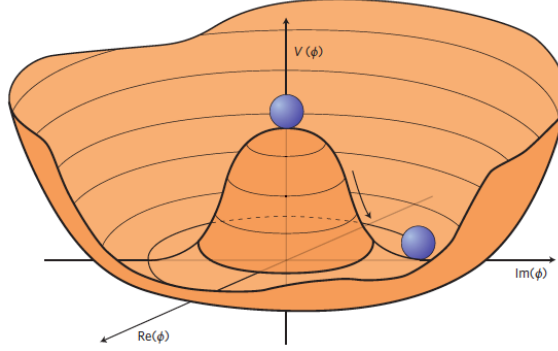
Expressed in terms of the real scalar fields ϕ_1 and ϕ_2 , this can be written as:

$$\mathcal{L} = \frac{1}{2}(\partial_\mu \phi_1)(\partial^\mu \phi_1) + \frac{1}{2}(\partial_\mu \phi_2)(\partial^\mu \phi_2) - \frac{1}{2}\mu^2(\phi_1^2 + \phi_2^2) - \frac{1}{4}\lambda(\phi_1^2 + \phi_2^2)^2 \quad (2.24)$$

We would like to check the vacuum expectation value, i.e. the expected value of this field in a vacuum, by finding the value(s) of ϕ which minimizes the potential term of the Lagrangian. For this minimum to be finite, $\lambda > 0$. If we choose $\mu^2 > 0$, then the minimum of the potential occurs when $\phi_1 = \phi_2 = 0$. If, however, $\mu^2 < 0$, the field potential has an infinite set of minima defined like so and visualized in Figure 2.2 [14]:

$$\phi_1^2 + \phi_2^2 = \frac{-\mu^2}{\lambda} = v^2 \quad (2.25)$$

¹⁰See Ref [13], Section 6.5 for an in-depth look at these cancellations.

Figure 2.2: Visualizing the Higgs potential when $\mu^2 < 0$ [14]

Obviously the physical vacuum state can only have *one* value, corresponding to a particular point satisfying this equation. By “falling” into a single stable vacuum state, the symmetry of this potential is *spontaneously* broken.

In the SM, we require not one, but *two* complex scalar fields: a neutral field (to give mass to Z bosons) and a charged field (for the W^\pm bosons). The Higgs field can be shown to give the gauge bosons and fermions their mass by expanding the Higgs field about its minimum and identifying the mass terms of the Lagrangian. Rather than reproduce the entire argument for acquiring Z and W^\pm masses here, the reader is encouraged to follow the discussion in Ref [7].

The Higgs boson discovered at the LHC in 2012 is chargeless and has a mass of 125.6 GeV and spin = 0 [15]. Its branching ratios to SM particles have been predicted (but not all observed). The most important decay modes with [branching ratios](#) are listed in Table 2.3 [10]. The largest [branching ratio \(BR\)](#) is $H \rightarrow b\bar{b}$; a Higgs boson decays to a $b\bar{b}$ pair about 58.4% of the time. This decay mode will be important for the [Beyond the Standard Model \(BSM\)](#) search described in Chapter 5.

Decay Channel	Branching Ratio	Observed?
$H \rightarrow \gamma\gamma$	2.27×10^{-3}	Yes
$H \rightarrow ZZ$	2.62×10^{-2}	Yes
$H \rightarrow W^+W^-$	2.14×10^{-1}	Yes
$H \rightarrow \tau^+\tau^-$	6.27×10^{-2}	Yes
$H \rightarrow b\bar{b}$	5.84×10^{-1}	Yes
$H \rightarrow Z\gamma$	1.53×10^{-3}	No
$H \rightarrow \mu^+\mu^-$	2.18×10^{-4}	No

Table 2.3: Summary of the major decay modes of the Higgs boson

2.2.4 Theory of Flavor Physics

In Section 2.2, all known elementary particles were described in very basic detail. This section will provide details about quarks and their interactions. The different species of quarks are often referred to as *flavors*, hence the study of quark interactions is called *flavor physics*.

As mentioned before, without the weak interaction, quarks cannot change their flavor. The weak interaction (specifically decays involving W^\pm bosons) allow for quarks to change from one flavor to another. The flavor-changing process can be written like so:

$$q \rightarrow q' + W \quad (2.26)$$

where q and q' are different flavors of quarks. Since charge must be conserved, the sign of W and ℓ will depend on the quarks involved.

The SM Lagrangian contains a term accounting for the coupling strengths between various quarks. These couplings are written in the so-called *CKM matrix* [10]:

$$\begin{pmatrix} |V_{ud}| & |V_{us}| & |V_{ub}| \\ |V_{cd}| & |V_{cs}| & |V_{cb}| \\ |V_{td}| & |V_{ts}| & |V_{tb}| \end{pmatrix} = \begin{pmatrix} 0.97446 \pm 0.00010 & 0.22452 \pm 0.00044 & 0.00365 \pm 0.00012 \\ 0.22438 \pm 0.00044 & 0.97359^{+0.00010}_{-0.00011} & 0.04214 \pm 0.00076 \\ 0.00896^{+0.00024}_{-0.00023} & 0.04133 \pm 0.00074 & 0.999105 \pm 0.000032 \end{pmatrix} \quad (2.27)$$

where $|V_{qq'}|$ is the strength of the coupling between quarks q and q' . The CKM matrix is unitary, so:

$$|V_{ud}|^2 + |V_{us}|^2 + |V_{ub}|^2 = 1 \quad (2.28)$$

$$|V_{cd}|^2 + |V_{cs}|^2 + |V_{cb}|^2 = 1 \quad (2.29)$$

$$|V_{td}|^2 + |V_{ts}|^2 + |V_{tb}|^2 = 1 \quad (2.30)$$

All coupling values listed in this table were either determined by measurements or by constraints from unitarity. A few properties of flavor physics are apparent from the CKM matrix:

- Quarks couple most strongly to their own generation, e.g. up quarks are coupled primarily to down quarks, charm to strange, and top to bottom.
- Up, down, strange, and charm quark have nontrivial couplings outside of their generations.
- Top and bottom quarks have very small couplings outside their generation.

The next section will use the CKM matrix and the measured properties in Table 2.1 to explain the long lifetime of hadrons containing b -quarks (B -hadrons).

2.2.4.1 Calculating Heavy Flavor Hadron Lifetime

As mentioned before, quarks cannot exist bare on their own; they must be confined within a hadron to produce a color-neutral composite particle. An entire thesis could be dedicated to the physics of hadrons containing b -quarks (i.e. B -hadrons), but this section will focus on one of the most readily observed but important traits of B -hadrons: their relatively long lifetimes.

In general, the lifetime τ of a particle can be written in terms of its total decay rate Γ (sometimes called “total decay width”) [7]:

$$\tau = \frac{\hbar}{\Gamma} \quad (2.31)$$

For ease of notation, we’ll use “natural units” ($\hbar \equiv c \equiv 1$) for most of this section. The total decay rate is equal to the sum of all its individual decay rates Γ_j :

$$\Gamma = \sum_j \Gamma_j \quad (2.32)$$

Each individual decay rate from initial state i to final state(s) f can be written like so (Fermi’s Golden Rule):

$$\Gamma_{fi} = 2\pi |T_{fi}|^2 \rho(E_i) \quad (2.33)$$

where T_{fi} is the transition matrix element and $\rho(E_i)$ is the density of states at energy E_i . The branching ratio for a particular decay mode j is:

$$BR(j) = \frac{\Gamma_j}{\Gamma} \quad (2.34)$$

To determine the lifetime τ_B of a B -hadron¹¹, we’ll analyze the lifetime τ_b of the b -quark. Of course, one might ask: if your goal is to find the lifetime of a B -hadron, why are we focused on decay modes of b -quarks? Can we relate τ_b and τ_B ? The answer is yes¹². b -quarks are much more massive than the other quarks¹³. In fact, the other quark(s) in a B -hadron can be ignored at first order; we think of them as mere “spectators”. Therefore, B -hadron lifetimes are understood through the Spectator Model to be nearly identical, i.e. $\tau_B \approx \tau_b$. The validity of this model has been confirmed through B -hadron lifetime measurements [10].

¹¹When referring to quarks, we use lowercase letters, and for hadrons we use uppercase.

¹²Of course it is or I wouldn’t have asked!

¹³Excluding the t , of course. However, the t never forms hadrons due to its short lifetime.

To determine τ_b , it is helpful to separate the total decay rate into [semileptonic](#) and [hadronic](#) terms¹⁴ [16]:

$$\Gamma_{\text{TOT}} = \Gamma_{\text{sl}} + \Gamma_{\text{had}} \quad (2.35)$$

The lifetime can therefore be written entirely in terms of the semileptonic BR and decay rate:

$$\tau_b = \frac{\hbar}{\Gamma_{\text{TOT}}(b)} = \frac{\hbar}{\Gamma_{\text{sl}} + \Gamma_{\text{had}}} = \frac{\hbar}{\Gamma_{\text{sl}} + \Gamma_{\text{had}}} \times \frac{\Gamma_{\text{sl}}}{\Gamma_{\text{sl}}} = \frac{\hbar BR(\text{sl})}{\Gamma_{\text{sl}}} \quad (2.36)$$

where $BR(\text{sl})$ is the semileptonic branching ratio of the b -quark for each leptonic mode (i.e. $BR(\text{sl}) = BR(e^-, \nu_e) = BR(\mu^-, \nu_\mu) = BR(\tau^-, \nu_\tau)$). Therefore, to calculate τ_b , we need to measure/calculate Γ_{sl} and $BR(\text{sl})$.

The semileptonic b -quark decay rate to a lighter quark q can be expressed like so¹⁵:

$$\Gamma_{\text{sl}}(b \rightarrow q) = \frac{G_F^2 m_b^5}{192\pi^3} |V_{qb}|^2 F(\epsilon) \quad (2.37)$$

where $F(\epsilon) = 1 - 8\epsilon^2 + \epsilon^6 - \epsilon^8 - 24\epsilon^4 \ln \epsilon$ is the phase space factor written in terms of $\epsilon \equiv \frac{m_q}{m_b}$. This approximation of the semileptonic decay width of B -hadrons is called the “free-quark approximation”. Historically, measuring Γ_{sl} was essential in calculating the CKM matrix entries $|V_{cb}|$ and $|V_{ub}|$. For this exercise in calculating τ_b , however, we shall use the known CKM matrix values and a more advanced Γ_{sl} approximation from Isgur, Scora, Grinstein, and Wise (ISGW model) [17]:

$$\Gamma_{\text{sl}} = 2.70 \times 10^{-11} |V_{cb}|^2 = 2.70 \times 10^{-11} \times (0.04214)^2 = 4.79 \times 10^{-14} \quad (2.38)$$

$BR(\text{sl})$ can be measured experimentally, but it can also be approximately theoretically in a quite intuitive way. First, consider the Feynman diagram for b -quark decay (Figure 2.3). The possible decays of the virtual W^- are¹⁶:

$$3 \times \begin{pmatrix} \bar{u} \\ d \end{pmatrix}, \quad 3 \times \begin{pmatrix} \bar{c} \\ s \end{pmatrix}, \quad \begin{pmatrix} e^- \\ \nu_e \end{pmatrix}, \quad \begin{pmatrix} \mu^- \\ \nu_\mu \end{pmatrix}, \quad \begin{pmatrix} \tau^- \\ \nu_\tau \end{pmatrix} \quad (2.39)$$

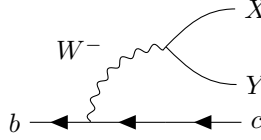
The factor of 3 in front of the quark-antiquark doublets is used to account for the three possible color states of the quarks. Let us (naively) assume that each decay mode (accounting for colors) has equal branching ratio, i.e.:

$$\frac{1}{3} BR(\bar{u}, d) = \frac{1}{3} BR(\bar{c}, s) = BR(e^-, \nu_e) = BR(\mu^-, \nu_\mu) = BR(\tau^-, \nu_\tau) \quad (2.40)$$

¹⁴Although rare purely [leptonic](#) b -decays are possible, they are highly suppressed.

¹⁵Calculation detailed in Ref [16].

¹⁶The $\begin{pmatrix} \bar{u} \\ s \end{pmatrix}$ and $\begin{pmatrix} \bar{c} \\ d \end{pmatrix}$ final states are suppressed by a factor of $|V_{us}|^2 \sim |V_{cd}|^2 \sim 0.04$, so they have been left out of this naive calculation.

Figure 2.3: Weak decay of the b -quark

Due to unitarity, we also know that:

$$3 \times BR(\bar{u}, d) + 3 \times BR(\bar{c}, s) + BR(e^-, \nu_e) + BR(\mu^-, \nu_\mu) + BR(\tau^-, \nu_\tau) = 1 \quad (2.41)$$

Writing entirely in terms of $BR(\mu^-, \nu_\mu)$, we get:

$$3 \times BR(\mu^-, \nu_\mu) + 3 \times BR(\mu^-, \nu_\mu) + BR(\mu^-, \nu_\mu) + BR(\mu^-, \nu_\mu) + BR(\mu^-, \nu_\mu) = 9 \times BR(\mu^-, \nu_\mu) = 1 \quad (2.42)$$

Therefore, we get:

$$BR(\mu^-, \nu_\mu) \approx \frac{1}{9} = 11\% \quad (2.43)$$

which is remarkably close to measured values (e.g. 10.99% and 10.33% for B^+ and B^0 mesons, respectively [10]), considering that we neglected to account for the suppressed inter-generational quark decays, the suppression of τ decays due to phase space effects from the large τ mass, and the QCD enhancement of quark final states.

Finally, we can check our predicted value of τ_b and compare it to measured B -hadron lifetimes.

$$\tau_b = \frac{\hbar BR(\text{sl})}{\Gamma_{\text{sl}}} = \frac{6.582 \times 10^{-25} \times 0.11}{4.79 \times 10^{-14}} = \mathbf{1.511 \times 10^{-12} \text{sec}} \quad (2.44)$$

To compare this approximate value against recently measured B -hadron lifetimes, it is useful to express it as $c\tau_b \approx 464.7\mu\text{m}$. Let's compare this against a B^0 lifetime measurement released by the CMS collaboration in 2017 [18]:

$$c\tau_{B^0} = 454.1 \pm 1.4(\text{stat}) \pm 1.7(\text{syst})\mu\text{m} \quad (2.45)$$

Our approximation (464.7 μm versus 454.1 μm) is a pretty good estimate of the B -hadron lifetime, all things considered!

In this section, a fairly simple calculation of an approximate B -hadron lifetime was presented and compared against recently experimental results to show the validity of the exercise. In the next section, several properties of B -hadrons will be presented, making use of this lifetime calculation.

2.2.5 Properties of Heavy Flavor Hadrons

This section will present four major properties of b -quarks and B -hadrons:

- Mass
- Fragmentation function
- Lifetime (and hence decay length)
- Decay charged particle multiplicity

b -Quark Mass

As stated in Section 2.2, the b -quark is the second-most massive quark with a mass of 4.18 GeV/ c^2 [10]. Measuring the b -quark mass was an important step in measuring Γ_{sl} and hence $|V_{ub}|^2$ [19]. Precision measurements of the b -quark mass could also be used to probe the SM by measuring the coupling of b -quarks to the Higgs field. The b -quark mass can also be used to determine the c -quark mass, which can also be used to probe the SM precisely. In the meantime, however, knowing the b -quark mass is useful because its high mass means that b -quark decays can access many different final states¹⁷.

b -Quark Fragmentation Function

Bare quarks cannot exist on their own; to ensure [color confinement](#), they must be contained within a color-neutral hadron. To make this happen, a bare quark will “give up” a bit of its energy to pull a quark-antiquark pair from the vacuum, giving it other quarks with which to hadronize. This process, called [hadronization](#), continues until there are no bare quarks remaining. Figure 2.4 shows a qualitative picture of the hadronization process [7]. Hadronization is difficult to model, as it is inherently non-perturbative [20]. Instead, hadronization processes are characterized by their [fragmentation function](#), a function describing the probability of a parton k producing a hadron h with energy fraction $z = \frac{E_h}{E_k}$. Because a b -quark is so heavy, it only needs to give up a small fraction of its energy to pull a $q\bar{q}$ pair out of the vacuum (where $q = u, d, s, \text{ or } c$). In practice, this means that b -quark fragmentation produces several hadrons, but the B -hadron will contain the about **80%** of the original b -quark’s energy [8]. Figure 2.5 [21] illustrates the fragmentation function $D(z)$ for b and c quarks produced using the “Peterson Model” [21] of fragmentation.

¹⁷i.e. the b -quark has a lot of energy, giving more options for final states.

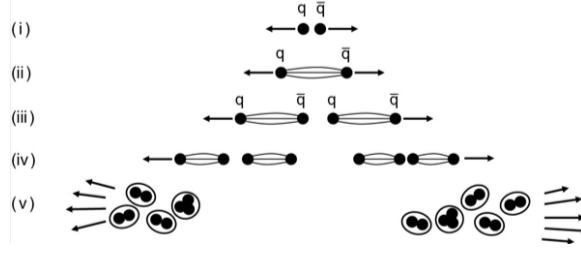
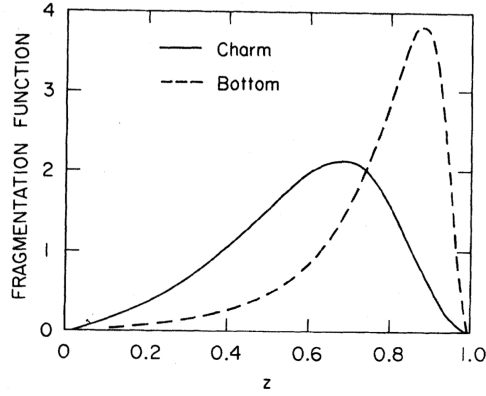


Figure 2.4: A qualitative picture of the hadronization process [7]

Figure 2.5: Comparison of Fragmentation Function Shapes for b and c quarks. [21]

b -Quark Lifetime

In the previous section, we calculated the b -quark (and hence B -hadron) lifetime:

$$\tau_b = 1.511 \times 10^{-12} \text{sec} \quad (2.46)$$

This is a much longer lifetime than other hadrons (for comparison, the charm D^\pm meson has a mean lifetime of $1.040 \times 10^{-12} \text{sec}$ [10]); because the b -quark has such a small CKM mixing angle for $b \rightarrow c$ and $b \rightarrow u$, it takes longer on average for the b -quark to decay. When a B -hadron is produced at high momentum, this means that it can travel a significant distance L before decaying:

$$L_B = \beta \gamma c \tau_B = \frac{p}{m_B} c \tau_B \quad (2.47)$$

where p is the momentum of the B -hadron, τ_B is its lifetime, and m_B is its mass. For example, a B^0 meson with mass = $5.279 \text{ GeV}/c^2$ [10] and momentum = $60 \text{ GeV}/c^2$ will have decay length:

$$L_{B^0}^{p=60} = \frac{60}{5.279} (454.1 \mu\text{m}) \approx 5.161 \text{mm} \quad (2.48)$$

The larger the momentum boost of the B -hadron, the larger the decay length.

Another way to parameterize the distance traveled by a b -quark prior to hadronization and decay is the [impact parameter](#) d_0 of their associated tracks [22]. More information about impact parameter can be found in Section 3.5.1.

b -Quark Hadronization Charged Particle Multiplicity

On average, a B -hadron decay produces 5.36 charged particles [23]. This property is useful when attempting to identify B -hadron decays in experiment, because charged particles often are easier to measure (detailed further in Chapter 3).

2.3 Open Problems in the Standard Model

The SM is a very useful theory, but it does not provide explanations for all the physical phenomena we see and is a very fine-tuned model. In addition to its failure to account for gravity, there are theoretical problems with the SM, including [7]:

- **Hierarchy Problem:** at low energy, the “loop corrections” to the Higgs boson (Feynman diagrams involving a closed loop) are perfectly reasonable. At high energies (e.g. Λ_{Planck}), however, these corrections are quadratic in Λ . It is hard to accept that corrections on the order of $\sim 10^{38}$ GeV perfectly cancel out to give a Higgs mass around $\sim 10^2$ GeV.
- **Large number of free parameters:** the SM has a total of 21 parameters¹⁸: 12 fermion masses, 3 coupling constants (one for each force), 2 Higgs potential parameters, and 4 mixing angles for the CKM matrix. This large number of parameters reflects the nature of the SM; it is a theory designed to agree with observed phenomena, not a “higher-order” explanation. There are hints of patterns or relationships between these parameters, but thus far no deeper principles have been discovered.
- **Flavor/Generation Problems:** although there appear to be exactly three generations of quarks and three of leptons, the SM does not provide any explanation of *why* this is the case. Additionally, the SM does not explain why quarks are coupled very strongly to their own generation, yet neutrinos regularly oscillate between generations.
- **Grand Unification Scale:** At low energies, the three fundamental forces described by the SM differ dramatically in strength. We expect the force strengths to unify at some [Grand](#)

¹⁸22, if you include the strong CP violation phase σ_{CP} .

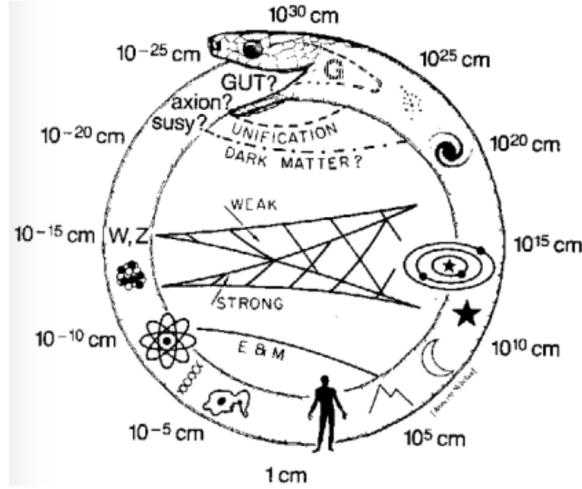


Figure 2.6: An artistic representation of Grand Unification Theory [25]

[Unification Theory \(GUT\)](#) energy scale; when the Universe was inflating, we expect that all forces could be described by a single GUT scalar. At high ($\sim 10^{15}$ GeV) energies, the SM forces are *almost* identical in strength; something else is needed to correct for these small discrepancies [24]. Figure 2.6 shows an artistic representation of the concept of GUT [25].

Before diving into a possible solution to these problems, we shall take a brief detour and discuss cosmology.

2.4 Cosmology and the Standard Model

The past few sections have been entirely devoted to observable SM matter. It has been known since the mid 1930s [7] that only a fraction of the mass in the Universe is found in luminous (observable matter) stars. This can be shown in multiple ways, but perhaps the simplest way to see this is through studying galactic velocity curves. Galactic rotational velocity curves are not the only source of evidence for the existence of dark matter, but this is the only method of detection which shall be discussed in this thesis¹⁹. After presenting some proof for the existence of dark matter, this section shall briefly present the [Friedmann-Lemaître-Robertson-Walker \(FLRW\)](#) model of the expanding Universe, ending with a summary of the thermal history of the Universe.

¹⁹For more methods of dark matter detection, see Ref [26].

2.4.1 Observing Dark Matter through Galactic Velocity Curves

A galactic velocity curve is a plot of the velocity of objects within a galaxy as a function of their radial distance from the gravitational center of the galaxy. The mass $M(r)$ contained within some radius r can be related to the orbital velocity v at r via Kepler’s Third Law [26]:

$$GM(r) = v^2 r \quad (2.49)$$

where G is the gravitational constant. One basic technique for measuring v is [hydrogen-line profiles](#) [27]. Hydrogen is the most abundant element in the cosmos, making up about 80% of the Universe’s observable mass. When the magnetic dipole of the hydrogen electron is parallel to that of the nucleus, the total energy of the hydrogen atom is slightly higher than if the dipoles were anti-parallel. The transition from one of these states to the other (called a neutral-hydrogen [hyperfine transition](#)) produces a photon with a 21cm wavelength (1420 MHz frequency). By measuring the shifts in the observed frequency for this line, one can measure the relative velocity of points in a galaxy.

Figure 2.7 shows the observed velocity curve (black dots) for NGC 6503 [28]. For comparison, the predicted curves based on the visible matter from gas and the galactic disk are shown as dotted lines. If visible matter were the only contribution to the galactic mass, then we would observe a drop-off in velocity as the radius increases but the mass contained within that radius remains the same (see the “disk” curve). This is not what was observed; as radius increases, the galactic velocity remains flat, indicating that *something* must be contributing to the galactic mass in and beyond the edge of the disk. We call this non-observable massive material [dark matter](#). The effect of a dark-matter halo on the velocity curve is shown as a third dotted line; although this model does not fully explain the data, this prediction more closely matches the data than the observable-matter-only models.

2.4.2 The Expanding Universe

Having given some brief evidence for the existence of dark matter, let us take a step back and describe the FLRW model of the Universe. Physicists have known since the 1920’s that the Universe is expanding [26]. To restrict our set of possible models for the expanding Universe, we shall use the [Cosmological Principle](#): we shall assume that the matter in the Universe is [homogeneous](#) and [isotropic](#)²⁰. One result of this is that we assume our local area of the Universe (i.e. the Earth, Solar System, and Milky Way Galaxy are not “special” or different from the rest of the Universe in any

²⁰Of course, the Universe is not *perfectly* homogeneous and isotropic; the Earth is much more dense than most of the Universe, for example! The Universe is only homogeneous and isotropic on a “cosmological” scale.

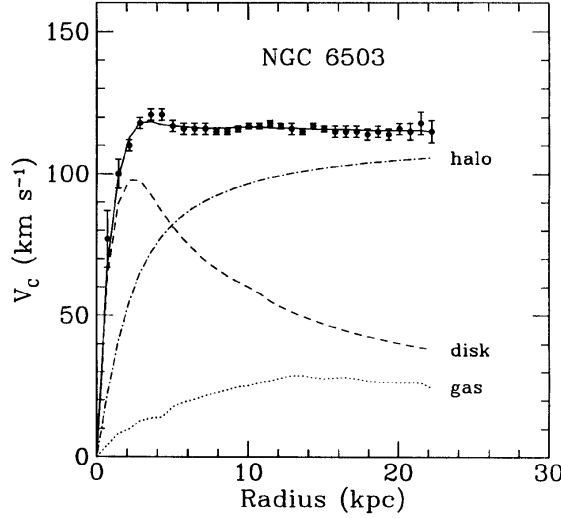


Figure 2.7: Galactic rotational velocity curve for NGC 6503. For comparison, the expected curves due to the gas, disk, and dark matter halos are shown as dotted lines [28]

meaningful way. This is a good thing; we can take measurements from Earth without fearing that we are biased by our location in the Universe.

The expansion of Universe is quantified by the [Hubble parameter](#) $H(t)$:

$$H(t) = \frac{\dot{R}(t)}{R(t)} \quad (2.50)$$

where $R(t)$ is the [cosmic scale factor](#) and $\dot{R}(t)$ is its time derivative. The current expansion of the Universe H_0 , is called the [Hubble constant](#). The evolution of the scale factor is governed by the [Friedmann equation](#) [29]:

$$H^2(t) = \frac{8\pi G}{3}\rho(t) - \frac{kc^2}{R(t)^2} \quad (2.51)$$

where G is Newton's gravitational constant, $\rho(t)$ is the energy density of the Universe as a function of time, c is the speed of light, and k is the intrinsic curvature of the Universe. This can be re-written like so:

$$\frac{k}{H^2 R^2} = \Omega_{tot} - 1 \quad (2.52)$$

where $\Omega_{tot} \equiv \frac{\rho}{\rho_{cr}}$ is the ratio of the total energy density to the [critical density](#) ρ_{cr} , i.e. the energy density at which the Universe is neither expanding nor contracting. We know that $H^2 R^2 \geq 0$, so there is a correspondence between the sign of k and the signal of $\Omega_{tot} - 1$ (i.e. the eventual fate of the Universe given \sim infinite time):

- $k = +1$: $\Omega_{tot} > 1$, “closed” or contracting Universe

- $k = 0$: $\Omega_{tot} = 1$, “flat” or static Universe
- $k = -1$: $\Omega_{tot} < 1$: “open” or expanding Universe

2.4.3 Thermal History of the Universe

In this section, we shall discuss the different species of matter in the early Universe in the context of a “thermal timeline”. Each period in the timeline shall correspond to a type of matter which was created then “frozen out”, i.e. the Universe became too cold or too empty for that matter species to be created or self-interact anymore. Before that, however, we shall briefly cover two types of equilibrium: [chemical equilibrium](#) and [kinetic equilibrium](#) [26]. Although this thesis shall not cover *how* these concepts are used to understand the thermal history of the Universe, these are the guiding principles for forming our history and must be briefly mentioned.

Consider some process where species i , j , k , and l interact like so²¹:

$$i + j \rightarrow k + l \quad (2.53)$$

Each species has a chemical potential μ , the energy absorbed or released when the particle number N for that species is changed. If $\mu_i + \mu_j = \mu_k + \mu_l$, then the species are said to be in “chemical equilibrium”. Kinetic equilibrium, on the other hand, is governed by the exchange of energy and momentum between particles. The Universe must be dense enough for the particles to efficiently exchange energy and momentum between them; if the Universe is too sparse, then the particles will not be able to interact with each other. Kinetic equilibrium conditions for relativistic and non-relativistic particles can be derived from phase space factors and the Boltzmann equation.

Very generally, we are interested in the interaction rate $\Gamma = \frac{1}{\tau_{\text{interaction}}}$ for various processes. If $\Gamma \gg H$, the interaction can proceed and its constituents are in thermal equilibrium. If $\Gamma \sim H$, the interaction cannot proceed anymore and “freezes out”.

Now, let us briefly list the eras of the early Universe chronologically [26] [30]:

- Baryogenesis and Leptogenesis. This is the origin of matter-antimatter asymmetry. For every 10^9 matter-antimatter pairs, there was 1 additional matter particle.
- EWK phase transition. The electromagnetic and weak forces begin to behave distinctly. $T \sim 100$ GeV, $t \sim 20 \times 10^{-12}$ sec.

²¹For example, consider the weak process $e^- + e^+ \rightarrow \nu_e + \bar{\nu}_e$.

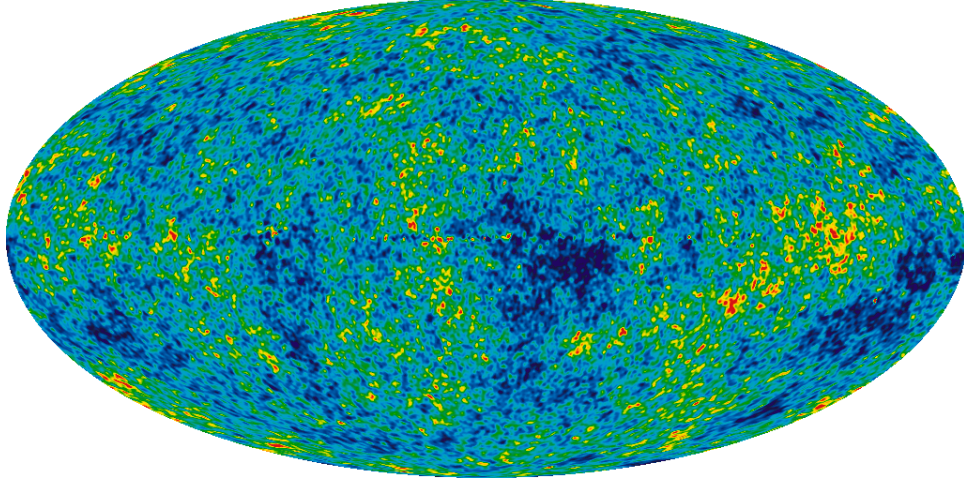


Figure 2.8: All-sky image of the Cosmic Microwave Background. Structures are an artifact of early Universe anisotropies. [31]

- QCD phase transition. Quarks can no longer exist freely and must be bound into mesons or baryons. $T \sim 150 \text{ MeV}$, $t \sim 20 \times 10^{-6} \text{ sec}$.
- Dark Matter freeze-out. This is the point at which the Universe is too sparse for [Dark Matter \(DM\)](#) particles to self-interact. If the dark matter candidate is a supersymmetric neutralino (covered in Section 5.1), then $T \sim 25 \text{ MeV}$. DM [relic abundance](#) shall be discussed in more detail in the following section.
- Neutrino decoupling. Prior to this era, neutrinos were in equilibrium with the primordial plasma through interactions such as $p + e^- \leftrightarrow n + \nu$, $p + \bar{\nu} \leftrightarrow n + e^+$, and $n \leftrightarrow p + e^- + \bar{\nu}$. $T \sim 1 \text{ MeV}$, $t \sim 1 \text{ sec}$.
- Big Bang Nucleosynthesis. The first light elements (primarily helium and deuterium) are formed through beta decay, inverse beta decay, and electron capture. $T \sim 100 \text{ keV}$, $t \sim 3 \text{ min}$.
- Recombination Era and Photon Decoupling. Protons and electrons form neutral hydrogen. Because there are no more free electrons with which to scatter, the photons decouple and form a very faint “background” of radiation seen all over the Universe, the [Cosmic Microwave Background](#). Figure 2.8 shows an all-sky image of the Cosmic Microwave Background [31]. $T \sim 0.3 \text{ eV}$.

2.4.4 Dark Matter Properties

Chapter 5 shall present a search for electroweakly-product supersymmetry, making use of cosmological constraints on dark matter self-annihilation. In this subsection, we shall review some known properties of dark matter and its relic abundance after freeze-out.

Because dark matter does not absorb or scatter photons, we know that it must be electrically neutral [32]. It must also be long-lived (either stable or with a lifetime \sim age of the Universe), because we can still observe dark matter relics today [33]. Based on comparisons between numerical simulations and observations, dark matter cannot be “hot” (relativistic); “cold” (non-relativistic) and “warm” dark matter (2–3 keV) have not be ruled out. Dark matter cannot be baryonic because only about 4 – 5% of the energy of the Universe comes from baryonic matter; experimentally, the cold dark matter density of the Universe has been measured to be $\Omega_{\text{DM}}h^2 = 0.12$ [34] [35]. One might suspect that neutrinos could be a SM dark matter candidate. Neutrino mass constrains, however, limit their relic abundance to $\Omega_\nu h^2 < 0.003$, which is much smaller than the dark matter abundance. Additionally, neutrinos would be relativistic at the epoch of dark matter filamental structure formation, failing the not-hot requirement [36].

Assuming that our dark matter candidate meets the above criteria, one can relate the relic density $\Omega_{\text{DM}}h^2$ to the self-annihilation cross-section²². Following the calculation in Ref [36], the thermally-averaged self-annihilation cross-section is²³:

$$\langle \sigma v \rangle \approx 3 \times 10^{-26} \text{cm}^3 \text{s}^{-1} \quad (2.54)$$

We shall use this value in Chapter 5.

2.5 Introduction to Supersymmetry

Thus far, this chapter has been dedicated to the Standard Model. Sections 2.2-2.2.5 reviewed the SM, with a special focus on electroweak unification, electroweak symmetry breaking through the Higgs mechanism, and flavor physics. Section 2.3 presented a few problems with the SM; this section shall present a possible solution to these problems through supersymmetry (SUSY).

²²When the cosmic expansion rate \sim to the self-annihilation cross-section, the dark matter has “frozen out”.

²³This assumes only cold weakly-interacting dark matter

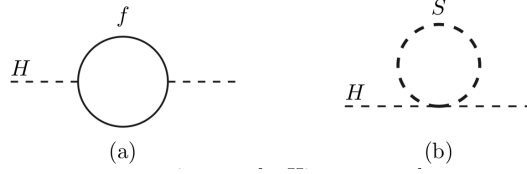


Figure 2.9: Fermionic loop correction to the Higgs mass

2.5.1 What is SUSY?

To begin our explanation of SUSY, we shall focus on the “hierarchy problem” in the SM. This problem emerges when one attempts to calculate a loop correction to the Higgs mass. For example, consider the Dirac fermion loop²⁴ shown at left in Figure 2.9 [37]. This loop yields a correction:

$$\Delta m_H^2 = -\frac{|\lambda_f|^2}{8\pi^2} \Lambda_{\text{UV}}^2 + \dots \quad (2.55)$$

where Λ_{UV} is an ultraviolet momentum cutoff scale (this cutoff regulates the loop integral). The terms in the ellipses are proportional to m_f^2 and grow at most logarithmically with Λ_{UV} . If we naively choose $\Lambda_{\text{UV}} \sim M_{\text{Planck}}$, then this loop correction to m_H^2 is ~ 36 orders of magnitude larger than m_H itself. It’s not sufficient to simply pick a smaller Λ_{UV} ; such a theory will require a Lagrangian containing more than two derivatives, which will probably fail either unitarity or causality [38]. Additionally, the introduction of some higher mass “regulator” particle will not help the situation, because the m_H^2 correction will be sensitive to the *heaviest* particle to which the Higgs couples. For example, consider introducing a heavy complex scalar boson S with mass m_S coupled to the Higgs with Lagrangian term $-\lambda_S |H|^2 |S|^2$, as shown at right in Figure 2.9. This results in the correction:

$$\Delta m_H^2 = \frac{\lambda_S}{16\pi^2} [\Lambda_{\text{UV}}^2 - 2m_S^2 \ln(\Lambda_{\text{UV}}/m_S) + \dots] \quad (2.56)$$

One can get rid of the Λ_{UV}^2 term by using dimensional regularization on the loop integral instead of a momentum cutoff. This still leaves the term proportional to m_S^2 , which cannot be eliminated without fine-tuning other terms in the correction. This holds even if the SM Higgs is only indirectly or extremely weakly coupled to the high-mass particle.

To fix this problem, we’ll need cancel out the dangerous parts of Δm_H^2 without fine-tuning of masses or sensitivities. Comparing (2.55) and (2.56), one might notice that the fermionic and bosonic terms have opposite sign. If we introduce a scalar boson for each fermion with $\lambda_S = |\lambda_f|^2$, then the Λ_{UV}^2 terms from the left and right of Figure 2.9 will nicely cancel. Similarly, we can

²⁴It doesn’t really matter which fermion you pick; the result stays the same.

introduce a fermion for each boson to cancel out higher-order terms. This is the basic idea behind supersymmetry: there exists a symmetry pairing each SM fermion with a SUSY scalar boson partner and pairing each SM boson with a SUSY fermion partner.

2.5.2 Terminology in SUSY

SUSY theories are somewhat notorious for their strange terminology and notation. The following section describes the [Minimal Supersymmetric Standard Model \(MSSM\)](#), the most basic SUSY extension of the SM. Other models may have additional particles or states not described here.

The states within a SUSY theory are called [supermultiplets](#) [39]. All particles within the same supermultiplet must have the same mass²⁵. Each supermultiplet contains an equal number of fermionic and bosonic states (which are [superpartners](#) of each other). The superpartners of SM fermions (called [sfermions](#), i.e. “scalar fermions”) are named by adding an “s-” prefix; the superpartner of the electron is called the “selectron” and the superpartner of a quark is called a “squark”, and so on. The superpartners of SM gauge bosons (called [gauginos](#)) are named by adding an “-ino” suffix; for example, the superpartners of the Higgs are called the “Higgsinos”. Superpartners are denoted graphically by adding a tilde above their SM symbol (e.g. the superpartner of the top t , the stop, is denoted \tilde{t}).

In Section 2.2.1, we found that electroweak unification results in four gauge fields (B_μ and $W^{(k)}$, $k = 1, 2, 3$) with four bosons W^\pm , W^0 and B^0 prior to symmetry breaking²⁶. The partners to the gauge bosons, called “gauginos”, consist of four fermions: the charged winos (\tilde{W}^\pm), the neutral wino (\tilde{W}^0), and the bino (\tilde{B}^0). As the only SM scalar, the Higgs is a special case: in order to protect electroweak symmetry from anomalies, the Higgs has *two* supermultiplets [37], one with isospin $Y = \frac{1}{2}$ and another with $Y = -\frac{1}{2}$. The $Y = \frac{1}{2}$ Higgs multiplet gives masses to up-type quarks, and the $Y = -\frac{1}{2}$ multiplet gives masses to down-type quarks. This results in four Higgsino states: a positively-charged up-type Higgsino (\tilde{H}_u^+), a negatively-charged down-type Higgsino (\tilde{H}_d^-), and down-type and up-type neutral Higgsinos (\tilde{H}_u^0 and \tilde{H}_d^0). MSSM also results in four additional SM Higgs bosons: two charged Higgs bosons (H^\pm), two [CP-even](#) Higgs bosons (h_0 and H_0), and one [CP-odd](#) Higgs boson (A_0) [10]. The neutral Higgsinos, neutral wino, and bino are superpartners of the charged gauge bosons and charged Higgs bosons. The charged Higgsinos and charged winos are superpartners of the neutral gauge bosons and neutral Higgs bosons. After symmetry breaking in

²⁵This and the other properties of supermultiplets are derived in Ref [39] and Ref [37].

²⁶We formed W^\pm from a linear combination of $W^{(1)}$ and $W^{(2)}$ and the Z and photon from a combination of B_μ and $W^{(3)}$.

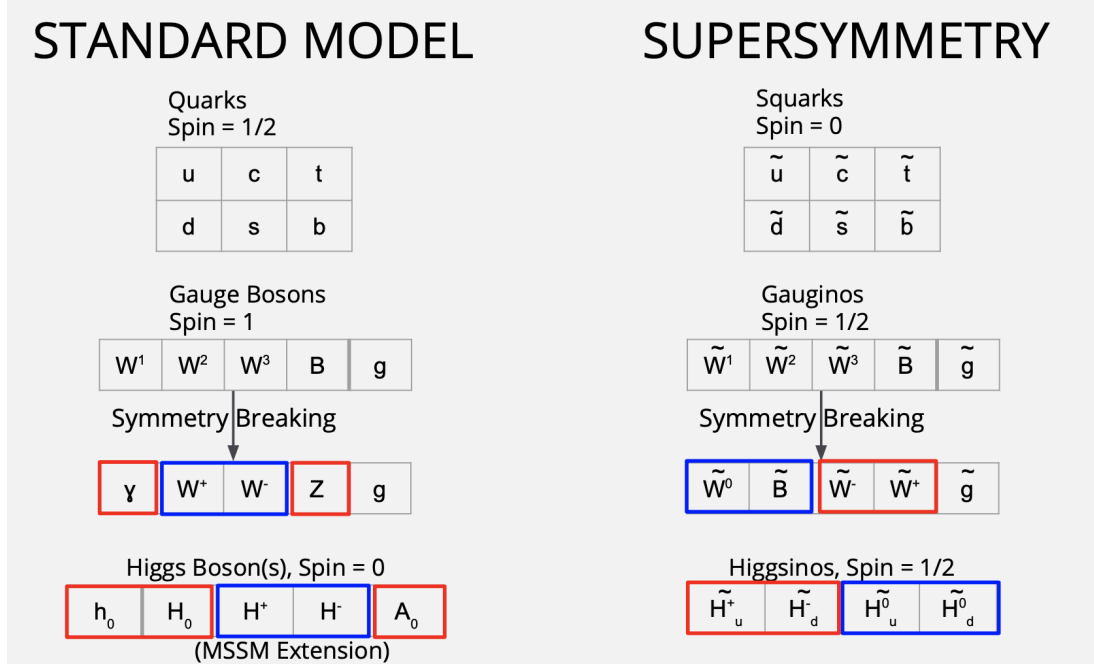


Figure 2.10: A table showing a MSSM extension to the SM. The red boxes show the superpartnership between the neutral SM bosons and the charged Higgsinos and winos. The blue boxes show the superpartnership between the charged SM bosons and the neutral Higgsinos, neutral wino, and bino.

the SM, the W^0 and B^0 mix to create the photon and Z ; similarly, the wino, bino, and Higgsino mass eigenstates mix to create observable states. We call the charged observable states “charginos” ($\tilde{\chi}^\pm$) and the neutral ones “neutralinos” ($\tilde{\chi}^0$). Conventionally, these are labeled in ascending order by mass, i.e. $m_{\tilde{\chi}_1^0} < m_{\tilde{\chi}_2^0} < m_{\tilde{\chi}_3^0} < m_{\tilde{\chi}_4^0}$, $m_{\tilde{\chi}_1^\pm} < m_{\tilde{\chi}_2^\pm}$.

The interactions between particles in SUSY models are governed by a “superpotential”. The usual MSSM superpotential is [40]:

$$W_{MSSM} = \bar{u}\mathbf{y}_u QH_u - \bar{d}\mathbf{y}_d QH_d - \bar{e}\mathbf{y}_e LH_d + \mu H_u H_d \quad (2.57)$$

where Q , L , \bar{u} , \bar{d} , and \bar{e} are matter [superfields](#) and H_d are the up- and down-type Higgs superfields. \mathbf{y}_u , \mathbf{y}_d , and \mathbf{y}_e are 3×3 Yukawa coupling matrices. To get the full SUSY Lagrangian, one must add gauge interactions and SUSY symmetry breaking terms. The relationship between the SM and SUSY mass eigenstates and observables is shown in Figure 2.10, with the (non-obvious) superpartners shown with colored boxes.

2.5.3 R-Parity

In 1978, theorists noticed that SUSY models with the superpotential shown in Equation 2.57 contain an exact symmetry of the Lagrangian, given by:

$$(-1)^R = (-1)^{3B-L+2S} \equiv (-1)^{3(B-L)+2S} \quad (2.58)$$

where B is [baryon number](#), L is [lepton number](#), and S is particle spin. This symmetry is known as [R-parity](#). SM particles have R-parity of $+1$, and SUSY particles have R-parity of -1 . There are a few interesting consequences to R-parity conservation at collider experiments:

- SUSY particles will always be produced in pairs
- SUSY particles can never decay entirely to SM particles. Because of this, the [Lightest Supersymmetric Particle \(LSP\)](#) must be stable and electrically neutral.

In addition to these experimental consequences, [R-parity Conserving \(RPC\)](#) SUSY models have important phenomenological results as well. The LSP neutralino provides an excellent stable dark matter candidate, and R-parity conservation explains the stability of the proton [41]. It should be noted, however, that there are many classes of [R-parity Violating \(RPV\)](#) SUSY models, which can also contain DM candidates and explanations for proton stability.

2.5.4 Electroweakly-Produced SUSY Scenarios

This thesis shall present a search for electroweakly-produced SUSY in Chapter 5. This subsection shall review the SUSY physics scenario in this search.

Motivated by the 125 GeV SM Higgs, this search assumes a “split-SUSY” scenario in which all but the electroweak gauginos are decoupled ($\gg O(1 \text{ TeV})$) [42]. The particle content is assumed to be MSSM-like. R-parity is conserved, and the LSP is the lightest neutralino (or [gravitino](#), if specified). With these constraints in mind, this analysis targets scenarios with two [electroweakinos](#) no heavier than $\sim 1 \text{ TeV}$ with the mass splitting between them $\geq 200 \text{ GeV}$. The “heavy state” is either wino-like or Higgsino-like²⁷, and the “light state” is dominated by some electroweakino flavor other than the one chosen for the heavy state. A light Higgsino model is favored due to naturalness arguments [43], but the models considered here are all fairly simple and general. In total, four combinations are considered:

$$(\tilde{\chi}_{\text{heavy}}, \tilde{\chi}_{\text{light}}) = (\tilde{W}, \tilde{B}), (\tilde{H}, \tilde{B}), (\tilde{W}, \tilde{H}), (\tilde{H}, \tilde{W}) \quad (2.59)$$

²⁷Bino is not considered for “heavy state”, as the production cross-section is suppressed due to sfermion decoupling.

We can further constrain our search space using the thermally-averaged DM self-annihilation cross-section, presented in Section 2.4.4:

$$\langle \sigma \nu \rangle \approx 3 \times 10^{-26} \text{cm}^3 \text{s}^{-1} \quad (2.60)$$

The coupling between dark matter and the Universe’s thermal equilibrium is fixed within RPC SUSY models, so this constraint can be transformed to a constraint on the LSP mass. For wino and Higgsino LSP dark matter, this corresponds to $\lesssim 1$ TeV and $\lesssim 3$ TeV limits, respectively²⁸.

The bino LSP scenario is a less well-motivated because bino pairs rarely annihilate into SM particles; in this case, the expected DM relic abundance is too large²⁹. This tension can be resolved in two ways: the “ Z/h ” funnel or the introduction of another SUSY particle slightly above the bino mass. The Z/h funnel [44] requires that $M_{\text{LSP}} \sim \frac{m_Z(m_h)}{2}$, i.e. the bino mass is about half the Z or h masses; this requirement results in $\Omega_{\text{DM}} h^2 \simeq 0.12$, matching our expectations from observation as described in Section 2.4.4. The bino dark matter relic abundance can also be corrected by co-annihilation with a slightly more massive gluino [45], stau [46], stop [47], or wino [48] [49], or by mixing with a wino or Higgsino (“well-tempered neutralino”) [50]. In the co-annihilation scenario, the “heavy state” particle must be some ewkino other than the bino and its co-annihilator.

The target mass spectra are summarized in Figure 2.11.

²⁸Lighter LSP masses are allowed if other DM sources contribute to the relic abundance.

²⁹You can even get an “overclosure”, where $\Omega_{\text{DM}} h^2 > 1$.

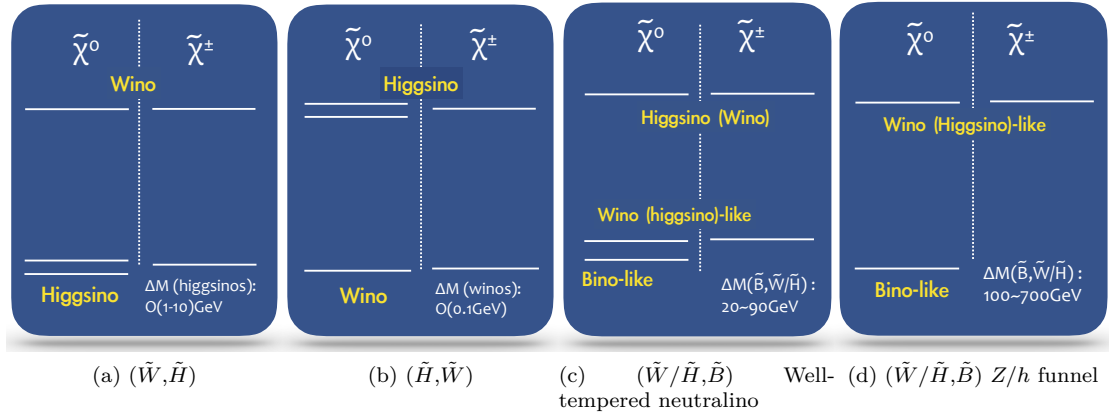


Figure 2.11: Electroweakino mass spectra in target physics scenarios. (a) Wino heavy states / higgsino light states: (\tilde{W}, \tilde{H}) (b) higgsino heavy states / wino light states: (\tilde{H}, \tilde{W}) (c) wino or higgsino heavy states / bino light state: $(\tilde{W}/\tilde{H}, \tilde{B})$. To resolve the tension with DM relic abundance in bino LSP scenario, (c) mixes the bino LSP with a $20 \sim 100$ GeV heavier wino or higgsino. This mass splitting can be as large as $100 \sim 700$ GeV in (d), which is a special case of (c) where the bino mass is about half the Z or Higgs mass. Figure credit to Dr. Shion Chen.

CHAPTER 3

The LHC and ATLAS: Simulation and Data Collection from Detector to Disk

“Any sufficiently advanced technology is indistinguishable from magic.”

— Arthur C. Clarke, *Profiles of the Future* [51]

This chapter will describe how data is collected, simulated, and processed in the ATLAS experiment at the Large Hadron Collider. First, the Large Hadron Collider and ATLAS detector are described in general. The components of the ATLAS detector are detailed in terms of their role in collecting and recording collision data. The section on data collection closes with basic descriptions of object reconstruction in ATLAS data. Next, the focus shifts from data to simulation with a description of Monte Carlo simulation methods. The final section describes the data processing chain: once data is collected off the detector or produced via Monte Carlo simulation, how are the samples augmented, altered, and distributed to meet users’ needs? This section will include details of specific software contributions I made to the flavor-tagging software group.

3.1 Introduction to Collider Physics

Collider physics experiments provide the evidence needed to confirm or refute theories about elementary particles and fundamental forces. To understand the reasoning behind the design of these experiments, a little background information is needed.

3.1.1 Luminosity and Cross Section

As the name implies, a collider experiment is performed by colliding particles together and observing the results. These particles are too small for us to aim them at each other one-at-a-time; instead,

we squeeze many particles together in a [bunch](#), accelerate two bunches towards each other, and quantify the chances of a head-on particle collision occurring.

For example, let's say we want to observe some particle physics process using our collider experiment. The probability of this process occurring is quantified via its [cross section](#) σ_{event} . This probability is given in units of [barns](#); a “barn” is a unit of area equal to 10^{-28} m^2 [52]. The name comes from a joke by Enrico Fermi that a Uranium atom target (which has a cross-sectional area of ~ 1 barn) is “as easy to hit as the broad side of a barn”. The larger the cross section, the easier it is to hit the target (or the more likely it is for a process to occur). For example, let's do a ballpark estimate of the rate of W^\pm boson production [52]. We can estimate roughly the cross section for W^\pm production from the Fermi coupling³⁰:

$$\sigma(pp \rightarrow W) \sim G_F \sim 1.17 \times 10^{-5} \text{ GeV}^{-2} \frac{0.39\text{mb}}{1 \text{ GeV}^{-2}} \sim 10^{-6} \text{mb} = 1\text{nb} \quad (3.1)$$

We can expect approximately 1 collision out of a billion to produce a W boson.

Having quantified the probability of a process occurring during a collision, we next need to quantify our collision rate. We talk about this as either [instantaneous luminosity](#) (denoted L) or [integrated luminosity](#) (denoted L_{int}). Instantaneous luminosity is the collision rate per-second, and the integrated luminosity is the integral of instantaneous luminosity over some period of time. The units for instantaneous luminosity are $\frac{1}{\text{m}^2 \text{sec}}$; the numerator is the number of particles involved, $\frac{1}{\text{sec}}$ is the rate at which particles pass each other, and $\frac{1}{\text{m}^2}$ is the area of overlap for collision.

Using both these values, we can quantify the per-second rate of a process occurring in our collider experiment:

$$N_{\text{event}} = L\sigma_{\text{event}} \quad (3.2)$$

If we replace L with L_{int} , this equation gives the number of [events](#) expected over a period of time. There isn't very much we can do to increase the cross section for a particular process³¹; what we *can* control is the luminosity.

3.2 The Large Hadron Collider

The [Large Hadron Collider \(LHC\)](#) is the highest energy collider particle physics experiment and largest machine ever built [53] [54]. The LHC is part of [European Organization for Nuclear Research \(in French, Conseil européen pour la recherche nucléaire\) \(CERN\)](#) and is shown in cartoon form

³⁰The fraction $\frac{0.39\text{mb}}{1 \text{ GeV}^{-2}}$ appears in this calculation for converting from natural units to barns.

³¹If the cross section is energy dependent, we can build a collider with higher center-of-mass energy, but that's about it

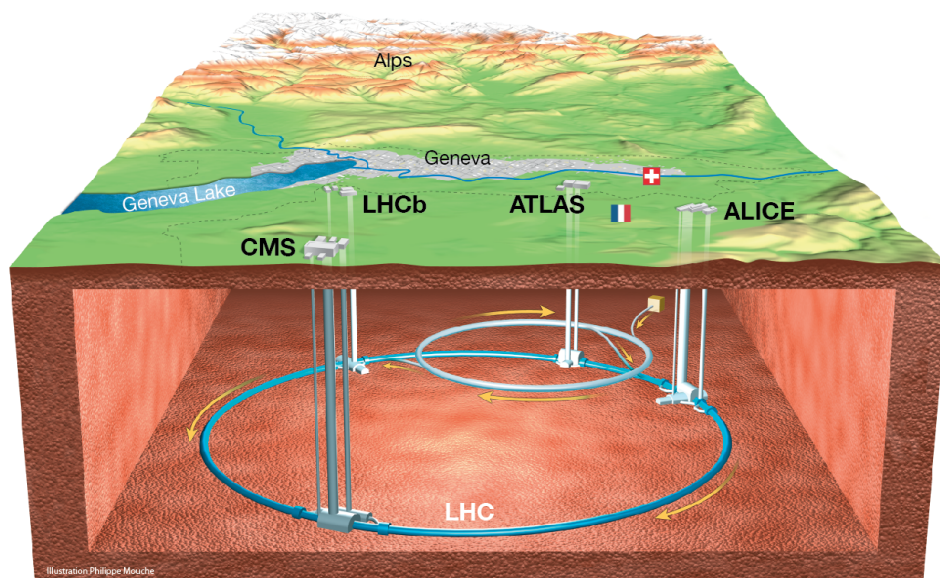


Figure 3.1: Cartoon illustrating the LHC relative to local borders and geography [55]

in Figure 3.1 [55]. The LHC is made of two “rings” located 45-170 m underground straddling the Genevan border of Switzerland and France. The detectors at the LHC will be described in detail in Section 3.3; first, let’s briefly discuss the LHC accelerator rings.

3.2.1 LHC Rings

The LHC’s accelerator rings are the largest single component of the machine. The rings are housed in a 26.7 km tunnel, originally built for the LEP collider between 1984 and 1989 [54]. Inside this ring are small metal tubes (called the [beam line](#)) with a high vacuum inside through which the bunches of protons travel. There are two beam lines: one running clockwise, the other counter-clockwise. These beam lines are allowed to cross inside the detectors; this allows the bunches of protons to meet (and potentially collide) inside the detector, where the detector machinery can observe some of the decay products.

Prior to collision, the protons are accelerated to an extremely high momentum. The energy available during a collider scattering process comes almost entirely from the momentum of the incoming particles; the higher the proton momenta, the higher energy process we can observe. First, the proton beam lines are accelerated through several smaller rings (called the “accelerator

complex”), reaching a [center-of-mass](#) energy of ~ 900 GeV. The proton velocity (and hence energy) is increased using [Radiofrequency Cavities \(RF Cavities\)](#), special metallic chambers which can generate oscillating electromagnetic fields inside. RF cavities are also used to synchronize the beams in orbit. The proton bunches are focused (i.e. pushed closer together) and accelerated (i.e. their trajectories are curved into a circle) using very powerful magnets (~ 8.3 T magnetic fields). Both the RF cavities and magnets must be [superconducting](#); they are kept at a temperature below 2 K to handle the necessary current. Protons in the main LHC rings have an average center-of-mass energy of 13 TeV. The bunches are about $2.5 \mu\text{m}$ wide with 1.15×10^{11} protons per bunch [56]. The instantaneous luminosity of the LHC beam is 10^{34} cm^{-2} per second.

3.2.2 Detectors

There are four main detector experiments at the LHC: ATLAS, CMS, ALICE, and LHCb [57]. Although ATLAS will be described in detail in Section 3.3, a brief description of each detector will be provided here.

ATLAS and CMS are the two “multi-purpose” detectors at the LHC. These detectors were designed to detect as many types of particles as well as possible. They are not designed with a single goal in mind; this means that physicists can use the data collected at these detectors to search for whatever physics processes they like. ATLAS and CMS are based off similar designs, but each of the two associated scientific collaborations made different choices when designing their detector. For example, the CMS detector is bathed in an extremely powerful (~ 4 T) magnetic field; this curves charged particles more strongly, allowing CMS to be a more compact detector.

The other two detectors, ALICE and LHCb, were built with specific purposes in mind. ALICE was built to observe [quark-gluon plasma](#) through lead ion collisions; the LHC runs lead-ion beams for a portion of the year for ALICE. Right after the Big Bang, the Universe was filled with so much energy that protons and neutrons could “melt”, freeing their quarks from their bonds. By recreating the highly energetic conditions of that time, physicists can study the quark-gluon plasma and learn more about the fundamental nature of quarks (see Section 2.4 for information about the early Universe). LHCb was built to study the [matter-antimatter asymmetry](#) via the study of b - and c -quarks. B -mesons exhibit matter-antimatter asymmetry in their decays [58], and understanding this asymmetry within B -hadron physics allows physicists to understand why we observe so much more matter than antimatter in the Universe. Although the SM provides some explanation for the matter-antimatter asymmetry, it is not sufficient to explain the size of the discrepancy observed.

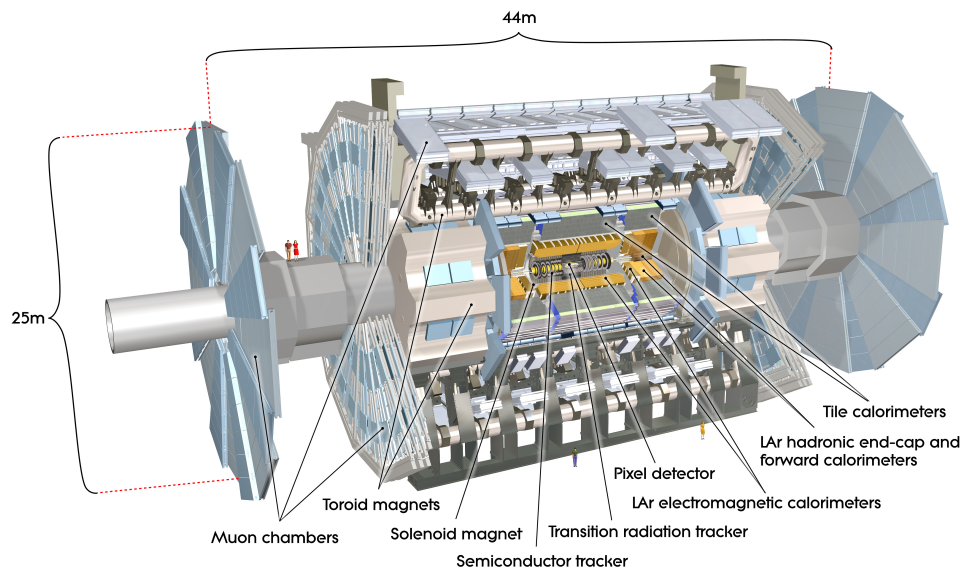


Figure 3.2: Rendered cut-away view of the ATLAS detector, with two humans shown on the left in red for size reference. [59]

Physicists hope to find hints of new physics at LHCb (possibly through rare decays involving b -quarks) to explain the matter-antimatter asymmetry. The details of how these detectors work is beyond the scope of this thesis.

3.3 The ATLAS Detector

The ATLAS detector, a general-purpose detector located at one of the four interaction points along the LHC ring, will be described here with a focus on hardware. The ATLAS detector (shown in cut-away in Figure 3.2 [59]) is about 25 m tall, 44 m long, and weighs about 7000 tonnes [60]. In Figure 3.2, the beam line enters the detector through the pipes at the left and right. The bunches are allowed to collide at the very center of the detector, and decay products radiate away from that central point. Therefore, the detector will be described “inside-out”, to mirror the order in which decay particles encounter the layers of the detector. Figure 3.3 shows a rendered cross-sectional slice of the ATLAS detector, with labels indicating which types of particles can be detected by each layer. Information about data collection can be found in Section 3.4.

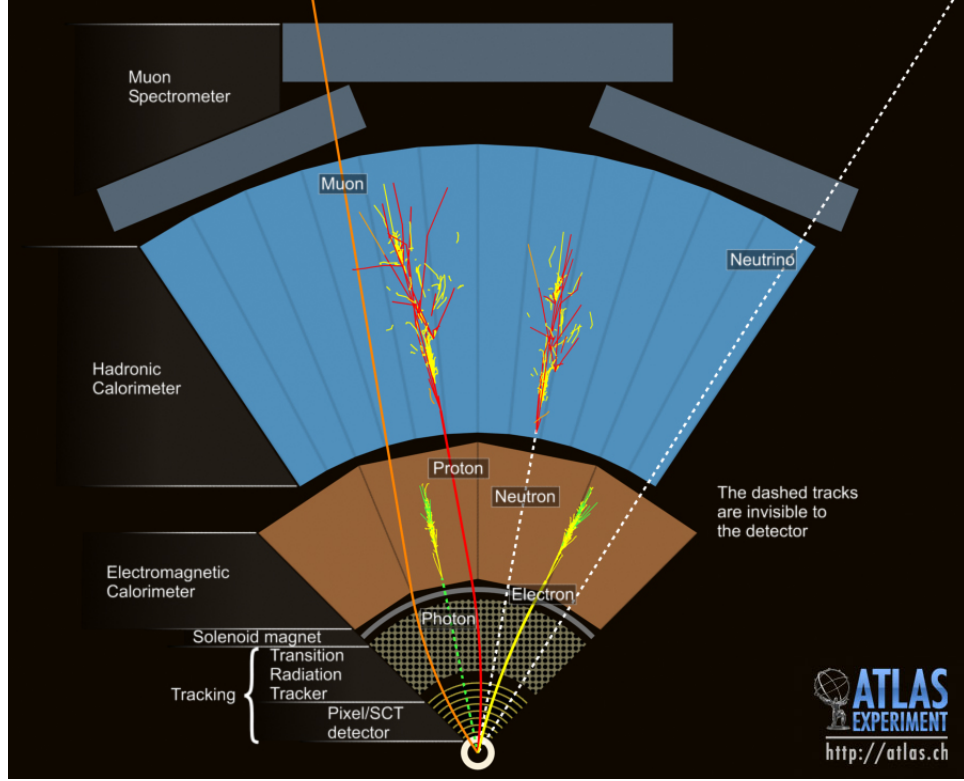


Figure 3.3: Cross-sectional slice of the ATLAS detector, showing what types of particles can be measured in each layer [61]

3.3.1 Coordinate System

As stated previously, bunches of protons circling in the LHC rings are allowed to pass through each other (and hopefully collide) inside detectors like ATLAS. In order to describe these $p - p$ collisions and the detector itself, it is necessary to introduce the coordinate system to be used throughout this thesis.

We define the origin of our right-handed coordinate system at the nominal interaction point [60]. The z -axis points along the beam line. The x - y plane (often called the transverse plane) is orthogonal to the z -axis. The positive x -axis points from the origin towards the center of the LHC ring and the positive y -axis points towards the sky.

In the transverse plane, position is described in terms of cylindrical coordinates: radial distance r from the beam line and azimuthal angle ϕ from the positive x -axis. The polar angle θ described the angle from the positive z -axis. We also define pseudorapidity η for massless objects and rapidity y from massive ones: $\eta = -\ln(\theta/2)$ and $y = \frac{1}{2} \ln(\frac{E+p_z}{E-p_z})$. Distance ΔR in the pseudorapidity-

azimuthal space is defined as $\Delta R = \sqrt{\Delta\eta^2 + \Delta\phi^2}$. “Transverse” physical values, such as transverse momentum p_T , are defined in the x-y transverse plane unless stated otherwise.

3.3.2 The Inner Detector

The **Inner Detector (ID)** is the very first part of the detector to “see” particles from a collision and is designed to precisely measure the trajectory of charged particles (called **tracking**) within a pseudorapidity range of $|\eta| < 2.5$ ³². A computer-generated rendering of the inner detector is shown in Figure 3.4 [62]; this image shows the “barrel” (i.e. the main cylindrical body) and the “endcaps” (i.e. the caps at the end of the cylinder) for each part of the ID. The ID consists of three components: the **Insertable b-Layer (IBL)** [63], the pixel detector, the transition radiation tracker (TRT), and the semiconductor tracker (SCT). The ID is bathed in a 2 T magnetic field generated by the solenoid magnet, so any charged particles in the ID will move along curved trajectories³³. The IBL and pixel detector are both “pixel” detectors made of small silicon sensor squares arranged in a grid. The IBL is an extra layer of pixels inserted inside the pixel detector to provide better track resolution. These pixels can sense when an electrically charged particle passes through them; their small size³⁴ allows for a very precise reconstruction of the trajectory of particles in the ID. The outermost part of the ID, the TRT, is a “straw” detector; instead of pixels, this detector consists of tubes of ionizable gas with a wire in the center. The wire and the straw casing have a very high electric potential difference between them. When a charged particle passes through the wire, it ionizes the gas, creating electrons (which drift towards the wire) and ions (which drift towards the straw walls). The large difference in potential amplifies the effect of the electrons on the wire, creating a detectable signal. Although the TRT does not provide such fine resolution as the pixel detectors, it is much cheaper to use the TRT than to build the entire ID out of pixels.

3.3.3 Calorimeters

The calorimeters are designed to measure the energy of particles by collecting the energy deposited during **particle showers**. ATLAS has two types of calorimeters, each designed to collect different types of energy: the **Electromagnetic Calorimeter (ECAL)** and **Hadronic Calorimeter (HCAL)**. A computer-generated image of the calorimeters is shown in Figure 3.5 [64].

³²Electrons identification using the ID is only done with a range of $|\eta| < 2.0$

³³This is useful for track reconstruction, discussed in Section 3.5.1

³⁴Each pixel is approximately $50 \times 400 \mu\text{m}^2$.

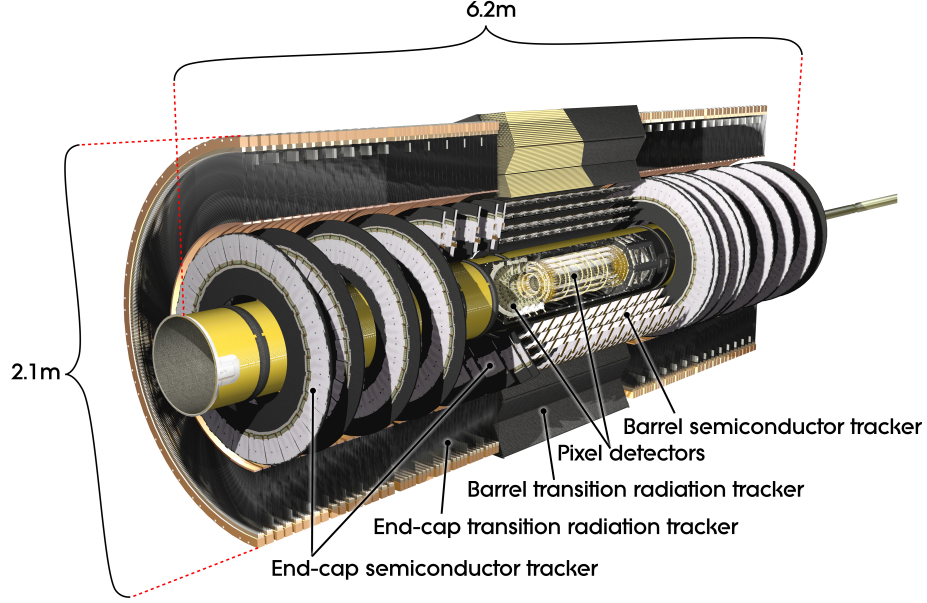


Figure 3.4: Rendered image of the ID [62]

The ECAL consists of a barrel ($|\eta| < 1.475$) and endcaps ($1.375 < |\eta| < 3.2$) filled with liquid argon with sheets of lead in between. The ECAL interactions with electrons (via [bremsstrahlung](#)) and photons (via e^+e^- pair production) can be characterized by the [radiation length](#) X_0 , the average distance over which the energy of an electron is reduced by bremsstrahlung radiation by a factor of $\frac{1}{e}$ ³⁵. X_0 also represents about $\frac{7}{9}$ of the mean free path of e^+e^- pair production [7]. When photons and electrons pass through the ECAL, they radiate or convert in the dense lead, then ionize in the liquid argon. The liquid argon produces [scintillation](#) light, which is collected, amplified, and measured by photon detectors. In terms of radiation lengths X_0 in liquid argon, the ECAL is $22X_0$ thick in the barrel and $24X_0$ thick in the endcaps.

As the ECAL is designed to measure the energy of electromagnetic particle showers, so the HCAL is designed to measure the energy of hadronic particle showers. The HCAL consists of a tile barrel calorimeter ($|\eta| < 1.7$) and liquid argon endcap calorimeters ($|\eta| > 1.7$). Liquid argon endcaps are used for their radiation-hardness and budgetary concerns. The tile barrel calorimeter of the HCAL is made from steel absorbers and scintillating tiles. Unlike the ECAL, scintillation occurs in the tiles of the ECAL barrel. Hadronic showers are characterized by the [nuclear interaction length](#) λ_I , the mean distance between hadronic interactions of relativistic hadrons [7]. The nuclear interaction

³⁵Note that X_0 depends on the material through which the electrons and photons are passing.

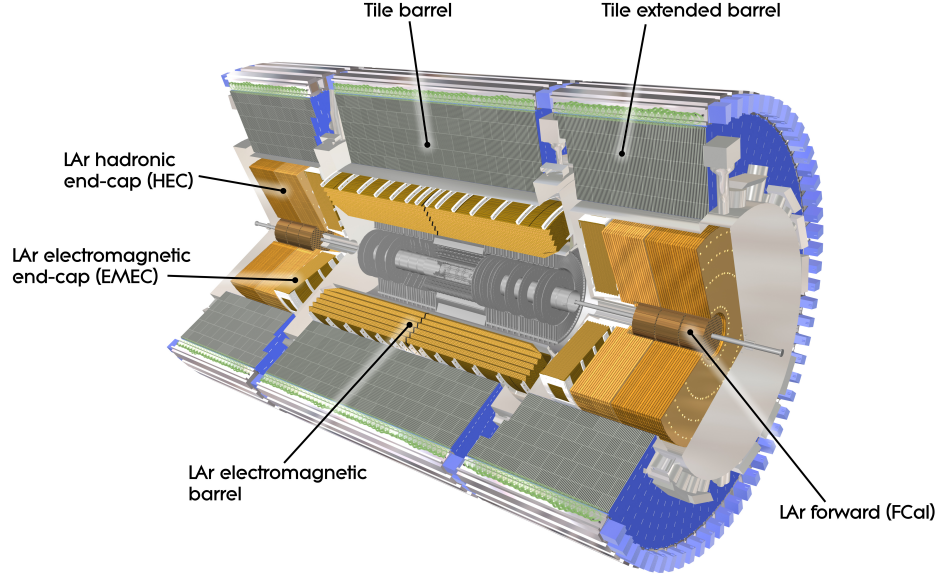


Figure 3.5: Rendered image of the calorimeters [64]

length is much larger than the radiation length. For example, in iron $\lambda_l \approx 23$ cm, whereas $X_0 \approx 1.8$ cm. Because of this, the HCAL is much thicker than the ECAL ($2.28 - 4.25$ m vs. 50 cm). In terms of interaction lengths of a pion in lead or steel³⁶, the HCAL is $9.7\lambda_l$ thick in the barrel and $10\lambda_l$ thick in the endcaps [60].

3.3.4 Muon Spectrometer

Because the calorimeters have (hopefully) absorbed all hadronic and electromagnetic particles, the only interacting particles remaining at the outermost layer of ATLAS are muons. At relativistic speeds, muons have a relatively long lifetime in the lab rest frame, so when they're produced inside the ATLAS detector they can travel 10 meters or more before decaying. In order to reconstruct these muons, a system of detectors called the **Muon Spectrometer (MS)** plus large toroid magnets are used. The magnetic field bend the muon tracks as they pass through the MS, allowing for reconstruction of their kinematic properties. In total, four different types of detectors are used in the MS: monitored drift tubes (MDT), cathode strip chambers (CSC), resistive plate chambers (RPC), and thin gap chambers (TGC) [60]. The MS can measure the momentum of muons in $|\eta| < 2.7$ and trigger on

³⁶ $\lambda_l \sim 20$ cm.

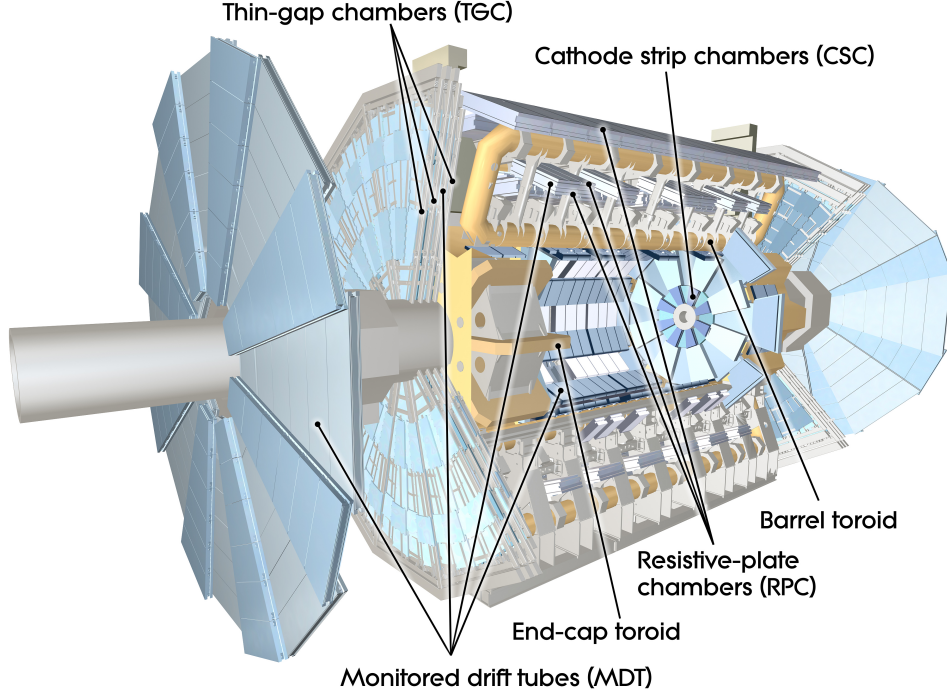


Figure 3.6: Rendered image of the MS [65]

muons in $|\eta| < 2.4$ ³⁷. A computer-rendered image of the MS is shown in Figure 3.6 [65].

3.4 Data Collection

Having described the hardware of the ATLAS detector, we shall now turn our attention to its functionality during collisions. Data collection for physics analysis is done by the [Trigger and Data Acquisition \(TDAQ\)](#) system, which shall be described now. Data collection at the LHC is done in waves, called *runs*. Run 1 of $p-p$ data collection at an average center-of-mass energy of 8 TeV took place from 2010-2013 [66], and Run 2 at 13 TeV took place from 2015-2018.

3.4.1 Trigger System

When the LHC is running, proton bunch crossings occur at a 40 MHz rate, or approximately once every 25 ns [67]. The average number of collisions per bunch crossing ([pileup](#)) depends on the number of protons per bunch and how tightly the bunches are packed. Figure 3.7 shows the

³⁷Triggering will be described in Section 3.4.1.

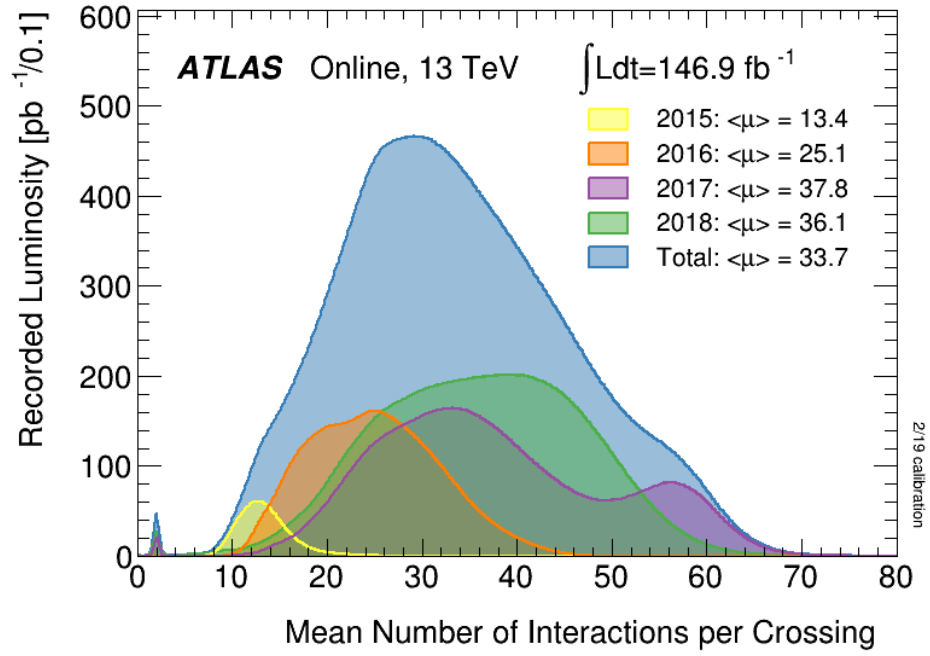


Figure 3.7: Plot of the recorded luminosity as a function of pileup for 2015-2018 data collected at ATLAS [70]

recorded luminosity as a function of pileup for data collected at ATLAS in 2015-2018. In 2018, most recorded data had between 35-45 pileup events. Each event produces about 1 MB of data [68], so if the data from every single event were saved in 2018, then our 2018 disk usage would be³⁸:

$$40 \times 10^6 \frac{\text{events}}{\text{sec}} \times 1 \frac{\text{MB}}{\text{event}} \times \frac{10^6 \text{sec}}{\sim 3 \text{ months}} \approx 13.3 \text{EB} \quad (3.3)$$

where EB is *exabytes*, or 10^{12} MB. This is approximately equal to the total amount of data managed by Google [69]. This amount of disk usage is completely unaffordable, and many of those events will have no deep inelastic scattering collisions, making them worthless for physics analysis. Therefore, ATLAS uses a [trigger](#) system to identify interesting events, signalling to the detector that the data from a given event should be saved to disk. The trigger process is divided into two stages: [Level-1 Hardware Trigger \(L1 Trigger\)](#) and [High-Level Trigger \(HLT\)](#)

³⁸Assuming a conservative total run time of 3 months.

3.4.1.1 Level-1 Hardware Trigger

The ATLAS Level-1 trigger (hereafter referred to as the “L1 trigger”) is the first step in winnowing down the massive event rate. The L1 trigger must receive information from the detector, process it, and make a decision about whether the event is potentially worth saving in less than $2.5 \mu\text{s}$ [71]. This reduces the event rate from 40 MHz to less than 75 kHz, reducing the peak data rate from $O(100 \text{ PB/s})$ to about 160 GB/s [72]. A typical CPU cannot handle these processing decisions fast enough; the $2.5 \mu\text{s}$ latency necessitates the use of custom electronics. The L1 trigger can be broken down into four main components:

- L1Calo: trigger hardware for the calorimeter system.
- L1Muon: trigger hardware for the muon system.
- Central Trigger Processing (CTP): processing unit combining information from L1Calo and L1Muon to make the trigger decision.
- Trigger Timing and Control (TTC): signals to the detector [read out](#) system whether or not to read out the information held in the pipeline based on the CTP decision.

Very basically, the L1 system uses information from the detector to make a trigger decision then signals to the detector electronics to read out their data.

3.4.1.2 High-Level Trigger

After reading out the detector information for a given event, the event is processed again to further reduce the event rate from 75 kHz to 1-1.5kHz [72]. This is done via the [HLT](#), a server farm located in a room nearby the ATLAS detector. The HLT makes a trigger decision within 300 ms as to whether an event is worth saving permanently; if the HLT trigger fires, then the full event data is pushed from the HLT server to a permanent storage disk. This reduces the peak data rate from 160 GB/s to about 1.5 GB/s, a much more manageable rate. The HLT has more time, event information, and compute power available than the L1 trigger, so the HLT can reconstruct event kinematics more precisely and trigger on more complex event topologies than the L1 trigger. The HLT provides ~ 2500 unique trigger configurations (called [trigger chains](#)); because ATLAS is a multi-purpose detector, these chains gives physicists many options for event topologies for analysis.

3.4.1.3 Trigger Prescales

In order to tune the trigger rate for the chains, physicists can adjust the trigger [prescale factor](#). If a given trigger has a prescale factor of N , then that trigger will randomly fire on one out of every N events passing its selection criteria [72]. The prescale factor can be adjusted for both the L1 and HLT triggers in a given chain, providing further flexibility for ATLAS physicists. The prescale factor can also be used to disable a trigger entirely (by setting N to be very large).

3.5 Reconstruction and Simulation

Having described the ATLAS hardware, it is now time to turn towards software. This section shall describe two use cases for software in ATLAS: event reconstruction and Monte Carlo simulation. In event reconstruction, the trajectories and energy deposits of particles in the detector are used to identify physics objects (e.g. leptons, hadrons, missing energy) to be used in physics analysis. [Monte Carlo \(MC\)](#) simulation is a method for generating “fake” data with any desired event topology, including possibly [BSM](#) physics signals. In MC simulation, physicists first describe a physics process, then run a series of simulated randomized trial events of that process. Those trial events are then fully simulated in the ATLAS detector to show what those events would look like in real data. Finally, the simulated data is reconstructed in the same way as real data to make a proper comparison between simulation and reality.

3.5.1 Object Reconstruction

When different types of objects pass through the layers of the ATLAS detector, they leave tracks and energy deposits, as shown in Figure 3.3. The raw detector measurements are converted into physics objects in two steps. The first stage in this process is track and energy deposit reconstruction; after this, more complex objects are created and identified.

Particle tracks are reconstructed using the ATLAS inner detector and muon spectrometer (described in Section 3.3). This process is done in three stages [73]:

- Pre-processing: Raw pixel detector data is converted into clusters, raw SCT data is converted into space-points, TRT timing information is transformed into drift circles.
- Track-finding: Tools such as Kalman filtering [74] and global χ^2 fitting [75] are used to identify tracks in the pixel and SCT detector data. Ambiguities are resolved and fake tracks rejected at this stage. Selected tracks are then extended into the TRT and associated with TRT

drift circles. Finally, the extended tracks are refitted using information from all three inner detectors.

- A complementary track-finding strategy is also done “inside-out”: unused track segments in the TRT are extended inwards to the SCT and pixel detectors. This improves the tracking efficiency for secondary tracks from conversions or long-lived particle decays
- Post-processing: A dedicated vertex-finding algorithm is used to first reconstruct the [primary vertex](#), then to reconstruct photon conversions and secondary decays.

Association of tracks to the muon spectrometer shall be described later in this section in the context of muon reconstruction.

The energy reconstruction process is used to identify clusters of energy within the calorimeters. To aid in this process, the calorimeters are each divided into a grid of elements in $\eta \times \phi$ -space called “towers” [76]. The ECAL is divided into 200×256 towers (0.025×0.025 in $\Delta\eta \times \Delta\phi$), and the HCAL is divided into 100×64 towers (0.1×0.1 in $\Delta\eta \times \Delta\phi$). These towers are used in two different methods of clustering:

- Sliding-window clustering: first, the energy inside each calorimeter tower is calculated. Next, a fixed-size sliding-window algorithm is used to identify groups of towers whose total energy is at least 3 GeV (ECAL only) or 15 GeV (ECAL + HCAL). The fixed size of these clusters allows for precise cluster energy calibration.
- Topological clusters: first, towers with a signal-to-noise³⁹ ratio of at least 6 (ECAL) or 4 (HCAL) are identified as “seeds”. The seeds are sorted in descending order in signal-to-noise ratio⁴⁰, then adjacent cells with signal-to-noise ratio above 3 (ECAL) or 2 (HCAL) are added to the seeds⁴¹. This process is repeated until the seed list is empty.

Having reconstructed our tracks and energy deposits, we are now ready to tackle physics object reconstruction.

³⁹Signal can either be the cell energy or its absolute value. Noise is the expected RMS of the electronics noise for the current gain and conditions.

⁴⁰In this case, signal is always $|E|$. Noise is defined in the same way as the seed-finding step.

⁴¹Note that cells cannot be reused, so the “best” seeds get to claim adjacent cells first.

Electrons

Electrons are reconstructed by matching an ECAL tower seed⁴² to a reconstructed track using a spatial matching requirement of $|\Delta\eta| < 0.05$ and $-0.2 < \Delta\phi < 0.05$ [77]. Electrons within the central region of the detector ($|\eta| < 2.47$) are then identified using a likelihood-based (LH) method using measurements from the tracking system, the calorimeter system, and quantities that combine both tracking and calorimeter information. Finally, the electron identification efficiency is calibrated to data using $Z \rightarrow ee$ events [73].

Photons

Photons are reconstructed using the same ECAL seeding method as used for electrons, but require that the seed have no matching Inner Detector tracks (unconverted photons) or a matching track in the SCT and TRT only (converted photons) [78]. Photons are then identified using either a cut-based, log-likelihood-ratio (LLR)-based, or covariance-matrix-based method [73].

Muons

Muons reconstruction is first performed independently in the Inner Detector and Muon Spectrometer [79]. Four types of muon identification are provided by ATLAS:

- Combined (CB): ID and MS tracks are combined via a global refit procedure to improve the track fit
- Segment-tagger (ST): an ID track is matched via extrapolation to at least one track segment in the MS
- Calorimeter-tagged (CT): an ID track is matched to an energy deposit in the calorimeters. Optimized for the $|\eta| < 0.1$ region and momentum range $15 < p_T < 100$ GeV
- Extrapolated (ME): muon trajectory reconstructed from a MS track, required to be loosely compatible with the primary interaction point. Used in the region $2.5 < |\eta| < 2.7$, which is not covered by the ID

Muons are calibrated using $J/\psi \rightarrow \mu\mu$ and $Z \rightarrow \mu\mu$ data [79].

⁴²Identified using sliding-window clustering.

Jets

When quarks and hadrons are produced in the ATLAS detector, they hadronize and form jets, collimated cones of hadrons and their decay products. Jets are reconstructed via the anti- k_t jet clustering algorithm [80] with radius parameter $R = 0.4$. The anti- k_t algorithm clusters high- p_T jets first and is selected because it respects three major guidelines for jet reconstruction [73]:

- Infrared safety: the addition of soft particles between two particles belonging to the same jet does not alter the recombination of these two particles into a jet⁴³.
- Collinear safety: jet reconstruction should not alter if a particle splits into two collinear particles.
- Order independence: the same hard scattering process should be reconstructed at parton-, particle-, and detector-level.

The anti- k_t algorithm clusters jets by first calculating distances d_{ij} between objects⁴⁴ i and j and distances d_{iB} between an object i and the beam B , where the distances defined like so:

$$d_{ij} = \min(p_{Ti}^{-2}, p_{Tj}^{-2}) \frac{\Delta_{ij}^2}{R^2}, \quad d_{iB} = p_{Ti}^{-2} \quad (3.4)$$

where p_{Ti} is the transverse momentum of object i and $\Delta_{ij}^2 = (y_i - y_j)^2 + (\phi_i - \phi_j)^2$. The smallest distance is identified, and if it is d_{ij} , then objects i and j are combined and the procedure restarted. If the smallest distance is d_{iB} , then object i is called a jet and removed from the list of objects.

b -Jets

As described in Section 2.2.5, jets originating from b -quarks (b -jets) have several unique properties that make it possible to distinguish them from u , d , s , and c -jets. After reconstruction, b -jets are identified using a multivariate boosted decision tree b -tagging algorithm called “MV2c10”⁴⁵ [81]. MV2c10 is trained using simulated $t\bar{t}$ samples as the b -jet signal and a background sample composed of 7% c -jets and 93% light-flavor jets. The inputs to *MV2c10* are calculated using three separate algorithms:

- IP3D/IP2D: These algorithms are designed to reconstruct the Impact Parameter (IP) d_0 of tracks associated to a jet (see Figure 3.8 [82] for a visualization of d_0). Tracks associated

⁴³This also works the other way: the absence of a soft particle should not change the association either.

⁴⁴These objects can be particles, pseudojets, etc.

⁴⁵This name used to correspond to the fraction of c -jets used in the training sample, but the name is now meaningless.

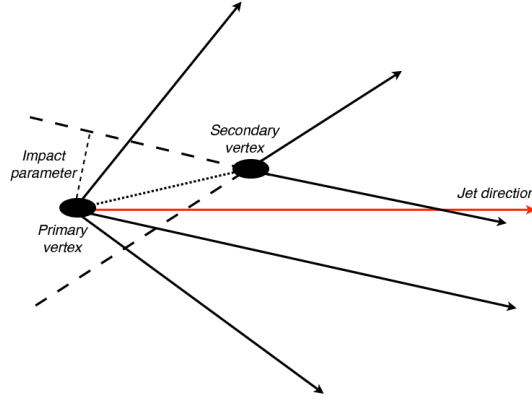


Figure 3.8: Cartoon showing the calculation of impact parameter d_0 for a track associated to a jet [82]

with b -jets have a larger impact parameter than tracks associated with non- b -jets due to the long b -quark lifetime. IP2D calculates a discriminant value based on the transverse impact parameter significance, d_0/σ_{d_0} , whereas IP3D calculates its discriminant using transverse and longitudinal IP, accounting for correlation between the two.

- SV: The secondary vertex algorithm reconstructs a displaced vertex within a jet by first identifying the points at which pairs of track cross (vertex candidates), then removing possible fake vertices or vertices from material interactions via cleaning requirements
- JetFitter: This algorithm uses a modified Kalman filter to find a common line on which the primary vertex and the b and c vertices lie, approximating the B -hadron flight path.

Using inputs from these three algorithms along with several measured variables, *MV2c10* calculates a discriminant value. The efficiency for b -jet identification⁴⁶ depends on the choice of cut value for this discriminant. *MV2c10* calibration will be discussed in-depth in Chapter 4.

Large- R Jets

When a physics object decays into hadronizing children particles (e.g. $h \rightarrow b\bar{b}$), the shape and relative position of the child jets will depend on the boost of the parent object. If the parent object decays (nearly) at rest, the child jets will be approximately back-to-back and easy to resolve. If the parent object decays with significant boost, however, the children particles will also be boosted,

⁴⁶And c and light-jet rejection.

causing the jets to collimate. If the boost is large enough, the two jet cones will no longer be distinguishable and will instead appear as a single “fat” large- R jet. Like the standard small- R jets, large- R jets are reconstructed using the anti- k_t algorithm with $R = 1.0$ [83] [84]. The large- R jets are groomed to remove soft components from the underlying event or pileup, leaving behind only hard-scatter constituents [85]. Many different tagging and identification criteria are available for large- R jets; an analysis-specific example can be found in Section 5.3.

Missing Energy

Some particles, such as neutrinos, do not interact with the detector material at all and are hence undetectable. Their presence can be inferred by momentum imbalance in an event. We quantify this as missing momentum transverse to the beamline p_T^{miss} and its magnitude (called “missing energy”, MET or E_T^{miss}) [86]. p_T^{miss} is calculated by first reconstructing all visible objects, then calculating the sum of their transverse momenta. If that sum is not equal to zero, then we know there is some momentum missing. Therefore, p_T^{miss} is equal to the negative sum of the momenta of all visible objects. MET is calibrated using two types of data samples: $Z \rightarrow \mu\mu$, where the expected MET is zero, and $W \rightarrow e/\mu\nu$, where the neutrino gives nonzero expected MET .

3.5.2 Monte Carlo Simulation

This subsection will describe the purpose and general strategy for MC simulations in ATLAS. Information about MC simulation processing can be found in Section 3.6.

MC simulations are an extremely useful tool for ATLAS physicists for understanding both observed and unobserved physics processes. Simulations can be presented in a format identical to the output of the ATLAS data acquisition system *or* in an object-based format with the “true” object labels attached [87]. Generally, the ATLAS simulation process can be divided into three steps:

- Generation of events and immediate particle decays
- Simulation of the detector and physics interactions
- Digitization of energy deposits in the sensitive regions of the detector into detector readouts

A flowchart showing the entire MC simulation chain is shown in Figure 3.9 [87]⁴⁷. Each of these steps shall be described below; note, however, that the details of *how* Monte Carlo generators perform

⁴⁷This flowchart includes some optional steps, such as pileup simulation, which shall not be addressed here.

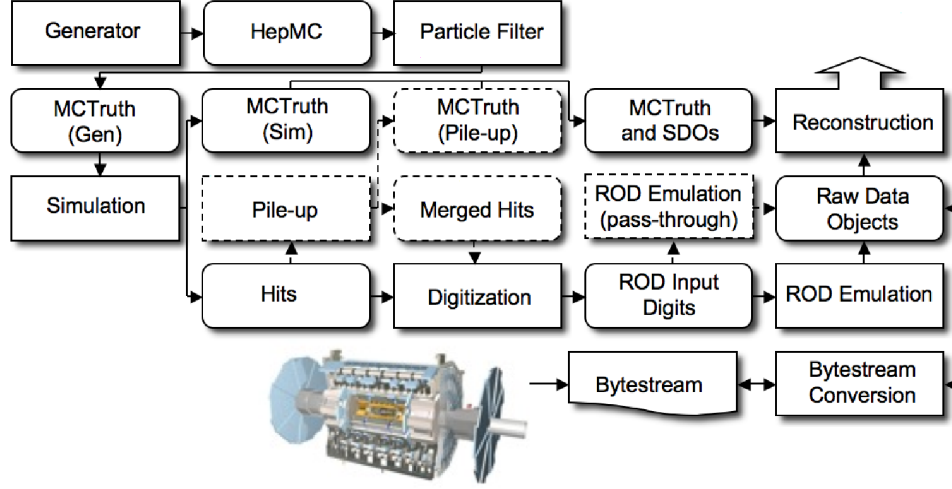


Figure 3.9: Flowchart of the ATLAS MC Simulation Process [87]

the necessary calculations to simulate physics processes in a timely fashion is beyond the scope of this document.

Generation

The first step in running a MC simulation is identifying the physics processes one wishes to simulate. Once the process has been described (for example, events containing two jets simulated for all leading-order Feynman diagrams, filtered to only include jet above a certain p_T threshold), it must be encoded into an input file for the MC generator to read⁴⁸. The generator will then simulate the events described, applying a generation filter if one is specified, for as many events as the physicist requests. This is the “Monte Carlo” part of the MC simulation chain: each event is randomly sampled and has no bearing on the prior or posterior events. At this stage, only prompt decays and stable particles are simulated. The output of the generator is saved in an object-oriented C++ format called “HepMC” [88] along with the [truth record](#), which details particle interactions in the generator, including incoming and outgoing particles.

Simulation

The generator output file is used as input to the simulator. In this stage, the stable particles from the generation stage are allowed to propagate and decay in the detector. Particle interactions with the ATLAS detector are simulated using GEANT4 [89]; details about the precise alignment of the

⁴⁸The format of this input file will depend on the generator software used.

components of the ATLAS detector can be set at run time by the user. The energies deposited in the sensitive pieces of the detector are saved as “hits” with the total energy deposited, position, and time. The truth record stores information about truth tracks (i.e. the actual path of a simulated particle) and truth decays for certain particles. The simulation output is saved as a “hits” file along with the simulation truth record.

Digitization

The ATLAS digitization software uses the simulation “hits” file as input to convert those hits into simulated detector measurements. The hits are converted into detector signals (e.g. voltage), then into “digit” inputs to the detector readout electronics. This stage also includes pileup and detector noise simulations. The output of the digitization step is identical to an actual data file except for the inclusion of “truth” objects from the previous simulation steps. This allows for easy comparisons between data and MC simulation.

3.6 Data Processing and Management

Having covered the core concepts of data and simulation processing at ATLAS, we shall now cover the actual processing of real and simulated data. This section shall describe the Worldwide LHC Computing Grid and its uses as well as the ATLAS data model and distributed data management system.

3.6.1 The Worldwide LHC Computing Grid

The LHC’s computing requirements far exceed the budget available to CERN. The laboratories and universities collaborating on the LHC, however, have access to national, regional, and local computing facilities [90]. In 2002, these facilities were linked into a single computing service called “The Worldwide LHC Computing Grid”, often simply called [The Grid](#)⁴⁹. Computing sites in the Grid are divided up into different layers, or “tiers” [91]:

- Tier-0: These facilities are responsible for storing the first copies of raw and reconstructed data and reprocessing data during LHC down-times. Tier-0’s are also responsible for distributing data to Tier-1’s. There are only two Tier-0 sites: the CERN Data Centre (Geneva) and the

⁴⁹This is now the world’s largest computing grid!

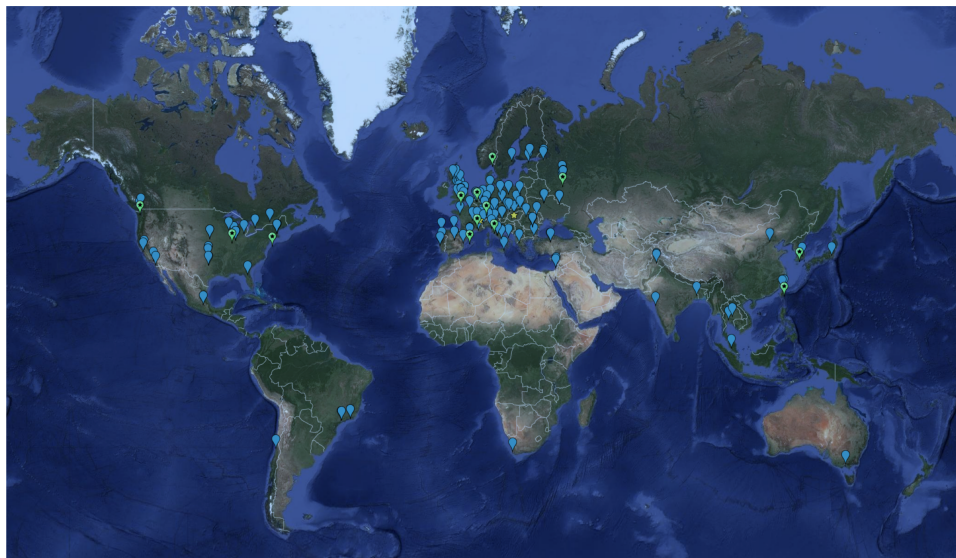


Figure 3.10: Map of all major LHC Grid sites [92]

Wigner Research Center for Physics (Budapest). These two facilities are connected to each other by three 100 Gb/s high-speed connection lines.

- Tier-1: Tier-1 sites are responsible for storing raw and reconstructed data, performing large-scale reprocessing of data, and storing the output of these reprocessing campaigns. Tier-1's are also responsible for distributing data to Tier-2's and storing simulated data produced at Tier-2's. There are a total of 13 Tier-1 sites, each connected to the Tier-0's by a 10 Gb/s connection.
- Tier-2: These sites are typically located at major universities and scientific facilities. Tier-2's are responsible for storing data and providing computing power for physics analyses and simulation. There are about 160 Tier-2 sites.
- Tier-3: These are the local computing sites at LHC member organizations. They have no responsibility for data management or processing and can be thought of as “endpoints” in the Grid.

Figure 3.10 shows a map of all Tier-0, Tier-1, and Tier-2 sites in the Grid [92]. Much of the work in this thesis was completed using the Tier-3 Grid site in the University of Pennsylvania Department of Physics and Astronomy.

3.6.2 Distributed Analysis in ATLAS

It's one thing to have access to the Grid of computing facilities, but how exactly are these resources made available to and used by the 2000+ physicists working at ATLAS [93]? The basic analysis workflow proceeds like so:

- A user or analysis team prepares an analysis task by identifying the input dataset(s) and testing their analysis code locally
- The analysis job is submitted to the Grid using [Production and Distributed Analysis \(PanDA\)](#), an ATLAS-specific software workload management system. PanDA identifies an appropriate Grid site⁵⁰ and prepares the analysis jobs for submission to the site
- The Grid site interacts with computing and storage resources via Grid middleware software. Once the task is complete, the output is either saved at that Grid site or piped to a requested site
- The user or analysis team can access the output of their task by downloading it to their Tier-3 or by using it as input to additional Grid tasks

The Tier-0, -1, and -2 Grid sites have a total of ~ 84 PB of total disk space available, of which 72 PB are used as of October 2018 [92]. In Run 2, Tier-0 and Tier-1 CPU capacity was completely used, whereas Tier-2 CPU usage was slightly below capacity; overall Grid usage was ~ 20 -40% greater than the amount pledged by member sites. The Grid runs about half a million jobs per day⁵¹, and ATLAS physicists use about 90k CPU cores at any given time [94]. In 2011, it took about three million core-hours to reconstruct one petabyte of ATLAS data containing one billion events [95]; in 2016, ATLAS used a total of one billion core-hours [96]. Figure 3.11 illustrates the total CPU hours delivered per month by the Grid, broken down by utilization by each LHC experiment [92] [97]⁵². ATLAS computation and LHC Grid power have a minor positive feedback loop effect on each other; when the LHC makes improvements to the Grid, ATLAS has more power available for more advanced analysis techniques, causing greater demands on the Grid.

Despite the overhead of submitting and monitoring Grid jobs, this system provides many advantages to the user. In general, large data analysis tasks cannot be handled in one gigantic “block” and must be broken up into many smaller sub-tasks [87]; the Grid's distributed design makes it easy to

⁵⁰Often this is a site with the correct dataset already downloaded.

⁵¹Excluding local batch jobs and interactive sessions.

⁵²CPU was benchmarked using the HS06 benchmarking suite.

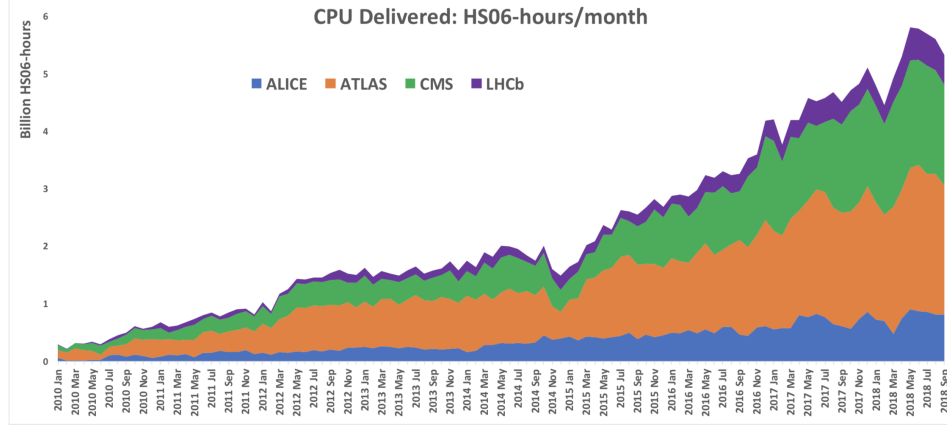


Figure 3.11: Total CPU delivered by the LHC grid per month during Run 2, broken down by per-experiment usage [92] [97]

split these sub-tasks between different sites on the fly. Additionally, many ATLAS computing tasks require access to [Athena](#) [98], the ATLAS physics analysis software framework. Grid users get access to compiled and updated version of Athena regularly⁵³, requiring no maintenance or checks on their part. Athena is a very large⁵⁴ C++ library, but users can submit Grid Athena tasks using a Python wrapper for their convenience. The Grid also provides a mechanism for retrying and redistributing analysis tasks on the fly⁵⁵. Instead of having users resubmit their own tasks, the Grid will simply retry them (either at the same Grid site or at a different one). Users can also configure their Grid jobs by hand, specifying their desired Grid site and number of sub-tasks manually.

3.6.3 The ATLAS Data Model

In order to better understand ATLAS data management, we must first discuss the ATLAS data model. The vast majority of LHC analysis code is built using a C++ analysis framework called ROOT [99]. ROOT can also be used to save files (called ROOT files) containing persistent C++ objects associated with physics events [100]. A single ROOT file rarely contains a complete set of data of interest to the user; instead, files are aggregated into *datasets*. These datasets are the operational unit for distributed data management; datasets are copied and transferred around the Grid as opposed to individual files. Datasets can be aggregated together into *containers* for ease of

⁵³As well as many other useful software packages.

⁵⁴Enterprise-scale

⁵⁵Grid tasks are known to fail not infrequently due to hardware problems, software package misconfigurations, and user errors.

analysis⁵⁶.

3.6.4 Distributed Data Management in ATLAS

ATLAS Distributed Data Management (DDM) is performed using a system called Rucio [100]⁵⁷. Although the architecture of this system is beyond the scope of this document, the basic concepts behind Rucio shall be listed here.

Every Rucio user is given an *account*, a unit for assigning privileges and access rights to a user. All actions within Rucio are conducted within the scope of this account. Rucio datasets are structured as described in the previous subsection. Most ATLAS data is organized hierarchically: a single data run is composed of many events, a data-taking period is composed of many runs, and a year of data-taking is composed of many periods. In order to uniquely identify a file within Rucio, each file is given a unique identifier, the Logical File Name (LFN), which can never be reused. Similarly, each dataset is uniquely labeled using a Dataset ID (DID) [101], also called a Dataset Name (DSN). LFNs and DIDs are each made of two strings: the scope identifier and the file/dataset name. The scope identifier usually identifies the user or group which produced the file. Every user account has a their own scope, and centralized ATLAS dataset production is also given its own unique scope. Dataset properties are labeled with status flags and with metadata attributes. Notably, Rucio does *not* contain a concept of dataset versioning. Dataset versions are usually labeled in their dataset name; the dataset name string can be used to determine which versions of ATLAS software were used to produce that dataset.

The most useful part of Rucio for users is the ability to download and transfer datasets between Grid sites with ease. When a user logs in to a Grid site, they can use Rucio to copy entire datasets (or individual files from datasets) to that site. Users can also use Rucio to make dataset “replica rules”, which replicate the dataset to a desired Grid site⁵⁸. Rucio is also useful to the entire ATLAS organization because it allows for tracking of dataset access; many ATLAS datasets are created and never used, wasting valuable disk space. During Run 2 of the LHC, ATLAS implemented much stricter dataset deletion policies, and Rucio was essential in managing these policies. These policies shall be mentioned briefly in the following section.

⁵⁶For example, one might create a container containing all $p - p$ collision datasets from 2018.

⁵⁷The original DDM system was named Don Quixote. In the Cervantes novel, Rucio is the name of Don Quixote’s squire’s donkey. For this reason, the donkey is the logo of the Rucio project.

⁵⁸The user can also set a “lifetime” for this replica, after which it will be deleted to save disk space.

3.6.5 Flavor Tagging Derivation Software

In this section I shall describe my personal contributions to ATLAS software and dataset production. I shall describe my role in ATLAS software as the flavor-tagging derivation software contact, highlight some of the improvements I made to flavor-tagging software, and describe a major bug I identified and fixed.

3.6.6 ATLAS Derivation Software

In Sections 3.4 and 3.5, I described how data is collected and reconstructed and how MC samples are simulated in ATLAS. After reconstruction, data and MC samples are both stored in a format called [Analysis Object Data \(xAOD\)](#) [102]. The “x” in xAOD is used to denote the fact that xAOD files can be read directly by ROOT code (in Run 1, these files were called “AODs” and were *not* readable by ROOT). Although a physicist could use xAOD files as inputs for analysis, this would probably be a poor decision. xAOD files are very large and have no event-level filtering applied; if you wanted to run a data analysis using xAOD files, you would waste a huge amount of time crawling through the file event-by-event looking for event topologies of interest. Additionally, the xAOD file would contain many physics objects you don’t need while simultaneously not including some special objects you’d like to include⁵⁹.

Instead of running directly on xAODs, most physics analyses go through two stages of sample size reduction: derivation and tuple production. Derivations are produced from xAOD files, and tuples are produced from derivations. Derivations (which shall be described in more detail momentarily) are usually 1 – 5% the size of the original xAOD; tuple sizes can vary wildly. An average derivation dataset will be 10 – 100 GBs (small enough to store on a local Tier 3 Grid site), and tuples will usually be a few GB (small enough to store on your local machine). Additionally, tuples are a [flat](#), i.e. non-relational, making them extremely easy to read and interpret in ROOT.

The process of transforming an xAOD into a derivation file, called a [Derived Analysis Object Data \(DAOD\)](#), is the first step in which the ATLAS data pipeline is separated by physics application. At its core, there are four processes occurring during derivation production:

- Skimming: the removal of entire events based on some criteria related to the features of the event.

⁵⁹Since the xAOD format is common among all of ATLAS, you need approval from the collaboration if you want to add something new to the xAODs.

- Thinning: the removal of individual objects within an event based on some criteria related to the features of the event.
- Slimming: the removal of variables within a given object type, applied to all objects of that type for all events.
- Augmenting: calculating and creating new objects or variables for all events.

The first three derivation transformations (skimming, thinning, and slimming) reduce the size of the DAOD, whereas the final transformation type (augmenting) increases the DAOD size. Because the transformations needed will vary dramatically between groups in ATLAS, derivation production is divided up by physics application. In the next section, I shall describe the ways in which I contributed to flavor-tagging software through derivation production and management.

3.6.7 Flavor-Tagging Derivation Software

I began to work on flavor-tagging derivations initially as a part of my work on p_T^{rel} muon-in-jet triggers (see Section 4.5.2); I had to make several changes to the designated p_T^{rel} DAODs in order to complete the trigger studies. I served as the flavor-tagging derivation software contact from October 2016 to December 2018. In general, my tasks as derivation software contact were to maintain and improve the flavor-tagging derivation software and request derivation production through the official ATLAS pipeline whenever flavor-tagging users needed new derivation samples. In addition to supporting flavor-tagging users, I assisted in several major changes to ATLAS software (listed approximately in chronological order):

- ATLAS changed internal software releases, from Release 20.7 to Release 21. This also involved a brand new way of setting up derivation tasks, using the multi-process version of the ATLAS reconstruction called [AthenaMP](#) [3].
- ATLAS switched our version control software from SVN to git/Gitlab. At the same time, ATLAS implemented a continuous-integration development practice based on the Jenkins pipeline tool.
- Due to success in data-taking in Run 2, ATLAS implemented a policy of removing old/unused datasets and set stricter size caps on derivation sizes.
- The actual flavor-tagging of jets was moved from xAOD production to DAOD production

I will discuss each of these very briefly.

When I took over flavor-tagging derivations in the fall of 2016, the software had not been “cleaned up” in several years. The code was disorganized and filled with redundant definitions, out-of-date container names, and commented-out blocks; I reorganized the code and created a documentation page for flavor-tagging derivations. I also spent a few weeks contacting flavor-tagging users to understand exactly *what* they wanted in their derivation files and what objects could be safely removed.

Around this time (fall-winter 2016), the change from Release 20.7 to Release 21 began ⁶⁰. For derivations, most of the changes were under-the-hood; although the file formats did not change much, the way in which derivation tasks were processed changed dramatically. In Release 21, derivation processing took full advantage of AthenaMP, which allowed users to run multiple processes in the same task, by creating [trains](#). To run a “train” of DAODs over an xAOD, the user specifies multiple derivation formats to be produced. At runtime, Athena identifies common algorithms and tools used between formats and only initializes them *once*; this way, the various formats can share these tools, speeding up and streamlining production. This works best if the derivation formats share many tools in common and have similar event selection efficiencies; if one of the formats in the train selects many more events than the others, it will slow down the train and possibly even cause a crash. While I was testing the flavor-tagging derivation trains, I found a major bug in the setup of jet software within trains; instead of picking all *unique* software tools in the train, the code was only identifying the *first* occurrence of a given jet-building software tool. This is a problem if, for example, you need different jet collections in different derivation files (in fact, this is how I identified the problem). Luckily, because I had begun my Release 21 checks early, we were able to fix the problem with the jet derivation software team before trains were adopted for all ATLAS data processing.

At the same time as the Release 20.7 to Release 21 transition, ATLAS also changed version control software and changed to a continuous-integration development model. In Run 1 and Release 20.7, ATLAS used SVN for managing versions of software. SVN is a *centralized* version control system; all the software is contained within a single repository, which is centrally managed by ATLAS. For Run 2 and Release 21, ATLAS changed to git, a *distributed* version control system; every user has the right to create and manage access to repositories on their own. This makes [branching](#) much easier; a user can check out a repository, create a parallel working branch, and request to merge her changes into production entirely on her own. For 2016-2017, derivation software contacts (including me)

⁶⁰The names don’t really have any meaning: Release 20.7 was used at the end of Run 1 and start of Run 2, and Release 21 was used for the remainder of Run 2

had to separately manage both a Release 20.7 *and* a Release 21 version of the derivation software on SVN and Gitlab, respectively. For this reason, I was very glad when we abandoned Release 20.7 and SVN, moving entirely to git.

During 2016, ATLAS collected about 40 fb^{-1} of data, and pleased physicists requested many derivation samples. In fact, this was a problem: there are many different varieties and versions of DAODs, i.e. the same xAOD can be made into many different derivation files. Although DAODs are smaller than xAODs, DAOD storage uses more disk than any other sample type at the LHC. In fact, ATLAS nearly ran out of disk space in 2016; at one point, the derivation team was informed that we had less than two months' time before all ATLAS disks were full, and there was no money in the CERN budget to buy more. To deal with this, derivation size caps were tightened and enforced more strongly; I made the necessary changes to the flavor-tagging DAODs well within the schedule. At the same time, the derivation team implemented a “redundancy” policy: if a dataset was several versions out-of-date, it would be deleted automatically⁶¹. I worked with the flavor-tagging users to make sure that everybody understood the policy and that nobody's datasets were deleted without warning. Additionally, the derivation team provided tools to check whether DAODs had been accessed in the past six months. I found that many flavor-tagging DAODs had never been access, and after checking for users' consent, I deleted them, clearing over 0.6 PB of disk in an instant.

Finally, I oversaw a major change to flavor-tagging in derivations as a part of the AthenaMP campaign. Previously, basic jet reconstruction and flavor-tagging were run during xAOD production, then repeated if necessary during DAOD production. This was not ideal; the flavor-tagging setup in xAOD production was fairly rigid, and since many users didn't need flavor-tagging, it slowed down production needlessly. Therefore, the flavor-tagging step was moved from xAOD production to DAOD production; in a moment, it became my responsibility to maintain flavor-tagging derivation software for the entire collaboration, not just for the flavor-tagging group. During my debugging and validation, I noticed that the interaction between jet and flavor-tagging derivation software would *not* be able to meet all our use cases; the jet reconstruction software did not provide a way to select which flavor-tagging algorithm was applied and only used the default tagging algorithm. I had to *prove* to the jet team that this was not fixable from our side before they were willing to meet with me to discuss the problem. Eventually, I got the jet derivation software team to meet with me and get their support in changing the jet-reconstruction setup to allow users to select the flavor-tagging algorithm of their choosing.

My final accomplishment as flavor-tagging derivation contact was not actually a part of the

⁶¹If an old dataset was still being used, derivation contacts could request an extension.

flavor-tagging derivation software. In 2017, I noticed that flavor-tagging DAOD tasks on the grid were often running out of memory. After some searching, I found a major memory leak in the flavor-tagging software: in a piece of low-level flavor-tagging code, memory was allocated for a particular object, but never deleted or freed. I fixed the leak and found that the flavor-tagging DAODs ran much more smoothly.

CHAPTER 4

$p_{\text{T}}^{\text{rel}}$ Calibration

“Alone we can do so little; together we can do so much.”

— Helen Keller [103]

This chapter describes the $p_{\text{T}}^{\text{rel}}$ method of flavor-tagging calibration, the single largest project in this thesis. First, flavor-tagging calibration is motivated and described within the context of the ATLAS experiment. Next, the datasets and samples used and the method behind the $p_{\text{T}}^{\text{rel}}$ calibration are described. Section 4.5 describes my personal contributions to the $p_{\text{T}}^{\text{rel}}$ calibration from the start to end of Run 2. The systematic uncertainties considered in this calibration are listed, followed by the current state-of-the-art results. This chapter concludes with a description of potential future work in $p_{\text{T}}^{\text{rel}}$ and the next steps for the $p_{\text{T}}^{\text{rel}}$ analysis team.

4.1 Introduction to $p_{\text{T}}^{\text{rel}}$

The identification of jets containing B -hadrons, ***b*-tagging**, is an essential part of many different searches and measurements at the ATLAS experiment. Since the fraction $\frac{t \rightarrow Wb}{t \rightarrow Wq, q=u,d,s} = 0.957 \pm 0.034$ [10], identifying b -jets is essential to almost all top quark physics searches, such as top-quark identification [104], $t\bar{t}Z$ and $t\bar{t}W$ cross-section measurements [105], spin-correlation measurements in $t\bar{t}$ pairs [106], and searches for BSM physics such as flavor-changing neutral currents [107]. b -jets are also useful in Higgs measurements, either in association with or directly produced from the Higgs. In $t\bar{t}H$ Higgs production [108], b -quarks are used to identify the top quarks producing a Higgs boson. Although $h \rightarrow b\bar{b}$ has the largest cross-section of all Higgs final states ($\sim 58.4\%$), it was not observed until 2018 [109] because of the inherent difficulty and messiness of $b\bar{b}$ final states. $h \rightarrow b\bar{b}$ final states are also used in BSM di-Higgs production searches [110] due to their favorable branching ratio. As b -tagging plays a critical role in these analyses, it is important to have a thorough understanding of

b -tagging performance in data, not just in simulation⁶². Taking advantage of the large semi-leptonic branching ratio of B -hadrons (see Section 2.2.4.1 for a calculation of this branching ratio), this chapter presents a calibration of the b -tagging efficiency in 2016-2017 ATLAS data in a sample of jets containing muons using a kinematic variable that is independent from the b -tagging algorithms.

As described in Section 2.2.5, b -quarks are more massive than other hadronizing quarks and B -hadrons carry a larger fraction of their parent b -quark's energy as compared to light-flavor hadrons. When the final state particle is a muon, we can define and use the variable p^* (the momentum of the muon in the hadron rest frame) to discriminate between B -hadron and non- B -hadron decays. Figure 4.1 shows the p^* distributions for B -hadrons as compared to charmed and light-flavor hadrons.

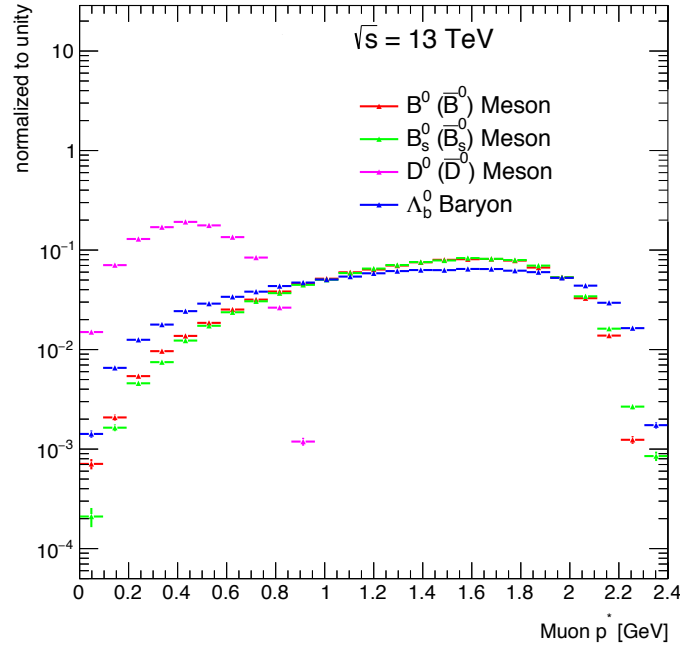


Figure 4.1: p^* distributions of final state muons from semileptonically decaying B^0 , B_s^0 , D^0 mesons and Λ_b^0 baryons in red, green, purple and blue, respectively. Due to the lower D^0 -mass the respective final state muon has less energy and hence a smaller p^* . Only muons from direct b -hadron decays are included. Figure credit to Dr. Bingxuan Liu.

The problem with calculating p^* is that it requires you to reconstruct the momentum of the parent hadron entirely, including unobservable energy from possible neutrinos. Rather than use p^* to discriminate between b - and non- b -jets, we shall use p_T^{rel} , defined in semileptonic b -decays as the

⁶²An extensive summary of flavor-tagging efforts at the ATLAS experiment in Run 1 can be found in Ref [111].

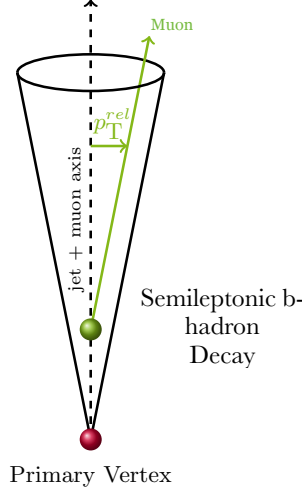


Figure 4.2: Schematic drawing showing a jet cone in black with a b -hadron in the jet, decaying semileptonically at a secondary vertex shown in green. The final state muon is shown in green as well as the projection of its momentum transverse to the jet+muon axis, the p_T^{rel} .

transverse momentum p_T of the lepton relative to the combined lepton and jet axis [three-vector](#):

$$p_T^{\text{rel}} = \|\vec{p}_\mu \times \vec{u}\|, \text{ where } \vec{u} = \frac{\vec{p}_{\text{jet}+\mu}}{\|\vec{p}_{\text{jet}+\mu}\|} \quad (4.1)$$

Figure 4.2 illustrates the p_T^{rel} of a muon in a semileptonic B -hadron decay. Although p_T^{rel} can be defined using muons or electrons, we prefer to use muons because electron identification efficiency drops at low p_T , but remains flat for muons. As described in Section 2.2.4.1, B -hadrons decay semileptonically to muons about 10% of the time. Calibration measurements performed with the p_T^{rel} method using Run 1 ATLAS data are documented in [112].

The b -tagging algorithm calibrated in this section is called “MV2c10”, which was described in Section 3.5.1. The MV2 classifier family [22] is a set of gradient-boosted decision tree algorithms used to identify whether or not a jet originates from a b -quark. The p_T^{rel} variable is not used as an input to the *MV2c10* algorithm, so any correlation between p_T^{rel} and the input variables is not exploited. *MV2c10*⁶³ outputs a number between -1 and 1, with larger positive values corresponding to a higher probability of a jet to originate from a b -quark decay. The b -tagging software group in ATLAS provides several recommended *MV2c10* [working points](#), which are cut values placed on the output corresponding to a nominal b -tagging efficiency determined in a simulated $t\bar{t}$ sample. Four working points of the *MV2c10* algorithm, 60%, 70%, 77% and 85%, are calibrated in this chapter.

⁶³Recall that *MV2c10* is the MV2 algorithm trained on a background sample of 7% c -jets and 93% light jets

Very generally, the p_T^{rel} calibration method for each working point works like so⁶⁴:

- p_T^{rel} distribution templates are produced using di-jet MC samples with a muon filter (for b - and c -quark templates) or by a data-driven approach (light-quark templates)⁶⁵.
- p_T^{rel} distributions are produced for jets passing the *MV2c10* algorithm at this working point (tagged jets) and for jets failing the algorithm (untagged jets).
- The b , c , and light p_T^{rel} distributions are fitted to the tagged and untagged data distributions to calculate the fractions of b , c , and light jets in data (f_b , f_c , and f_l , respectively), requiring that $f_b + f_c + f_l = 1$.
- After this fit procedure, the fraction f_b^{tag} , f_c^{tag} , f_l^{tag} , f_b^{untag} , f_c^{untag} , and f_l^{untag} are used to calculate the number of tagged and untagged b -jets in data:

$$N_b^{(\text{un})\text{tagged}} = N_{\text{data}}^{(\text{un})\text{tagged}} \times f_b^{(\text{un})\text{tagged}} \quad (4.2)$$

- The b -tagging efficiency is then calculated like so:

$$\varepsilon_b = \frac{N_b^{\text{tagged}}}{N_b^{\text{tagged}} + N_b^{\text{untagged}}} \quad (4.3)$$

- Finally, the b -tagging efficiency in data is presented as scale factors κ_b to relate the efficiency back to MC:

$$\kappa_b = \frac{\varepsilon_b^{\text{data}}}{\varepsilon_b^{\text{MC}}} \quad (4.4)$$

These scale factors are used to correct the b -tagging efficiency in the simulation. Because b -tagging performance depends strongly on the transverse momentum of the jet (p_T^{jet}), the scale factors are derived in bins of p_T^{jet} . The bins used are: 20-30 GeV, 30-40 GeV, 40-50 GeV, 50-70 GeV, 70-90 GeV, 90-110 GeV, 110-140 GeV, 140-170 GeV, and 170-200 GeV. The choice of bin boundaries is further explained in Section 4.2.

4.2 Datasets and Samples

The calibration measurement discussed in this chapter is performed using a \bar{b} data sample enriched in semileptonic b -decays. This is done by selecting events using muon-in-jet triggers then applying some loose kinematic cuts on the jets and muons. All data must satisfy the “Good Run List” selection

⁶⁴Detailed description in Section 4.4.

⁶⁵Note that this stage does not depend on working point, so these templates are reused for all working points.

requirement; events pass this selection if the LHC declared stable beams, the ATLAS detector was running properly, and the magnetic fields were operating as normal [113].

4.2.1 Trigger Selection

Muon-in-jet triggers (triggers requiring a muon spatially matched to a jet, both passing some p_T threshold) are used to select multi-jet events enriched with semileptonic b -decays. The spatial matching is made within a cone of $\Delta R = \sqrt{\Delta\eta^2 + \Delta\phi^2} < 0.5$ around the jet axis, where η is pseudorapidity and ϕ is azimuthal angle in the plane transverse to the beam axis. A $|\Delta z| < 2$ mm is also required, where $|\Delta z|$ is the distance of closest approach along the beam axis of the muon track to the primary vertex. These muon-in-jet triggers are part of the HLT trigger system (described in Section 3.4.1). They are supported by L1 hardware triggers that select events with at least one high- p_T muon or with a high- p_T muon and jet (without a spatial matching requirement).

Due to the steeply falling p_T^{jet} spectrum and the large cross section of multi-jet events, different trigger prescale factors are applied based on the p_T thresholds of the muon-in-jet triggers. This means that only a fraction of the events fulfilling the muon-in-jet trigger requirement are recorded, where the recorded fraction varies for each muon-in-jet trigger configuration, in order to record a sufficient number of muon-in-jet events across a large p_T^{jet} range. To maximize the event yield, multiple muon-in-jet triggers are used with each one defining an exclusive p_T^{jet} bin, ensuring that the trigger yields sufficient events and is fully efficient across the whole p_T^{jet} region. The choice of p_T^{jet} binning was entirely motivated by the triggers.

The effective luminosities collected by each trigger before offline selection for 2016 and 2017 are detailed in Table 4.1. Note that the thresholds given for these triggers refer to online quantities (prior to jet calibration); the offline thresholds, determined via bootstrapped trigger turn-on curves (see Section 4.5 for details), motivate the choice of binning.

4.2.2 MC Samples

A PYTHIA8 di-jet muon-filtered MC sample is used to produce the b - and c -jet p_T^{rel} templates. This sample was produced using the A14 PYTHIA8 tune with the NNPDF23LO set of PDFs [114] [115]. The sample is divided into multiple p_T^{jet} slices to provide sufficient statistics across the entire p_T^{jet} spectrum. The muon filtering requirement is applied at generator level, so muons originating from processes simulated after event generation are not included in this sample. This biases the relative amount of heavy-flavor and light-flavor jets in the filtered sample; muons produced in heavy-flavor

Table 4.1: Summary of p_T^{jet} bins and the thresholds applied in the corresponding triggers.

Jet p_T Bin	Jet p_T Threshold	Muon p_T Threshold	Effective Luminosity	
			2016	2017
[20 GeV, 30 GeV], [30 GeV, 40 GeV]	15 GeV	4 GeV	4.66 pb ⁻¹	3.61 pb ⁻¹
[40 GeV, 50 GeV]	25 GeV	4 GeV	5.35 pb ⁻¹	4.32 pb ⁻¹
[50 GeV, 70 GeV]	35 GeV	4 GeV	6.83 pb ⁻¹	6.64 pb ⁻¹
[70 GeV, 90 GeV], [90 GeV, 110 GeV]	55 GeV	4 GeV	40.18 pb ⁻¹	16.60 pb ⁻¹
[110 GeV, 140 GeV]	85 GeV	6 GeV	272.97 pb ⁻¹	173.92 pb ⁻¹
[140 GeV, 170 GeV]	110 GeV	6 GeV	500.27 pb ⁻¹	382.62 pb ⁻¹
[170 GeV, 200 GeV]	150 GeV	6 GeV	1492.73 pb ⁻¹	1249.31 pb ⁻¹

jets are created by the generator whereas muons in light flavor jets (for example, decays in flight) are created during the simulation step (after the generator) and do not yet exist at the filtering step. Two different sets of MC samples are used, one matching the 2016 pileup distribution and the other matching the 2017 pileup distribution. In total, 15.7 million events with the 2016 profile and 17 million events with the 2017 profile were used.

In addition to the muon-filtered MC, an unfiltered di-jet PYTHIA8 NNPDF23LO sample is also used. The unfiltered MC, which does not suffer from the muon-filtering bias, is used to determine the relative fraction of direct and cascade b -decays in each p_T^{jet} bin and for calculating the b -tagging efficiency in simulation. Once again, different sets of MC are used for 2016 and 2017. In total, 37.1 million events with 2016 profile and 45.4 million events with 2017 profile were used.

The EvtGen simulation package [116] is used to simulate the decays of B -hadrons with the appropriate branching fractions. All MC samples are simulated with the full ATLAS detector simulation based on the GEANT4 toolkit [117].

Summaries of the unfiltered and muon-filtered di-jet MC can be found in Tables 4.2 and 4.3, respectively. For completeness, the [ATLAS Metadata Interface \(AMI\)](#) tags have been included; these tags are used internally within ATLAS to track which software versions were used to produce these samples.

Table 4.2: Unfiltered MC Samples Summary

Slice	Jet p_T Range	Scatter Process Type	Dataset ID	AMI tags	Number of Events
JZ1W	20 – 60 GeV	Soft (inelastic)	361021	e3569_s3126 r9364_p3652 (2016) r10201_p3652 (2017)	5339106 (2016) 8802080 (2017)
JZ2W	60 – 160 GeV	Hard	361022	e3668_s3126 r9364_p3652 (2016) r10201_p3652 (2017)	8350535 (2016) 10645935 (2017)
JZ3W	160 – 400 GeV	Hard	361023	e3668_s3126 r9364_p3652 (2016) r10201_p3652 (2017)	10757379 (2016) 12273564 (2017)
JZ4W	400 – 800 GeV	Hard	361024	e3668_s3126 r9364_p3652 (2016) r10201_p3652 (2017)	12689608 (2016) 13700062 (2017)

Table 4.3: Muon-Filtered MC Samples Summary

Slice	Jet p_T Range	Scatter Process Type	Dataset ID	AMI tags	Number of Events
JZ0W	0 – 20 GeV	Soft (inelastic)	427000	e3968_s3126 r9364_p3652 (2016) r10201_p3652 (2017)	2188153 (2016) 2784106 (2017)
JZ1WA	20 – 40 GeV	Soft (inelastic)	427030	e3968_s3126 r9364_p3652 (2016) r10201_p3652 (2017)	3577323 (2016) 4041700 (2017)
JZRW1B	40 – 60 GeV	Hard	427031	e3968_s3126 r9364_p3652 (2016) r10201_p3652 (2017)	4272861 (2016) 4489927 (2017)
JZRW2	60 – 160 GeV	Hard	427032	e3968_s3126 r9364_p3652 (2016) r10201_p3652 (2017)	1830464 (2016) 1881318 (2017)
JZRW3	160 – 400 GeV	Hard	427033	e3968_s3126 r9364_p3652 (2016) r10201_p3652 (2017)	1907006 (2016) 1929887 (2017)
JZRW4	400 – 800 GeV	Hard	427034	e3968_s3126 r9364_p3652 (2016) r10201_p3652 (2017)	1944891 (2016) 1961046 (2017)

4.3 Object and Event-Level Selections

4.3.1 Jet selections

Jets are reconstructed from clusters of topologically connected calorimeter cells, which are then reconstructed into jets by the anti- k_t algorithm with $R = 0.4$ [118]⁶⁶. The jets must pass a selection of $|\eta| < 2.5$. Additionally, jets must satisfy a requirement based on a discriminant called “Jet Vertex Tagger” (JVT), which reduces the number of pileup jets by a factor of $\sim 10 - 100$ (depending on p_T^{jet}) while retaining 92% of true hard scattering collisions [119]. In all the p_T bins, at least two jets with $p_T > 20$ GeV are selected; the 20 GeV cutoff is required because jet reconstruction efficiency decreases below that threshold (i.e. it becomes difficult to distinguish jet below 20 GeV from pileup), and at least two jets are required because b -jets are produced in pairs (a di-jet topology).

4.3.2 Muon selections

To select semileptonic b -decays and suppress light jets, the event is required to contain at least one muon with p_T that exceeds a threshold value. Since muons inside more energetic jets have a harder p_T spectrum, the muon p_T threshold requirement depends on the p_T^{jet} bin considered. The muon p_T threshold also helps to suppress light jet contributions at high p_T^{jet} and maintain a (relatively) flat ratio of b to c to light jets in the b -enhanced region. Table 4.4 shows the raw MC yields of b and c -jets and relative amounts of b , c , and light jets for two scenarios: “minimal” muon p_T cuts (i.e. muon p_T cuts equal to those used in the trigger) and variable muon p_T cuts (as specified in Table 4.5). With the minimal muon p_T cuts, the relative amount of light jets increases substantially at high p_T^{jet} ; the variable muon p_T cut controls the relative amount of light jets in these bins. In both cases, the relative amount of c -jets remains flat. The variable cuts do reduce the MC statistics slightly, but this was not found to be a problem in the final results. Therefore, we choose to use the variable muon p_T cuts to control the relative amount of light jets at high p_T^{jet} without significant loss of heavy-flavor MC statistics.

Muons must also be spatially matched to a jet within a $\Delta R < 0.4$ cone. In addition, the muon-in-jet triggers require that the triggering muon satisfy $d_0 < 2$ mm and $|z_0 \cdot \sin \theta| < 4$ mm, where d_0 and z_0 are the transverse and longitudinal impact parameters, respectively⁶⁷. This ensures that the muon is consistent with production at the primary vertex of the event. Only muons satisfying the

⁶⁶See Section 3.5 for more details on the anti- k_t algorithm.

⁶⁷Transverse impact parameter is defined as the distance of closest approach to the beam line, and longitudinal impact parameter is the value of z at the point of closest approach. See Section 3.5.1 for details.

Table 4.4: Relative b , c , and light fractions minimal (left) and variable (right) muon p_T cuts.

Jet p_T Bin [GeV]	Minimal (Trigger-Like) Muon p_T Cuts			Variable Muon p_T Cuts		
	4 GeV ($p_T^{\text{jet}} < 85$ GeV) 6 GeV ($85 < p_T^{\text{jet}} < 200$ GeV)			5 GeV ($p_T^{\text{jet}} < 40$ GeV) 6 GeV ($40 < p_T^{\text{jet}} < 90$ GeV) 8 GeV ($p_T^{\text{jet}} > 90$ GeV)		
	b -jet %	c -jet %	light-jet %	b -jet %	c -jet %	light-jet %
[20, 30]	55.%	27.%	17.%	55.%	27.%	17.%
[30, 40]	55.%	28.%	17.%	55.%	28.%	17.%
[40, 50]	52.%	29.%	20.%	57.%	30.%	13.%
[50, 70]	47.%	27.%	26.%	52.%	29.%	19.%
[70, 90]	45.%	26.%	29.%	51.%	28.%	21.%
[90, 110]	41.%	26.%	32.%	52.%	30.%	18.%
[110, 140]	48.%	28.%	24.%	52.%	29.%	18.%
[140, 170]	43.%	29.%	28.%	48.%	30.%	22.%
[170, 200]	41.%	29.%	30.%	46.%	31.%	23.%

“tight” selection criteria [79], i.e. muons measured in the inner tracking system as well as the outer muon spectrometer, passing the most stringent hit requirements, are used to ensure good muon resolution and to suppress muons from “fake” sources (for example, [decay-in-flight](#) or combinatorial fakes⁶⁸). Finally, all muons considered in this analysis must pass $|\eta| < 2.5$.

The object selections are summarized in Table 4.5.

Table 4.5: List of selection criteria for muon-in-jet samples

Muon-in-jet trigger requirement (data only)	
Jet Selections	$p_T > 20$ GeV $ \eta \leq 2.5$ JVT Cut
Muon Selections	$ \eta \leq 2.5$ $ d_0 < 2$ mm $ z_0 \cdot \sin \theta < 4$ mm Tight Quality
Muon p_T Requirement	5 GeV (if $p_T^{\text{Jet}} < 40$ GeV) 6 GeV (if $40 < p_T^{\text{Jet}} < 90$ GeV) 8 GeV (if $p_T^{\text{Jet}} > 90$ GeV)
Muon-Jet Matching	$\Delta R < 0.4$

4.3.3 Event Selections: $b\bar{b}$ - and Light-Enhanced Regions

In $p - p$ collisions b -quarks are mostly produced in pairs (for example, when a gluon splits to a $b\bar{b}$ pair). Therefore, if one jet in an event is identified as a b -jet, the probability of finding a second b -jet

⁶⁸Here, “combinatorial fakes” refers to incorrect matching between objects, such as a muon spatially matched to an unrelated jet “faking” a muon-in-jet topology.

in the event is enhanced. To improve the b -jet purity of the jet sample used for the p_T^{rel} calibration, the following procedure is applied:

- Require at least one jet to be identified as a b -jet by the *MV2c10* algorithm at 85% working point.
 - If multiple candidate b -jets are identified, preferentially choose the jet without a matched muon as the tag b -jet.
 - If multiple jets without a matched muon are tagged, or if all tagged jets contain muons, select the tag b -jet from the candidates randomly.
- Remove the tag b -jet to avoid bias and perform the analysis using the remaining jets.

This $b\bar{b}$ -enhancement procedure is applied to the data selected for the measurement and to the unfiltered MC used to obtain the simulation efficiency for data-MC scale factor determination.

A light-jet-enhanced region is defined in data events by applying the same trigger and object selections as in the $b\bar{b}$ -enhanced region, but requiring that *all* the jets in the event must fail the 85% working point *MV2c10* cut. The resulting set of events is enriched in light-jets, low in b -jet contamination, and statistically independent from the events used to measure the b -tagging efficiency. This region is used to derive data-drive light-jet templates.

4.4 Method

To calculate the b -tagging efficiency ε_b for a given b -tagging algorithm using Equation (4.3), two quantities need to be determined: N_b^{tagged} , the number of b -jets tagged by the algorithm, and N_b^{untagged} , the number of b -jets that the algorithm failed to tag. In MC, the number of b -jets passing or failing the b -tagging criteria can be retrieved directly using truth information (see Section 3.5.2). In data, these quantities need to be measured independently for each b -tagging working point under study. A template fit method is applied to measure the flavor fractions and hence the b -tagging efficiency in data. Sections 4.4.1 and 4.4.2 describe how the p_T^{rel} templates are derived for b -, c -, and light-flavor jet, while in Section 4.4.3 and 4.4.4 a detailed explanation of the template fit procedure is given together with the b -tagging efficiency extraction. Because the templates exhibit p_T^{jet} dependence, templates are generated with the same p_T^{jet} binning as the data distributions when performing the fitting procedure.

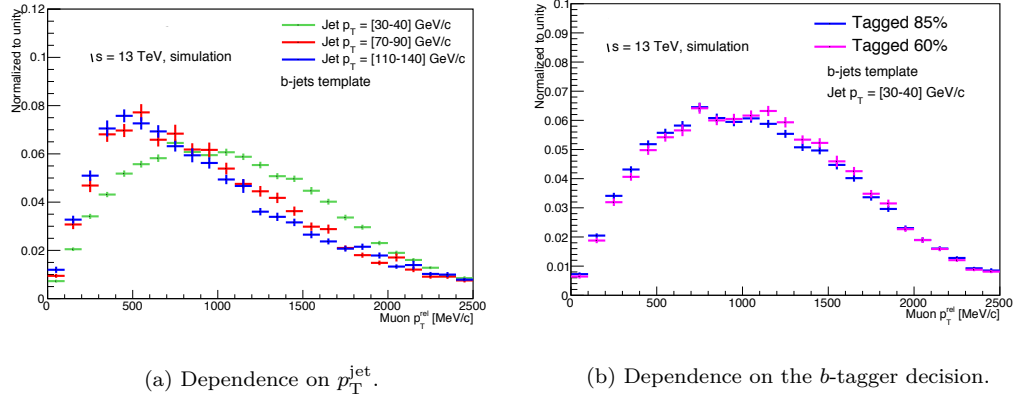


Figure 4.3: The dependence of the p_T^{rel} b -template shape on the p_T^{jet} and the decision of the b -tagging algorithm are shown on the in plots (a) and (b), respectively. In (a), the b -jet template is shown for three different p_T^{jet} -bins in green, red and blue with the statistical uncertainties depicted as error bars. A clear dependence on p_T^{jet} is observed. In (b), the b -jet template passing the 85% and 60% $MV2c10$ working points are compared to show the small dependence on tagger decision. Figure credit to Dr. Valentina Vecchio.

4.4.1 b and c Templates

Templates for the p_T^{rel} spectrum of b - and c -jets are generated from muon-filtered MC samples, described in Section 4.2.2. The event selection criteria described in Section 4.3 are not applied; no dependency on the event selection is found in the b - or c -templates, and dropping the event selection maximizes the limited MC statistics in the muon-filtered sample.

4.4.1.1 Bottom Template

The b -jet template differs in each p_T^{jet} bin, as showed in Figure 4.3a. Because of these differences, templates for b -jets are derived exclusively for each p_T^{jet} bin. The cause of the differences seen here is the relative amounts of cascade and direct decays: the fraction of cascade decays increases from 25% in the 30-40 GeV p_T^{jet} bin to 50% of 170-200 GeV p_T^{jet} bin.

The b -jet template shapes also show a small dependence on the applied MV2 b -tagging requirement, as can be seen in Figure 4.3b. This is expected, since MV2 is calculated using boost and impact parameter displacement information, to which p_T^{rel} is invariant. The tagged (untagged) b -jet p_T^{rel} distribution is used to determine the amount of b -jets in the tagged (untagged) data sample.

Figure 4.4 shows the p_T^{rel} distribution for direct and cascade B -hadrons decay. The direct decay template (where muons are produced from B -hadrons) has a harder spectrum than the cascade

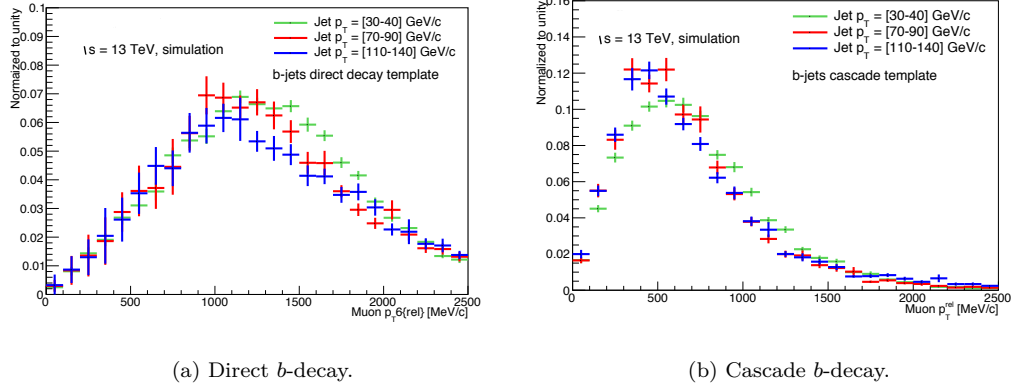


Figure 4.4: Distribution of p_T^{rel} for muons coming from direct and cascade decay of a B -hadron in three different p_T^{jet} bins. Figure credit to Dr. Valentina Vecchio.

decay template (where B -hadrons decay to charmed hadrons, which then produce muons). Because of this, p_T^{jet} bins with a large fraction of direct decays will have a [harder](#) p_T^{rel} spectrum than those with a larger fraction of cascade decays. The direct decays templates differ slightly with p_T^{jet} ; the 30-40 GeV direct template is slightly harder than the higher- p_T^{jet} templates. This same effect is magnified in the cascade templates.

There are two factors affecting the amount of direct or cascade decays in a given p_T^{jet} bin: semileptonic p_T^{jet} correction and muon p_T requirement effects.

In direct semileptonic b -decays, the muon carries a larger fraction of the original hadron energy than in the cascade decay. If one corrects the p_T^{jet} for the presence of the muon (i.e. add the muon p_T to the p_T^{jet}), the correction is larger in direct b -decays than in cascade decays. Therefore, the p_T^{jet} from a corrected direct decay will be softer than for a corrected cascade decay with the same p_T^{jet} and muon p_T . In the high p_T^{jet} [slices](#), both direct and cascade decays pass the selection, but the amount of cascade decays is increased due to this correction effect.

The lowest p_T^{jet} slice appears to have a harder p_T^{rel} spectrum; this is because cascade decays in this slice are less likely to pass the muon p_T requirement, so this bin contains mostly direct decays.

4.4.1.2 Charm template

The c -jet template is created using all available c -jets, and the same c -jet template is used in all p_T^{jet} bins. Small differences in the charm jet templates due to statistical fluctuations can be seen in Figure 4.5. As in the b -template case, the direct c decays are harder than the cascade decays.

The effect of direct-versus-cascade decays, however, is much smaller than for b -decays because charm cascade decays passing the selection criteria are very rare. In a charm cascade decay, the intermediate particles are kaons or pions (long-lived particles not expected to decay in the inner detector), which are not available at muon-filtering time and which result in a negligible cascade contribution to the charm template.

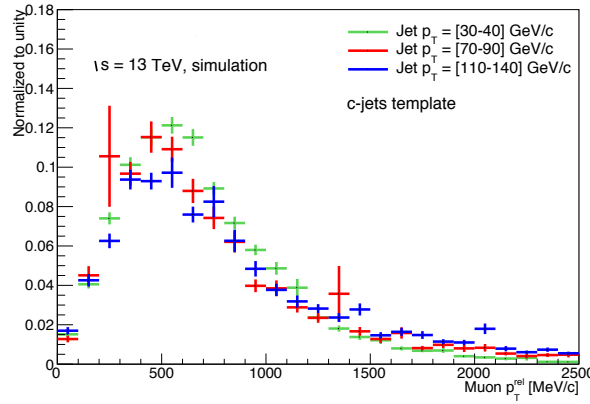


Figure 4.5: Charm jets templates in different p_T^{jet} bins. Figure credit to Dr. Valentina Vecchio.

4.4.2 Light Template

The light-jet template must be determined from data; the unfiltered di-jet MC contains too few light jets with spatially matched muons, and the muon-filtered MC applies the muon filter before muons from light-quark processes are simulated. The light-jet template is generated with the data events that pass the same trigger used to define the b -enhanced region, but requiring that *exactly zero* jets in the event pass the 85% working point $MV2c10$ cut. The objects selection and matching between muons and jets is also the same as in the b -enhanced region. This creates a disjoint set of light-jet enriched events with low b -jet contamination. The b - and c -jet contamination in the light-jet sample is estimated using the unfiltered di-jet MC sample and then adjusted using data during the fitting procedure. More details about the fitting procedure can be found in the following section.

4.4.3 Template fit

Figure 4.6 shows the normalized p_T^{rel} distributions in a single p_T^{jet} bin of muons for the three jet flavors. The b -template shows a harder p_T^{rel} spectrum compared to the c - and light-jet templates.

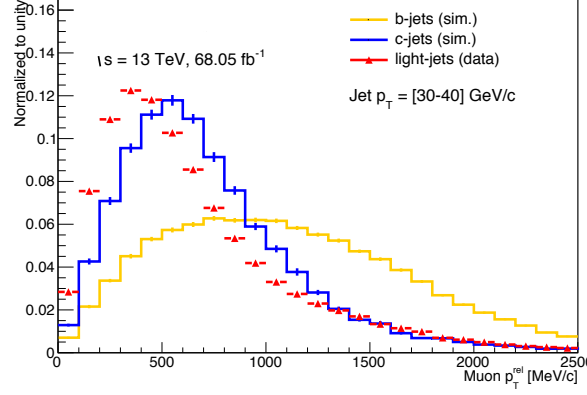


Figure 4.6: Muon p_T^{rel} spectra for the b -, c - and light-jet templates in yellow, blue and red, respectively. The heavy flavor templates are generated from simulation, while the light-jet template is extracted in a data-driven approach. Figure credit to Dr. Valentina Vecchio.

Using the b -, c - and light-flavor templates, a log-likelihood fit is performed to the b -tagged and untagged data distributions as shown in Figure 4.8. Assuming Poisson statistics, the likelihood \mathcal{L} for the expectation value λ given k observed events is

$$\mathcal{L}(\lambda|k) = \frac{\lambda^k}{k!} \exp(-\lambda). \quad (4.5)$$

Using the natural logarithm, the likelihood of multiple Poisson observations becomes a sum over p_T^{rel} bins i with the log-likelihood

$$\log \mathcal{L}_i(\lambda_i(SF_b, SF_c) | N_i^{\text{data}}) = N_i^{\text{data}} \log \lambda_i(SF_b, SF_c) - \lambda_i(SF_c), \quad (4.6)$$

$$\lambda_i(SF_b, SF_c) = f_b SF_b N_i^b + f_c SF_c N_i^c + (1 - f_b SF_b - f_c SF_c) N_i^{\text{light}}, \quad (4.7)$$

$$\text{where } N_i^{\text{light}} = N_i^{\text{data-l-enhanced}} - \hat{f}_b SF_b N_i^b - \hat{f}_c SF_c N_i^c \quad (4.8)$$

where N_i^{data} is the number of observed events in the i^{th} p_T^{rel} data bin, N_i^b is the number of events in the i^{th} bin of the b template, N_i^c is the number of events in the i^{th} bin of the combined c -template and $N_i^{\text{data-l-enhanced}}$ is the number of data events in the i^{th} p_T^{rel} bin of the light template. The fractions f_b and f_c represent the b - and c -jets fractions in the b -enhanced region, while \hat{f}_b and \hat{f}_c are the fractions in the light-enhanced region. These fractions also account for template normalizations. The free parameters of the fit are SF_b and SF_c , which are correction factors of the flavor fractions estimated by the unfiltered simulation. The fit assumes that the correction of the heavy flavor fractions is the same in the light- and b -enhanced region. These correction factors are used to correct f_b , f_c , \hat{f}_b , and \hat{f}_c ; these fractions are first determined from unfiltered di-jet MC, then corrected after fitting.

Figure 4.7 shows a prefit plot for tagged and untagged jets where the fractions of the different jet flavors is fixed to the prediction from the simulation. The fit to the b -tagged p_T^{rel} distribution using fractions from MC (i.e. “pre-tagged”) is shown in Figure 4.7a, while the untagged fit result is shown in Figure 4.7b.

The **overflow bin** is not considered during fitting. The long tails in the p_T^{rel} distribution in data cause the overflow bin to become the most statistically significant bin. This tail, however, cannot come from single B -hadron decays; p_T^{rel} for a single B -hadron decay will be at most half of the B -hadron mass. We are not confident that the MC replicates the p_T^{rel} tails well. Because of this, any attempts to fit templates to the data distribution when including the overflow bin are entirely driven by the data overflow bin (where MC is not well simulated systematically or statistically), ignoring differences in the distribution in the hadron mass range. Therefore, the p_T^{rel} range of the templates is confined to 0-2.5 GeV.

4.4.4 Efficiency Extraction

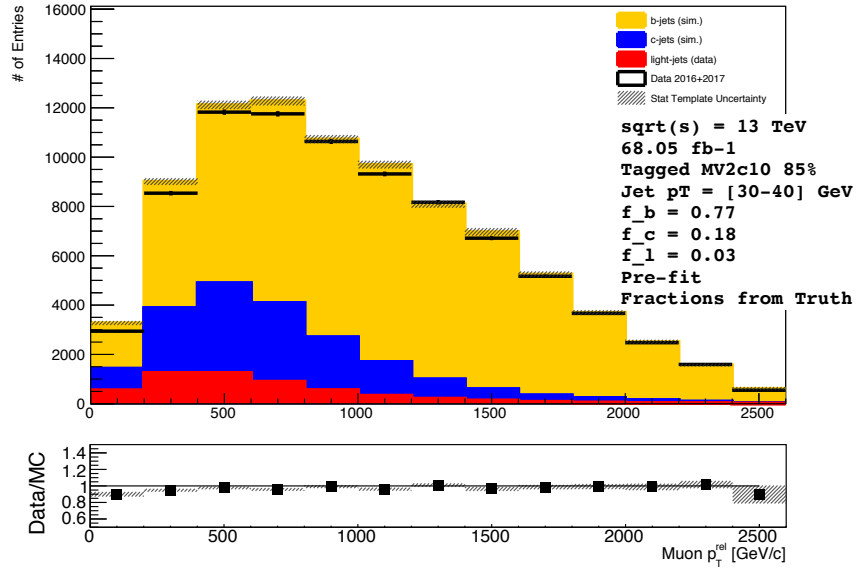
The p_T^{rel} fit is used to determine the flavor composition of the tagged and untagged data samples. With the resulting b -fractions f_b , the b -tagging efficiency defined in Equation (4.3) can be calculated as

$$\varepsilon_b^{\text{data}} = \frac{f_b^{\text{tagged}} \cdot N_{\text{data}}^{\text{tagged}}}{f_b^{\text{tagged}} \cdot N_{\text{data}}^{\text{tagged}} + f_b^{\text{untagged}} \cdot N_{\text{data}}^{\text{untagged}}}, \quad (4.9)$$

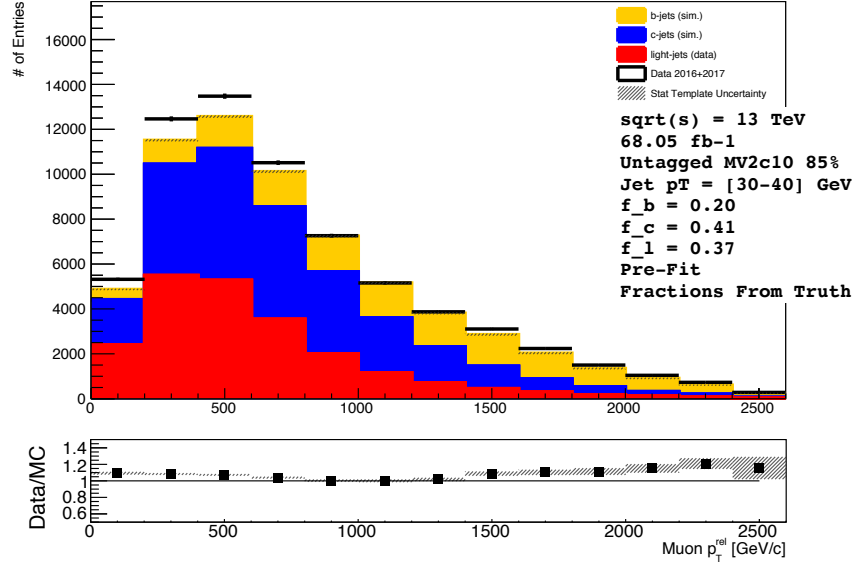
where N_{data} is the number of jets in the respective data samples. This procedure is repeated for all the p_T^{jet} regions defined in Section 4.2. Comparing the resulting efficiencies to the predictions from the unfiltered simulation, according to Equation (4.4), scale factors κ_b are calculated.

4.5 Upgrading the Calibration

A timeline of the p_T^{rel} analysis can be found in Chapter 1. My personal technical contributions to the p_T^{rel} analysis (validating muon-filtered MC and creating muon-in-jet trigger turn-on curves) are listed below. I also updated our selection criteria from Run 1; because these criteria were described earlier in this section, I shall not reiterate their description here. Having worked on this analysis for approximately four years, I have also played an essential role in the physics discussions and decision-making among our team; the p_T^{rel} method detailed in this chapter was formed after many hours of group discussions and Skype chats.

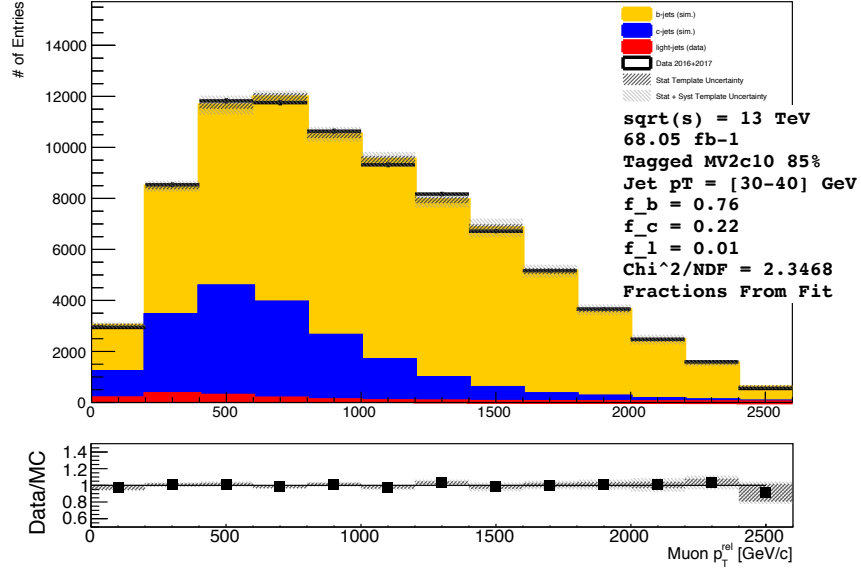


(a) Tagged fit result.

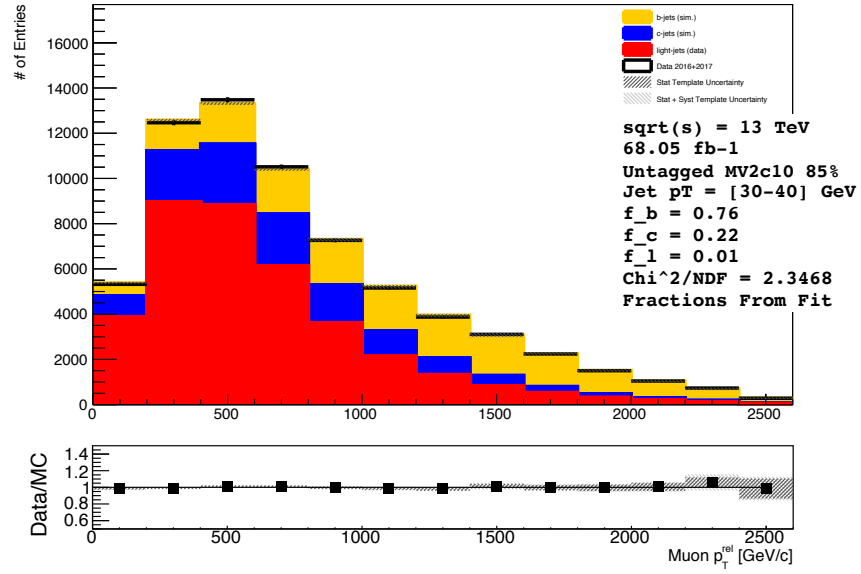


(b) Untagged fit result.

Figure 4.7: Prefit p_T^{rel} distributions. The distribution on the top is b -tagged by *MV2c10* at $\varepsilon_b^{\text{nom}} = 85\%$, while the distribution on the bottom is untagged. The data is shown in black, while the templates are shown as a stack.



(a) Tagged fit result.



(b) Untagged fit result.

Figure 4.8: Postfit p_T^{rel} distributions. The distribution on the top is b -tagged by $MV2c10$ at $\varepsilon_b^{\text{nom}} = 85\%$, while the distribution on the bottom is untagged. The data is shown in black, while the templates are shown as a stack.

4.5.1 MC Validation

Between Run 1 and Run 2, the MC production group changed the way in which muon-filtered di-jet MC is generated. PYTHIA8 offers the ability to weight hard-scatter $2 \rightarrow 2$ processes by \hat{p}_T , the transverse momentum of the hard scattering process [120]. In Run 2, this internal reweighting tool was used to produce muon-filtered MC⁶⁹. Table 4.3 lists the muon-filtered MC samples used, divided into hard- and soft-scatter and p_T^{jet} slices. Because most of the slices are indeed hard-scatter, this reweighting allowed ATLAS to generate muon-filtered di-jet MC more quickly than in Run 1. Because this was a new technique, however, we needed to implement a different MC normalization system and check that the new MC was not biased as compared to the old.

First, we checked the normalization for the newly reweighted MC. In this section, “MC15” refers to the new MC for Run 2 with the internal \hat{p}_T reweighting, and “DC14” refers to the Run 1 MC without this reweighting. As always, MC samples must be normalized according to their cross section θ and expected efficiency ϵ . Each MC slice is normalized by $\frac{1}{N}$, where N is some normalization factor. For the normalization, we use a histogram h from the MC slice, where h has one weighted entry per input event. For hard-scatter p_T^{jet} slices (40-200 GeV), the normalization factor N is calculated using the integral of h like so:

$$N = \frac{\epsilon\theta}{h \rightarrow \text{Integral}()} \quad (4.10)$$

The normalization factor for the soft-scatter p_T^{jet} slices (0-40 GeV) is calculated very similarly, but instead of taking the integral of the weighted histogram, we simply count the number of entries in the histogram:

$$N = \frac{\epsilon\theta}{h \rightarrow \text{NumberOfEntries}()} \quad (4.11)$$

A very simple way to check whether these normalization factors is to weight the p_T^{jet} slices, then plot the highest- p_T jet in each event. If the weighting has been done correctly, the slices will form a smoothly falling spectrum with no discontinuities. Figure 4.9 shows the falling p_T^{jet} spectra for Run 1 and Run 2 MC. The Run 1 and Run 2 MC have the same inclusive falling p_T^{jet} spectrum, with no discontinuities due to the new weighting scheme. Figures 4.10 and 4.11 show the same spectra, selecting only b - and light-flavor jets, respectively. One can easily see that the agreement between Run 1 and Run 2 MC shows no bias for jet flavor. Other kinematic distributions were checked, but the old MC behavior was replicated well by the new MC.

⁶⁹Dr. James Monk (of the Niels Bohr Institute at the University of Copenhagen) suggested this reweighting.

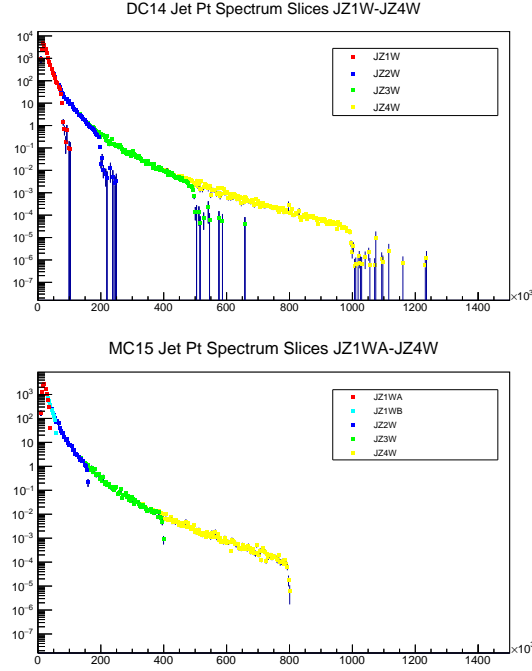


Figure 4.9: Falling p_T^{jet} spectra for the Run 1 (top) and Run 2 (bottom) MC. The Run 2 MC uses a different internal reweighting scheme, so the spectrum is sliced differently than in Run 1.

4.5.2 Trigger Turn-on Curves

As mentioned several times in this chapter, the p_T^{rel} method relies on data collected with muon-in-jet triggers. These triggers are classified by their offline⁷⁰ muon and p_T^{jet} thresholds, i.e. the lowest muon and p_T^{jet} values the trigger will accept. This does *not* mean that all objects whose true p_T values are above these thresholds will pass the trigger; for objects near the threshold, fluctuations in their measured p_T value mean that they may or may not pass the trigger. Additionally, these fluctuations may depend on the type of object being considered; for example, a b -jet and a light jet will not fluctuate in exactly the same way and may have different probabilities of passing the trigger selection in this near-threshold region. Once the object p_T is “far enough” away from the threshold value, fluctuations in measured p_T value will not cause the object to fail the trigger selection and the efficiency for objects to pass the trigger plateaus. The region between the threshold and the efficiency plateau region for a trigger is called the **turn-on** region. In this analysis (and in all ATLAS analyses) only data from the trigger plateau region is used to avoid possible flavor-dependence in the turn-on region. To identify the trigger efficiency plateau, one must produce trigger **turn-on curves**,

⁷⁰i.e. their calibrated values after data collection.

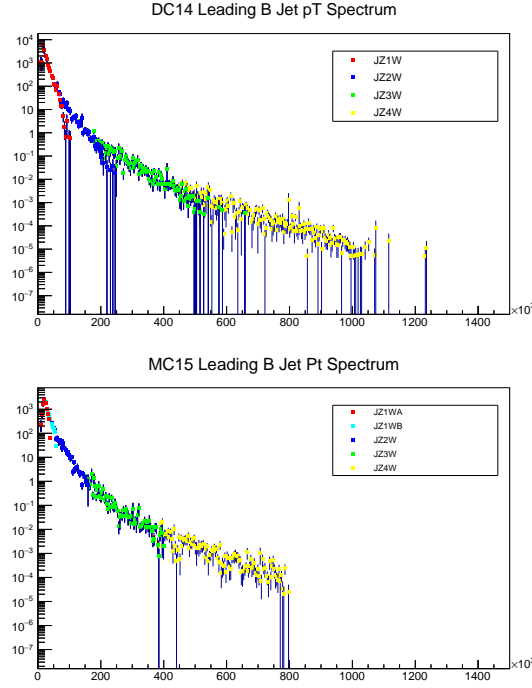


Figure 4.10: Falling p_T^{jet} spectra for the Run 1 (top) and Run 2 (bottom) MC, filtered to only include b -jets. The Run 2 MC uses a different internal reweighting scheme, so the spectrum is sliced differently than in Run 1.

plots showing the trigger efficiency across a p_T range.

In this analysis, trigger turn-on curves were produced using the [bootstrapping](#) method [121]. The bootstrapping method works as follows:

- Consider a trigger on some physics object (e.g. a jet) with offline threshold X GeV. We want to identify the trigger turn-on within some range $[X, X + n]$ GeV
- First, identify a second trigger (called the [support trigger](#)) that is fully efficient by X GeV. This provides a fully-efficient sample of jets across the entire $[X, X + n]$ range. Call this the *full* sample.
- Next, identify jets passing the support trigger *and* the trigger being studied. This sample is a subset of the full sample containing only jets which pass the trigger of interest. Call this the *partial* sample⁷¹

⁷¹Note that because the triggers may have different pre-scale values, the partial sample will not necessarily contain all the jets passing the trigger of interest. The partial sample, however, will be completely unbiased and replicate the trigger behavior accurately.

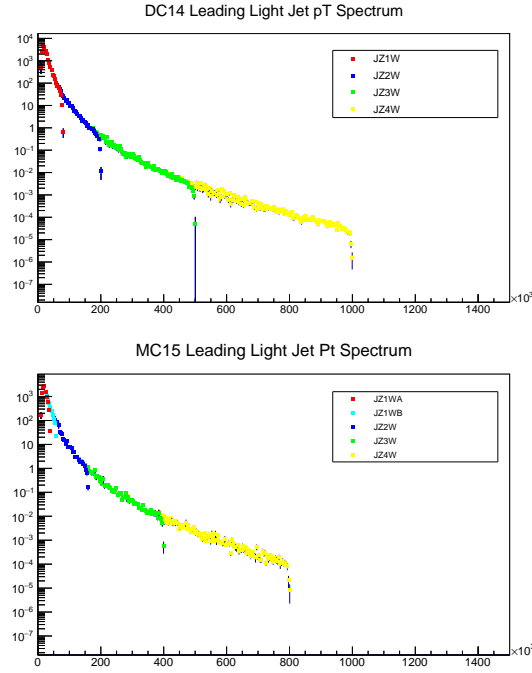


Figure 4.11: Falling p_T^{jet} spectra for the Run 1 (top) and Run 2 (bottom) MC, filtered to only include light-flavor jets. The Run 2 MC uses a different internal reweighting scheme, so the spectrum is sliced differently than in Run 1.

- Now consider a distribution $T = \frac{\text{partial}}{\text{full}}$ of the highest- p_T muon or jet in an event
 - Below the turn-on value, the partial set will be much smaller than the full set (and hence the value of T will be small)
 - Above the turn-on value, the partial set and the full set will be identical (and hence the value of T will reach some maximum and plateau)
- We call the curve T our turn-on curve and the start of the plateau our turn-on point. The trigger is fully efficient for all values beyond the turn-on point

For the muon-in-jet triggers, one might consider using single-jet or single-muon triggers as support triggers. This will not work, however, due to the large prescales on these single-object triggers; the set of events passing these triggers, passing the prescale, *and* passing the muon-in-jet selection is basically empty. Instead, the lower- p_T muon-in-jet triggers were used as support for the high- p_T triggers, and the turn-on for the lowest- p_T muon-in-jet trigger was chosen conservatively. More details about the lowest- p_T muon-in-jet trigger studies can be found below.

An example p_T^{jet} turn-on plot for the muon $p_T > 4$ GeV, $p_T^{\text{jet}} > 35$ GeV (mu4j35) trigger is shown in Fig. 4.12. In this plot, the $p_T > 4$ GeV, $p_T^{\text{jet}} > 25$ GeV (mu4j25) trigger is used as the support, since it is fully efficient at lower p_T^{jet} than the mu4j35 trigger. In order to compare the samples, the mu4j35 jets must also fire the mu4j25 trigger. The upper part of the figure shows the p_T^{jet} distribution for each trigger and the bottom shows the ratio of the two, i.e. the turn-on plot. A very sharp turn-on can be seen at 35 GeV; the turn-on value is conservatively set to 40 GeV (i.e. 5 GeV above the observed turn-on value).

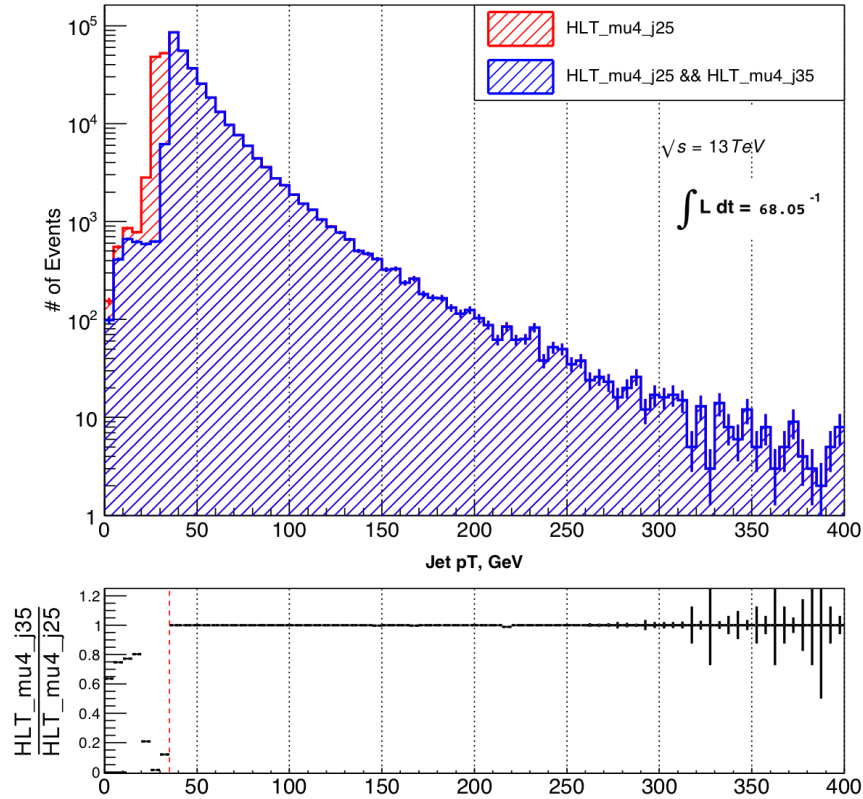


Figure 4.12: p_T^{jet} distribution for samples of jets passing mu4j25 or (mu4j35 and mu4j25) triggers. The turn-on curve can be seen in the ratio plot at the bottom

Turn-on curves were also produced in ΔR and ΔZ ; although not necessary for the analysis, we studied these curves to validate that the muon-in-jet triggers were working as expected. In order to produce these curves, one must identify the muon-jet pair which fired the trigger and calculate the spatial match between them. This presented an additional challenge: due to *further* bugs in

the trigger setup⁷², the online trigger matching information was not saved correctly⁷³, making it impossible to identify exactly which muon and which jet fired the muon-in-jet trigger in a given event. To deal with this, the following method was used to reconstruct the muon-jet trigger pair:

- Identify the highest- p_T muon above the muon- p_T trigger threshold
- Find the highest- p_T jet above the jet- p_T trigger threshold spatially matched to the muon: $\Delta R < 0.5$, $\Delta Z < 0.2$
- Label the first match found as the “trigger-firing” muon-jet pair

One might notice a bias in this procedure (and in fact, in the bootstrap procedure described above): these selection algorithms are biased towards high- p_T objects. This was a choice we were forced to make due to the fact that we cannot identify the actual muon and jet which fired the trigger online. We tried other methods (for example, randomly selecting objects above the trigger threshold), but found that the high- p_T selection gave the best results. Instead of using a lower- p_T trigger for support, we used triggers with the *same* muon and p_T^{jet} thresholds, but without a spatial matching requirement (which were provided for exactly these sorts of checks). Example ΔR and ΔZ turn-on curves for the mu4j35 trigger can be seen in Figures 4.13 and 4.14, respectively.

4.5.3 Studying the Lowest- p_T Muon-In-Jet Trigger

Although we can estimate the turn-on point for the lowest- p_T muon-in-jet trigger (mu4j15, which has 4 GeV muon and 15 GeV p_T^{jet} thresholds) by studying the other muon-in-jet triggers, there is no support trigger available for the bootstrap method of turn-on curve production. Several studies were made to better understand the mu4j15 trigger, which shall be described below.

In our initial studies of the mu4j15 trigger, an interesting feature was noted that did not occur with any other muon-in-jet trigger. Because the mu4j15 trigger has such a low p_T^{jet} threshold, it is common for the highest *or* second-highest- p_T jet to trigger the event⁷⁴. This is best illustrated with Figure 4.15; in data (but not in MC), we can observe two “bumps” in the p_T^{jet} distribution around 22 and 37 GeV. This double-bump shape is only observed in the mu4j15 distribution at low p_T^{jet} .

⁷²The person in charge of these triggers has earned my ire!

⁷³To be specific, the container meant to store the matching information between muons and jets was instead filled with `null pointers`.

⁷⁴Usually the second-highest- p_T jet does not meet the trigger threshold requirement.

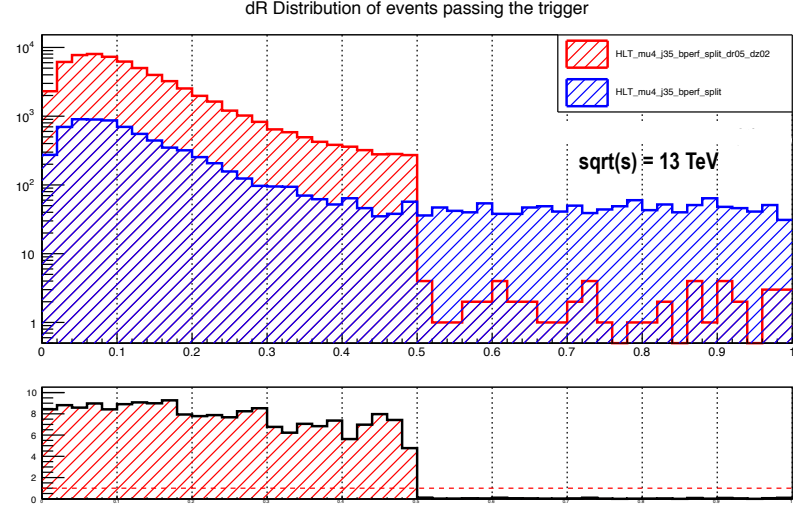


Figure 4.13: ΔR distribution for samples of jets passing mu4j35 triggers with (red) and without (blue) spatial matching. The turn-on curve can be seen in the ratio plot at the bottom

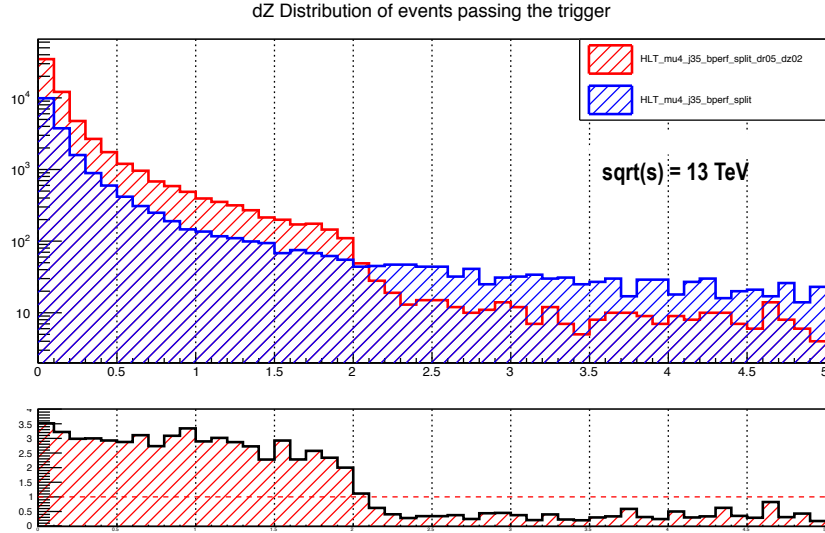


Figure 4.14: ΔZ distribution for samples of jets passing mu4j35 triggers with (red) and without (blue) spatial matching. The turn-on curve can be seen in the ratio plot at the bottom

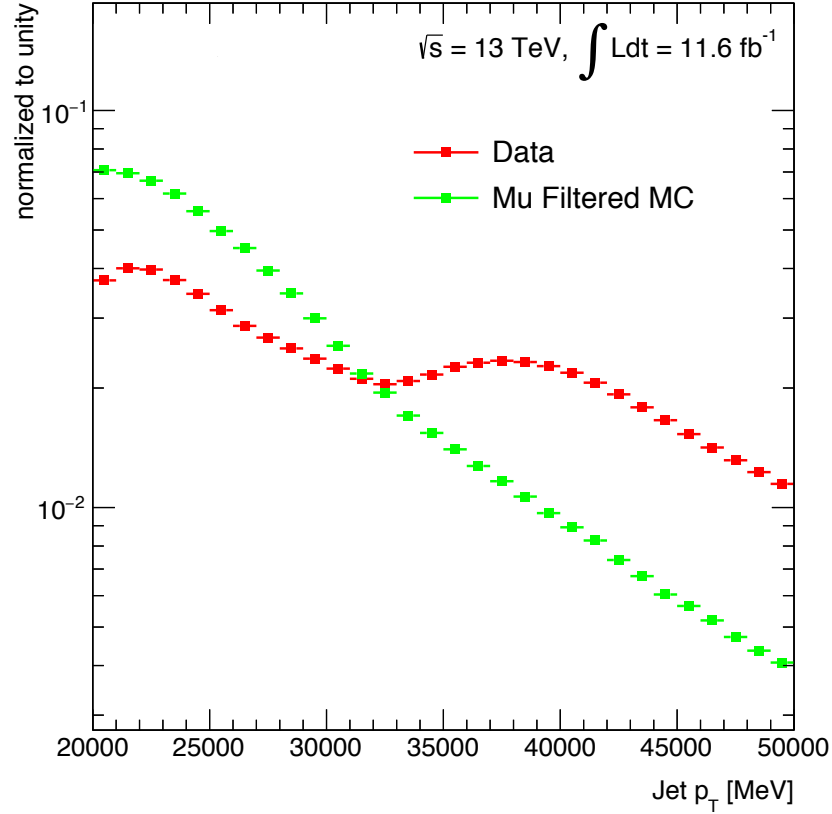


Figure 4.15: Comparison of the p_T^{jet} spectrum in $[20, 60]$ p_T bin between data and MC. Figure credit to Dr. Bingxuan Liu.

Not shockingly, there was *another* bug in the muon-in-jet triggers in MC; the muon-in-jet triggers were not simulated properly, so the possibilities for studying this disagreement are limited. To check whether this data-MC discrepancy biases our template shape, two studies were performed⁷⁵.

4.5.3.1 Jet p_T Reweighting

The most basic attempt to model the low p_T trigger behavior in MC was by a simple reweighting technique. The same event selections are applied as in the nominal analysis, except the b -tagging criteria in Table 4.5 are applied to MC in addition to data. In each p_T^{jet} bin in Table 4.1, the MC is normalized to data, then reweighted via scale factors in p_T^{jet} in steps of 2 GeV to make the MC match the data. Figure 4.16 shows these scale factors across the p_T^{jet} spectrum. The scale factors at

⁷⁵Note that this work was shared equally between myself, Bing, and Ingo, so I cannot take full credit for this!

high p_T^{jet} are close to 1 (meaning that data and MC look similar in this region), whereas the scale factor fluctuate away from 1 wildly at low p_T^{jet} . The fitting results did not change in any systematic or substantial way after reweighting.

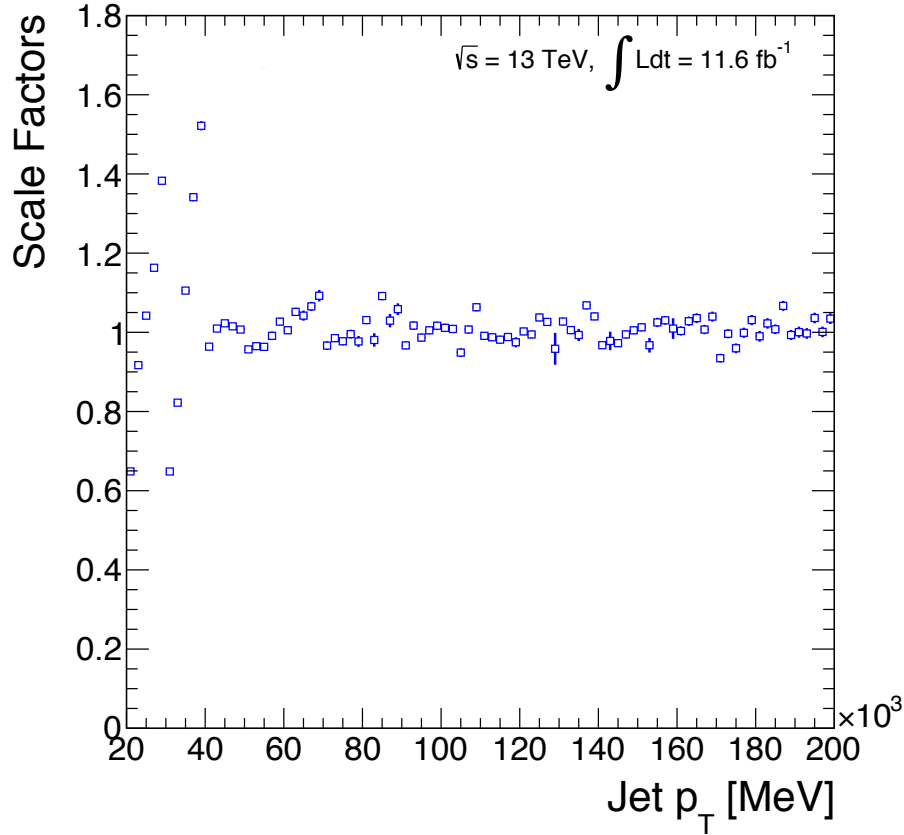


Figure 4.16: Scale factors applied to correct p_T^{jet} in MC in p_T^{jet} reweighting method of trigger correction. Figure credit to Dr. Bingxuan Liu.

4.5.3.2 Trigger Emulation

As reweighting the p_T^{jet} distribution did not systematically change the fitting results, a second attempt was made to model the low- p_T trigger behavior in data via a trigger emulation method. Once again, note that the MC samples do not have muon-in-jet triggers simulated due to a production-level trigger calculation issue; since a proper simulation of the triggers was not available, we attempted to emulate the trigger ourselves. As described in Section 3.5.1, jet energies are measured using calorimeter towers: the jet deposits energy in the calorimeter towers, and if the energy deposited

in a given tower exceeds a 5 GeV threshold, then the energy is added to the total for that jet. We attempted to emulate this behavior like so:

- Take the offline p_T^{jet} quantity and smear it according to a Gaussian distribution. Take this value to be the “online” p_T^{jet} .
- Divide the “online” p_T^{jet} into three equal energy deposits (our emulated “towers”), then smear each deposit
- Re-sum the deposits with energy above 5 GeV; this is your emulated online trigger p_T^{jet}
- Check whether your emulated online trigger p_T^{jet} passes your trigger threshold or not

The analysis was run using a fully-emulated trigger in place of the actual muon-in-jet triggers, checking various values for the mean and standard deviations for the Gaussian smearings. No significant biases were observed in the final results; based on this result, our trigger emulation method was not sufficient to replicate the true trigger behavior in MC.

4.6 Additional Studies

This section describes two very important studies done for p_T^{rel} . I did not personally write and run the code for these studies, but I contributed heavily in designing these studies and in interpreting their results. The technical work shown here was completed by Valentina Vecchio.

4.6.1 Extrapolation from Semileptonic to Inclusive b -Decays

The p_T^{rel} scale factors may not be safely usable in an inclusive sample of B -hadron decays without assigning a systematic uncertainty to the semileptonic-to-inclusive extrapolation. Studies in Run 1 assigned a 4% systematic uncertainty to this extrapolation across the entire p_T^{jet} spectrum [111]; for Run 2, however, we wanted to reduce this uncertainty for our precision measurement. Semileptonic and hadronic b -decays have slightly different b -tagging efficiencies due to intrinsic differences in their decay properties and in the way the jets are experimentally selected. Because semileptonic jets must contain a high- p_T , well-reconstructed muon, they are more likely than hadronic decays to contain well-reconstructed low momentum charged particles from the secondary decay vertex. These charged particles improve the performance of the *MV2c10* algorithm.

In the upper plot on Figure 4.17, one can see that the low- p_T hadronic b -jets show a 15% loss in b -tagging efficiency as compared to the semileptonic jets. One can “correct” the p_T^{jet} by removing

the muon calorimeter energy deposits and adding the muon p_T to the p_T^{jet} ; this is a better proxy for the B -hadron energy, although it is still impossible to re-sum the neutrino energy contribution. The lower plot on Figure 4.17 shows the improved tagging efficiency agreement between the semileptonic and inclusive b -decays after correcting for the muon-in-jet energy.

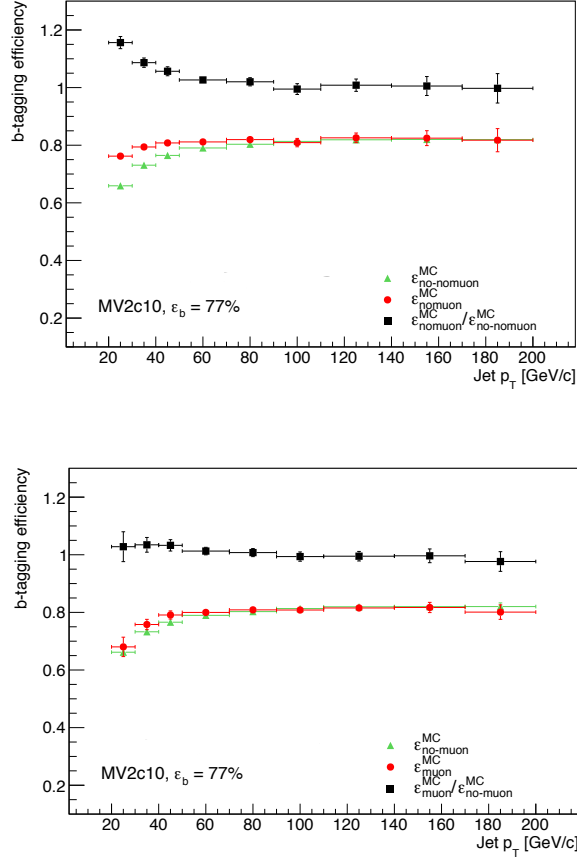


Figure 4.17: Simulated b -tagging efficiency as a function of p_T^{jet} of jets containing muons (red curve), jets not containing muons (green curve) and their ratio (black curve). The semileptonic correction to p_T^{jet} applied in the bottom plot. Figure credit to Dr. Valentina Vecchio.

In order to estimate the semileptonic-to-inclusive extrapolation uncertainty, a comparison was made between b -tagging scale factors for jets containing a muon within $\Delta R < 0.4$ and for jets failing this requirement using the [tag-and-probe](#) technique in a high purity sample of b -jets from dileptonic $t\bar{t}$ data events (36.1 fb^{-1} of data collected during 2015 and 2016). The following selections are applied to define the signal region:

- One prompt electron with $p_T > 25$ GeV and $|\eta| < 2.47$, excluding the $1.37 < |\eta| < 1.57$ region.
- One prompt muon with $p_T > 25$ GeV and $|\eta| < 2.4$.
- Opposite electric charge between the prompt electron and the prompt muon.
- Two jets of $p_T > 20$ GeV and $|\eta| < 2.5$.
- At least one b -tagged jet at the 85% working point of the *MV2c10* tagger (the “tag” for tag-and-probe).

It is estimated from the MC simulation that these selections ensure a 91% efficiency of $t\bar{t} \rightarrow e\mu + 2j$ in the signal region. The main background processes are from single-top and diboson production, which contribute about 8% of the signal region events. The production of W and Z bosons in association to jets and to top-quark pairs represent a 1% contribution. A good agreement between data and simulation is found in all the kinematic distributions.

In this tag-and-probe study, the 85% b -tagged jet is fixed as the “tag” while the other jet is used as the “probe” to measure the b -tagging efficiency⁷⁶. If both jets in the event are b -tagged, then both of them are used as probes. The simulated b -tagging efficiency is computed using the information from the MC truth as follows.:

$$\varepsilon_b^{\text{sim}} = \frac{N_{\text{truth}-b}^{\text{pass}}}{N_{\text{truth}-b}} \quad (4.12)$$

To calculate this value in data, we first derive the “uncorrected” b -tagging efficiency (Equation (4.13)), then we correct it for the number of probe jet coming from b -quarks and for the b -quark mistag rate (estimated in $t\bar{t}$ simulation), shown in Equation (4.14):

$$\varepsilon_b^{\text{uncorr}} = \frac{N_{\text{data}}^{\text{pass}} - N_{\text{bkg}}^{\text{pass}}}{N_{\text{data}} - N_{\text{bkg}}} \quad (4.13)$$

$$\varepsilon_b^{\text{data}} = \frac{\varepsilon_b^{\text{uncorr}} - (1 - f_b^{t\bar{t}}) \cdot \varepsilon_{\text{non}-b}^{t\bar{t}}}{f_b^{t\bar{t}}} \quad (4.14)$$

The resulting semileptonic and hadronic scale factors are found to be consistent with unity across the p_T^{jet} spectrum, as is their ratio. Figure 4.18 shows the comparison of b -tagging efficiency between jets with (top) and without (bottom) muons for data and simulated events. Figure 4.19 shows the ratio between the scale factors for jets with or without muons for the 77% working point: its flatness shows that the simulation reproduces the semileptonic and hadronic B -hadron decay

⁷⁶This works because if we identify one jet coming from a top quark, we are *certain* to find another, which is *certain* to decay to a b -jet.

topologies well. The distribution of the scale factor ratio as a function of p_T^{jet} has been fitted using a constant function. The result of the fit is compatible with unity for all the b -tagging working points: the uncertainty on the constant value from the fit is taken as the semileptonic-to-inclusive extrapolation uncertainty for the p_T^{rel} calibration.

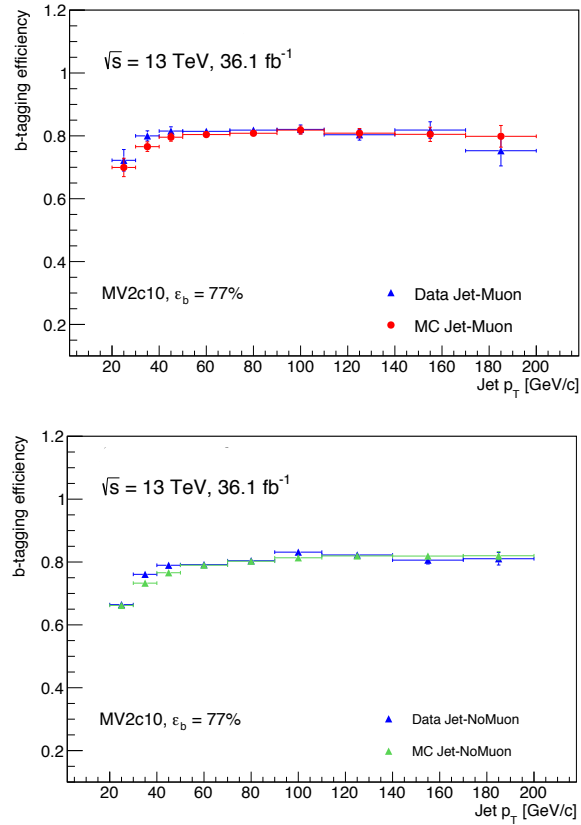


Figure 4.18: b -tagging efficiency in data and simulation as a function of p_T^{jet} for jet containing muons (top) and jets without muons (bottom). Figure credit to Dr. Valentina Vecchio.

4.6.2 Gluon-Splitting Studies

One of the physics scenarios which affects the b -template shape is gluon-splitting. In this situation, a gluon splits into a $b\bar{b}$ pair, which hadronize into (often overlapping) jets. If one of these jets decays semileptonically to a muon, this leads to a few potential problems for p_T^{rel} :

- The muon may be matched to the wrong jet

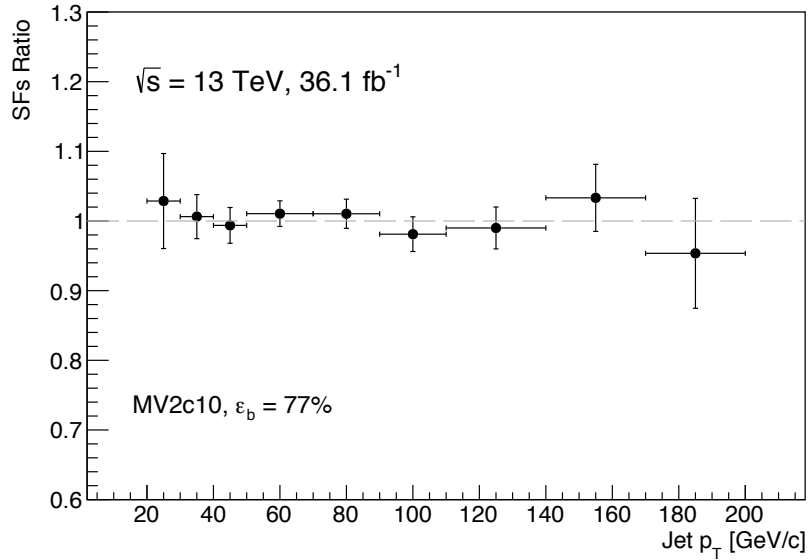


Figure 4.19: Ratio between the b -tagging efficiency scale factor of jets with and without muons for the 77% working point as a function of p_T^{jet} . Figure credit to Dr. Valentina Vecchio.

- The hadron energy (i.e. the energy deposited in the jet) may not be measured correctly due to overlap in the calorimeter, as a result, the muon's direction will be interpreted relative to this combined jet axis instead of the axis corresponding to its parent hadron

The effect of gluon-splitting on template shapes was minimal in Run 1 due to the high degree of tolerable uncertainty; for Run 2, gluon-splitting became more important because p_T^{rel} is being used for a precision measurement. Therefore, studies were undertaken to better understand the effect of gluon-splitting on the p_T^{rel} analysis.

Before investigating the actual effect on the templates, we first checked the prevalence of gluon-splitting jets as a function of p_T^{jet} . Although we suspected that the *absolute* amount of gluon-splitting events may be off in the MC, it is useful to check how the *relative* amount changes with respect to p_T^{jet} . We began with unfiltered di-jet MC sample, selecting only b -jets by checking their truth label. We then identified $g \rightarrow b\bar{b}$ events using the special MC truth label “TruthFlavourExtended”; this is calculated by searching the truth record for each jet and labeling each according to its spatially-matched truth hadrons. The resulting plot can be seen in Figure 4.20. One can readily observe from this figure that as p_T^{jet} increases, the amount of b -jets containing two B -hadrons increases (from $\sim 1\%$ to $\sim 20\%$). This matches our expectation: when a low- p_T $g \rightarrow b\bar{b}$ is created, the two b -jets produces

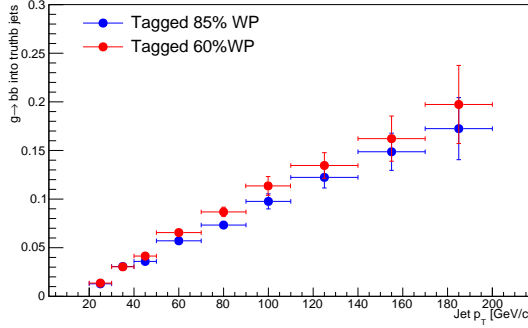


Figure 4.20: Fraction of b -jets which are also $g \rightarrow b\bar{b}$ jets as a function of p_T^{jet} . Figure credit to Dr. Valentina Vecchio.

will have no boost and decay in a back-to-back, well-resolved topology. If the gluon has a large boost, the b -jets will be collimated and less easily resolved; in this case, the two jets are more likely to be reconstructed as a single “fat jet”. No dependence on b -tagging working point is observed.

Figure 4.21 shows the effect of gluon-splitting on the b -jet p_T^{rel} templates as compared to the inclusive template for two p_T^{jet} bins. In the low p_T jet bin at the top, the two p_T^{rel} templates have a very similar shape. In the high p_T jet bin on the bottom, however, the two templates have a very different shape; the gluon-splitting template is quite flat between 0.5-2 GeV, with a large tail beyond 2 GeV.

After conversing with the MC production experts⁷⁷, they confirmed that the amount of gluon-splitting in the MC may not accurately reflect the data; in fact, they both agreed it could easily be several times under-predicted in MC. Therefore, we decided to perform a stability test: we varied the fraction of gluon-splitting in the b -template and checked the impact on our p_T^{rel} fit plots.

Figure 4.22 shows the post-fit plots when the gluon-splitting fraction of the b -template is set to the value predicted by the simulation (see Figure 4.20). One can readily observe that the fit performance in the low p_T^{jet} slice is already acceptable; the χ^2/ndf is close to one and the prediction agrees well with data. This is not true for the high p_T^{jet} slice, where the data and show large disagreement in the tails (> 1.75 GeV) of the distribution. As stated previously, in a jet with a single B -hadron, p_T^{rel} values greater than half the hadron mass are nonphysical; p_T^{rel} values above ~ 2.5 GeV can only occur due to measurement errors or effects such as gluon-splitting. In fact, we already saw in Figure 4.21 that the gluon-splitting template *has* a major excess in the tails of the p_T^{rel} distribution. Therefore, we hypothesized that increasing the relative fraction of gluon-splitting

⁷⁷Specifically, with Prof. Marjorie Shapiro and Dr. Zach Marshall, both of UC Berkeley.

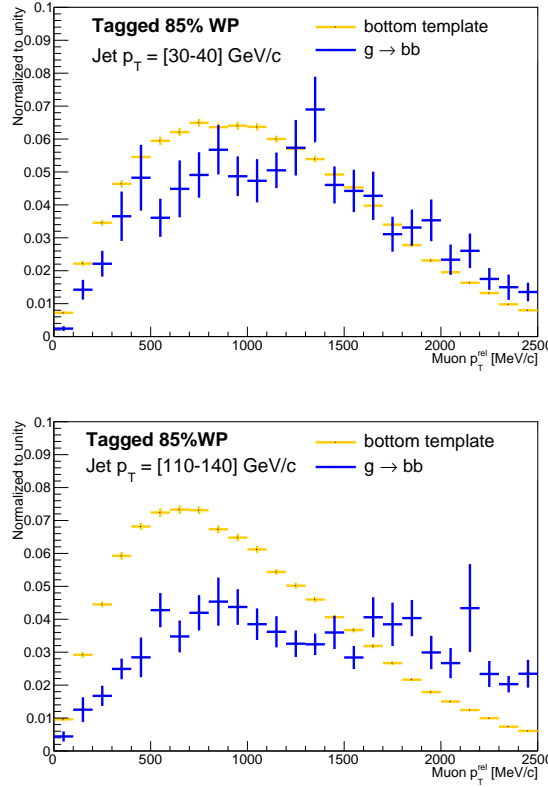


Figure 4.21: b -template comparison between inclusive b -jets (yellow curve) and gluon-splitting b -jets (blue curve). Top plot shows the p_T^{jet} bin between 30 and 40 GeV. Bottom plot shows the p_T^{jet} bin between 110 and 140 GeV. Figure credit to Dr. Valentina Vecchio.

jets could improve the quality of fit at high p_T^{jet} .

To test this, we created b -templates with an increased gluon-splitting fraction and checked the quality of fit. We tried gluon-splitting scale-factor values between 1.2-3 and found that a value of 2.5 gave the best performance in the p_T^{jet} slice 11-140 GeV (which is the lowest p_T slice with major disagreement between data and MC in the p_T^{rel} tails). Figure 4.23 shows a comparison between the nominal b -template and the b -template with 2.5 times more gluon-splitting events. Figure 4.24 shows the post-fit plots with 2.5-times enhancement of gluon-splitting. As compared to the fit results using the nominal amount of gluon-splitting (Figure 4.22), these results show much better agreement in the tails of the p_T^{rel} distribution in the high p_T^{jet} bin. Additionally, the low p_T^{jet} fit is stable when increasing the amount of gluon-splitting.

At this point, this study is still a work-in-progress. We plan to work closely with the MC production experts to understand this issue and (ideally) help them make improvements to ATLAS

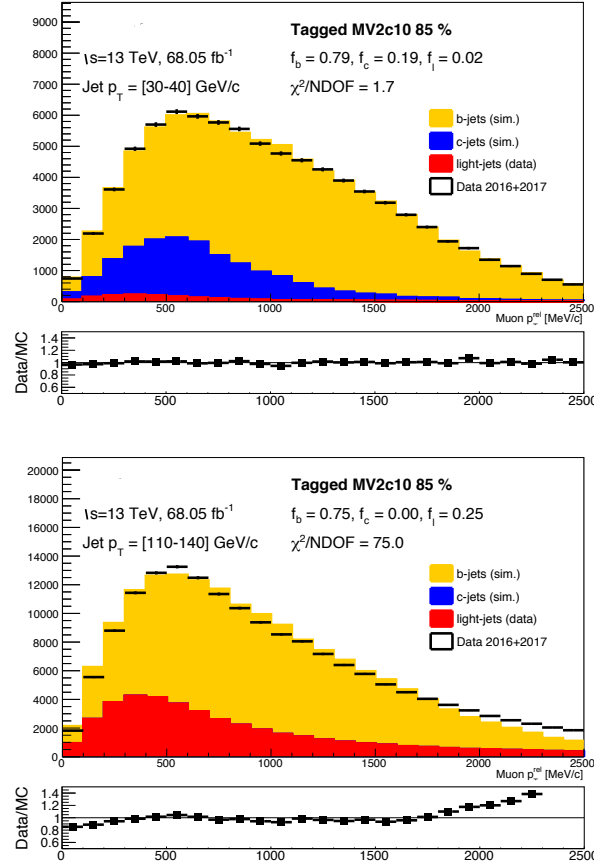


Figure 4.22: p_T^{rel} distribution in data and MC after the template fit. The b -template here has the nominal amount of gluon-splitting as predicted by the unfiltered di-jet MC. Top plot shows the p_T^{jet} bin between 30 and 40 GeV. Bottom plot shows the p_T^{jet} bin between 110 and 140 GeV.

MC in the future.

4.7 Systematic Uncertainties

Multiple sources of systematic uncertainties have been considered for this measurement. These systematics can be broadly categorized into detector and calibration uncertainties, physics modeling uncertainties, MC statistical uncertainties, and template selection uncertainties.

In general, two kinds of systematics are used. Two-sided systematics are evaluated by doing an up- and downwards variation of the parameter under study and propagating the resulting effects to the scale factors. The systematic is then assumed to be symmetric and half the difference between

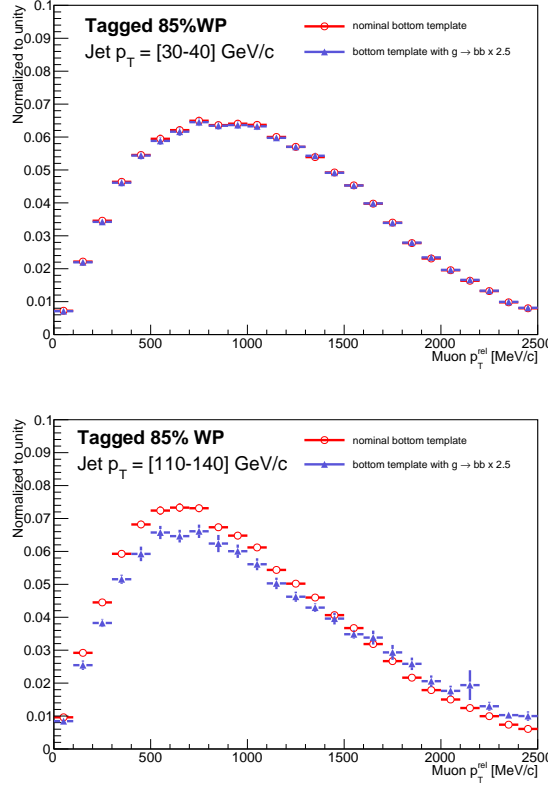


Figure 4.23: b -template comparison with nominal gluon-splitting (red) and 2.5-times enhanced gluon-splitting (blue). Top plot shows the p_T^{jet} bin between 30 and 40 GeV. Bottom plot shows the p_T^{jet} bin between 110 and 140 GeV. Figure credit to Dr. Valentina Vecchio.

the two variations is taken as a systematic. Single-sided systematics are evaluated by doing a variation and using the full difference to the nominal value as the uncertainty. The total systematic uncertainty is calculated from the sum in quadrature of all systematic uncertainties. Tables 4.9, 4.8, 4.7, and 4.6 summarize the systematic uncertainties for all the WPs. The most recent systematic uncertainty tables can be found in Appendix A.2; it should be noted that some systematics are missing or calculated in the “Run 1” style, so these tables are works-in-progress. The remaining systematics to be added or updated are listed in Section 4.9.

4.7.1 Detector and Calibration Uncertainties

This analysis accounts for several uncertainties related to detector resolution and performance/calibration for jets and muons.

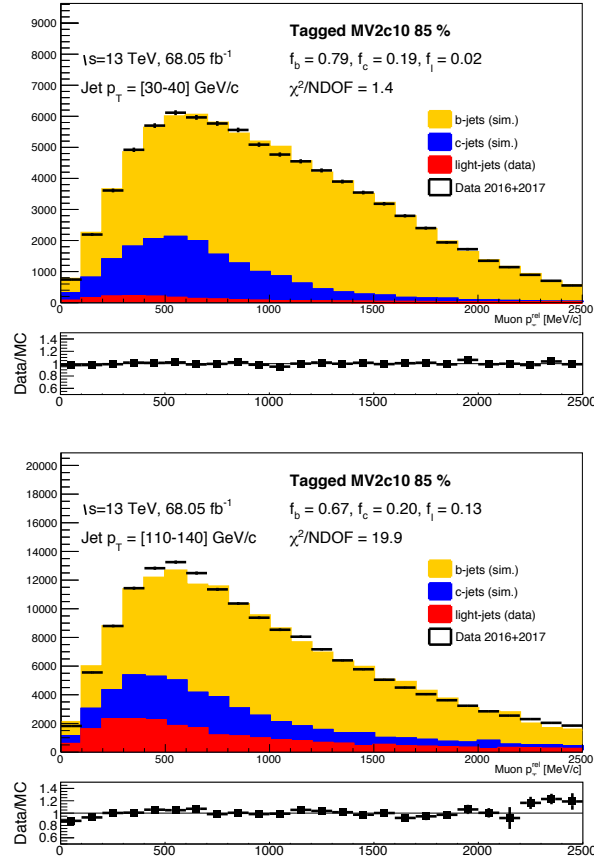


Figure 4.24: p_T^{rel} distribution in data and MC after the template fit. The b -template here has 2.5 times the nominal amount of gluon-splitting as predicted by the unfiltered di-jet MC. Top plot shows the p_T^{jet} bin between 30 and 40 GeV. Bottom plot shows the p_T^{jet} bin between 110 and 140 GeV.

The jet energy scale calibration includes several MC-based, *in-situ*-validated corrections for pile-up effects: per-event area-based pile-up removal, calculated using median p_T density ρ , and residual p_T dependent N_{PV} and μ corrections, where N_{PV} is the number of reconstructed primary vertices and μ is the mean number of interactions per bunch crossing. The uncertainties on these corrections arise from potential MC mismodeling of N_{PV} , μ , and ρ topology and from p_T dependence of N_{PV} and μ terms used in the residual pile-up correction.

Jets originating from gluons, light quarks or heavy quarks differ in hadronization and jet structure and hence in calorimeter response. To cover uncertainty in calibrating the jet energy scale for gluon-initiated jets (called “flavor response”), a systematic variation is applied by comparing the calorimeter response for b -jets produced by different MC generators. The differences in jet energy

scale calibration for quark- and gluon-initiated jets (called “flavor composition”) are considered by comparing the two using a PYTHIA8 dijet sample. Finally, differences in response between jets in forward and central η regions are handled similarly and validated in an *in-situ* tag-and-probe approach using dijet events [122].

Other jet uncertainties have been combined into nuisance parameters (NPs). 67 NPs are determined in *in-situ* Z/γ +jet and multi-jet p_T balance estimates and are then reduced to a set of six uncertainties via an eigen-decomposition. Five of these NPs constitute the greatest-magnitude principal components, and the remaining components are combined together quadratically into a single NP. A similar NP method is used to combine uncertainties related to the jet energy resolution [122].

For the p_T^{rel} calibration only combined (CB) reconstructed muon tracks (as described in Section 3.5.1) were used. In this measurement, uncertainty in muon track reconstruction is included by applying a Gaussian smearing of muon tracks in both the ID and MS using the respective precision $\pm 1\sigma_{\text{ID,MS}}$. The muon momentum scale in simulation is calibrated to data by studying $J/\psi \rightarrow \mu\mu$ and $Z \rightarrow \mu\mu$ decays. The systematic and statistical uncertainties on this correction are propagated throughout the presented measurement and their impact on the SFs is calculated [79]. Finally, the muon spectrometer alignment is calibrated by checking the *sagitta* of muon tracks with the ATLAS magnets turned off; when the magnets are turned off, the muons will travel in a straight line because they are no longer bathed in a magnetic field. Uncertainties related to the alignment of the MS are also propagated through the analysis [123].

4.7.2 Modeling Uncertainties

The physics modeling uncertainties accounted for in this analysis have been grouped into those pertaining to muons and to jets.

4.7.2.1 Muon Uncertainties

The muons studied in this analysis originate both from direct $b \rightarrow \mu + X$ decays and from cascade $b \rightarrow c \rightarrow \mu + X$ decays. The branching fraction of B -hadrons decaying directly is measured to be $BR(b \rightarrow \mu X) = 10.86 \pm 0.16$ [10, 111]: the percent uncertainty on this measurement is then used to vary the *in-situ* direct decay fraction entering in the b -template. Both an up and down variation have been performed: the difference in the results is taken as a systematic uncertainty.

In order to reduce contributions from “fake” signal muons (for example, from decay-in-flight muons from pion or kaon decays), tight muon reconstruction quality criteria are required in the

analysis. Despite this, misidentified particles or decay-in-flight muons can still make the selection. Due to the muon filter on the MC simulation, the amount of these fake muons is underestimated in the simulation. To estimate the effect of additional fake muons, their amount has been increased in the simulation by reweighting jets with a fake muon by a factor of two and propagating the impact to the resulting scale factors.

4.7.2.2 Jet and Hadron Uncertainties

The muon p_T^{rel} depends on the knowledge of the relative directions of the muon and the B -hadron. While the muon direction is measured with high precision, two aspects influence the knowledge of the B -hadron direction. First, the difference between the B -hadron flight direction and the reconstructed jet direction is studied in simulation. Second, the precision of the jet direction reconstruction is estimated by comparing calorimeter and track jets. These systematic effects have been found to be 0.004 and 0.008 in ϕ and η , respectively [111]. In order to estimate a jet angular resolution uncertainty, the jet direction has been varied within a Gaussian distribution with the widths set to $\Delta\phi = 0.004$ and $\Delta\eta = 0.008$. These jets are then used to redo the measurement and the difference is taken as the systematic uncertainty.

For the p_T^{rel} calibration it is necessary to have a muon inside the jet cone, which is usually the case only for semileptonically decaying B -hadrons. The tagging efficiency on this sample, however, differs with respect to the inclusive b -tagging efficiency (i.e. b -jets which decay hadronically or semileptonically). This effect will cancel out in the calculation of the data-to-MC SFs as long as it is well modeled in the simulation. Possible bias due to differences in the modeling quality between the semileptonic and inclusive decays are found to be negligible in early ATLAS data. This measurement as function of the p_T^{jet} was done on a set of $t\bar{t}$ events by comparing SFs determined in hadronic and leptonic top decays. This uncertainty is found to be independent from p_T^{jet} and varies from 1.35% for the 60% $MV2c10$ working point to the 0.7% for the 85% $MV2c10$ working point. The full procedure is described in Section 4.6.1.

4.7.3 MC Statistical Uncertainties

Two sources of MC statistical uncertainty have to be taken into account in this analysis. The simulation statistical uncertainty represents statistical limitations on the number of events in Equation (4.3) and is propagated to the simulation efficiency and the scale factors. The template statistical uncertainty covers changes in the template shapes due to statistical fluctuations. To evaluate this, ten

thousand pseudo-experiments were performed to generate new templates according to a bin-by-bin Gaussian variation whose mean value and standard deviation are set to the numbers extracted from the nominal templates. A Gaussian fit is performed on the distribution of the fraction of b -jets generated by the pseudo experiments: the resulting mean value is used to compute the b -tagging efficiency in data, then compared to the nominal value to assess the template statistical uncertainty.

4.7.4 Template Selection Uncertainties

Since the light template is generated from data it is clear that there will still be some remaining heavy-flavor jets after the selection is applied. The amount of heavy flavor contamination is estimated from the unfiltered simulation and corrected for in the analysis using SF_b and SF_c (as described in Section 4.4.3). To account for the limited knowledge of this value, the flavor contamination fractions are varied up and down by one standard deviation and the scale factor is recalculated with the resulting numbers.

The Jet Vertex Tagger (JVT) [124] is used to reject pile-up jets. It has been checked that uncertainty on the estimated efficiency of the algorithm has no effect on the p_T^{rel} analysis. Since this algorithm rejects jets with specific kinematic properties the choice of the JVT working point may have an impact on the measurement. To account for this, the JVT criterion has been exchanged for a loose and tight criterion when generating the templates. In data, the JVT cut has no effect because pileup is reduced effectively by the other selections (such as the trigger). In unfiltered MC, the JVT cut removes very few jets and has no effect on the simulated b -tagging efficiency. Therefore, only the impact on the template shapes is used to re-evaluate the measured efficiencies.

Table 4.6: Systematic uncertainties for the $MV2c10$ tagging algorithm at 85% nominal b -tagging efficiency

Systematic Uncertainty Source	Systematic Uncertainty in $p_T^{\text{jet}} [GeV]$ Bins								
	[20, 30]	[30, 40]	[40, 50]	[50, 70]	[70, 90]	[90, 110]	[110, 140]	[140, 170]	[170, 200]
Detector and Calibration Uncertainties	0.647	0.288	0.424	0.108	0.33	0.247	0.272	1.627	1.237
Modeling Uncertainties	0.713	0.712	0.711	0.725	0.703	0.706	0.919	6.447	1.443
MC Statistical Uncertainties	0.569	0.641	0.522	0.485	0.693	0.943	0.588	1.0	1.406
Template Selection Uncertainties	0.009	0.0	0.01	0.0	0.003	0.008	0.016	0.458	0.136
DataStats	0.517	0.628	0.680	0.817	0.613	1.195	0.586	0.615	0.516
TotalSystematicErr	1.109	0.994	0.973	0.875	1.035	1.199	1.119	6.738	2.363

Table 4.7: Systematic uncertainties for the *MV2c10* tagging algorithm at 77% nominal *b*-tagging efficiency

Systematic Uncertainty Source	Systematic Uncertainty in $p_T^{\text{jet}} [GeV]$ Bins								
	[20, 30]	[30, 40]	[40, 50]	[50, 70]	[70, 90]	[90, 110]	[110, 140]	[140, 170]	[170, 200]
Detector and Calibration Uncertainties	0.649	0.371	0.677	0.29	0.484	0.647	0.654	4.679	1.929
Modeling Uncertainties	0.937	0.929	0.948	0.931	0.935	1.017	1.073	4.027	3.14
MC Statistical Uncertainties	0.789	0.648	0.718	0.55	1.177	2.002	6.09	1.646	3.168
Template Selection Uncertainties	0.035	0.012	0.01	0.009	0.007	0.061	0.05	0.787	0.467
DataStats	2.191	0.777	0.728	1.405	0.599	0.975	0.480	0.512	0.460
TotalSystematicErr	1.371	1.183	1.360	1.113	1.572	2.330	6.216	6.434	4.877

Table 4.8: Systematic uncertainties for the *MV2c10* tagging algorithm at 70% nominal *b*-tagging efficiency

Systematic Uncertainty Source	Systematic Uncertainty in $p_T^{\text{jet}} [GeV]$ Bins								
	[20, 30]	[30, 40]	[40, 50]	[50, 70]	[70, 90]	[90, 110]	[110, 140]	[140, 170]	[170, 200]
Detector and Calibration Uncertainties	0.678	0.66	1.215	0.491	0.756	1.369	0.766	4.428	2.019
Modeling Uncertainties	1.366	1.202	1.145	1.146	1.138	1.133	1.308	3.873	1.347
MC Statistical Uncertainties	1.008	0.79	0.911	0.821	1.554	2.475	6.352	2.102	3.135
Template Selection Uncertainties	0.023	0.006	0.031	0.017	0.097	0.143	0.167	0.343	0.282
DataStats	0.759	0.850	0.709	0.836	0.619	0.949	0.467	0.547	0.528
TotalSystematicErr	1.807	1.570	1.892	1.484	2.062	3.041	6.529	6.251	3.963

Table 4.9: Systematic uncertainties for the *MV2c10* tagging algorithm at 60% nominal *b*-tagging efficiency

Systematic Uncertainty Source	Systematic Uncertainty in $p_T^{\text{jet}} [GeV]$ Bins								
	[20, 30]	[30, 40]	[40, 50]	[50, 70]	[70, 90]	[90, 110]	[110, 140]	[140, 170]	[170, 200]
Detector and Calibration Uncertainties	1.244	0.306	1.703	0.745	0.978	1.679	2.076	2.952	2.694
Modeling Uncertainties	2.396	1.574	2.114	1.844	1.644	2.879	2.72	3.496	2.895
MC Statistical Uncertainties	0.943	1.014	1.012	0.954	1.996	2.773	6.044	2.646	4.447
Template Selection Uncertainties	0.032	0.032	0.026	0.035	0.213	0.137	0.237	0.081	0.573
DataStats	0.736	0.838	0.756	0.772	0.662	1.029	0.536	0.668	0.768
TotalSystematicErr	2.825	1.876	2.883	2.195	2.758	4.324	6.942	5.273	5.959

4.8 Results

As discussed in Section 4.1, the *b*-tagging efficiency is computed by performing a template fit to the tagged and untagged p_T^{rel} distributions. The procedure is repeated for all p_T^{jet} bins and for four working points for the algorithm *MV2c10*. The p_T^{jet} -dependent *b*-tagging efficiency ε_b in the selected data sample measured for the *MV2c10* algorithm for the nominal efficiencies $\varepsilon_b^{\text{nom}} = 85\%, 77\%, 70\%$, and 60% is shown in Figures 4.25. Results from data are shown in the black dots with uncertainty bands depicted in green, while the MC prediction is shown in red. The scale factors (data/MC) are shown on the right with statistical and systematic uncertainties. The scale factors are generally consistent with unity; some discrepancy can be seen in the highest and lowest p_T^{jet} bins.

For comparison, the *b*-tagging efficiency and scale factors are shown for the tag-and-probe and

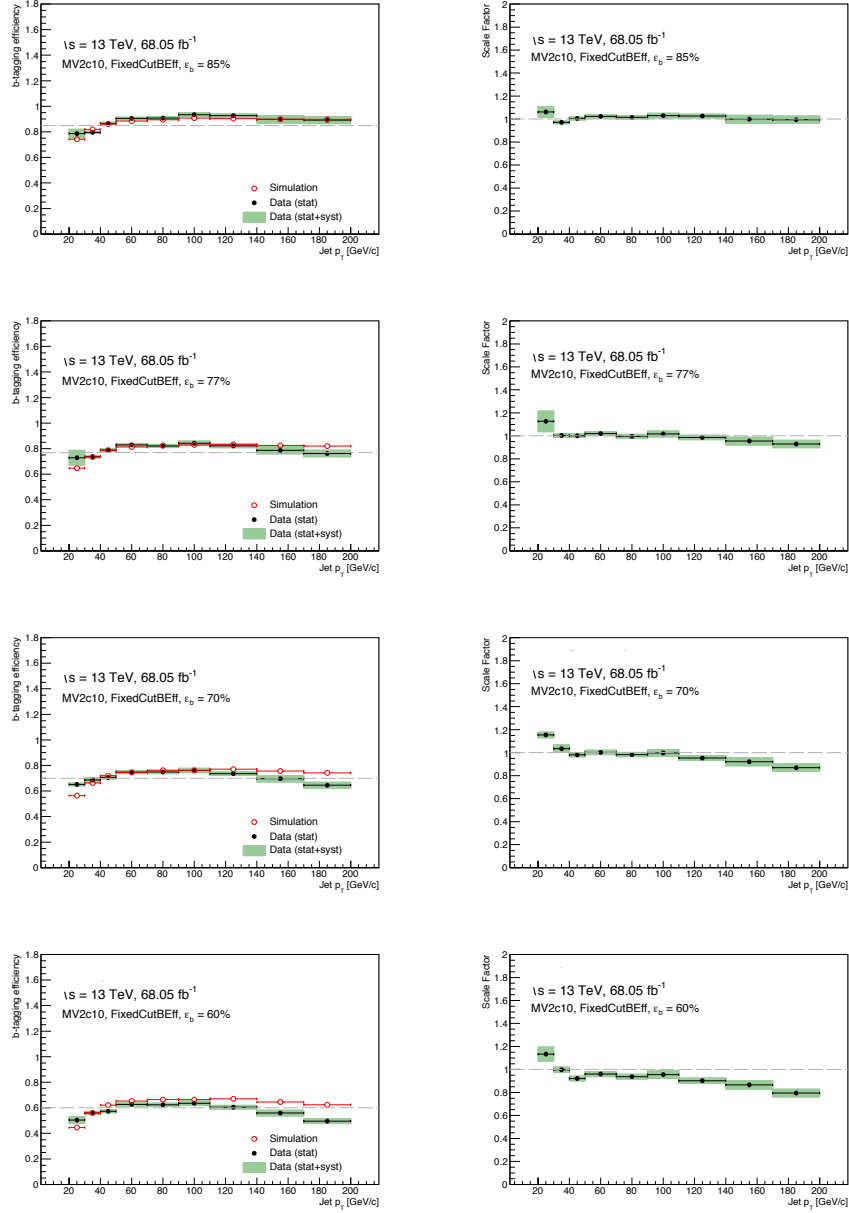


Figure 4.25: p_T^{jet} -dependent efficiencies (left) and scale factors (right) measured by the p_T^{rel} method for the MV2c10 algorithm for the nominal efficiency of $\epsilon_b^{\text{nom}} = 85\%, 77\%, 70\%$, and 60% (top to bottom). MC predictions are shown in gray while the data is depicted in black dots. The statistical and systematic uncertainties are shown in the green error bands.

likelihood-based calibrations for the 70% working point in Figure 4.26 [81]. These results are produced using $t\bar{t}$ events instead of $b\bar{b}$. The scale factors from the likelihood method are mostly consistent within uncertainty. The results may disagree in the lowest p_T^{jet} bins, but it is difficult to compare since they use different events ($t\bar{t}$ versus $b\bar{b}$) and different p_T^{jet} binning (p_T^{rel} is binned more finely than either $t\bar{t}$ -based method over a smaller p_T^{jet} range). However, for most of the p_T^{jet} range, results are consistent between the $t\bar{t}$ -based and the p_T^{rel} method results.

4.9 Future Work

The p_T^{rel} analysis has gone through several delays and transformations, reducing the uncertainty on these results but delaying the publication time scale. The following section shall describe the remaining work to be done on the Release 21 version of this analysis and possible applications of p_T^{rel} in the future.

Systematic Uncertainties

The momentum of the muon in the b -hadron rest-frame, p^* , is a key distribution for this measurement. While its modeling is crucial, measurements of this distribution provided by the BABAR and Delphi collaborations [125, 126] do not fully agree within their uncertainties. The p^* spectrum of muons has been studied in the simulations discussed in Section 4.2. In Release 20.7, it was found that the p^* distribution in simulation agrees with the Delphi results; this has not yet been re-checked in Release 21. Assuming the simulation agrees with the Delphi results, this systematic shall be evaluated by reweighting the simulated p^* distribution to match that from BABAR, propagating the uncertainty through the analysis.

Energetic gluon decays may result in jets with two or more heavy flavor hadrons inside the jet cone due to gluon-splitting. These jets have a different tagging efficiency, different probability to contain a muon, and a different p_T^{rel} . Therefore, their modeling has a large impact on this measurement. Details about the gluon-splitting studies can be found in Section 4.6.2; although this has been studied and somewhat understood, additional work is needed to assign a systematic uncertainty to the amount of gluon-splitting in the templates.

During the fragmentation process, the energy of the initial b -quark is passed on to the generated hadrons (this is described in detail in Section 2.2.5). To evaluate an uncertainty on the fragmentation fraction X_b in simulation, X_b shall be altered by 5% in an up-down variation to estimate conserva-

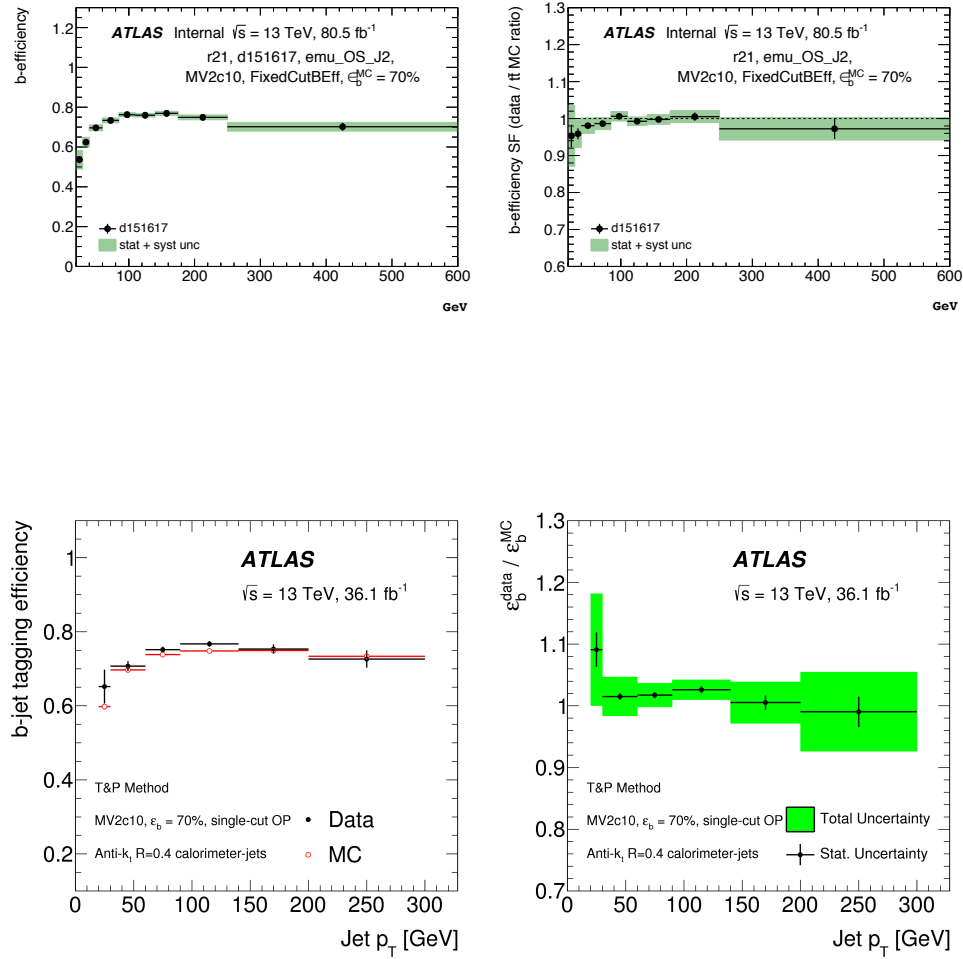


Figure 4.26: p_T^{jet} -dependent efficiencies (left) and scale factors (right) measured by the likelihood-based (top) and tag-and-probe (bottom) $t\bar{t}$ methods for the $MV2c10$ algorithm for the nominal efficiency of $\epsilon_b^{\text{nom}} = 70\%$. MC predictions are shown in red while the data is depicted in black dots. The statistical and systematic uncertainties are shown in the error bands. [81]

tively the systematic uncertainty due to the limited knowledge of the hadronization process. This systematic has not yet been evaluated.

The p_T^{rel} measurement depends on the modeling of the final state particles in the b -hadron rest-frame. Therefore, the fractions of hadrons (B^0 , B^+ , B_s , b -baryons) produced during the fragmentation process have to be well modeled. This modeling is limited by how precisely these fractions have been measured. For this measurement the fragmentation fractions have been set to the estimates by the [Heavy Flavor Averaging Group \(HFAG\)](#) [127]. To evaluate a systematic uncertainty, the events shall be reweighted to match flavor fractions measured by the CDF collaboration [128]. Table 4.10 compares the simulation and inclusive measurements.

Table 4.10: Fractions of b -hadrons as produced in simulated Z^0 -decays, inclusive measurements performed at CDF [128], and compared to the average provided by the HFAG [127].

Hadron Fraction	Z^0 -decays (MC)	Tevatron	HFAG-combination
B^+ fraction	0.410 ± 0.007	0.350 ± 0.020	0.406 ± 0.005
B^0 fraction	0.410 ± 0.007	0.350 ± 0.020	0.406 ± 0.005
B_s^+ fraction	0.100 ± 0.008	0.100 ± 0.010	0.105 ± 0.005
b -baryon fraction	0.080 ± 0.010	0.199 ± 0.044	0.083 ± 0.010

Gluon-Splitting: Assign a Systematic or Cut-Off at High p_T^{jet} ?

In the high p_T^{jet} (110-200 GeV) regions, the data shows an excess in the tail of the p_T^{rel} distribution (~ 1.75 -2.5 GeV) which cannot be accounted for using the nominal MC templates. Based on the truth studies presented in Section 4.6.2, we believe that this excess in data is caused by gluon-splitting. As described in that section, we found that increasing the amount of gluon-splitting events in our b -templates by $2.5 \times$ produced a better fit to data in the high p_T^{jet} region. We felt, however, that we could not yet comfortably assign a systematic uncertainty to this reweighting.

There are a few outside factors the team will also need to consider when deciding how to handle gluon-splitting in p_T^{rel} .

First, p_T^{rel} is used as a cross-check for the $t\bar{t}$ -based flavor-tagging calibrations, the default calibrations used by most ATLAS physicists. p_T^{rel} loses discriminating power for high values to p_T^{jet} because the p_T^{rel} distribution becomes more and more similar for b , c , and light jets at high values of p_T^{jet} . Because of this, p_T^{rel} scale factors at high p_T^{jet} may have large systematic uncertainties, making them less useful as a cross-check for $t\bar{t}$ calibrations. p_T^{rel} scale factors will also eventually be combined with b -tagging scale factors from other calibrations to produce a full Run 2 combined flavor-tagging

result. If p_T^{rel} scale factors are provided at high p_T^{jet} with large uncertainties, the uncertainty for those bins in the combined result will be driven by p_T^{rel} . Since the full combined Run 2 result seeks to provide as low an uncertainty as possible, the high p_T^{jet} results for p_T^{rel} will not be useful.

Second, such a high p_T^{jet} cut-off does not harm the primary application of the p_T^{rel} calibration in Run 2: the measurement of $R_b = \frac{t \rightarrow bW}{t \rightarrow qW}$, $q = u, d, s$. Because the $t\bar{t}$ -based flavor-tagging calibrations assume $R_b = 1$, they cannot be used for the R_b measurement. The p_T^{rel} method, on the other hand, makes no such assumptions about top quark physics. About 93% of all top quarks used for the R_b measurement are found between 30-140 GeV, so providing p_T^{rel} calibration results for high values of p_T^{jet} will not benefit this measurement anyways.

The ongoing analysis team will need to decide how to assign a systematic to the gluon-splitting reweighting, or come up with a systematic method to reject bins with major contributions from gluon-splitting from these results.

Future Applications

In addition to the measurement of $\frac{t \rightarrow bW}{t \rightarrow qW}$, the p_T^{rel} method could be used to make improvements to ATLAS MC and for online tagging efficiency monitoring.

As mentioned in Section 4.6.2, there are known problems with the gluon-splitting fraction in ATLAS MC. Because p_T^{rel} is sensitive to the template shape differences from gluon-splitting jets, p_T^{rel} could provide a way to measure the amount of $g \rightarrow b\bar{b}$ splitting across the p_T^{jet} spectrum. Even if this fraction were estimated coarsely, it could be used to validate the fraction in MC, which experts estimate could be easily 100-200% underestimated. The p_T^{rel} team has worked closely with MC production experts throughout this analysis, and plans to validate and possibly correct this value in MC are already underway. Such MC improvements would benefit a variety of ATLAS physicists.

Because p_T^{rel} relies on $b\bar{b}$ events instead of $t\bar{t}$, it is possible to collect enough data in a *single* day of $p-p$ collisions to perform a b -tagging calibration⁷⁸. As mentioned in Section 4.5, Bing attempted to use the TADA framework to produce an online b -tagging monitoring tool for Run 2. If some of the technical limitations of the TADA framework were removed (for example, by changing the trigger setup of the TADA framework), one could use p_T^{rel} to monitor the b -tagging efficiency in data on a daily basis during data collection, helping physicists catch problems earlier.

⁷⁸This would require non-prescaled muon-in-jet triggers in the monitoring toolset.

CHAPTER 5

Searching for Electro-weakino Pair Production in a Fully-Hadronic Final State

“The future depends on what you do today.”

— Mahatma Gandhi

This chapter describes a search for electroweak supersymmetry in fully-hadronic final states. This chapter begins with a description of the targeted supersymmetry model and the fully-hadronic signatures it could produce. The datasets and samples used are briefly detailed, followed by a description of object-level and event-level selection criteria. The next section provides an overview of background processes and details several methods by which to validate or estimate their contributions in data. This chapter concludes with a section on potential future work and next steps for physicists interested in this model and final state.

5.1 Signal Signature

Section 2.5 presented the basics of SUSY models and R-parity conservation. In this chapter, we shall describe the target SUSY scenario in this thesis. First, however, let us put this search into the context of the larger ATLAS SUSY search campaign.

5.1.1 SUSY Production Cross-Sections

Before searching for a particular SUSY particle, we want to have an idea of the cross-section for processes producing that particle. Figure 5.1 shows the cross-section for various SUSY production modes as a function of SUSY particle mass in MSSM-like SUSY models [129].

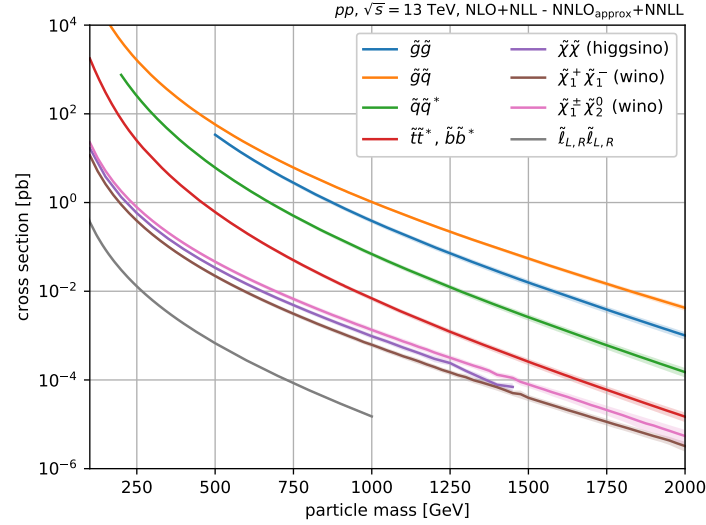


Figure 5.1: Cross-section plots for various SUSY production modes as a function of SUSY particle mass [129]

The modes with the largest cross-section are gluino-gluino ($\tilde{g}\tilde{g}$), gluino-squark ($\tilde{g}\tilde{q}$), and squark-squark ($\tilde{q}\tilde{q}$, $\tilde{t}\tilde{t}$, and $\tilde{b}\tilde{b}$) production [130]. This makes these the “low-hanging fruit” for the LHC due to the advantageous strong production cross-section; many searches have already been done for gluino and squark pair-production [131] [132] [133] [134] [135] [136] [137] [138]. Figures 5.2, 5.3, and 5.4 show the most recent exclusion limits from ATLAS for stop, gluino, and sbottom pair-production, respectively [139]. Similar searches have also been done at CMS [140] [141] [142] [143] [144].

After the $\tilde{g}\tilde{g}$, $\tilde{g}\tilde{q}$, $\tilde{q}\tilde{q}$, $\tilde{t}\tilde{t}$, and $\tilde{b}\tilde{b}$ modes, the next set of modes are the so-called “electroweakly-produced” SUSY modes: the higgsino, wino, and slepton modes. The higgsino, wino, and bino are often referred to as “electroweakinos” or **electroweakinos**; we shall use this convention in this chapter. The exact SUSY model/scenario used in the search presented here shall be described below. Figures 5.5, 5.6, 5.7, and 5.8 show the most recent exclusion results from ATLAS for electroweakino pair-production.

5.1.2 Target Signatures

Section 2.5.4 summarized the physics scenario considered for this search. In total, four signal modes are considered:

$$(\tilde{\chi}_{\text{heavy}}, \tilde{\chi}_{\text{light}}) = (\tilde{W}, \tilde{B}), (\tilde{H}, \tilde{B}), (\tilde{W}, \tilde{H}), (\tilde{H}, \tilde{W}) \quad (5.1)$$

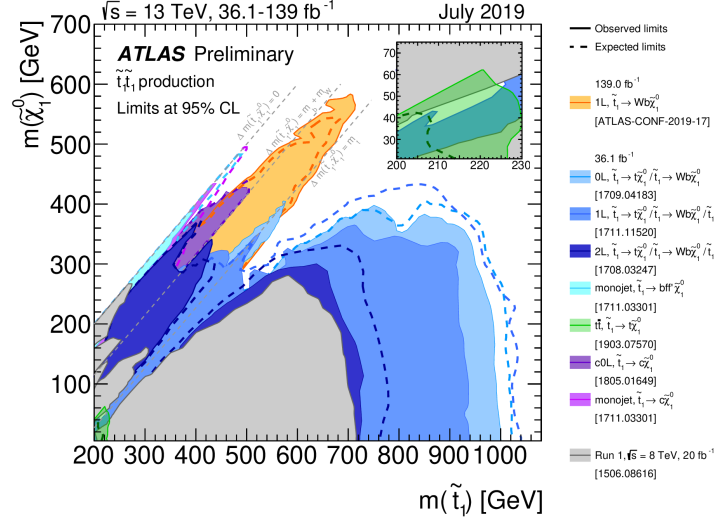


Figure 5.2: Exclusion results from ATLAS for stop pair-production as a function of stop mass and LSP mass for a few simplified SUSY models [139]

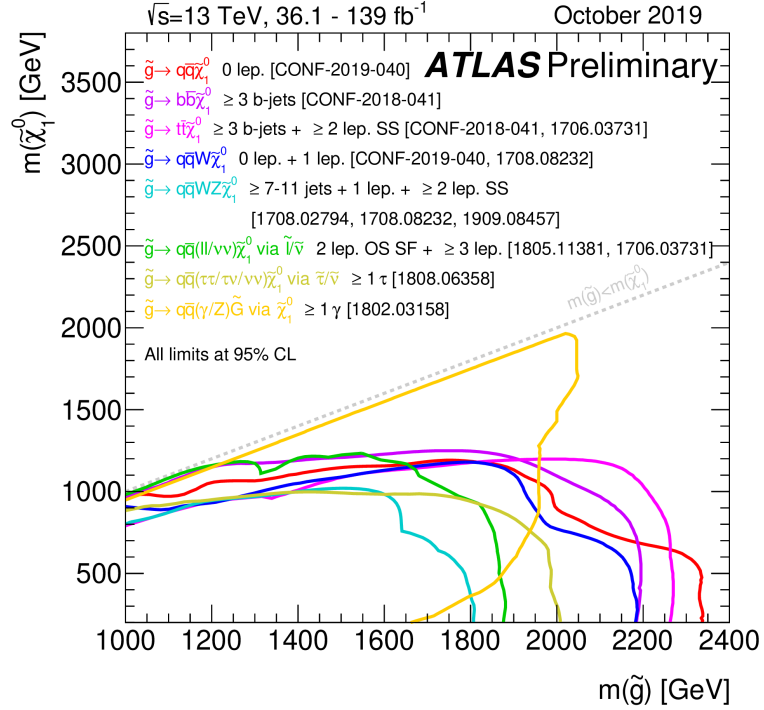


Figure 5.3: Exclusion results from ATLAS for gluino pair-production as a function of stop mass and LSP mass for a few simplified SUSY models [139]

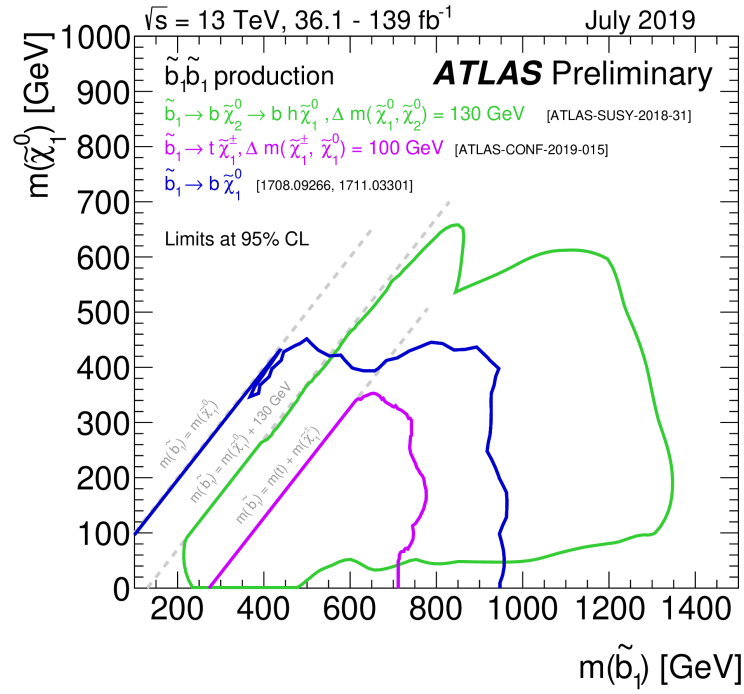


Figure 5.4: Exclusion results from ATLAS for sbottom pair-production as a function of stop mass and LSP mass for a few simplified SUSY models [139]

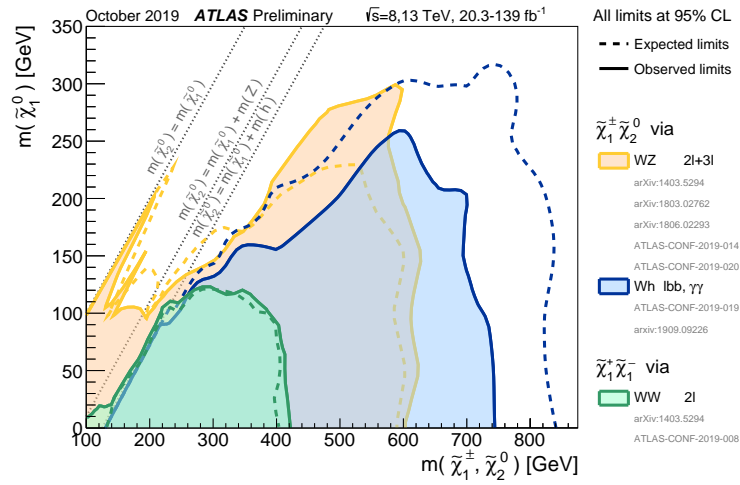


Figure 5.5: Exclusion results from ATLAS for $C1N2$ electroweakino pair-production in WZ final states [139]

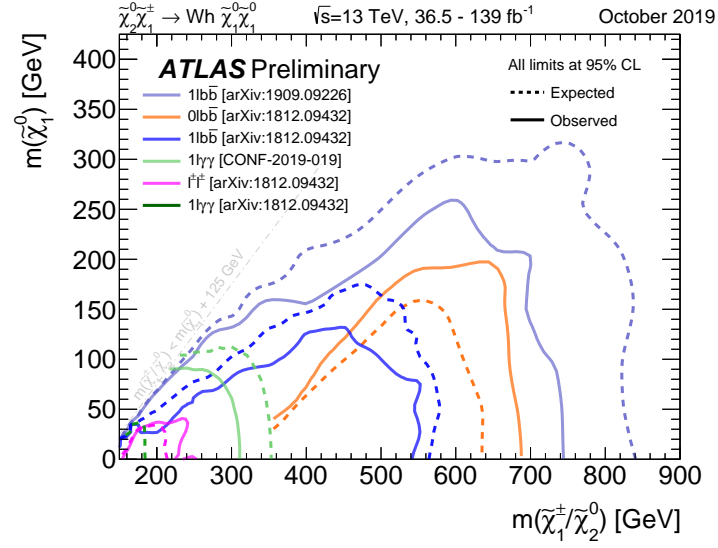


Figure 5.6: Exclusion results from ATLAS for $C1N2$ electroweakino pair-production in Wh final states [139]

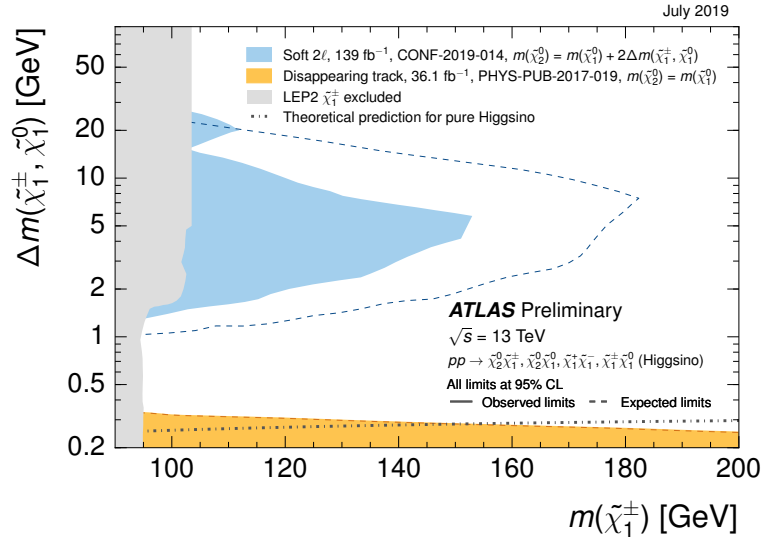


Figure 5.7: Exclusion results from ATLAS for higgsino pair-production [139]

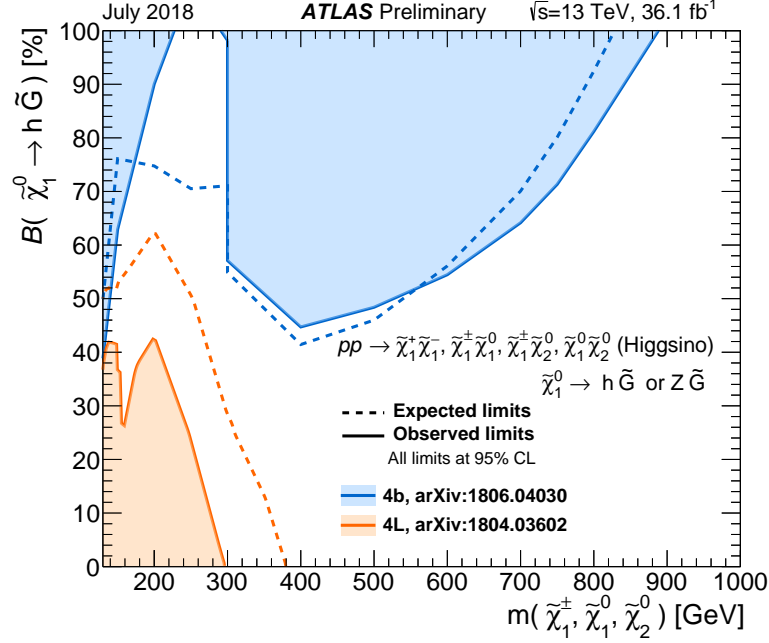


Figure 5.8: Exclusion results from ATLAS on a general gauge mediation model [139]

The targeted signature is the direct pair production of “heavy state” electroweakinos, which each decay into an LSP neutralino $\tilde{\chi}_1^0$ and a SM boson (W , Z , of h):

$$pp \rightarrow \tilde{\chi}\tilde{\chi} \rightarrow XX\tilde{\chi}_1^0\tilde{\chi}_1^0 \quad (5.2)$$

where $\tilde{\chi}\tilde{\chi} = \tilde{\chi}_1^\pm\tilde{\chi}_1^\pm/\tilde{\chi}_1^\pm\tilde{\chi}_2^0$ and $XX = WW/WZ/Wh/ZZ/Zh$. Most of the effort in this search has been focused on the “Big-3” final states:

- $\tilde{\chi}_1^\pm\tilde{\chi}_1^\mp \rightarrow WW\tilde{\chi}_1^0\tilde{\chi}_1^0$
- $\tilde{\chi}_1^\pm\tilde{\chi}_2^0 \rightarrow WZ\tilde{\chi}_1^0\tilde{\chi}_1^0$
- $\tilde{\chi}_1^\pm\tilde{\chi}_2^0 \rightarrow Wh\tilde{\chi}_1^0\tilde{\chi}_1^0$

The associated Feynman diagrams for these states (with relevant boson decays) are shown in Figure 5.9.

Although four different signal models are listed in Equation (5.1), it should be noted that only (\tilde{W}, \tilde{B}) interpretations have been done at this stage in the analysis; (\tilde{H}, \tilde{B}) reinterpretation studies are presented in Section 5.6 and are planned for a future result. The (\tilde{W}, \tilde{B}) signature is used as a benchmark throughout this analysis; we expect (and have seen in MC) that results optimized to

this model still generalize well to other models. higgsino/wino LSP models are possible, but haven't been investigated at ATLAS during Run 1 or Run 2 due to the many possible final states available in such models.

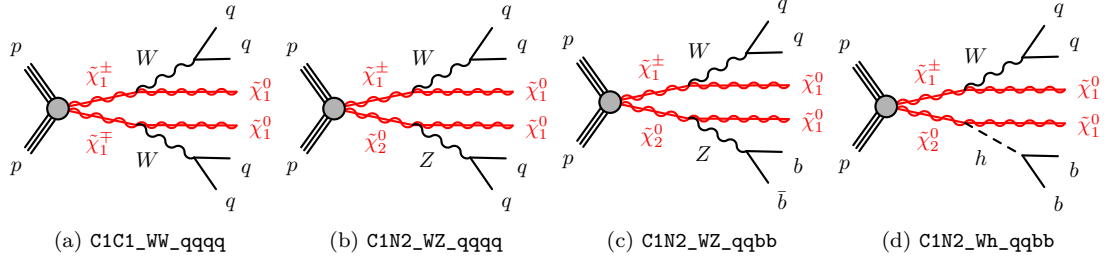


Figure 5.9: WW/WZ/Wh benchmark models with wino-dominant chargino-neutralino pair production decaying into bino-dominant LSP.

The benchmark model for a neutralino-only signal has yet to be finalized, but the candidates are:

- $(\tilde{\chi}_{\text{heavy}}, \tilde{\chi}_{\text{light}}) = (\tilde{H}, \tilde{a})$: $\tilde{H}\tilde{H} \rightarrow ZZ(Zh) \tilde{a}\tilde{a}$ where $(\tilde{H}, \tilde{H}) = (\tilde{\chi}_1^\pm, \tilde{\chi}_1^0)$, $(\tilde{\chi}_1^\pm, \tilde{\chi}_2^0)$, $(\tilde{\chi}_2^0, \tilde{\chi}_1^0)$ and \tilde{a} is axino.
- $(\tilde{\chi}_{\text{heavy}}, \tilde{\chi}_{\text{light}}) = (\tilde{W}, \tilde{H})$: $\tilde{\chi}_2^\pm \tilde{\chi}_2^0 \rightarrow ZZ(Zh) \tilde{\chi}_1^\pm \tilde{\chi}_1^0$, where $\tilde{\chi}_1^\pm$ decays into $\tilde{\chi}_1^0$ with very soft/undetected decay products.
- $(\tilde{\chi}_{\text{heavy}}, \tilde{\chi}_{\text{light}}) = (\tilde{H}, \tilde{B})$: $\tilde{\chi}_2^0 \tilde{\chi}_3^0 \rightarrow ZZ(Zh) \tilde{\chi}_1^0 \tilde{\chi}_1^0$ (Fig 5.10)

The (\tilde{W}, \tilde{H}) model will probably not be chosen because higgsino/wino LSP models have many possible final states with even more possible decays, making such searches very complicated. Regardless of which of these models is chosen, we plan to reinterpret the neutralino-only search as a GGM-inspired⁷⁹ higgsino-NLSP, gravitino-LSP model. In GGM models, the (nearly) massless gravitino \tilde{G} is the LSP. The target signature for this model is a pair of higgsinos which each decay promptly into the lightest neutral higgsino, which then decays into a gravitino and a Z or h boson [145]. If the higgsino mass $m_{\tilde{H}}$ is greater than the Higgs mass, $\tilde{\chi}_1^0$ is dominated by the higgsino component, and $\tan(\beta)$ (the ratio of expectation values in the Higgs doublet) is small, then the decay will be dominated by Higgs bosons. The branching ratio $\text{Br}(\rightarrow Z) = 1 - \text{Br}(\rightarrow h)$ is allowed to float; we plan to scan various values of this branching ratio during the interpretation. Wider interpretations are possible in future analyses.

⁷⁹GGM = Generalized Gauge Mediation

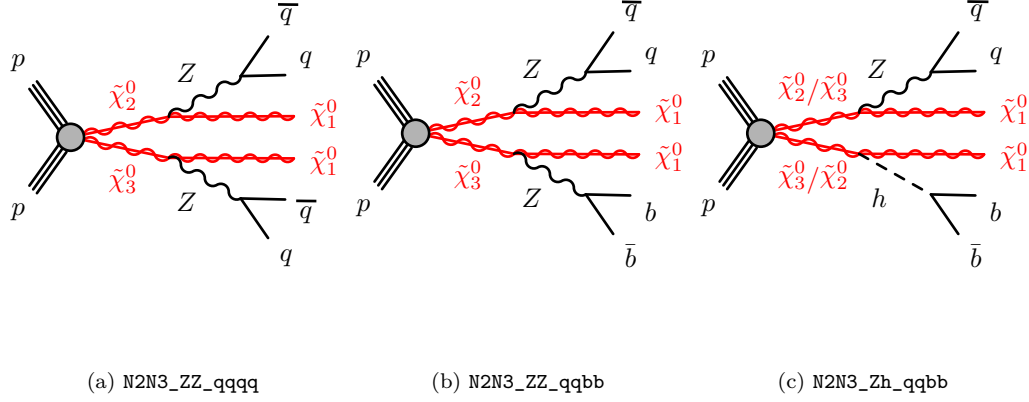


Figure 5.10: Neutralino-neutralino higgsino production model.

5.1.3 2B2Q Analysis Strategy

This thesis shall focus on the “boosted 2B2Q” final state for this search. This is a new signal region for this analysis; a previous results (Ref [146]) included only a resolved 2B2Q signal region. The boosted fully-hadronic 2B2Q signal region is advantageous for several reasons:

- W , Z , and h bosons all decay primarily to quarks; although leptonic decay modes might have smaller backgrounds, fully-hadronic modes can be sensitive to signals with smaller cross-sections.
- Searching for boosted decays provides sensitivity to large-mass-splitting signal modes which the resolved 2B2Q search might miss.
- Searches in a 4B final state (such as Ref [147]) are sensitive to $\tilde{H}\tilde{H} \rightarrow hh$ modes, but are not sensitive to final states containing a $\tilde{\chi}_1^\pm$, as the W boson does not have a $b\bar{b}$ final state.
- Searches in a 4Q final state will have larger background contributions; requiring two b -quarks is very useful for reducing SM backgrounds.

Happily, however, these modes (2B2Q boosted, 2B2Q resolved, 4Q, and 4B) are each best suited to different types of signatures. Providing many complementary modes for searching for these models gives confidence in our results and allows us to perform a more thorough search.

5.2 Datasets and Samples

The following section summarizes the data and MC simulation sample preparation.

5.2.1 Derivations

All data and MC samples used in this search are processed in the SUSY1 derivation format (for more information on derivation file formats in ATLAS, see Section 3.6.5) using software cache 21.2.45.0 or newer. The exact SUSY1 configuration can be found in [SUSY1.py](#). The events must pass at least one of the following selection criteria:

- $H_T > 150$ GeV where H_T is scalar sum of uncalibrated p_T of jets in the event.
- at least one electron, muon, or photon with $p_T > 100$ GeV
- at least two electrons or two muons with $p_T > 20$ GeV
- at least two photons with $p_T > 50$ GeV

5.2.2 Data Samples

This analysis uses a total of 139 fb^{-1} of data collected by the ATLAS detector during 13 TeV pp collisions from 2015-2018 (3.22 fb^{-1} in 2015, 33.0 fb^{-1} in 2016, 44.3 fb^{-1} in 2017, and 58.5 fb^{-1} in 2018). The data must satisfy the “Good Run List” selection requirement; events pass this selection if the LHC declared stable beams, the ATLAS detector was running properly, and the magnetic fields were operating as normal [113].

5.2.3 MC Samples

MC samples are used for modeling SM backgrounds and SUSY signals during the research and development stage.

5.2.3.1 SM Backgrounds

All MC for SM background simulation are centrally produced through ATLAS. The SM backgrounds considered in this analysis (along with information about their generation) are:

- diboson: Fully leptonic diboson decays are simulated using the SHERPA v2.2.2 (for $llll$, $lll\nu$, $ll\nu\nu$, $\ell\nu\nu\nu$) and SHERPA v2.2.1 (for $\nu\nu\nu\nu$) generator [148]. Included are matrix elements for

WW , WZ and ZZ processes and diagrams with four or six electroweak vertices, loop-induced processes such as $gg \rightarrow \ell\ell\ell$, electroweak $VVjj$ where V is a [vector boson](#), and semileptonic decays such as $WZ/ZZ \rightarrow qq\ell\ell$, $WZ/ZZ \rightarrow qq\nu\nu$, $WZ \rightarrow qq\ell\nu$. Only on-shell bosons are considered. All-hadronic diboson contributions are not considered, as the $E_T^{\text{miss}} > 200$ GeV selection makes them negligible.

- QCD multijet: Dijet processes are simulated using **SHERPA** with the CT10 [parton distribution function \(PDF\)](#) tune.
- W/Z +jets: Events containing W/Z bosons with associated jets are produced using the **SHERPA** v2.2.1 generator, making sure to properly assign mass to b -quarks and c -quarks. Matrix elements are calculated using the COMIX and OPENLOOPS generators for up to two partons at [next-to-leading order \(NLO\)](#) and up to four partons at [leading order \(LO\)](#). Parton showering is done with **SHERPA** using the ME+PS@NLO prescription. Events are normalized to the [next-to-next-to-leading order \(NNLO\)](#) QCD cross sections.
- $t\bar{t}$ (+SM bosons) and single-top: Top quark processes in Wt , $t-$ and $s-$ channels are produced with the POWHEG-Box v2 generator with NNPDF23LO set [149]. PYTHIA8 with perugia A14 tune is used for showering [150]. $t\bar{t}$ (single top) events are normalized to the NNLO + NNLL QCD(NLO) cross sections [151] [152], while the generator cross-section is used for tZ and $t\bar{t}$.

5.2.3.2 SUSY Signals

During signal generation, Decoupled SUSY particles are set with mass ~ 3 TeV. At this stage of the analysis, only $\tilde{\chi}_{\text{heavy}} = \tilde{W}$ signals have been used. We expect from theory that (\tilde{W}, \tilde{B}) and (\tilde{H}, \tilde{B}) signals should be very similar kinematically, allowing us to simply reweight the (\tilde{W}, \tilde{B}) samples to match the (\tilde{H}, \tilde{B}) cross-section and avoid regenerating signal samples. higgsino reinterpretation studies are available in Section 5.6 and are planned for a future result.

SUSY signal samples are generated at leading order with up to two additional partons using MADGRAPHv2.6.1 [153] interfaced with PYTHIA version 8.230 [150] and EvtGen 1.2.0 [116] to simulate the fully decay chain, parton showering, and hadronization (include b - and c -hadron decays). The parton distribution function used during simulation is NNPDF2.3LO [115] with the A14 [154] set of tuned underlying event and shower parameters (UE tune). The [Matrix Element-Parton Shower \(ME-PS\)](#) matching was performed with the CKKW-L prescription [155], with the matching scale set to one quarter of the produced electroweakino masses. Signal cross-sections and uncertainties

are calculated at NNLO in g_S (the strong coupling constant) using the PDF4LHC15_mc PDF set, following the recommendations of Ref. [156]. Resummation of soft gluon emissions is added at next-to-next-to-leading-logarithmic accuracy [157] [158] [159] [160].

Generating the fully electroweakino decay chain together with up to two additional partons is computationally very expensive. To save computing time, production up to electroweakino generation is done with matrix elements by MadGraph and subsequent decays are performed based on phase-space size. While this method discards the boson polarization information, this can be approximately recovered by a reweighting in helicity angle. This is done by reweighting the helicity angle distribution⁸⁰ from a flat distribution into a fully-longitudinally-polarized $\sin^2\theta^*$ shape; this polarization approximation is valid for signals for $\Delta m\left(\tilde{\chi}_1^\pm/\tilde{\chi}_2^0, \tilde{\chi}_1^0\right) > 300$ GeV and for both wino and higgsino production. A transversely-polarized or unpolarized boson decay will have a more imbalanced qq pair, as one of the quarks will be more aligned with the parent boson direction and the other will be less aligned. For longitudinally-polarized bosons, the qq pair will typically be balanced. The transversely-polarized or unpolarized bosons tend to have a 1-pronglike jet substructure [161], leading to worse boson tagging signal acceptance. Therefore, the longitudinal-polarization correction is necessary to increase our signal acceptance in simulation. Figure 5.11 visualizes the effect of this reweighting.

5.3 Object and Event-Level Selections

5.3.1 Object Definitions

This section shall review the methods used to reconstruct physics objects in this analysis. Like most SUSY analyses, we shall use two classes of selection criteria for reconstructed objects:

- “baseline”: This is a loose criteria used for defining the final state and orthogonal regions.
- “signal”: This is a tight criteria used for selecting a signal region. This selection is optimized to reject incorrectly-identified objects (i.e. [fakes](#)) as well as pileup contributions.

Both baseline and signal objects must pass an overlap removal requirement, described at the end of this subsection. The object reconstruction criteria are summarized in Table 5.1 and described in detail below.

⁸⁰i.e. the angle between the W/Z and one of its daughter particles in the W/Z rest frame.

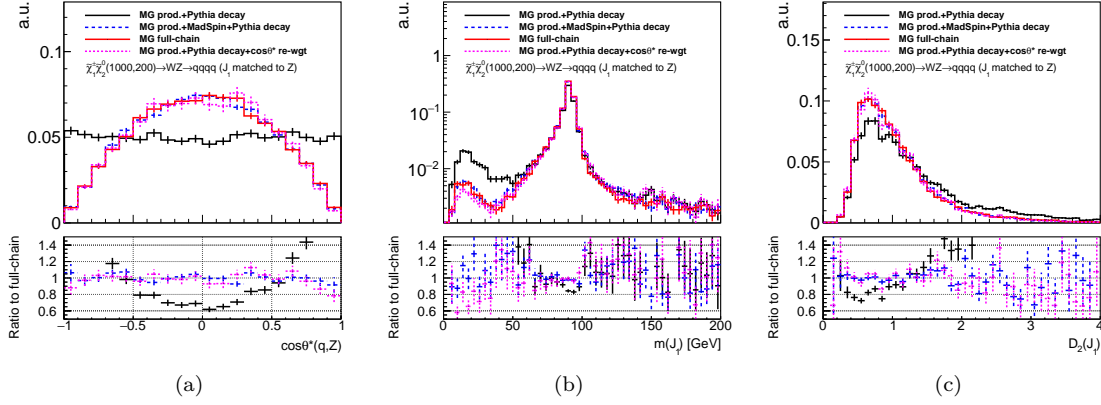


Figure 5.11: Reweighting the helicity angle of $\tilde{\chi}_1^\pm \tilde{\chi}_2^0 \rightarrow WZ \rightarrow qq\bar{q}\bar{q}$ signals with $(m_{\tilde{\chi}_1^\pm}, m_{\tilde{\chi}_2^0}) = (1000, 200)$ GeV. The black solid line is the nominal sample distribution. The blue dotted line is the distribution from MADSPIN interfaced between MADGRAPH and PYTHIA. The red solid line shows the distribution with both production and decay generated by MADGRAPH. Both the red and blue lines take boson polarization into account during decay chain simulation. The pink dotted line is the nominal sample after helicity angle reweighting: $w = 3 \sin^2 \theta^*/4$. (a) Helicity angle distribution for $Z \rightarrow qq$. (b) Leading large- R mass and (c) D_2 (i.e. “2-prongedness”) distribution. Figure credit to Dr. Shion Chen.

Electrons

Baseline electrons are reconstructed using ID tracks matched to electromagnetic clusters formed from calorimeter energy deposits using the super-cluster algorithm [162]. The baseline electrons must also pass $p_T > 6 \text{ GeV}$, $|\eta| < 2.47$, and the *LooseAndBLayerLLH* identification algorithm [163]. To reject fake electrons from pileup jets, baseline electrons must also pass a longitudinal impact parameter requirement: $z_0 \sin \theta < 0.5 \text{ mm}$. Fake and non-prompt electrons from heavy flavor decays are further reduced with a transverse impact parameter requirement: $|d_0/\sigma(d_0)| < 5$. In MC, electrons coming from photon conversion are rejected at truth level.

Muons

Baseline muons are reconstructed using the “combined” algorithm described in Section 3.5.1. The baseline muons must also pass a *Loose* identification criteria, $p_T > 5 \text{ GeV}$, $|\eta| < 2.7$, and $z_0 \sin \theta < 0.5 \text{ mm}$ longitudinal impact parameter requirement.

Property	Signal	Baseline
Electrons		
Kinematic	$p_T > 6 \text{ GeV}, \eta < 2.47$ (include crack)	$p_T > 6 \text{ GeV}, \eta < 2.47$
Identification	MediumLLH	LooseAndBLayerLLH
Isolation	FCLoose	–
Impact parameter	$ d_0/\sigma(d_0) < 5, z_0 \sin \theta < 0.5 \text{ mm}$	$ z_0 \sin \theta < 0.5 \text{ mm}$
Reco algorithm	Veto <code>author==16</code>	Veto <code>author==16</code>
Muons		
Kinematic	$p_T > 5 \text{ GeV}, \eta < 2.7$	$p_T > 5 \text{ GeV}, \eta < 2.7$
Identification	Medium	Loose
Isolation	FCLoose	–
Impact parameter	$ d_0/\sigma(d_0) < 3 \ \& \ z_0 \sin \theta < 0.5 \text{ mm}$	$ z_0 \sin \theta < 0.5 \text{ mm}$
Small-R jets (Anti- k_t $R = 0.4$ EMTopo)		
Calibration configuration	JES_data2017_2016_2015_Consolidated_EMTopo_2018_Rel21.config	
Calibration sequence (Data)	JetArea_Residual_EtaJES_GSC_Insitu	
Calibration sequence (MC)	JetArea_Residual_EtaJES_GSC	
Kinematic	$p_T > 20 \text{ GeV}, \eta < 2.8$	$p_T > 20 \text{ GeV}, \eta < 4.5$
Pileup mitigation	JVT Medium for $p_T < 120 \text{ GeV}, \eta < 2.5$	–
b -tagging	MV2c10 FixedCutBeff 85% WP, $ \eta < 2.5$	–
Large-R jets (Anti- k_t $R = 1.0$ LCTopo, trimming with $R_{\text{subject}} = 0.2, f_{\text{cut}} = 5\%$)		
Calibration configuration	JES_MC16recommendation_FatJet_Trimmed_JMS_comb_17Oct2018.config	
Calibration sequence	EtaJES_JMS	
Kinematics	$p_T > 200 \text{ GeV}, \eta < 2.0, m > 40 \text{ GeV}$ $p_T > 200 \text{ GeV}, \eta < 2.0$	
b -tagging	Ghost-associated AntiKt2PV0TrackJets passing MV2c10 FixedCutBeff 85% WP	

Table 5.1: Summary of object definitions.

Choosing a Baseline Lepton Definition

This analysis is a 0-lepton analysis, meaning that we require *exactly zero* leptons passing the baseline criteria. Therefore, our event selection efficiency is sensitive to the baseline lepton criteria. A variety of p_T , η , and lepton identification working points for muons and electrons were tested; the acceptance rate of 0-lepton events after overlap removal and 1-lepton background rejection for various baseline lepton definitions are shown in Figure 5.12. Based on these results, the LooseID⁸¹ working point and forward muon veto were selected for their high efficiency and 1-lepton background rejection power.

⁸¹Here, “ID” means identification, not inner detector!

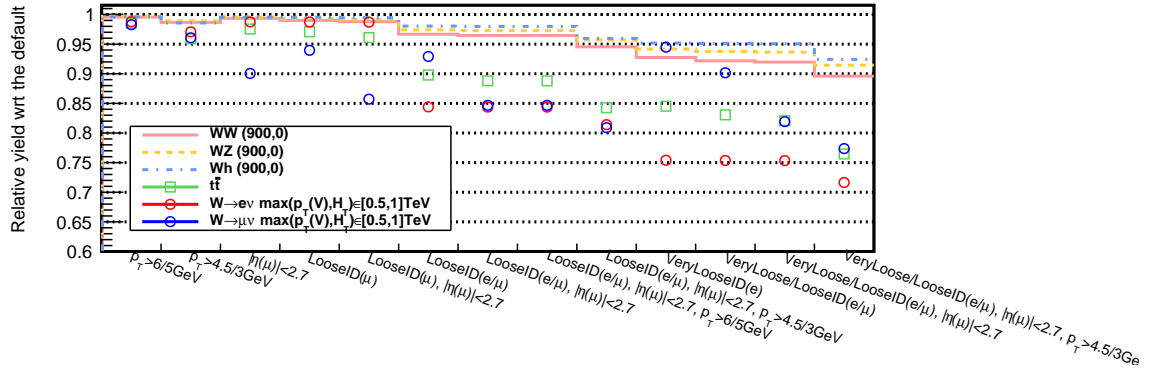


Figure 5.12: Acceptance rate for events with exactly zero baseline-leptons (after overlap removal and $E_T^{\text{miss}} > 200$ GeV preselection) for various baseline lepton definitions. The acceptance is normalized to the ‘default’ setup, where electrons/muons pass $p_T > 6/5$ GeV, $|\eta| < 2.47/2.5$ respectively as well as the Medium ID working point. The x-axis labels indicate the difference with respect to the ‘default’ setup. Figure credit to Dr. Shion Chen.

Small- R Jets

Small- R jets are reconstructed using the anti- k_t algorithm with $R = 0.4$ as described in Section 3.5.1. The baseline jets must also pass $p_T > 20$ GeV and $|\eta| < 4.5$. Pileup jets are suppressed using the jet vertex tagger (JVT) at the *Medium* working point for jets with $p_T < 120$ GeV and $|\eta| < 2.5$ [124]. Forward-region pileup jets are controlled using the forward jet vertex tagger (fJVT) at the *Loose* working point for jets with $p_T < 50$ GeV and $|\eta| < 2.5$ [164]. Signal jets must pass the baseline requirement as well as $p_T > 20$ GeV and $|\eta| < 2.8$. Signal b -jets are identified using the *MV2c10* algorithm at the 85% working point (described in Section 3.5.1). Jet-based event cleaning is done at the *Loose* working point [165].

Large- R Jets

When an object decays at high boost into hadronizing children particles, the child jets will be highly collimated and appear as a single large- R jet⁸². For this reason, large- R jets are essential for boosted physics searches. Large- R jets are reconstructed using the anti- k_t algorithm with $R = 1.0$ as described in Section 3.5.1. Jet grooming to reduce soft contributions from pileup jets is done using the ‘trimming’ algorithm [166]: jet constituents are reclustered using the k_t algorithm with $R_{\text{subjet}} = 0.2$, then subjets are discarded if they carry less than $f_{\text{cut}} < 5\%$ of the original p_T^{jet} . The jet mass is reconstructed using the **four-vector** sum of the remaining constituents.

⁸²For more details, see Section 3.5.1

At high p_T , two particles in the decay chain of a large- R jet can be reconstructed as a single topological cluster due to the calorimeter cell's angular resolution. In this case, charged particles can still be separately reconstructed as inner-detector tracks. The missing angular information worsens the jet mass resolution, but the ID track information can be used to improve it [167]. First, we reconstruct a large- R **track-jet** by **ghost-association** of ID tracks to the large- R calorimeter jet [168]. Next, we calculated the “track-assisted” mass m^{TA} like so:

$$m^{\text{TA}} = m^{\text{trk}} \times \frac{p_T^{\text{calo}}}{p_T^{\text{trk}}}, \quad (5.3)$$

where m^{trk} and p_T^{trk} are the invariant mass and transverse momentum of the large- R track-jet and p_T^{calo} is the transverse momentum of the original large- R jet. The ratio $\frac{p_T^{\text{calo}}}{p_T^{\text{trk}}}$ is used to correct for charged-to-neutral fluctuations. Figure 5.13 illustrates the superior resolution of track-assisted versus calo-jet mass reconstruction for $p_T > 1.2$ TeV [167].

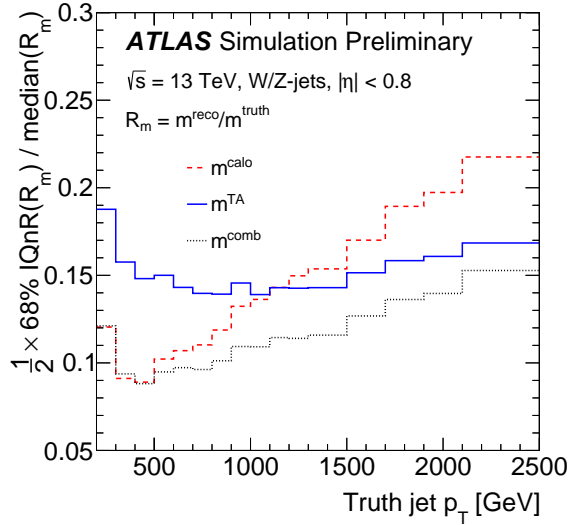


Figure 5.13: The jet mass resolution as a function of p_T^{jet} for jets produced from a boosted W boson. Three different jet mass reconstruction algorithms are displayed: the calo-jet mass (m^{calo}), the track-assisted mass (m^{TA}), and the combined TA+calo mass (m^{comb}). [167]

At low p_T , the calo-jet mass resolution has better resolution than the track-assisted mass. To provide good performance across the p_T spectrum, the two techniques are merged into a “combined” TA-plus-calo mass:

$$m^{\text{comb}} = \frac{\sigma_{\text{calo}}^{-2} m^{\text{calo}} + \sigma_{\text{TA}}^{-2} m^{\text{TA}}}{\sigma_{\text{calo}}^{-2} + \sigma_{\text{TA}}^{-2}}, \quad (5.4)$$

where σ_{calo} and σ_{TA} are the pre-estimated jet mass resolution of the calo- and TA-jet, respectively, as a function of $p_{\text{T}}^{\text{jet}}$ and η . Figure 5.13 illustrates the performance of m^{comb} across the 200 – 2500 GeV p_{T} range. Finally, $p_{\text{T}}^{\text{jet}}$ is scaled by $m^{\text{comb}}/m^{\text{calo}}$ to correct it to combined mass.

For this analysis, both baseline and signal large- R jets are required to pass $p_{\text{T}} > 200$ GeV, $|\eta| < 2$, and $m^{\text{comb}} > 40$ GeV.

b -jets associated to large- R jets (i.e. the b -jet multiplicity) are defined by [ghost-association](#) [169] of [track-jets](#) [170] by with $R = 0.2$ passing the 85% working point cut of the *MV2c10* algorithm. This narrow jet radius allows us to resolve collimated b -jets from boosted Z or h decays in signal events. Large- R jets with at least two b -tagged subjets undergo further momentum correction: the 4-momentum of the leading- p_{T} spatially-matched ($\Delta R < 0.8$) muon is added back into the jet to correct for energy lost in semileptonic b/c -decays. In simulation, we found that the leading muon has much higher momentum than any subleading muons; correcting the $p_{\text{T}}^{\text{jet}}$ for subleading muons gave little improvement to performance, so only the leading muon correction is performed for simplicity.

Missing Energy

The missing transverse momentum $\mathbf{p}_{\text{T}}^{\text{miss}}$ with magnitude $E_{\text{T}}^{\text{miss}}$ is reconstructed using the *SUSYTools* software package at the *Tight* working point [171]. $\mathbf{p}_{\text{T}}^{\text{miss}}$ is defined as the negative vector sum of the transverse momenta of all identified physics objects (electrons, photons, muons, hadronic taus, small- R jets) plus an additional soft term (constructed from all tracks associated to the primary vertex but not associated with any physics object). This allows $\mathbf{p}_{\text{T}}^{\text{miss}}$ to use the best calibration for physics objects while maintaining pileup independence in the soft term.

Overlap Removal

All baseline and signal objects undergo an overlap removal (OR) procedure to avoid double-counting objects. For example, high-energy electrons are sometimes recorded as jets, so overlap removal is needed to avoid double-counting such electrons. This procedure checks the electron, muon, and small- R jet collections for any shared inner detector tracks or overlap in ΔR ; objects overlapping or sharing tracks are removed. The OR procedure works like so:

1. Discard small- R jets that satisfy either of following (if the jet is b -tagged and $p_{\text{T}} < 250$ GeV, skip this step):
 - $\Delta R(e, j) < 0.2$

- $\Delta R(\mu, j) < 0.4$ and number of ghost-associated tracks for the jet is less than 3.

Jets passing the above criteria most likely originated from calorimeter energy deposits from electron showers or muon bremsstrahlung.

2. Discard electrons and muons within $\Delta(\ell, j) < 0.4$ of any remaining small- R jets.
3. Discard calorimeter-tagged muons sharing an ID track with an electron.
4. Discard electrons sharing an ID track with any remaining muons.

After the basic OR, an additional OR for large- R jets is performed by discarding all large- R jets within $\Delta(\ell, J) < 1.0$ of any remaining electrons.

Boson Tagging

The “boosted” signal region (described in Section 5.4) includes reconstructed large- R jets originating from $W/Z/h$ boson decays. We identify the parent boson of a large- R jet by checking that the jet mass and substructure are consistent with the expected two-body hadronic decay. This identification is available at several different working points; this analysis uses the 50% working point for its superior background rejection.

As an example, Figure 5.14a shows that the reconstructed jet masses for W jets peak around 80 GeV [172]. In addition to the jet mass, two jet substructure variables are also used to identify large- R jets originating from W/Z decays: the energy correlation ratio (D_2) and the number of tracks ghost-associated to the jet (n_{trk}). Figure 5.14b illustrates the D_2 distribution for W jets; notice that the W -jets are mostly found at low D_2 [172].

D_2 is defined using energy correlation functions, which are based on the energies and pair-wise angles of the jet sub-constituents [173, 174]:

$$D_2 = E_{\text{CF3}} \left(\frac{E_{\text{CF1}}}{E_{\text{CF2}}} \right)^3 \quad (5.5)$$

where the energy correlation functions (E_{CF}) are:

$$E_{\text{CF1}} = \sum_i p_{\text{T},i} \quad (5.6)$$

$$E_{\text{CF2}} = \sum_{ij} p_{\text{T},i} p_{\text{T},j} \Delta R_{ij} \quad (5.7)$$

$$E_{\text{CF3}} = \sum_{ijk} p_{\text{T},i} p_{\text{T},j} p_{\text{T},k} \Delta R_{ij} \Delta R_{jk} \Delta R_{ki}. \quad (5.8)$$

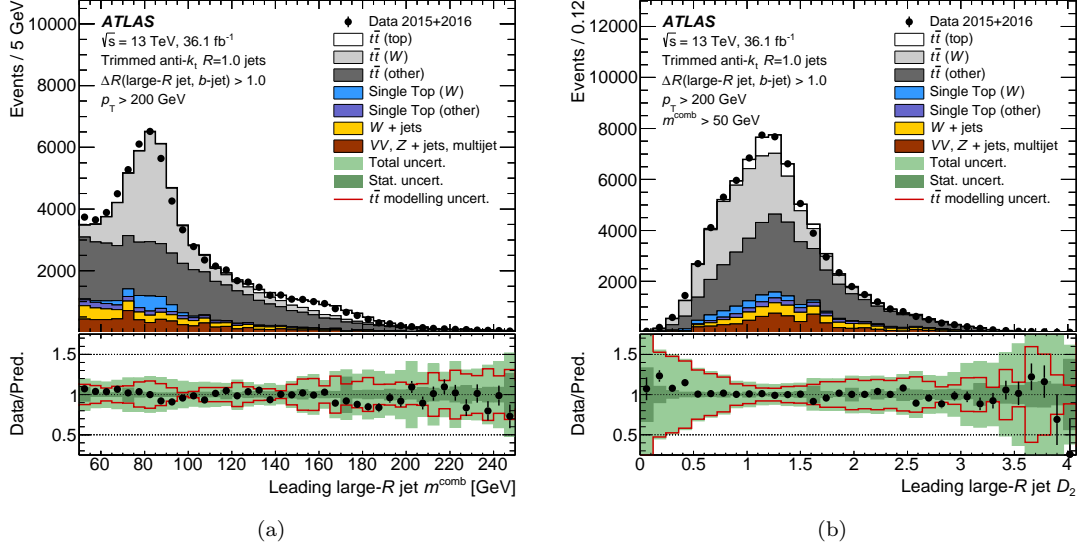


Figure 5.14: Data-MC comparison of the mass (a) and D_2 (b) of large- R jets in a $t\bar{t}$ -enriched sample containing many W bosons. [172]

D_2 can be thought of as a measure of the “3-prongness” over “2-prongness” of a jet; jets with real 2-prong substructure have low D_2 , but 1-prong (e.g. quark/gluon jets) or 3-prong (e.g. top jets) will have high D_2 .

The number of tracks ghost-associated to the jet (n_{trk}) is useful because the particle multiplicity for W/Z decays is not p_T -dependent; in contrast, the multiplicity of quark/gluon jets changes rapidly with p_T^{jet} . Adding an upper cut in n_{trk} improves discriminating power, especially for high- p_T jets.

5.4 Signal Region Definition

This section shall describe the signal region used in the “2B2Q boosted” analysis. This region definition was developed in 2019 for this analysis; for a previous 2B2Q result produced using small- R (resolved, non-boosted) jets, see Ref [146].

5.4.1 Event-Level Selection Criteria

5.4.1.1 Preselection

All events considered in this analysis must pass a trigger requirement and the boosted-region [preselection](#).

The selection starts by applying the boosted preselection described in Table 5.2. A lepton veto is required to suppress $t\bar{t}$ and other top backgrounds, $(W \rightarrow \ell\nu)+\text{jets}$, and $(Z \rightarrow \ell\ell)+\text{jets}$ backgrounds. QCD multijet background is reduced using a E_T^{miss} selection, and a $\min \Delta\phi(j, E_T^{\text{miss}})$ selection is used to reject events with large fake E_T^{miss} resulting from poorly measured jets. To suppress top-quark backgrounds (such as $t\bar{t}$ and single-top), a non-overlapping b -veto is applied. This veto checks for $R = 0.2$ track jets originating from b -quarks outside the cone of any large- R jets ($\Delta R > 0.8$). $R = 0.2$ b -track-jets inside the large- R jet cone are used in the signal definition; the non-overlapping b -veto helps reject such backgrounds. Top backgrounds (especially $t\bar{t}$) are further suppressed using a $m_{T2}^{100}(J_1, J_2)$ selection [175] [176].

The boosted preselection requirements are summarized in Table 5.2.

	Criteria	Comments
MET Trigger	✓	See Sec 5.4.1.
Event cleaning	✓	See Sec 5.4.1.
E_T^{miss}	$> 200 \text{ GeV}$	Plateau of MET trigger
$n_{\text{baseline lepton}}$	$= 0$	Veto leptonic backgrounds
$\min \Delta\phi(j, E_T^{\text{miss}})$	> 0.2	Veto QCD multi-jets
$n_{\text{Large-}R \text{ jets}}$	≥ 2	Boosted selection
$n_{b\text{-jet (outside J)}}^{\text{trk}}$	$= 0$	Veto top-related backgrounds ($t\bar{t}(+X)$, single-top)

Table 5.2: Summary of the boosted preselection. $n_{b\text{-jet (outside J)}}^{\text{trk}}$ is the number of $R = 0.2$ track b -jets outside cone of any of the large- R jets with $\Delta R > 0.8$.

5.4.1.2 Triggers

Events with offline $E_T^{\text{miss}} > 200 \text{ GeV}$ are selected using the MET triggers listed in Table 5.3. For each period, the lowest unscaled trigger is used. These triggers are $> 98\%$ efficient for $E_T^{\text{miss}} > 200 \text{ GeV}$; Figure 5.15 shows the turn-on plot for the `xe110_pufit_xe70_L1XE50` and `xe110_pufit_xe65_L1XE50` triggers in 2018 data [177].

5.4.1.3 Event Cleaning

Data events must come from luminosity blocks given in the Good Runs List. Incomplete events or data events suffering from noise bursts are removed by requiring that the liquid argon calorimeter, tile calorimeter, and semiconductor tracker all report no “errorState”. Events with badly measured jets, badly measured muons, or cosmic muons are also removed to avoid large fake MET. These objects are defined like so:

Chain name	HLT, L1 Trigger Thresholds	Unprescaled period
MET		
xe70	HLT: 70 GeV E_T	2015
xe90_mht_L1XE50	HLT: 90 GeV E_T , L1: 50 GeV E_T^{miss}	2016 A-D1
xe100_mht_L1XE50	HLT: 100 GeV E_T , L1: 50 GeV E_T^{miss}	2016 D1-F1
xe110_mht_L1XE50	HLT: 110 GeV E_T , L1: 50 GeV E_T^{miss}	2016 F2-
xe110_pufit_L1XE55	HLT: 110 GeV E_T , L1: 55 GeV E_T^{miss}	2017
xe110_pufit_xe70_L1XE50	HLT: 110 GeV E_T (two-stage), L1: 50 GeV E_T^{miss}	2018 B-C5
xe110_pufit_xe65_L1XE50	HLT: 110 GeV E_T (two-stage), L1: 50 GeV E_T^{miss}	2018 C5-

Table 5.3: Summary of included MET triggers. In the chain name, “mht” or “pufit” indicate the algorithm used for E_T^{miss} calculation in the HLT.

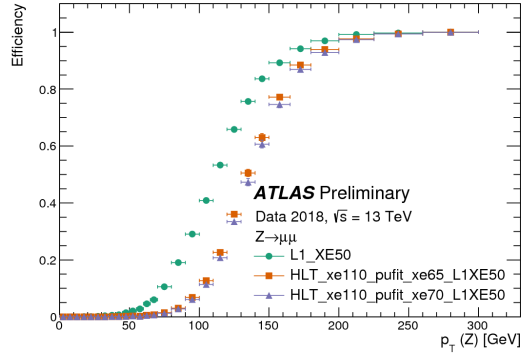


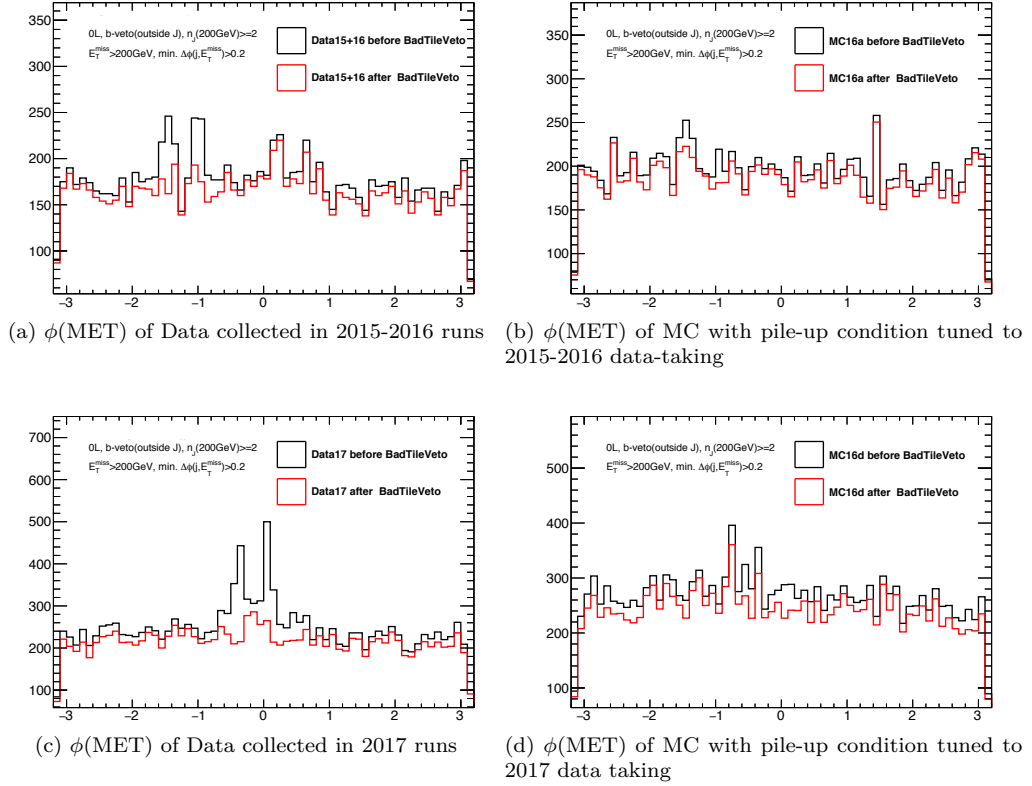
Figure 5.15: The combined L1 and HLT efficiency of the missing transverse energy trigger HLT_xe110_pufit_xe70_L1XE50 (primary chain in the beginning of 2018) and HLT_xe110_pufit_xe65_L1XE50 (primary chain since May 12th) as well as the efficiency of the corresponding L1 trigger L1_XE50 are shown as a function of the Z boson transverse momentum ($Z \rightarrow \mu\mu$ data was used to produce these plots). [177]

- Badly measured muons: $\frac{\sigma(q/p)}{q/p} > 0.2$ where q is charge, p is momentum, and $\sigma(q/p)$ is the fitting error.
- Cosmic muons: $|z_0| > 1\text{mm}$ or $d_0 > 0.2\text{mm}$.
- Badly measured jets: Defined in Ref [178].

In Run 2, the tile calorimeter suffered from dead modules; jets oriented towards these dead modules mis-measure the E_T^{miss} , so events with jets in these regions are vetoed. Table 5.4 gives the location of the dead tiles and Figures 5.16-5.17 show the difference in the E_T^{miss} distribution with and without the dead tile veto in data and MC.

Year	RunNumber	η region	ϕ region
2015	266904 - 284484	$0. < \eta < 0.9$	$0.8 < \phi < 1.0$
		$-1.6 < \eta < -0.9$	$1.9 < \phi < 2.1$
2016	302053 - 311481	$0. < \eta < 0.9$	$-1.33 < \phi < -1.13$
	306988 - 311481	$-0.9 < \eta < 0.$	$0.34 < \phi < 0.54$
2017	325713 - 340453	$-0.9 < \eta < 0.$	$-0.25 < \phi < -0.05$
		$0.8 < \eta < 1.7$	$0.14 < \phi < 0.34$
2018	350310 - 352514	$0. < \eta < 0.9$	$2.7 < \phi < -3.0$
	355261 - 364292	$0. < \eta < 0.9$	$\phi < -3.0$ or $3.0 < \phi$

Table 5.4: Location of dead tile modules over the Run2. Partially dead modules are not listed here.

Figure 5.16: $\phi(E_T^{\text{miss}})$ before (black) and after (red) applying the dead tile jet veto. The boosted preselection is applied. Figure credit to Yuta Okazaki.

5.4.1.4 Non-Collision Background Veto

An additional cleaning step is needed to reject non-collision backgrounds, i.e. events recorded when beam-induced particles interact with detector materials or residual gas in the beam pipe to create jet-like signatures [179]. These backgrounds can be seen in unusually data excesses in $\phi(E_T^{\text{miss}}) \sim [0, \pi]$

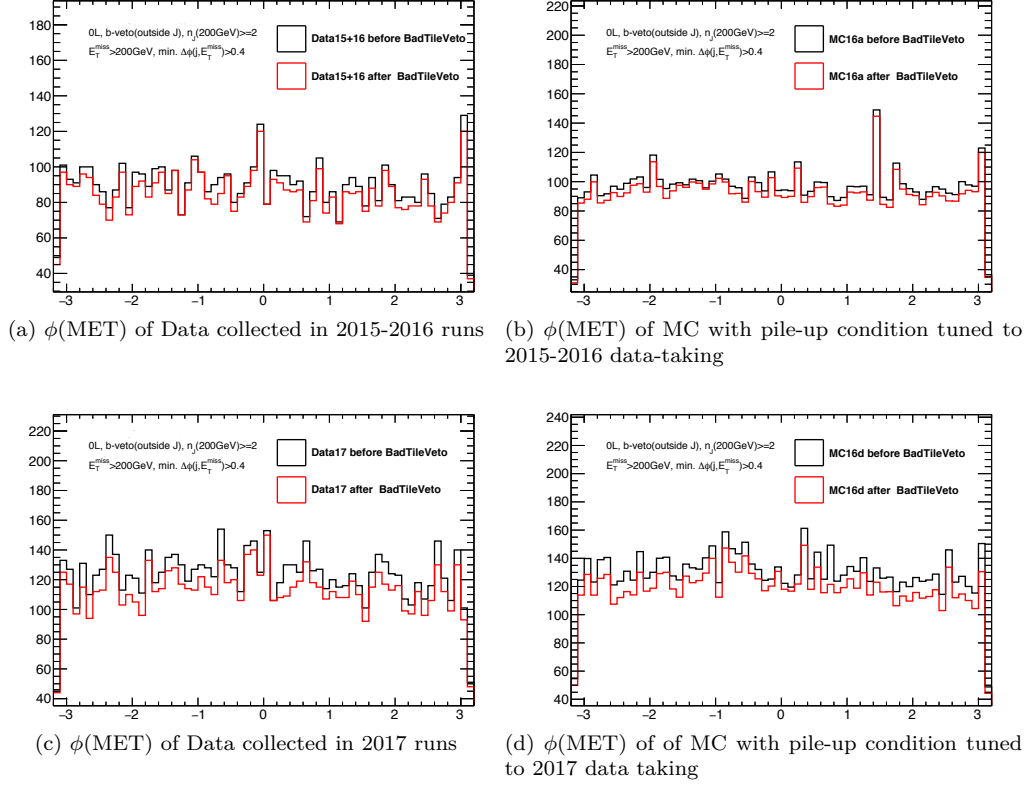


Figure 5.17: $\phi(E_T^{\text{miss}})$ before (black) and after (red) applying the dead tile jet veto. The boosted preselection with tightened $\min \Delta\phi(j, E_T^{\text{miss}})$ selection ($\min \Delta\phi(j, E_T^{\text{miss}}) > 0.4$) is applied. Figure credit to Yuta Okazaki.

or in the tails of distributions (e.g. $\min \Delta\phi(j, E_T^{\text{miss}}) > 2.9$ in Figure 5.18). Track-based MET is useful for suppressing these types of backgrounds, since the non-collision jets mostly interact with the calorimeter and leave small net track MET. Figure 5.19 shows the track-based MET and the $\Delta\phi$ between the nominal calo-based MET in the preselection region and in the non-collision-background-enhanced region ($\min \Delta\phi(j, E_T^{\text{miss}}) > 2.9$). The following selections are chosen to veto non-collision backgrounds:

- $E_{T,\text{track}}^{\text{miss}} > 75 \text{ GeV}$
- $\min \Delta R(E_T^{\text{miss}}, E_{T,\text{track}}^{\text{miss}}) < 2.0$

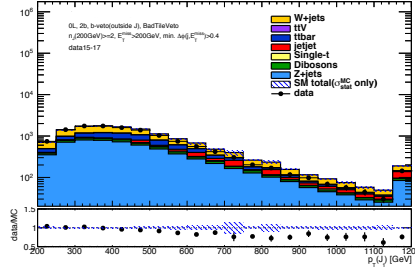
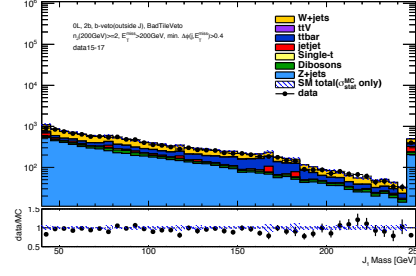
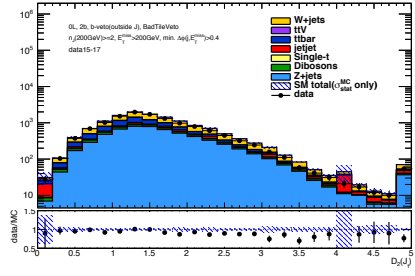
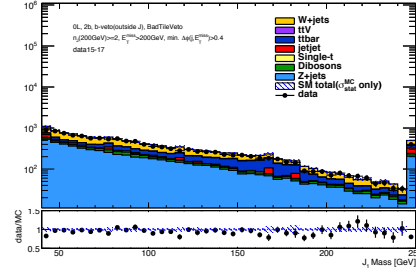
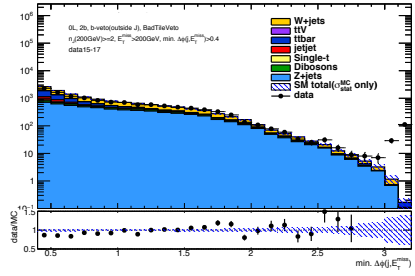
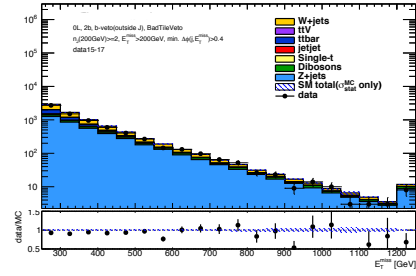
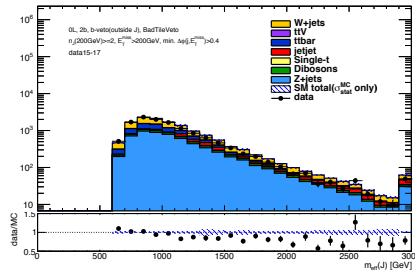
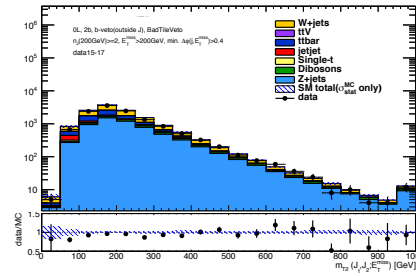
(a) leading large- R jet p_T (b) leading large- R jet mass(c) leading large- R jet D_2 (d) sub-leading large- R jet p_T (e) $\min \Delta\phi(j, E_T^{\text{miss}})$ (f) E_T^{miss} (g) $m_{\text{eff}}(J)$ (h) $m_{T2}^{100}(J_1, J_2)$

Figure 5.18: Kinematic variables between data and MC in the boosted preselection region. Figure credit to Yuta Okazaki.

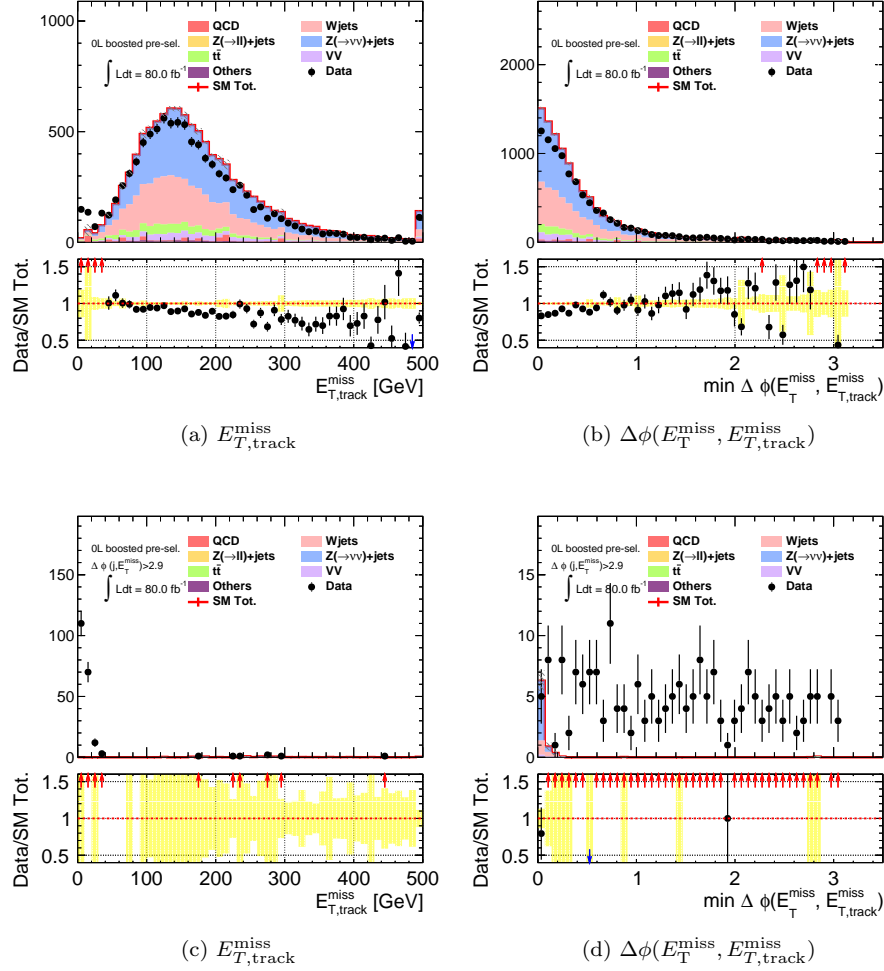


Figure 5.19: Non-collision background veto variables ($E_{T,\text{track}}^{\text{miss}}$, $\Delta\phi(E_T^{\text{miss}}, E_{T,\text{track}}^{\text{miss}})$) in (a,b) the boosted preselection region with $\min \Delta\phi(j, E_T^{\text{miss}}) > 0.4$, and (c,d) the boosted-preselection region with the $\min \Delta\phi(j, E_T^{\text{miss}}) > 2.9$, i.e. the non-collision-background-enhanced region. MC16a/d normalized to 80 fb^{-1} is used and overlaid with 2015-17 data. Figure credit to Dr. Shion Chen.

5.4.2 Discriminating Variables

In addition to the boson-tagging discriminants described in Section 5.3.1, this analysis makes use of several high-level variables. These variables are summarized in Table 5.5. Several kinematic distributions with only the preselection applied are shown in Figure 5.20.

Variable	Definition / Comments
$n_{\text{baseline lepton}}$	Number of baseline leptons after passing the overlap removal defined in Sec 5.3.1.
$n_{\text{Large-}R \text{ jets}}$	Number of large- R jets defined in Sec 5.3.1.
E_T^{miss}	Magnitude of the missing E_T vector.
$\min \Delta\phi(j, E_T^{\text{miss}})$	Minimum azimuthal angle between the E_T^{miss} vector and jets. Useful to reject processes with no real E_T^{miss} (e.g. QCD multi-jets) or with high jet multiplicity (e.g. $t\bar{t}$)
$n_{b\text{-jet}}^{\text{trk}}$ (inside J)	Number of $R = 0.2$ track b -jets ghost-associated with any of the large- R jets in the event.
$n_{b\text{-jet}}^{\text{trk}}$ (outside J)	Number of $R = 0.2$ track b -jets NOT ghost-associated with any of the large- R jets in the event.
$m(J_{1,2})$	Combined TA+calo mass of large- R jet; see section 5.3.1.
$m_{\text{eff}}(J)$	Effective mass defined by large- R jets: $m_{\text{eff}} := \sum_i p_T(J_i) + E_T^{\text{miss}}$.
$m_{T2}^{100}(J_1, J_2)$	Stransverse mass with the two leading large- R jets as the visible leg input Missing particle test mass is set to 100 GeV and the off-set is subtracted off i.e. $m_{T2}^{100}(J_1, J_2) := m_{T2}(\text{vis1} = J_1, \text{vis2} = J_2, E_T^{\text{miss}}; m_{\text{mis1}} = m_{\text{mis2}} = m_\chi) - m_\chi, m_\chi = 100 \text{ GeV}$

Table 5.5: Object multiplicity and kinematic variables used in the boosted category selection.

5.4.3 Boosted 2B2Q Signal Region

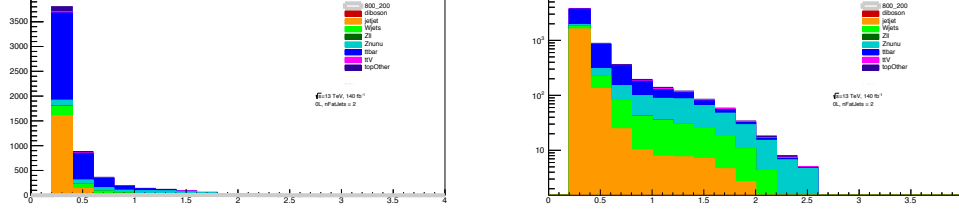
This signal region was developed using the following signal samples (described in Section 5.1):

- WZ and Wh signal: Wino-NLSP/bino-LSP signals C1N2_WZ_bbqq and C1N2_Wh_bbqq described in Fig 5.9.
- Zh signal: GGM higgsino samples with $\text{Br}(Z) = \text{Br}(h) = 50\%$.
- ZZ signal: GGM higgsino samples with $\text{Br}(Z) = 100\%$ by reweighting the $\text{Br}(Z) = \text{Br}(h) = 50\%$ samples.

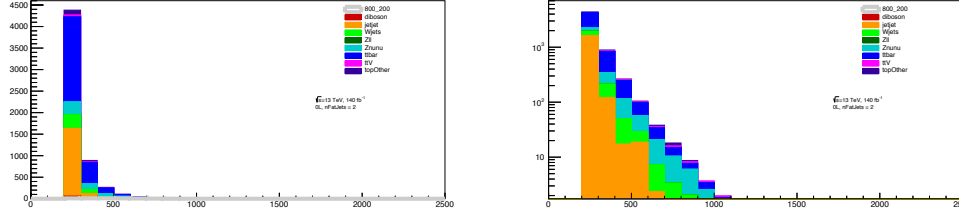
These respectively target $\tilde{\chi}_1^\pm \tilde{\chi}_2^0 \rightarrow WZ \tilde{\chi}_1^0 \tilde{\chi}_1^0$, $\tilde{\chi}_1^\pm \tilde{\chi}_2^0 \rightarrow Wh \tilde{\chi}_1^0 \tilde{\chi}_1^0$, and GGM higgsino decaying entirely to Z or with equal branching into Z and h . Signal models are required to have $\Delta M(\tilde{\chi}_1^\pm/\tilde{\chi}_2^0, \tilde{\chi}_1^0)$ at least 200 GeV; however, peak sensitivity is achieved with larger ΔM (500 GeV or greater) due to large- R jet selection effects (see Figures 5.26 and 5.27 for sensitivity estimates at various $\tilde{\chi}_1^\pm/\tilde{\chi}_2^0$ and $\tilde{\chi}_1^0$ masses).

In this **Signal Region (SR)**, one large- R jet is required to have 2 b -jets (coming from $Z/h \rightarrow b\bar{b}$ decays), while the other large- R jet must have at most 1 matched b -jet (i.e. a qq decay of W/Z)⁸³. Boson decays to b -quarks are identified by counting the number of ghost-associated $R = 0.2$ track b -jets. The $W/Z \rightarrow qq$ -candidate is then subjected to further selection; the W/Z -candidate has to pass the 3-variable-based boson-tagging 50% working point discussed in Sec 5.3.1. The Z/h -candidate has to pass a large- R jet mass-window selection: $[100, 135]$ GeV for h , $[70, 100]$ GeV for Z .

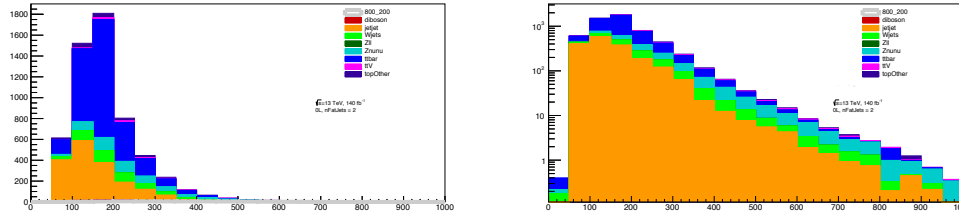
⁸³Allowing at least 1 jet tagged as a b -jet lets us recover qq decays containing a c -jet misidentified as a b -jet



(a) Preselection plot of $\min \Delta\phi(j, E_T^{\text{miss}})$, linear scale (b) Preselection plot of $\min \Delta\phi(j, E_T^{\text{miss}})$, logarithmic scale



(c) Preselection plot of E_T^{miss} , linear scale (d) Preselection plot of E_T^{miss} , logarithmic scale



(e) Preselection plot of $m_{T2}^{100}(J_1, J_2)$, linear scale (f) Preselection plot of $m_{T2}^{100}(J_1, J_2)$, logarithmic scale

Figure 5.20: Plots of various kinematics at preselection level. Linear scale at left, log scale on right.

After boson tagging the large- R jets, SM backgrounds are further suppressed using selections on $\min \Delta\phi(j, E_T^{\text{miss}})$ and $m_{T2}^{100}(J_1, J_2)$.

Before tightening the $\min \Delta\phi(j, E_T^{\text{miss}})$ and $m_{T2}^{100}(J_1, J_2)$ selections, the dominant background in this region comes from semileptonic $t\bar{t}$. $t\bar{t}$ is rejected massively by these selections because it has smaller $\min \Delta\phi(j, E_T^{\text{miss}})$, softer p_T^{jet} , and lower E_T^{miss} than the signal samples. After all selection

criteria have been applied, the dominant background in the signal region is $Z \rightarrow \nu\nu$.

The selection criteria values are optimized to the benchmark signal with a particular mass point, validating using the $N - 1$ plots (see Figures 5.22 for the SRWh optimization) and by performing a [grid search](#) in h -mass-window lower and upper edges, W -boson tagging working points, $\min \Delta\phi(j, E_T^{\text{miss}})$ values, and $m_{T2}^{100}(J_1, J_2)$ selection values. An $N - 1$ plot has all selection criteria applied except for the one being studied; this allows us to study and optimize each selection individually. The SRWZ selections is optimized for the mass point of $(\tilde{\chi}_1^\pm, \tilde{\chi}_1^0) = (700 \text{ GeV}, 100 \text{ GeV})$ in the wino-NLSP/bino-LSP `C1N2_WZ_bbqq` grid and SRWh is optimized for $(\tilde{\chi}_1^\pm, \tilde{\chi}_1^0) = (800 \text{ GeV}, 200 \text{ GeV})$ in the `C1N2_Wh_bbqq` grid. The SRZZ and SRZh selections are optimized for the GGM higgsino signal with higgsino mass $\tilde{\chi}_1^0 = 500 \text{ GeV}$ and branching ratios of $\tilde{H} \rightarrow Z\tilde{G}$ being 100% and 50% respectively.

As an example for the SRWh optimization, the selection values considered in this grid search (identified using $N - 1$ plots) are listed below, with the chosen value in bold:

- h large- R jet mass lower bound: 90, 95, **100**, 105, 110 [GeV]
- h large- R jet mass upper bound: **135**, 155 [GeV]
- W -boson large- R jet tagging working points: **50%**, 60%, 70%, and 80%
- $\min \Delta\phi(j, E_T^{\text{miss}}) > 0.6, 0.8, \mathbf{1.0}$
- $m_{T2}^{100}(J_1, J_2)$ selection values: 200, **250**, 300, 350, 400 [GeV]

Similar grid searches were done for WZ , ZZ , and Zh signal modes; in all cases, the chosen selections either gave optimal or near-optimal performance. For $Z \rightarrow b\bar{b}$ signals, the optimal large- R jet Z mass window found via grid search is [70, 100] GeV. The final sensitivity (Z_n -value) estimates are calculated using the `RooStats` [180] function `BinomialExpZ(s, b, sys)`, where s , b , and sys are the number of signal and background events and relative uncertainty on the background normalization, respectively. For this study, we assume $sys = 30\%$.

The optimized SR definition is shown in Table 5.6. The [cutflow](#) tables with signals and SM backgrounds are shown in Tables 5.7, 5.8, 5.9, and 5.10. The $N - 1$ plots are shown in Figures 5.22, 5.23, 5.24, and 5.25. The estimated Z_n -values [181] for all considered mass points for the WZ and Wh signals are shown in Figures 5.26 and 5.27. Based on the studies in Section 5.6, the wino-bino model has been reweighted to the higgsino-bino cross-section (by reweighting the signal cross-section by 0.2). Figure 5.28 shows the estimated Z_n values for a higgsino-bino signal, combining the Wh

and WZ results in quadrature. The estimated Z_n -values for the available GGM higgsino signal grid is shown in Figure 5.29, combining the Zh and ZZ results in quadrature. Figure 5.21 illustrates all the signal regions used in this analysis.

One can readily observe from the expected sensitivity plots (Fig 5.26 and 5.27) that we expect to achieve $4\text{-}5\sigma$ for several non-excluded mass points in the Wh final state. The Wh search achieves sensitivity for wino masses up to 1 TeV. The WZ sensitivity is lower due to the smaller signal cross-section and larger background contributions, especially from $Z \rightarrow \nu\nu$.

	Variable	SRWZ	SRZZ	SRWh	SRZh	SRVZ	SRVh
Boosted preselection	See Sec 5.4.1.1 and Tab 5.2						
2B2Q selection	$n_{\text{Large-}R \text{ jets}}(n_b^{\text{trk}} \leq 1)$ $n_{\text{Large-}R \text{ jets}}(n_b^{\text{trk}} = 2)$	$= 1$ ($W/Z \rightarrow qq$ -candidate) $= 1$ ($Z/h \rightarrow bb$ -candidate)					
W/Z -tag (on $W/Z \rightarrow qq$ -candidate jet) 50% WP (See Sec 5.3.1)	$n_{W \rightarrow qq}$ $n_{Z \rightarrow qq}$ $n_{W \text{ or } Z \rightarrow qq}$	$= 1$ - -	- $= 1$ -	$= 1$ - -	- $= 1$ -	- - $= 1$	- - $= 1$
Z/h -tag (on $Z/h \rightarrow bb$ -candidate jet)	m_J [GeV]	$\in [70, 100]$		$\in [100, 135]$		$\in [70, 135]$	
Further BG rejection	$\min \Delta\phi(j, E_{\text{T}}^{\text{miss}})$ $m_{\text{T}2}^{100}(J_1, J_2)$ [GeV]	> 1.0 > 250					

Table 5.6: Signal region definition for boosted 2B2Q analysis. $n_{W \rightarrow qq}$, $n_{Z \rightarrow qq}$ and $n_{W \text{ or } Z \rightarrow qq}$ are number of large- R jets passing the W -tag, Z -tag and W or Z tag, respectively. SRVZ is the logical OR of SRWZ and SRZZ, SRVh is the OR of SRWh and SRZh

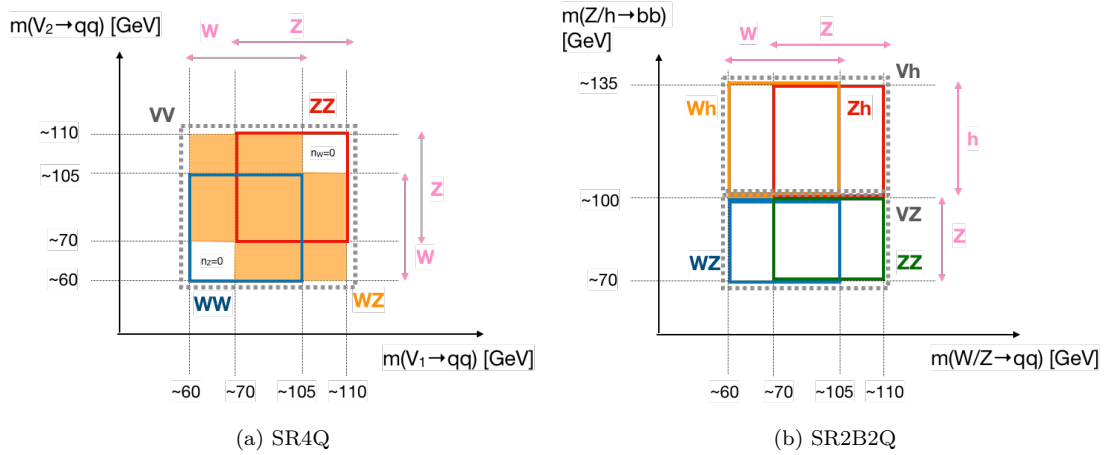


Figure 5.21: Illustration of the exclusive SRs in (a) 4Q and (b) 2B2Q category as function of reconstructed boson mass. The pink arrows represent the (approximate) mass window selection applied for reconstructed $W/Z/h$ -bosons. Overlap arises in the borders between SR bins involving $W \rightarrow qq$ and $Z \rightarrow qq$. Figure credit to Dr. Shion Chen.

	Preselection, nFatJet == 2	Preselection, nFatJet == 2 minDPhi > 1.0	Preselection, nFatJet == 2 minDPhi > 1.0 Higgs: 2 matched b-jets, 100 < FatJetMass < 135 W: 3-variable 50% eff. WP	Preselection, nFatJet == 2 minDPhi > 1.0 Higgs: 2 matched b-jets, 100 < FatJetMass < 135 W: 3-variable 50% eff. WP MT2 > 250
Signal	46.55 ± 0.93	32.96 ± 0.78	9.72 ± 0.44	8.05 ± 0.40
Total Bkg	5712.66 ± 140.08	470.30 ± 7.92	4.98 ± 0.72	1.15 ± 0.21
diboson	97.79 ± 3.09	31.70 ± 1.68	0.95 ± 0.36	0.25 ± 0.14
jetjet	1695.64 ± 138.37	0.00 ± 0.00	0.00 ± 0.00	0.00 ± 0.00
Wjets	459.78 ± 6.63	94.05 ± 3.23	0.67 ± 0.23	0.06 ± 0.05
Zll	9.84 ± 0.54	0.73 ± 0.19	0.00 ± 0.00	0.00 ± 0.00
Znununu	546.31 ± 8.82	216.66 ± 5.85	1.33 ± 0.33	0.45 ± 0.13
ttbar	2651.00 ± 16.65	89.64 ± 2.82	1.49 ± 0.46	0.16 ± 0.04
ttV	74.95 ± 1.35	22.37 ± 0.70	0.53 ± 0.10	0.23 ± 0.07
topOther	177.35 ± 8.04	15.15 ± 2.59	0.01 ± 0.01	0.00 ± 0.00

Table 5.7: Cutflow showing the cumulative effect of the SR selections on signal and bkg yields for Wh wino-bino signal (800 GeV NLSP, 200 GeV LSP). Errors shown are purely statistical.

	Preselection, nFatJet == 2	Preselection, nFatJet == 2 minDPhi > 1.0	Preselection, nFatJet == 2 minDPhi > 1.0 Z: 2 matched b-jets, 70 < FatJetMass < 100 W: 3-variable 50% eff. WP	Preselection, nFatJet == 2 minDPhi > 1.0 Z: 2 matched b-jets, 70 < FatJetMass < 100 W: 3-variable 50% eff. WP MT2 > 250
Signal	34.12 ± 1.60	26.93 ± 1.44	8.32 ± 0.82	6.22 ± 0.71
Total Bkg	5712.66 ± 140.08	470.30 ± 7.92	6.41 ± 0.92	1.81 ± 0.44
diboson	97.79 ± 3.09	31.70 ± 1.68	1.00 ± 0.27	0.11 ± 0.07
jetjet	1695.64 ± 138.37	0.00 ± 0.00	0.00 ± 0.00	0.00 ± 0.00
Wjets	459.78 ± 6.63	94.05 ± 3.23	1.16 ± 0.49	0.24 ± 0.21
Zll	9.84 ± 0.54	0.73 ± 0.19	0.00 ± 0.00	0.00 ± 0.00
Znununu	546.31 ± 8.82	216.66 ± 5.85	2.48 ± 0.60	0.91 ± 0.33
ttbar	2651.00 ± 16.65	89.64 ± 2.82	1.15 ± 0.27	0.39 ± 0.19
ttV	74.95 ± 1.35	22.37 ± 0.70	0.25 ± 0.08	0.16 ± 0.05
topOther	177.35 ± 8.04	15.15 ± 2.59	0.37 ± 0.30	0.00 ± 0.00

Table 5.8: Cutflow showing the cumulative effect of the SR selections on signal and bkg yields for WZ wino-bino signal (700 GeV NLSP, 100 GeV LSP). Errors shown are purely statistical.

	Preselection, nFatJet == 2	Preselection, nFatJet == 2 minDPhi > 1.0	Preselection, nFatJet == 2 minDPhi > 1.0 Higgs: 2 matched b-jets, 100 < FatJetMass < 135 Z: 3-variable 50% eff. WP	Preselection, nFatJet == 2 minDPhi > 1.0 Higgs: 2 matched b-jets, 100 < FatJetMass < 135 Z: 3-variable 50% eff. WP MT2 > 250
Signal	140.98 ± 4.00	90.24 ± 3.21	17.52 ± 1.46	9.65 ± 1.07
Total Bkg	5712.66 ± 140.08	470.30 ± 7.92	4.24 ± 0.68	0.95 ± 0.18
diboson	97.79 ± 3.09	31.70 ± 1.68	0.63 ± 0.33	0.07 ± 0.06
jetjet	1695.64 ± 138.37	0.00 ± 0.00	0.00 ± 0.00	0.00 ± 0.00
Wjets	459.78 ± 6.63	94.05 ± 3.23	0.59 ± 0.22	0.01 ± 0.01
Zll	9.84 ± 0.54	0.73 ± 0.19	0.00 ± 0.00	0.00 ± 0.00
Znununu	546.31 ± 8.82	216.66 ± 5.85	1.18 ± 0.30	0.55 ± 0.15
ttbar	2651.00 ± 16.65	89.64 ± 2.82	1.41 ± 0.46	0.13 ± 0.04
ttV	74.95 ± 1.35	22.37 ± 0.70	0.42 ± 0.09	0.19 ± 0.06
topOther	177.35 ± 8.04	15.15 ± 2.59	0.01 ± 0.01	0.00 ± 0.00

Table 5.9: Cutflow showing the cumulative effect of the SR selections on signal and bkg yields for Zh GGM higgsino signal (500 GeV NLSP, 0 GeV LSP). Errors shown are purely statistical.

5.5 Overview of Backgrounds

The SM backgrounds considered in this analysis are dibosons, QCD dijet, W/Z boson with jets, and top backgrounds ($t\bar{t}$, ttV , and single top). Section 5.2.3.1 provides details about how these backgrounds are generated.

After applying the boosted 2B2Q signal region selection criteria, the SM background is dominated by $Z \rightarrow \nu\nu$, followed by $t\bar{t}$ and diboson. The relative composition differs for each decay mode (WZ , Wh , ZZ , and Zh). $Z \rightarrow \nu\nu$ contributions arise when there are 4 [Initial-State Radiation](#)

	Preselection, nFatJet == 2	Preselection, nFatJet == 2 minDPhi > 1.0	Preselection, nFatJet == 2 minDPhi > 1.0 $Z \rightarrow b\bar{b}$: 2 matched b-jets, 70 < FatJetMass < 100 $Z \rightarrow q\bar{q}$: 3-variable 50% eff. WP	Preselection, nFatJet == 2 minDPhi > 1.0 $Z \rightarrow b\bar{b}$: 2 matched b-jets, 70 < FatJetMass < 100 $Z \rightarrow q\bar{q}$: 3-variable 50% eff. WP MT2 > 250
Signal	95.59 ± 5.27	64.57 ± 4.34	18.85 ± 2.44	9.38 ± 1.67
Total Bkg	5712.66 ± 140.08	470.30 ± 7.92	7.47 ± 1.34	1.93 ± 0.48
diboson	97.79 ± 3.09	31.70 ± 1.68	1.28 ± 0.39	0.48 ± 0.25
jetjet	1695.64 ± 138.37	0.00 ± 0.00	0.00 ± 0.00	0.00 ± 0.00
Wjets	459.78 ± 6.63	94.05 ± 3.23	1.04 ± 0.47	0.05 ± 0.17
Zll	9.84 ± 0.54	0.73 ± 0.19	0.00 ± 0.00	0.00 ± 0.00
Znnu	546.31 ± 8.82	216.66 ± 5.85	3.27 ± 1.10	0.99 ± 0.34
ttbar	2651.00 ± 16.65	89.64 ± 2.82	1.20 ± 0.34	0.25 ± 0.14
ttV	74.95 ± 1.35	22.37 ± 0.70	0.30 ± 0.08	0.16 ± 0.06
topOther	177.35 ± 8.04	15.15 ± 2.59	0.38 ± 0.30	0.00 ± 0.00

Table 5.10: Cutflow showing the cumulative effect of the SR selections on signal and bkg yields for ZZ GGM higgsino signal (500 GeV NLSP, 0 GeV LSP). Errors shown are purely statistical.

(ISR) jets, two of which are b -quark-initiated⁸⁴. The subleading backgrounds ($t\bar{t} \rightarrow b\bar{\ell}\nu_{\ell}bq\bar{q}$ and $VZ \rightarrow qq\nu\nu, \ell\nu qq$) enter into the sample due to the presence of a real $W \rightarrow qq$ large- R jet and a $b\bar{b}$ -tagged large- R jet which just happens to pass the mass-window criteria.

Although we can model our backgrounds purely using MC, it is preferable to use a data-driven background estimation method to get a more accurate estimate. Our signal region is in an extreme part of phase space and we are not confident that MC predicts all higher-order effects in this region well. For example, ISR jets are required for some of our SM backgrounds to enter the signal region, but we are not certain that the amount of ISR is well-predicted in MC. Figure 5.18 shows the ratios (at bottom) between data and MC for various kinematic variables in the preselection region. In some of these ratio plots, a clear slope can be seen, indicating that MC shows some bias as compared to data. Using a data-driven method allows us to predict our background yields without relying entirely on the MC. Additionally, our data-driven method of background estimation does *not* need to be very precise. We typically expect 1 background event in our signal region; the statistical uncertainty on 1 event is 100%. Therefore, our goal is to achieve a data-driven background estimate with less than 100% uncertainty. Although we could continue to work on MC-only background estimation, a data-driven estimate should have less theoretical uncertainty and allow us to steadily evaluate our statistical uncertainties.

5.5.1 Background Estimation

This section shall present the ABCD method of background estimation. The study results listed here are based entirely in MC; the actual estimate shall be data-driven. This method has been used in ATLAS analyses for years; for other examples, see [182] and [183].

At a basic level, the ABCD method proceeds like so (illustrated in Figure 5.30):

⁸⁴Or possible c -quark initiated, with the c -jets misidentified as b -jets

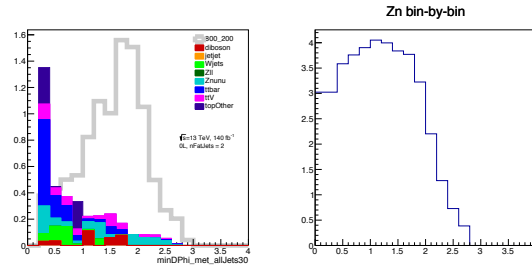
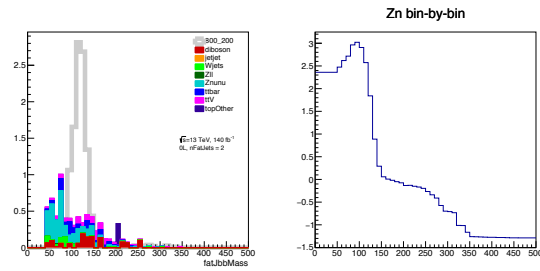
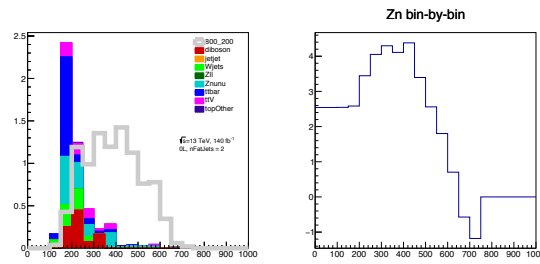
(a) $N-1$ plot of $\min \Delta\phi(j, E_T^{\text{miss}})$ (b) $N-1$ plot of $2b\text{-Large-}R \text{ Jet Mass}$ (c) $N-1$ plot of $m_{T2}^{100}(J_1, J_2)$

Figure 5.22: $N-1$ plots for 2B2Q boosted Wh SR. Wino-bino signal mass point (800 GeV NLSP, 200 GeV LSP) shown in grey. The plots on the right show the Z_n sensitivity as a function of selection criteria value.

- First, identify two independent analysis variables (or two variables with very well-understood correlations)

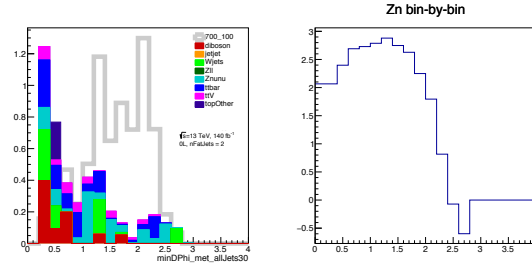
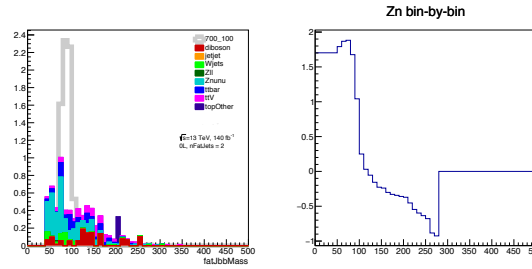
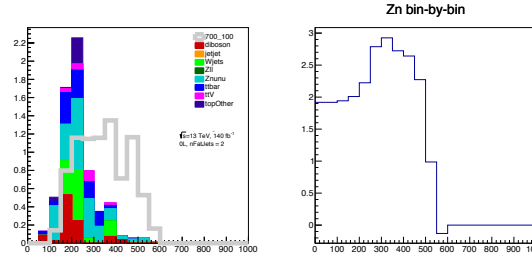
(a) $N - 1$ plot of $\min \Delta\phi(j, E_T^{\text{miss}})$ (b) $N - 1$ plot of $2b\text{-Large-}R \text{ Jet Mass}$ (c) $N - 1$ plot of $m_{T2}^{100}(J_1, J_2)$

Figure 5.23: $N - 1$ plots for 2B2Q boosted WZ SR. Wino-bino signal mass point (700 GeV NLSP, 100 GeV LSP) shown in grey. The plots on the right show the Z_n sensitivity as a function of selection criteria value.

- Using these two variables, create four exclusive regions in the two-dimensional plane. Label these regions as A, B, C, and D. Typically, region D should be identical to the signal region in the analysis.

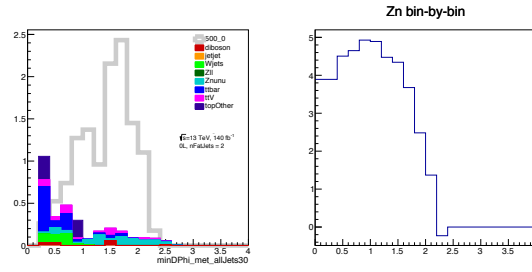
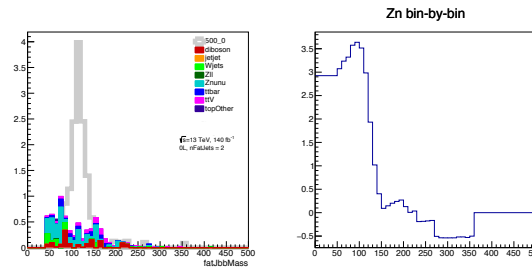
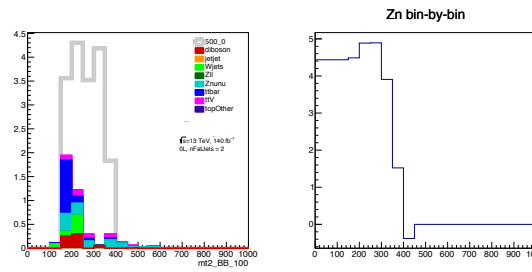
(a) $N-1$ plot of $\min \Delta\phi(j, E_T^{\text{miss}})$ (b) $N-1$ plot of $2b\text{-Large-}R \text{ Jet Mass}$ (c) $N-1$ plot of $m_{T2}^{100}(J_1, J_2)$

Figure 5.24: $N-1$ plots for 2B2Q boosted Zh SR. GGM higgsino signal mass point (500 GeV NLSP, 0 GeV LSP) shown in grey. The plots on the right show the Z_n sensitivity as a function of selection criteria value.

- If the axis variables are indeed independent, then $\frac{A}{D} = \frac{B}{C}$, where A , B , C , and D are the data yields in each respective region. This property allows one to estimate the background yield in region D (i.e. the signal region) using the yields in regions A, B, and C.

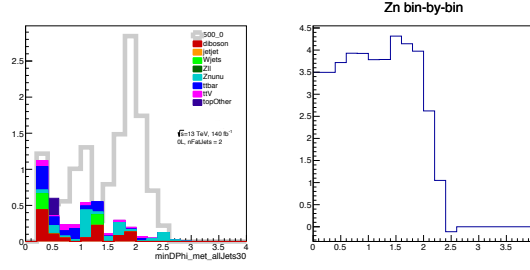
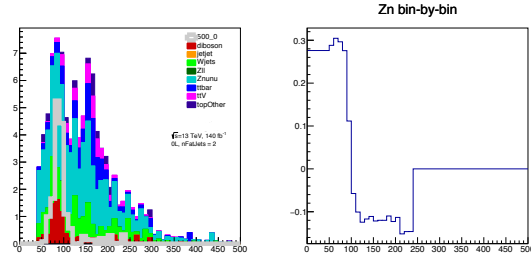
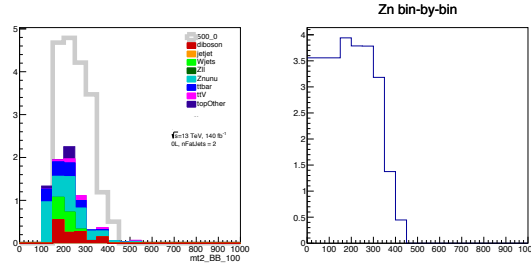
(a) $N-1$ plot of $\min \Delta\phi(j, E_T^{\text{miss}})$ (b) $N-1$ plot of $2b\text{-Large-}R \text{ Jet Mass}$ (c) $N-1$ plot of $m_{T2}^{100}(J_1, J_2)$

Figure 5.25: $N-1$ plots for 2B2Q boosted ZZ SR. GGM higgsino signal mass point (500 GeV NLSP, 0 GeV LSP) shown in grey. The plots on the right show the Z_n sensitivity as a function of selection criteria value.

For this method to produce a valid background estimate, three major conditions must be met. First, there must exist two independent analysis variables. Second, there must be sufficient data statistics in regions A, B, and C to provide an estimate in region D (if the statistics are too low,

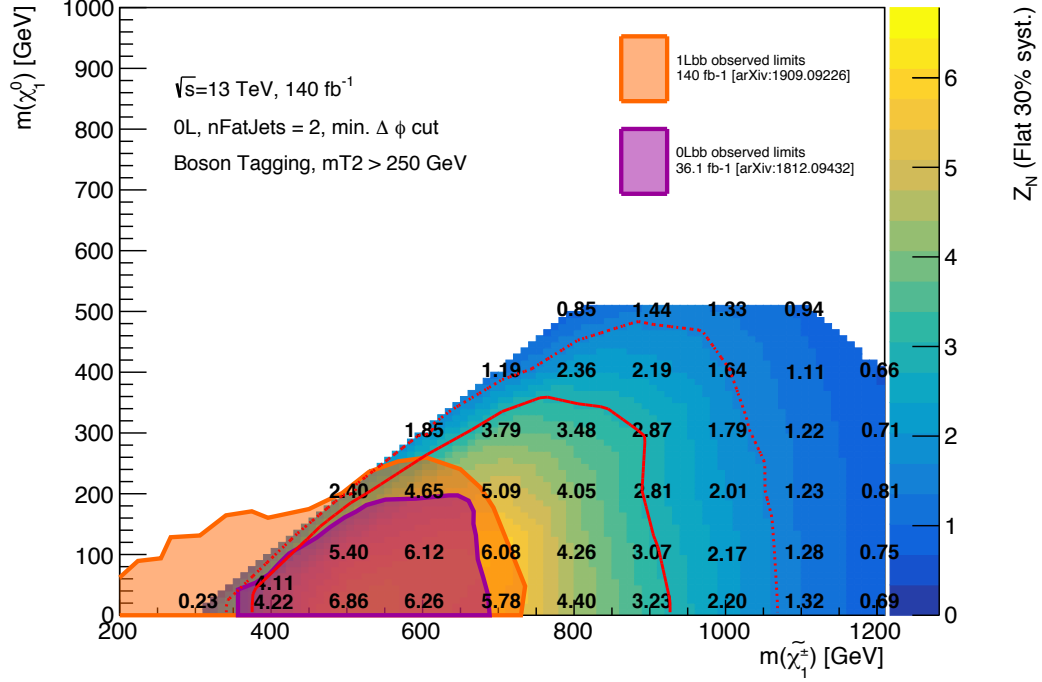


Figure 5.26: The expected sensitivity for Wh wino-bino signal search. Signal and background yields are estimated from simulation. Points inside the solid red curve have at least 3σ sensitivity, and points inside the dashed red curve have at least $Z_N = 1.64$ (exclusion). Previously observed limits are shown in purple.

the estimate will have a high degree of uncertainty). Finally, the expected signal contamination in regions A, B, and C (the non-signal-regions) must be sufficiently small; if the signal contamination is very large, then the predicted background yield will differ dramatically for a discovery result versus an exclusion. These problems are tied together; the choice of axis variables and region boundaries will determine the data statistics available and signal contamination in each region.

To ensure that region D is identical to the SR, we must apply a total of three cuts:

- $m_{T2}^{100}(J_1, J_2) > 250$
- One fat jet passes a H/Z mass window cut while the other passes a 3-variable-based W/Z boson-tagging 50% working point cut
- $\min \Delta\phi(j, E_T^{\text{miss}}) > 1.0$

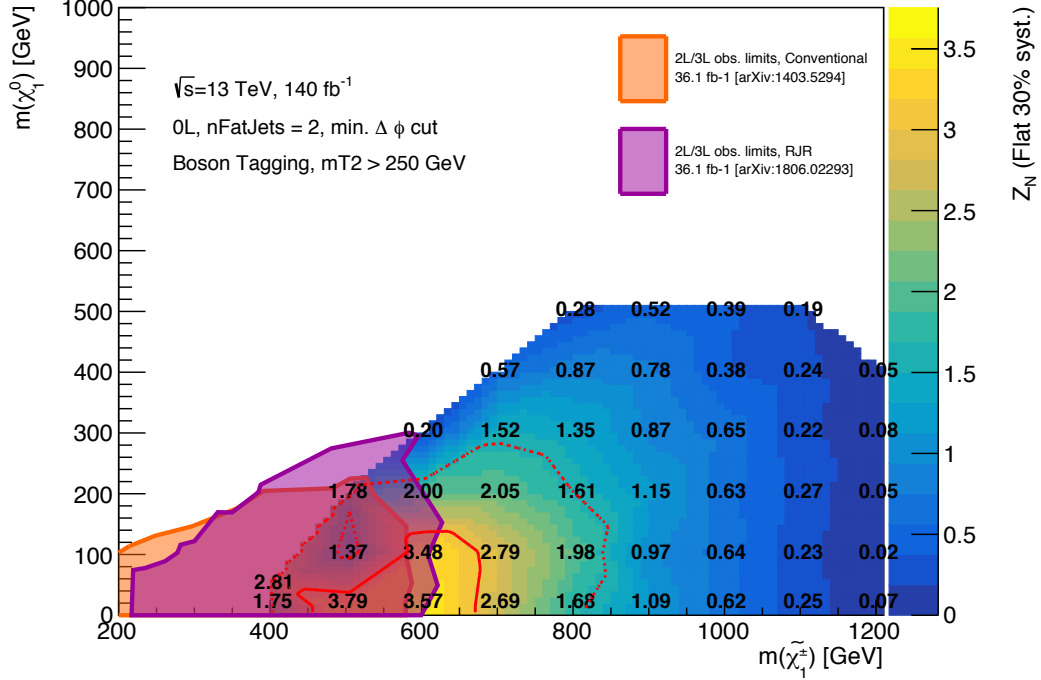


Figure 5.27: The expected sensitivity for WZ wino-bino signal search. Signal and background yields are estimated from simulation. Points inside the solid red curve have at least 5σ sensitivity, and points inside the dashed red curve have at least $Z_N = 1.64$ (exclusion). Previously observed limits are shown in purple and orange.

Based on these requirements, the x-axis for ABCD is $m_{T2}^{100}(J_1, J_2)$ and the y-axis is the 3-variable-based boson-tagging cut (where the other fat jet passes the H/Z mass window cut). We expect these two axis variables to be uncorrelated, as jet substructure and event-level kinematics are generally uncorrelated. The $200 - 250 m_{T2}^{100}(J_1, J_2)$ region is excluded from this analysis because it contains high signal contamination; it is not useful in the 2B2Q SR, and including it in regions A and C contaminates those regions with a large amount of signal. Outside of the cuts defined by these axis, we also require a $\min \Delta\phi(j, E_T^{\text{miss}})$ cut. If the default $\min \Delta\phi(j, E_T^{\text{miss}}) > 1.0$ SR cut is used in regions A, B, and C, then the background yield is massively reduced. Therefore, the $\min \Delta\phi(j, E_T^{\text{miss}})$ cut is loosened/alterd in the non-SR regions along each axis. For the low- $m_{T2}^{100}(J_1, J_2)$ region, the $\min \Delta\phi(j, E_T^{\text{miss}})$ is loosened from 1.0 to 0.6 to provide sufficient statistics in region C. For the failed- W/Z boson-tagging region, an upper cut on $\min \Delta\phi(j, E_T^{\text{miss}})$ is applied to reduce signal contamination in region B. These results were checked carefully to ensure that the altered

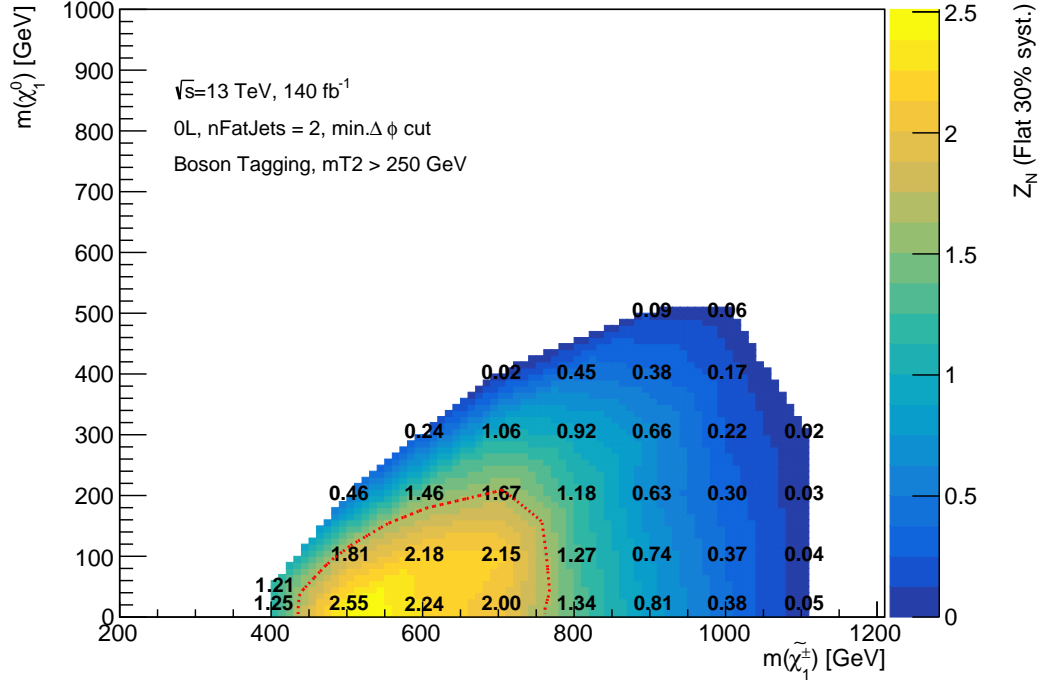


Figure 5.28: The expected sensitivity for $Wh + WZ$ higgsino-bino signal search. Signal and background yields are estimated from simulation. Points inside the solid red curve have at least 3σ sensitivity, and points inside the dashed red curve have at least $Z_N = 1.64$ (exclusion). Previously observed limits are shown in purple.

$\min \Delta\phi(j, E_T^{\text{miss}})$ cut in regions A, B, and C do not bias the results in D; no such bias was found and plots summarizing these results can be found in Appendix A.4. The axes choices and region definitions (with $\min \Delta\phi(j, E_T^{\text{miss}})$ cut definitions) are summarized in Figure 5.31.

5.5.1.1 ABCD Results

As of writing, this analysis has not been [unblinded](#) (unblinding approved December 2019, expected January 2020); thus the results presented here are estimated from MC only.

Figures 5.32, 5.33, 5.34, and 5.35 present the basic result for ABCD background estimation for Wh , WZ , Zh , and ZZ signal regions, respectively. Each figure is divided into four sections:

- Upper left: the ABCD background yields for regions A, B, C, and D with the ratio $R1 = \frac{A \times D}{B \times C}$, $1/R1$, and predicted and actual yields for D

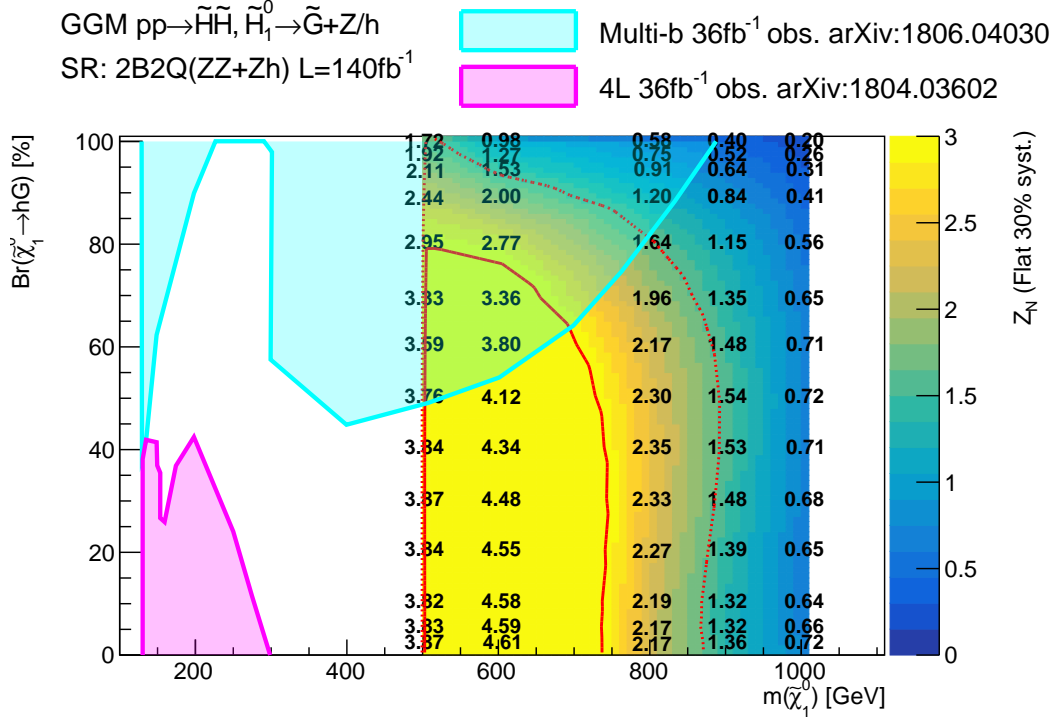


Figure 5.29: The expected sensitivity for the $Zh + ZZ$ GGM higgsino signal search as a function of gravitino mass (x-axis) versus branching ratio to the SM higgs (y-axis). Signal and background yields are estimated from simulation. Points inside the solid red curve have at least 5σ sensitivity, and points inside the dashed red curve have at least $ZN = 1.64$ (exclusion). Previously observed limits are shown in purple and teal.

- Upper right: the background composition of regions A, B, C, and D as pie charts
- Lower left: a check of the independence of regions $A + B$ from $C + D$ in x-axis variable $m_{T2}^{100}(J_1, J_2)$
- Lower right: a check of the independence of regions $A + C$ from $B + D$ in y-axis boson-cut variable.

By looking at the ratio plots in the bottom section of these results, one can see that the two axes are generally uncorrelated, with the best results achieved for the Wh and Zh signal regions. We can check the ABCD closure with the R1 ratio shown in the lower section of the ABCD plot

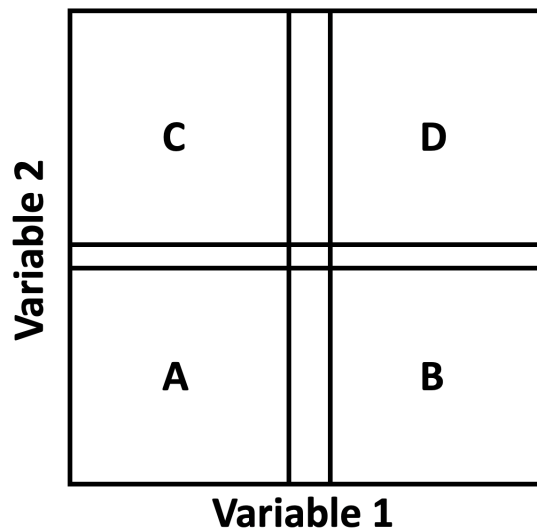


Figure 5.30: An image to illustrate the basics of the ABCD method

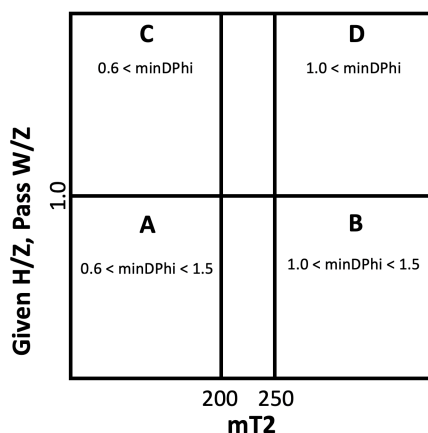


Figure 5.31: A summary of the cuts used in each ABCD region

at the upper left; once again, the best closure is achieved for Wh and WZ signal regions. The MC statistical error on these closure results is fairly high due to limited statistics (especially in $Z \rightarrow \nu\nu$ samples).

After unblinding, we will need to calculate the systematic uncertainty on this estimation. One source of uncertainty comes from signal contamination, described below. Beyond this, we must also consider the data statistics in regions A , B , and C , uncertainties related to non-closure (especially in WZ and ZZ signal regions), and the relative uncertainty on background composition (e.g.

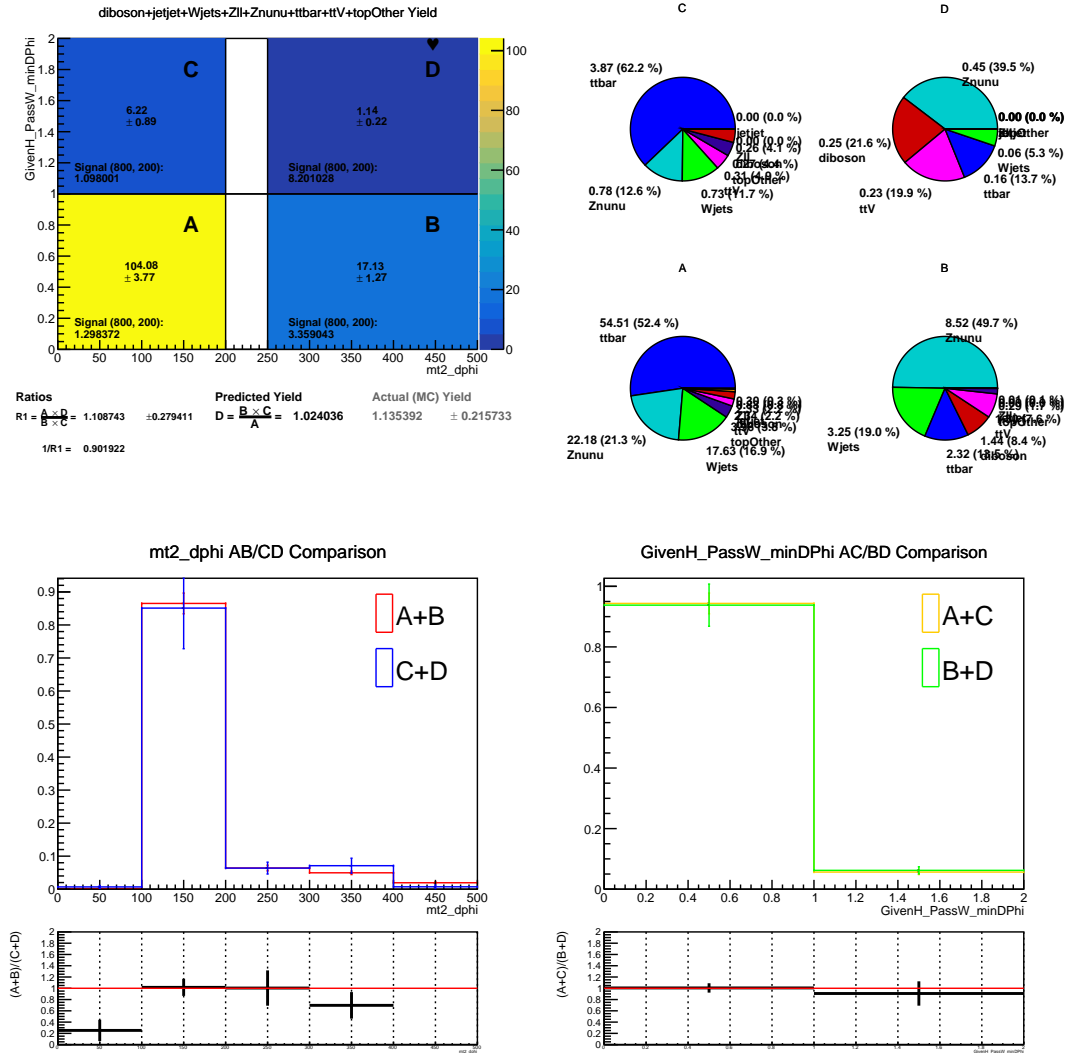


Figure 5.32: Basic ABCD results for Wh signal. Upper left: ABCD background yields. Upper right: background composition in regions A, B, C, D as piecharts. Lower left: checking the independence in $m_{T2}^{100}(J_1, J_2)$. Lower right: checking the independence in boson-cut variable.

how would the predicted background yield change if the relative composition of the MC-predicted backgrounds is altered). These studies shall be pursued by Joe Mullin after my graduation; I have provided him with a robust C++ library for ABCD methods.

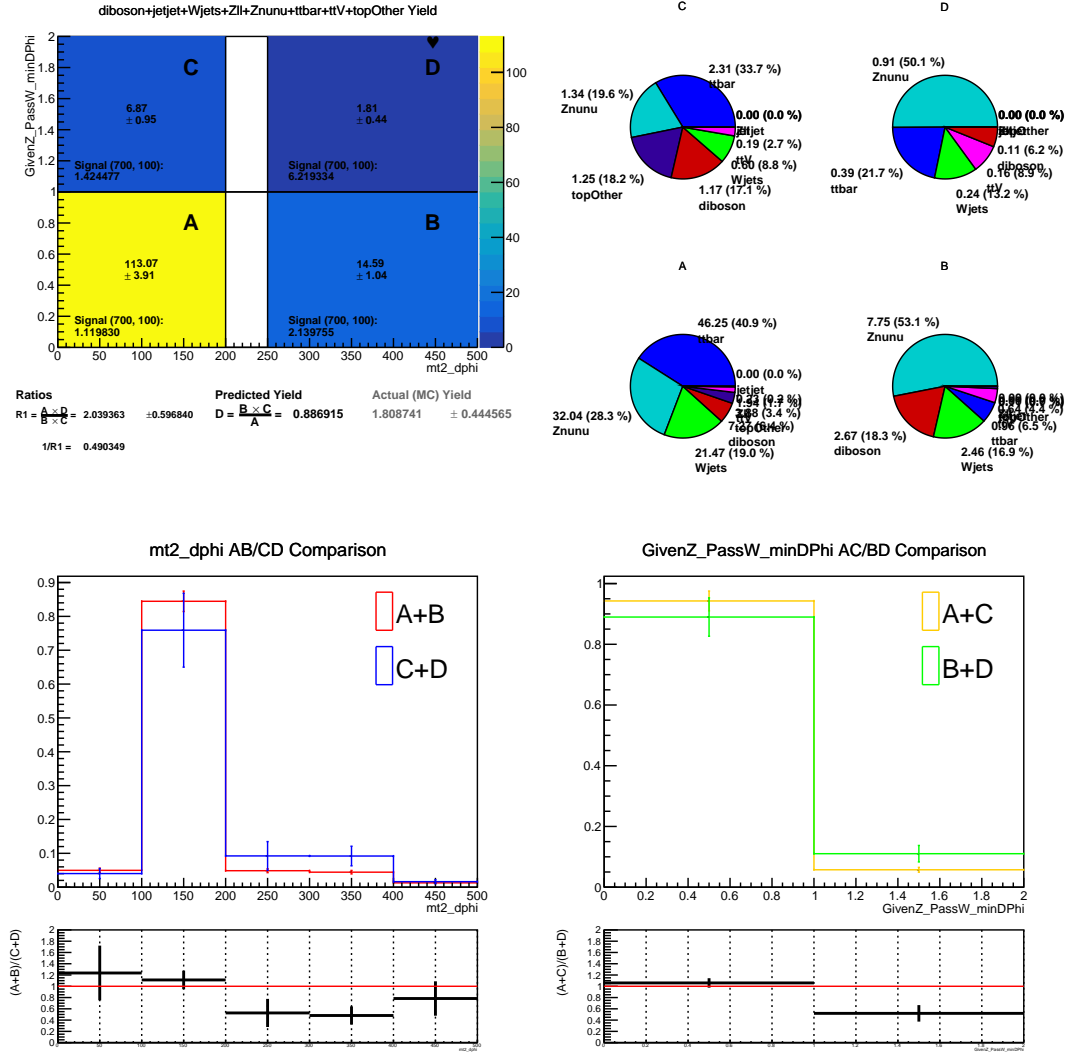


Figure 5.33: Basic ABCD results for WZ signal. Upper left: ABCD background yields. Upper right: background composition in regions A, B, C, D as piecharts. Lower left: checking the independence in $m_{T2}^{100}(J_1, J_2)$. Lower right: checking the independence in boson-cut variable.

5.5.1.2 Signal Contamination in non-SR Regions

When making an ABCD background estimate, it is important to consider the amount of potential signal contamination in the non-SR regions. Figures 5.36 (Wh) and 5.37 (WZ) show the amount of signal contamination in regions A, B, and C as a percentage of the total background yield (i.e. an entry of 100 means that the signal and background yields are identical). Results are shown for Wh and WZ only because full signal grids are not yet available for Zh and ZZ . One can readily observe

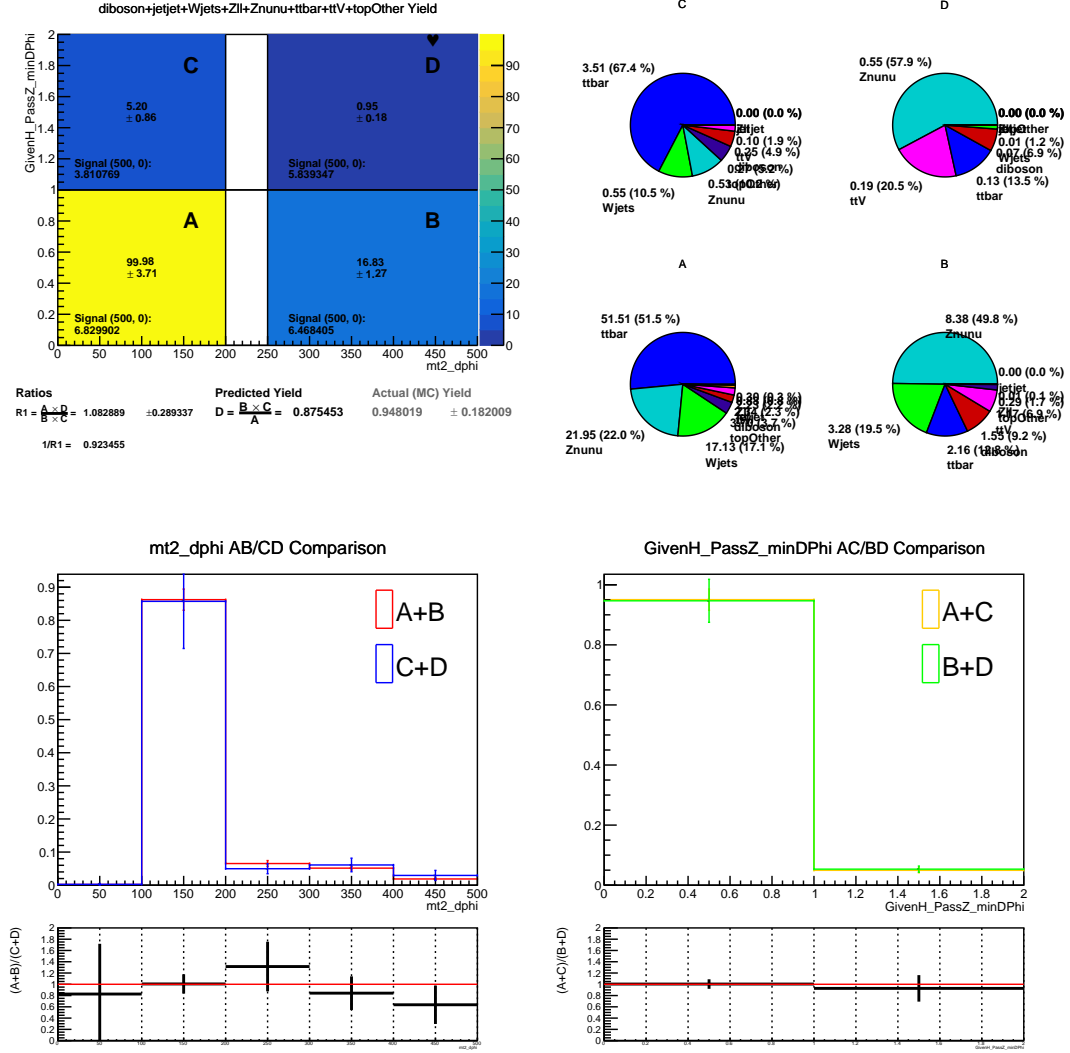


Figure 5.34: Basic ABCD results for Zh signal. Upper left: ABCD background yields. Upper right: background composition in regions A, B, C, D as piecharts. Lower left: checking the independence in $m_{T2}^{100}(J_1, J_2)$. Lower right: checking the independence in boson-cut variable.

that the high-contamination regions are excluded already. In region A, contamination remains low everywhere due to high background yields in this region. In region B, contamination increases for mass splittings between 500 – 800 GeV; larger mass splittings have better signal/bkg discrimination, and smaller splittings have less contamination. Region C is most contaminated for small mass splittings; one can observe that the contamination increases towards the left and diagonal regions of the plot.

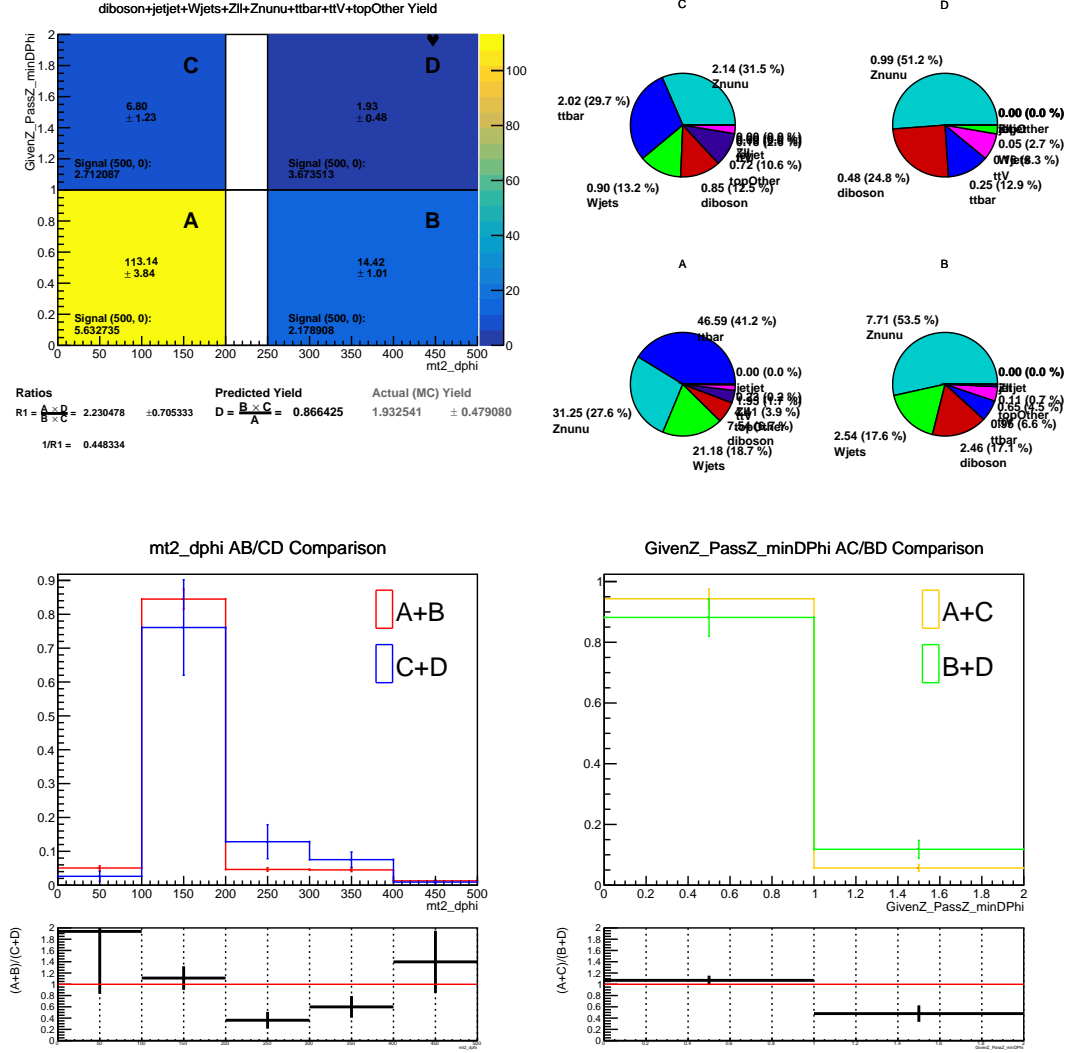


Figure 5.35: Basic ABCD results for ZZ signal. Upper left: ABCD background yields. Upper right: background composition in regions A, B, C, D as piecharts. Lower left: checking the independence in $m_{T2}^{100}(J_1, J_2)$. Lower right: checking the independence in boson-cut variable.

Because the presence of signal in regions A, B, and C can change the expected yields in those regions, it can also change the calculated background yield in the signal region, region D. Recall that we estimate the yield in region D using the regions in A, B, and C: $D = \frac{B \times C}{A}$; if the yields in these regions are larger due to signal contamination (especially in B and C, where signal contamination is a large percentage of total background), then the estimated background yield in region D will be larger as well. Call our estimate of background yield in D without signal contamination $D_{uncontam}$

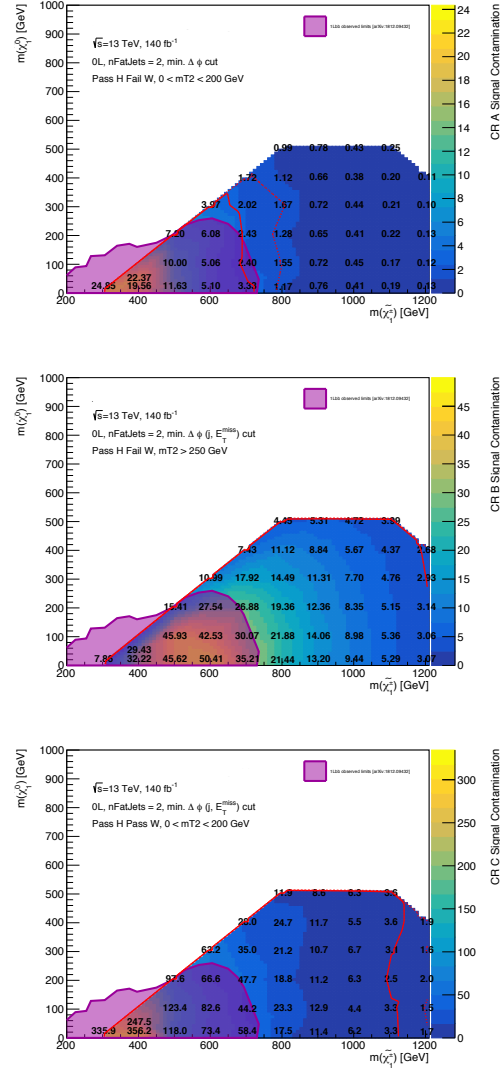


Figure 5.36: Signal Contamination as a percentage of background yield in Wh ABCD non-SR Regions. Region A on top, B in center, C on the bottom. Previously excluded points are contained within the purple curve.

and our estimate with signal contamination D_{contam} . We estimate the bias due to possible signal presence in non-SR regions as a percentage: $100 \times \frac{D_{contam} - D_{uncontam}}{D_{uncontam}}$. This is plotted in Figure 5.38 (Wh) and 5.39 (WZ). In general, the bias increases for smaller mass splittings and lower- p_T signals; this matches our expectation, since regions B and C suffer from greater signal contamination in these regions. The effect due to signal contamination is typically below 30-40%, although some special cases (e.g. low mass or small mass splittings) lead to much larger contaminations ($> 70\%$).

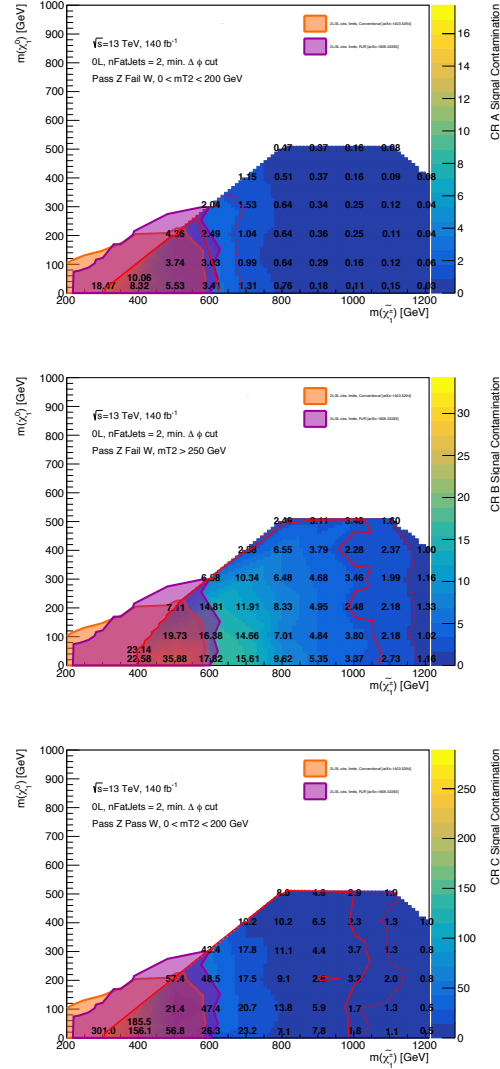


Figure 5.37: Signal Contamination as a percentage of background yield in WZ ABCD non-SR Regions. Region A on top, B in center, C on the bottom. Previously excluded points are contained within the orange and purple curves.

As mentioned previously, the total systematic uncertainty on the background estimate from the ABCD method must be less than 100%. The typical signal contamination bias is acceptable, and the atypical is barely tolerable. This bias estimate will be applied as a systematic uncertainty for each signal point.

5.6 Higgsino Reinterpretation Studies

This section presents the results of a study comparing (\tilde{W}, \tilde{B}) models to (\tilde{H}, \tilde{B}) models. We expect these models to have similar kinematic distributions (since the wino and higgsino produce similar mass eigenstates); this expectation is confirmed in the results of this study.

The wino produces two mass eigenstates: $\tilde{\chi}_1^\pm$ or $\tilde{\chi}_2^0$. The higgsino produces these two and an additional third mass eigenstate: $\tilde{\chi}_3^0$. Pair-production of winos results in two possible states: $\tilde{\chi}_1^\pm \tilde{\chi}_1^\mp$ or $\tilde{\chi}_1^\pm \tilde{\chi}_2^0$. Higgsino pair-production results in these plus two additional states: $\tilde{\chi}_1^\pm \tilde{\chi}_3^0$ (which should be nearly identical to $\tilde{\chi}_1^\pm \tilde{\chi}_2^0$ if the mass difference between eigenstates is small) and $\tilde{\chi}_2^0 \tilde{\chi}_3^0$. Therefore, the most important state found in the higgsino model which does **not** exist in the wino model is $\tilde{\chi}_2^0 \tilde{\chi}_3^0$ (which also has the smallest cross-section of all the possible states). Therefore, this study will focus on the $\tilde{\chi}_1^\pm \tilde{\chi}_1^\pm$ and $\tilde{\chi}_1^\pm \tilde{\chi}_2^0 / \tilde{\chi}_3^0$ final states shared between the two models.

Wino signal sample production is described in Section 5.1. For comparison studies, higgsino samples were produced privately (job options found [here](#)). Higgsino saqmples were generated in the same way as the wino samples except the input neutralino mixing matrix is set so that $\tilde{\chi}_1^0$ is bino-like and $\tilde{\chi}_2^0 / \tilde{\chi}_3^0$ is higgsino-like. This study focuses on two signal grid points with different mass splittings: $(\tilde{\chi}_{\text{heavy}}, \tilde{\chi}_{\text{light}}) = (800 \text{ GeV}, 0 \text{ GeV})$ and $(600 \text{ GeV}, 200 \text{ GeV})$. 500k higgsino pair-production events were generated privately for these two signal points for comparison against the official wino samples. All samples were produced in a TRUTH derivation format.

Table 5.11 shows an approximate comparison of the yields in a phase-space close to the WZ/Wh signal regions for the higgsino and wino models with background processes for comparison. Note that the inclusive cross-section for wino production is about 5 times bigger than for higgsino production. Across the table, the ratio between higgsino and wino yield remains flat around 0.2, as expected. The full boson-tagging cuts are not applied in this table because the jet-level substructure differs between TRUTH samples and fully-reconstructed MC. Instead, only the effect of requiring two b -initiated-jets is checked. Figures 5.40 and 5.41 show kinematic distribution comparisons between the two models at preselection level and with basic 2B2Q SR cuts applied for $(\tilde{\chi}_{\text{heavy}}, \tilde{\chi}_{\text{light}}) = (800 \text{ GeV}, 0 \text{ GeV})$ and $(600 \text{ GeV}, 200 \text{ GeV})$. In all cases, the ratio between the higgsino and wino templates is flat in the high-statistics regions, indicating that the models agree within uncertainty. Table 5.12 and Figures 5.42 and 5.43 show the same cutflow and comparisons with 4Q boosted WW and WZ SR selection. Distributions at preselection level are found in Figures 5.45 and 5.44.

	Preselection	Preselection minDPhi > 0.4	Preselection minDPhi > 0.4 MET > 250	Preselection minDPhi > 0.4 MET > 250 2 b-jets
Wino Wh (600,200)	80.16 \pm 0.31	80.16 \pm 0.31	67.33 \pm 0.29	18.17 \pm 0.15
higgsino Wh (600,200)	15.23 \pm 0.07	15.23 \pm 0.07	12.89 \pm 0.07	3.77 \pm 0.04
Ratio, higgsino/Wino (600,200)	0.19	0.19	0.19	0.21
Wino Wh (800,0)	39.24 \pm 0.11	39.24 \pm 0.11	36.37 \pm 0.10	9.49 \pm 0.05
higgsino Wh (800,0)	7.51 \pm 0.03	7.51 \pm 0.03	6.97 \pm 0.02	1.98 \pm 0.01
Ratio, higgsino/Wino (800,0)	0.19	0.19	0.19	0.21
Total Bkg	95537.16 \pm 385.47	95537.16 \pm 385.47	54873.04 \pm 118.07	5071.73 \pm 31.49
diboson	3369.65 \pm 333.79	3369.65 \pm 333.79	2376.19 \pm 14.93	185.98 \pm 4.00
jetjet	1818.30 \pm 145.11	1818.30 \pm 145.11	400.19 \pm 67.01	59.14 \pm 23.44
Wjets	29583.75 \pm 66.08	29583.75 \pm 66.08	15491.58 \pm 49.90	849.55 \pm 10.72
Zll	272.70 \pm 3.39	272.70 \pm 3.39	110.52 \pm 2.32	7.11 \pm 0.60
Znu	49070.22 \pm 102.54	49070.22 \pm 102.54	31360.85 \pm 79.98	1766.83 \pm 12.86
ttbar	9668.34 \pm 29.02	9668.34 \pm 29.02	4203.23 \pm 12.08	1803.63 \pm 7.94
ttV	379.25 \pm 3.12	379.25 \pm 3.12	243.46 \pm 2.50	102.71 \pm 1.62
topOther	1374.95 \pm 19.19	1374.95 \pm 19.19	687.02 \pm 13.52	296.78 \pm 8.92

Table 5.11: Comparison of wino and higgsino $\tilde{\chi}_1^\pm \tilde{\chi}_2^0 / \tilde{\chi}_3^0 \rightarrow Wh$ signal yields with basic 2B2Q selections applied. Uncertainties shown are purely statistical.

	Preselection	Preselection minDPhi > 0.4	Preselection minDPhi > 0.4 MET > 400	Preselection minDPhi > 0.4 MET > 400 0 b-jets
Wino WW (600,200)	50.13 \pm 0.18	46.97 \pm 0.17	17.43 \pm 0.10	17.09 \pm 0.10
higgsino WW (600,200)	12.04 \pm 0.07	11.22 \pm 0.06	4.31 \pm 0.04	4.23 \pm 0.04
Ratio, higgsino/Wino WW (600,200)	0.24	0.24	0.25	0.25
Wino WW (800,0)	22.71 \pm 0.06	21.29 \pm 0.05	14.45 \pm 0.05	14.23 \pm 0.04
higgsino WW (800,0)	5.43 \pm 0.02	5.10 \pm 0.02	3.46 \pm 0.02	3.41 \pm 0.02
Ratio, higgsino/Wino WW (800,0)	0.24	0.24	0.24	0.24
Wino WZ (600,200)	103.96 \pm 0.37	96.98 \pm 0.36	38.00 \pm 0.23	33.17 \pm 0.21
higgsino WZ (600,200)	21.37 \pm 0.09	19.97 \pm 0.08	7.68 \pm 0.05	6.69 \pm 0.05
Ratio, higgsino/Wino WZ (600,200)	0.21	0.21	0.20	0.20
Wino WZ (800,0)	47.87 \pm 0.12	44.91 \pm 0.12	30.52 \pm 0.10	26.69 \pm 0.09
higgsino WZ (800,0)	9.79 \pm 0.03	9.19 \pm 0.03	6.27 \pm 0.02	5.48 \pm 0.02
Ratio, higgsino/Wino WZ (800,0)	0.20	0.20	0.21	0.21
Total Bkg	180886.78 \pm 698.60	105561.20 \pm 403.52	14293.15 \pm 45.77	9041.73 \pm 36.82
diboson	5030.98 \pm 334.08	3531.88 \pm 333.82	746.15 \pm 8.08	455.60 \pm 6.26
jetjet	29552.00 \pm 589.33	2780.72 \pm 183.03	44.86 \pm 23.40	26.82 \pm 17.14
Wjets	51217.53 \pm 111.31	32975.76 \pm 74.00	3316.13 \pm 23.50	2193.69 \pm 19.21
Zll	710.47 \pm 6.16	312.74 \pm 3.68	14.72 \pm 0.76	9.82 \pm 0.64
Znu	62924.88 \pm 115.54	50855.04 \pm 103.92	9330.57 \pm 29.67	6297.27 \pm 25.49
ttbar	27260.20 \pm 48.52	12985.48 \pm 33.58	622.54 \pm 2.69	45.03 \pm 0.85
ttV	582.10 \pm 3.88	396.23 \pm 3.16	70.81 \pm 1.34	3.47 \pm 0.31
topOther	3608.62 \pm 31.27	1723.35 \pm 21.52	147.37 \pm 6.28	10.03 \pm 1.66

Table 5.12: Comparison of wino and higgsino $\tilde{\chi}_1^\pm \tilde{\chi}_1^\pm \rightarrow WW$ and $\tilde{\chi}_1^\pm \tilde{\chi}_2^0 \rightarrow WZ$ signal yields with basic 4Q selections applied. Uncertainties shown are purely statistical.

5.7 Future Work

As of writing, this search has not been completed. The analysis team is targeting a publication date in the spring of 2020. Although I will not be a part of the ATLAS collaboration by then, this section presents a few ideas for continuing work.

Systematic Uncertainties

Sample-production tools are already prepared to handle the experimental systematic uncertainties from the ATLAS object reconstruction software teams. Theoretical uncertainties related to MC

production are also already available. This thesis also presented the systematic uncertainty calculation for the ABCD method of background estimation (Section 5.5.1.2); other background estimation methods will have associated systematic uncertainties as well. Analyzers still need to perform a review of all the systematic uncertainties included in this analysis to ensure that nothing is being neglected. In addition, there are plans to re-optimize the boson-tagging algorithms used for large- R jets; this reoptimization would probably need its own systematic uncertainty evaluation.

Combining Resolved and Boosted Searches

Currently, the 2B2Q boosted and resolved signal regions are *not* disjoint; early estimates⁸⁵ place the estimated overlap between the two as high as 20% for some signal grid points. For the first round, our plan to combine boosted and resolved search results is to choose either the boosted or resolved result for each grid point, depending on which gives better sensitivity. In this way, the results are not so much combined as piecemealed together.

For a future result, however, one cannot ignore the potential increase in sensitivity from combining models. If the boosted and resolved regions were disjoint (for example, if the resolved search vetoed large- R jets), then the two results would be statistically independent and could easily be combined. Thus far, however, there is no clear choice of variable or cut to make the two disjoint; the cuts considered (such as a large- R jet selection/veto) cause loss of sensitivity for one team or the other. Some work is still needed to identify an appropriate way to make these two signal regions disjoint.

Additional Model Interpretations

As mentioned in this chapter, there are already plans for several different SUSY model interpretations for this analysis. It should be straightforward to include the higgsino-bino model by simply reweighting the wino-bino model to the appropriate cross-section. Once a neutralino-only model, i.e. $\tilde{\chi}_2^0 \tilde{\chi}_3^0$ (described in Section 5.1.2) has been chosen, reinterpretations of this signal may be possible as well.

⁸⁵As of writing, the resolved analysis team has not finished updating their SR definition from the previous analysis.

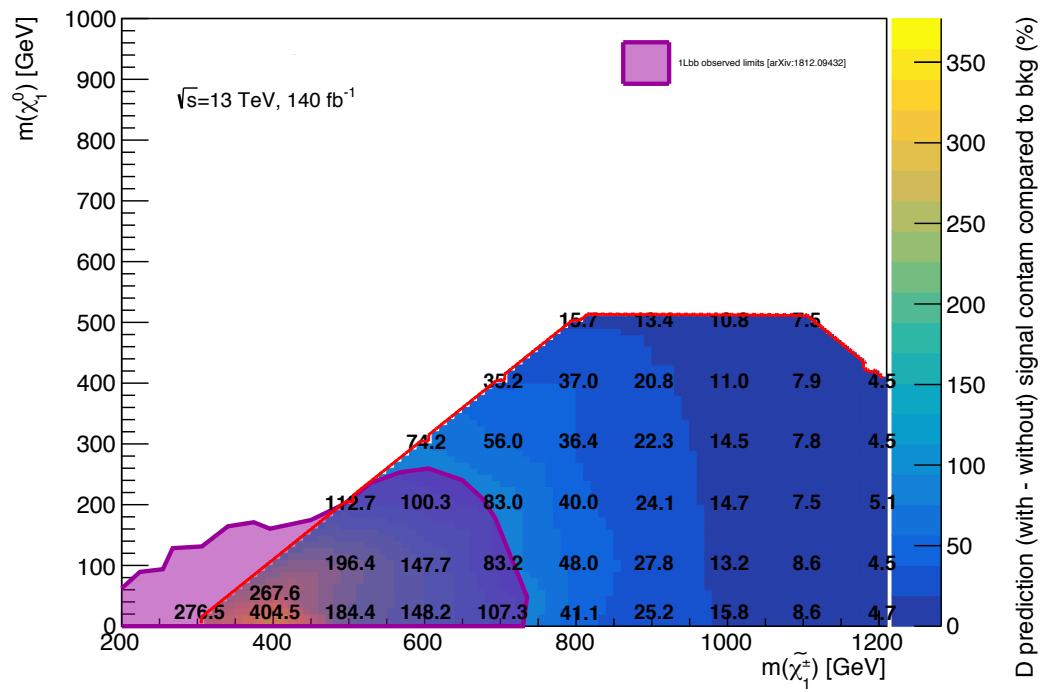


Figure 5.38: Estimated bias of background estimate in Wh region D due to signal presence in regions A, B, and C as a percentage of non-contaminated D background yield estimate

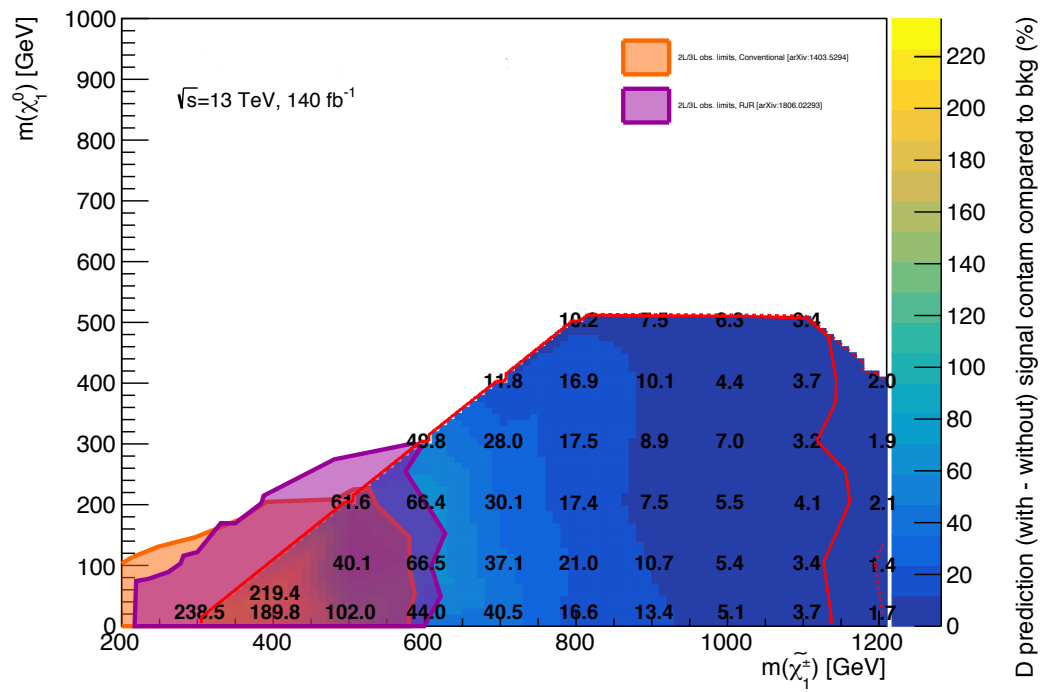
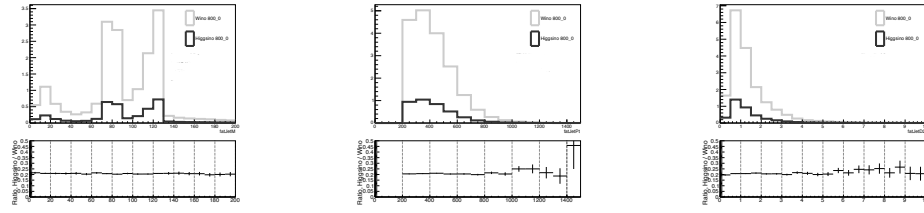
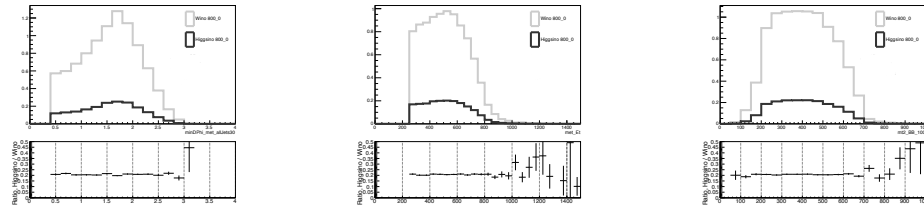


Figure 5.39: Estimated bias of background estimate in WZ region D due to signal presence in regions A, B, and C as a percentage of non-contaminated D background yield estimate

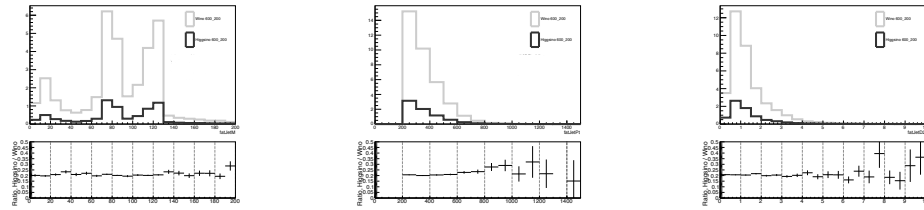


(a) 2B2Q basic cuts plot of Fat Jet Mass (b) 2B2Q basic cuts plot of Fat Jet p_T (c) 2B2Q basic cuts plot of Fat Jet D2

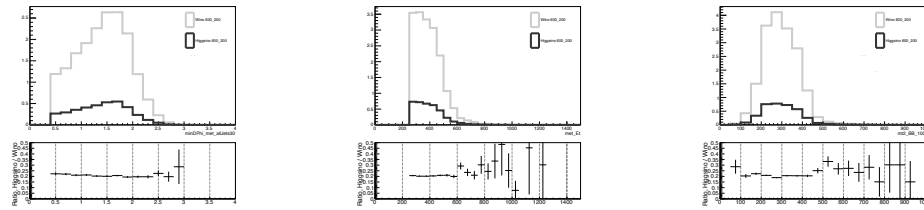


(d) 2B2Q basic cuts plot of $\min \Delta\phi(j, E_T^{\text{miss}})$ (e) 2B2Q basic cuts plot of E_T^{miss} (f) 2B2Q basic cuts plot of m_{T2}

Figure 5.40: Plots of assorted variables with basic 2B2Q variable and object cuts. Signal mass point $(\tilde{\chi}_1^\pm/\tilde{\chi}_2^0/\tilde{\chi}_3^0, \tilde{\chi}_1^0) = (800 \text{ GeV}, 0 \text{ GeV})$



(a) 2B2Q basic cuts plot of Fat Jet Mass (b) 2B2Q basic cuts plot of Fat Jet p_T (c) 2B2Q basic cuts plot of Fat Jet D2



(d) 2B2Q basic cuts plot of $\min \Delta\phi(j, E_T^{\text{miss}})$ (e) 2B2Q basic cuts plot of E_T^{miss} (f) 2B2Q basic cuts plot of m_{T2}

Figure 5.41: Plots of assorted variables with basic 2B2Q variable and object cuts. Signal mass point $(\tilde{\chi}_1^\pm/\tilde{\chi}_2^0/\tilde{\chi}_3^0, \tilde{\chi}_1^0) = (600 \text{ GeV}, 200 \text{ GeV})$

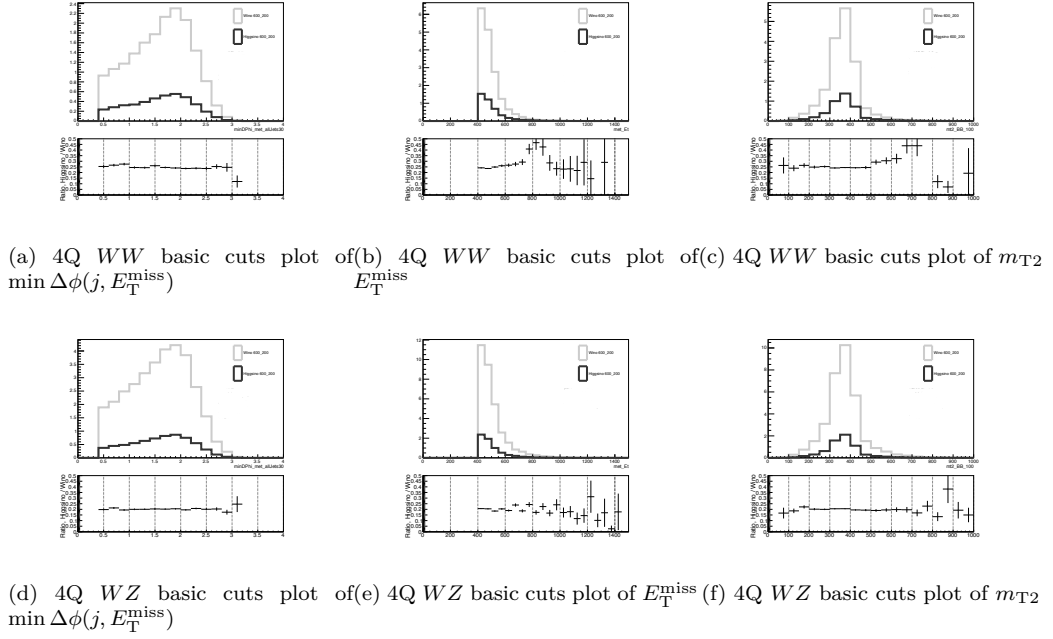


Figure 5.42: Plots of assorted variables with basic 4Q variable and object cuts with WW and WZ signals. Signal mass point $(\tilde{\chi}_1^\pm/\tilde{\chi}_2^0/\tilde{\chi}_3^0, \tilde{\chi}_1^0) = (600 \text{ GeV}, 200 \text{ GeV})$

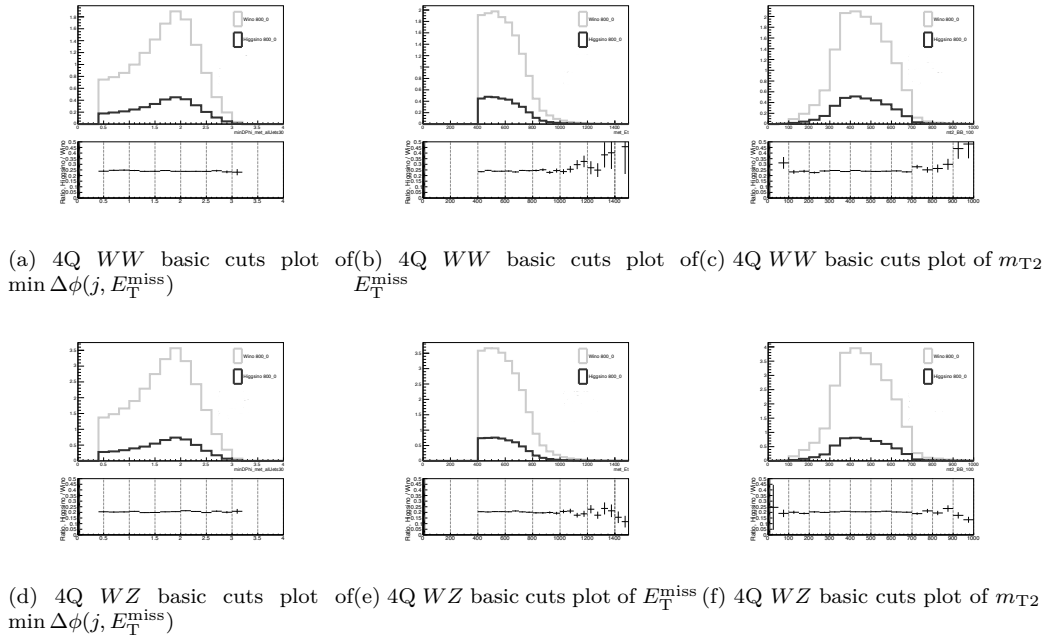
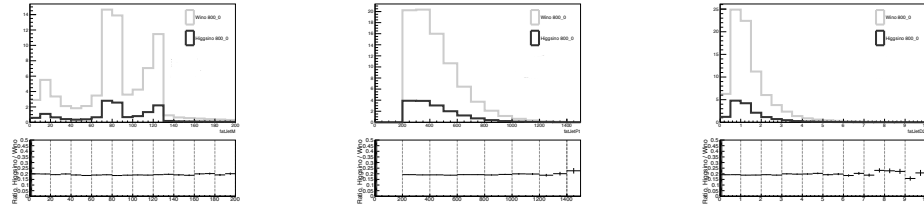
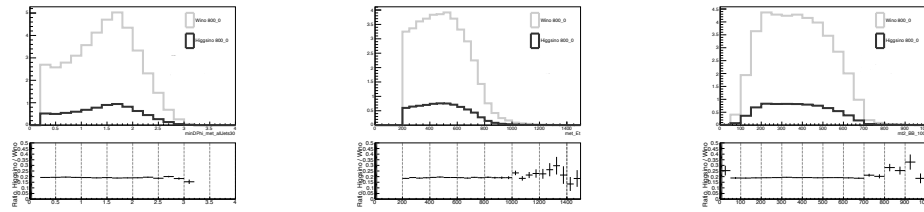


Figure 5.43: Plots of assorted variables with basic 4Q variable and object cuts with WW and WZ signals. Signal mass point $(\tilde{\chi}_1^\pm/\tilde{\chi}_2^0/\tilde{\chi}_3^0, \tilde{\chi}_1^0) = (800 \text{ GeV}, 0 \text{ GeV})$

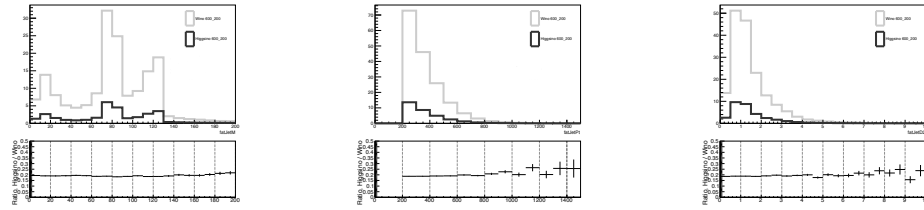


(a) Preselection plot of Fat Jet Mass (b) Preselection plot of Fat Jet p_T (c) Preselection plot of Fat Jet D2 Mass

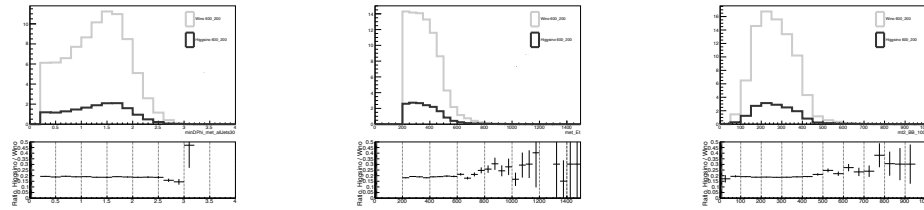


(d) Preselection plot of $\min \Delta\phi(j, E_T^{\text{miss}})$ (e) Preselection plot of E_T^{miss} (f) Preselection plot of m_{T2}

Figure 5.44: Plots of assorted variables at preselection level. Signal mass point $(\tilde{\chi}_1^\pm/\tilde{\chi}_2^0/\tilde{\chi}_3^0/\tilde{\chi}_1^0) = (800 \text{ GeV}, 0 \text{ GeV})$



(a) Preselection plot of Fat Jet Mass (b) Preselection plot of Fat Jet p_T (c) Preselection plot of Fat Jet D2 Mass



(d) Preselection plot of $\min \Delta\phi(j, E_T^{\text{miss}})$ (e) Preselection plot of E_T^{miss} (f) Preselection plot of m_{T2}

Figure 5.45: Plots of assorted variables at preselection level. Signal mass point $(\tilde{\chi}_1^\pm/\tilde{\chi}_2^0/\tilde{\chi}_3^0/\tilde{\chi}_1^0) = (600 \text{ GeV}, 200 \text{ GeV})$

CHAPTER 6

Conclusion

This thesis presented a calibration and a search using $\sqrt{s} = 13$ TeV data collected with the ATLAS detector during Run 2 of the LHC, as well as contributions to ATLAS derivation production software for flavor-tagging.

The flavor-tagging derivation software was first presented within the larger context of the ATLAS data pipeline. In addition to providing dataset production and software support to users, several major bugs were identified and fixed and new functionality was added while simultaneously reducing data sample sizes. Software services were provided smoothly, and several users communicated how important this task was for timely completion of their work.

The flavor-tagging algorithm *MV2c10* was calibrated using the p_T^{rel} method after a complete revamp of the Run 1 result. This calibration was performed using 68 fb^{-1} of data collected at $\sqrt{s} = 13$ TeV with the ATLAS detector at the Large Hadron Collider during Run 2. After a delay in data collection, the muon-in-jet triggers were calibrated using a bootstrap method. A new method of generating muon-in-jet MC samples was validated by comparison with older samples. After preparing the first result, a proposal was made to use the p_T^{rel} method to calibrate b -jets for a high-precision top quark branching ratio measurement. In the course of reducing the systematic uncertainties, it was found that this new high-precision result was sensitive to merged $g \rightarrow b\bar{b}$ jets. This effect, which increases with jet p_T , results in excesses in the tail of the p_T^{rel} distributions which are not well-modeled in current MC simulations. The p_T^{rel} analysis team is currently working to correct this issue and to assign values to a small few remaining systematics.

This thesis concludes with a search for electroweak-scale SUSY production in fully-hadronic final states with two b -quarks. The supersymmetry search was performed using 140 fb^{-1} of data collected at $\sqrt{s} = 13$ TeV with the ATLAS detector at the Large Hadron Collider in Run 2. This

search is being performed for the first time at ATLAS, and a new signal region was developed for this purpose based on simulated signal samples. These signal samples were also used to study kinematic differences between wino-bino and higgsino-bino production; outside of the expected discrepancies in cross-section, no major differences were found. Because the signal region explores a remote corner of phase space, the MC-simulated backgrounds may not properly reflect data yields. For this reason, a data-driven method of background estimation using the ABCD method was explored. The ABCD method performed better for $h \rightarrow b\bar{b}$ than for $Z \rightarrow b\bar{b}$ final states; in both cases, however, the ABCD method resulted in barely tolerable systematic uncertainties. For this reason, other data-driven background estimation methods may be preferable. This measurement was approved for unblinding a week before this thesis was defended, so all software tools were thoroughly documented for use by the continuing members of the team. Based on preliminary results, in the wino-bino scenario, this search is expected to provide sensitivity to charginos with masses up to 900 GeV (discovery) or 1 TeV (exclusion). For general-gauge-mediation higgsino models, this search will provide sensitivity for higgsinos with masses up to 600 GeV (discovery) or 800 GeV (exclusion) for all possible Z/h branching ratios. Finally, this signal region will also provide the first exclusion results for higgsino-bino scenarios.

APPENDIX A

Appendix

A.1 Motivating the Higgs Boson: Calculation Details

This section shall motivate the Higgs boson theoretically by showing that the “standard” approach (without a Higgs boson) to $\nu_e + \bar{\nu}_e \rightarrow W^+ + W^-$ scattering gives a divergent cross section at first order at high energies. Note that this section draws very heavily from Ref [13]; details of calculations can be found there.

Let us consider the process $\nu_e + \bar{\nu}_e \rightarrow W^+ + W^-$ (as shown in Figure A.1).

$$\nu_e(q_1) + \bar{\nu}_e(q_2) \rightarrow W^+(k_+) + W^-(k_-) \quad (\text{A.1})$$

where we define the following momentum four-vectors in the c.m.⁸⁶ frame:

$$q_1 \equiv (Q; 0, 0, Q)$$

$$q_2 \equiv (Q; 0, 0, -Q)$$

$$k_+ \equiv (Q; K \sin\theta, 0, K \cos\theta)$$

$$k_- \equiv (Q; -K \sin\theta, 0, -K \cos\theta)$$

$$P = q_1 - k_+ = k_- - q_2$$

The matrix element for this process is:

$$\mathcal{M} = -\frac{iG_F M_W^2}{\sqrt{s}} \bar{v}(v, q_2) \not{\epsilon}_-^* (1 - \gamma_5) \frac{\not{P} + m}{P^2 - m^2} \not{\epsilon}_+^* (1 - \gamma_5) u(v, q_1) \quad (\text{A.2})$$

where m is the electron mass, $\epsilon_\pm^\mu = (0; \hat{\epsilon}_\pm)$ represents the polarization of W^\pm in its rest frame, and G_F is the Fermi coupling constant, related to the weak coupling strength g_W like so:

$$\frac{G_F}{\sqrt{2}} = \frac{g_W^2}{8M_W^2} \quad (\text{A.3})$$

When the W^\pm bosons are longitudinally polarized, the polarization vector in the c.m. frame can be written as:

$$\epsilon_\pm^\mu = \left(\frac{K}{M_W}; \frac{Q \hat{\mathbf{k}}^\pm}{M_W} \right) \quad (\text{A.4})$$

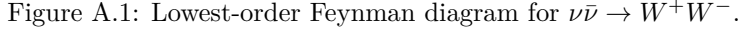
which, in the high energy limit $Q \simeq K \gg M_W$, becomes:

$$\lim_{K \rightarrow \infty} \epsilon_\pm^\mu \rightarrow \frac{k_\pm}{M_W} \quad (\text{A.5})$$

Therefore, the matrix element becomes:

$$\mathcal{M} = -\frac{iG_F}{\sqrt{2}} \bar{v}(v, q_2) \not{k}_- (1 - \gamma_5) \frac{\not{P} + m}{P^2 - m^2} \not{k}_+ (1 - \gamma_5) u(v, q_1) \quad (\text{A.6})$$

⁸⁶center-of-mass


$$\begin{aligned} k_+ &\rightarrow k_+ - q_1 = -P \\ k_- &\rightarrow k_- - q_2 = P \end{aligned}$$

Since $\not{P}\not{P} = P^2$, we get:

Finally, let's check the magnitude of this matrix element and relate it to the cross section:

As a result, the cross section in the high energy limit becomes:

where $s = (q_1 + k_+)^2$. This means that the cross section becomes larger as the momenta of the incoming particles become larger! Clearly, this sort of divergence is nonsensical. In fact, the second-order contribution to this amplitude grows as s^2 , making our problems even worse. There is a way out, thankfully: the introduction of a new particle will result in additional diagrams which will cancel out these divergences (see Ref [13], Section 6.5 for an in-depth look at these cancellations).

A.2 Up-to-date Systematic Uncertainty Tables for p_T^{rel}

The following tables list all systematic uncertainties in the p_T^{rel} analysis for each working point of the *MV2c10* tagging algorithm.

Table A.1: Systematic uncertainties for the $MV2c10$ tagging algorithm at 85% nominal b -tagging efficiency

Systematic Uncertainty Source	Systematic Uncertainty in $p_T^{\text{jet}} [GeV]$ Bins								
	[20, 30]	[30, 40]	[40, 50]	[50, 70]	[70, 90]	[90, 110]	[110, 140]	[140, 170]	[170, 200]
Detector and Calibration Uncertainties									
PileupOffsetMu	0.034	0.041	0.071	0.005	0.090	0.023	0.014	0.023	0.149
PileupOffsetNPV	0.156	0.085	0.241	0.054	0.124	0.064	0.010	0.293	0.350
PileupPtTerm	0.034	0.004	0.018	0.028	0.021	0.038	0.092	0.076	0.137
PileupRhoTopology	0.406	0.143	0.180	0.028	0.126	0.055	0.064	0.898	0.447
BJESResponse	0.245	0.108	0.148	0.034	0.123	0.077	0.011	0.068	0.040
FlavorComposition	0.187	0.030	0.053	0.023	0.016	0.079	0.074	0.123	0.003
FlavorResponse	0.097	0.030	0.045	0.000	0.003	0.031	0.081	0.053	0.074
EtaIntercalibrationModeling	0.127	0.066	0.115	0.001	0.080	0.013	0.070	0.100	0.016
EtaIntercalibrationTotalStat	0.051	0.058	0.086	0.012	0.034	0.045	0.033	0.005	0.001
EffectiveNP1	0.308	0.128	0.144	0.011	0.178	0.117	0.082	0.053	0.349
EffectiveNP2	0.030	0.045	0.083	0.014	0.033	0.033	0.003	0.079	0.150
EffectiveNP3	0.049	0.042	0.037	0.021	0.015	0.072	0.026	0.031	0.128
EffectiveNP4	0.043	0.008	0.017	0.030	0.017	0.050	0.013	0.034	0.000
EffectiveNP5	0.007	0.051	0.017	0.003	0.008	0.018	0.021	0.046	0.150
EffectiveNP6	0.014	0.019	0.032	0.008	0.000	0.015	0.013	0.031	0.020
EffectiveNP7	0.006	0.009	0.039	0.003	0.044	0.044	0.050	0.004	0.021
EffectiveNP8restTerm	0.021	0.014	0.008	0.009	0.008	0.012	0.053	0.025	0.033
JER_DataVsMC	0.016	0.006	0.002	0.005	0.036	0.025	0.003	0.054	0.044
JER_EffectiveNP_1	0.022	0.037	0.018	0.011	0.002	0.004	0.020	0.034	0.017
JER_EffectiveNP_2	0.002	0.010	0.028	0.001	0.018	0.035	0.007	0.024	0.015
JER_EffectiveNP_3	0.009	0.014	0.001	0.018	0.022	0.005	0.021	0.023	0.003
JER_EffectiveNP_4	0.002	0.022	0.007	0.012	0.037	0.003	0.053	0.025	0.016
JER_EffectiveNP_5	0.015	0.015	0.004	0.009	0.004	0.016	0.013	0.019	0.001
JER_EffectiveNP_6	0.007	0.001	0.011	0.009	0.002	0.020	0.023	0.044	0.042
JER_EffectiveNP_7restTerm	0.025	0.020	0.016	0.004	0.025	0.042	0.007	0.034	0.089
PunchThrough_MC16	0.001	0.014	0.001	0.023	0.027	0.005	0.047	0.036	0.850
MUON_SAGITTA_RESBIAS	0.003	0.004	0.016	0.001	0.050	0.032	0.005	0.275	0.197
MUON_SAGITTA_RHO	0.030	0.026	0.016	0.015	0.018	0.008	0.035	1.142	0.264
MuonID	0.021	0.026	0.026	0.007	0.010	0.002	0.087	0.259	0.338
MuonMS	0.021	0.068	0.006	0.043	0.054	0.009	0.112	0.493	0.044
MuonScale	0.016	0.003	0.045	0.009	0.001	0.076	0.041	0.015	0.126
Modeling Uncertainties									
AxisSmearing	0.045	0.050	0.075	0.119	0.023	0.049	0.544	4.421	0.471
FakeMuons	0.052	0.090	0.062	0.123	0.010	0.039	0.234	4.571	1.159
GluonSplitB	0.022	0.042	0.055	0.054	0.015	0.005	0.001	0.797	0.149
GluonSplitC	0.100	0.039	0.016	0.015	0.009	0.047	0.022	0.045	0.027
Extrapolation	0.702	0.702	0.702	0.702	0.702	0.702	0.702	0.702	0.702
MC Statistical Uncertainties									
SimulationStats	0.143	0.105	0.106	0.084	0.104	0.114	0.107	0.127	0.146
TemplateStats	0.551	0.632	0.511	0.478	0.685	0.936	0.578	0.992	1.398
Template Selection Uncertainties									
JVTEfficiency	0.009	0.000	0.010	0.000	0.003	0.008	0.016	0.458	0.136
DataStats	0.517	0.628	0.680	0.817	0.613	1.195	0.586	0.615	0.516
TotalSystematicErr	1.109	0.994	0.973	0.875	1.035	1.199	1.119	6.738	2.363

Table A.2: Systematic uncertainties for the $MV2c10$ tagging algorithm at 77% nominal b -tagging efficiency

Systematic Uncertainty Source	Systematic Uncertainty in $p_T^{\text{jet}} [GeV]$ Bins								
	[20, 30]	[30, 40]	[40, 50]	[50, 70]	[70, 90]	[90, 110]	[110, 140]	[140, 170]	[170, 200]
Detector and Calibration Uncertainties									
PileupOffsetMu	0.082	0.034	0.090	0.097	0.209	0.019	0.106	0.360	0.160
PileupOffsetNPV	0.164	0.113	0.385	0.006	0.037	0.080	0.048	0.450	0.775
PileupPtTerm	0.032	0.024	0.036	0.055	0.008	0.024	0.107	0.095	0.076
PileupRhoTopology	0.368	0.210	0.291	0.078	0.241	0.191	0.332	0.265	0.785
BJESResponse	0.319	0.208	0.191	0.120	0.096	0.145	0.136	0.062	0.036
FlavorComposition	0.094	0.010	0.161	0.140	0.156	0.118	0.011	0.261	0.106
FlavorResponse	0.058	0.013	0.131	0.104	0.059	0.164	0.219	0.268	0.442
EtaIntercalibrationModeling	0.094	0.018	0.143	0.034	0.021	0.141	0.126	0.364	0.178
EtaIntercalibrationTotalStat	0.051	0.051	0.129	0.053	0.015	0.054	0.057	0.148	0.137
EffectiveNP1	0.319	0.135	0.263	0.030	0.139	0.240	0.185	0.612	0.414
EffectiveNP2	0.057	0.023	0.103	0.059	0.004	0.067	0.100	0.146	0.465
EffectiveNP3	0.021	0.015	0.039	0.004	0.025	0.112	0.023	0.176	0.058
EffectiveNP4	0.046	0.019	0.057	0.010	0.062	0.197	0.053	0.063	0.020
EffectiveNP5	0.066	0.010	0.035	0.028	0.036	0.012	0.112	0.150	0.249
EffectiveNP6	0.033	0.006	0.034	0.021	0.038	0.065	0.061	0.160	0.019
EffectiveNP7	0.018	0.011	0.055	0.003	0.000	0.095	0.021	0.027	0.039
EffectiveNP8restTerm	0.041	0.012	0.001	0.001	0.050	0.034	0.115	0.057	0.147
JER_DataVsMC	0.007	0.014	0.003	0.035	0.010	0.149	0.008	0.013	0.136
JER_EffectiveNP_1	0.011	0.019	0.008	0.011	0.048	0.109	0.050	0.015	0.111
JER_EffectiveNP_2	0.004	0.061	0.007	0.026	0.022	0.018	0.043	0.064	0.023
JER_EffectiveNP_3	0.002	0.025	0.007	0.033	0.043	0.039	0.010	0.046	0.087
JER_EffectiveNP_4	0.012	0.034	0.001	0.041	0.000	0.026	0.071	4.418	0.086
JER_EffectiveNP_5	0.026	0.025	0.007	0.016	0.000	0.108	0.032	0.073	0.002
JER_EffectiveNP_6	0.042	0.015	0.001	0.014	0.033	0.111	0.050	0.118	0.013
JER_EffectiveNP_7restTerm	0.019	0.004	0.010	0.014	0.021	0.085	0.017	0.024	0.006
PunchThrough_MC16	0.016	0.012	0.027	0.012	0.030	0.168	0.147	0.224	0.495
MUON_SAGITTA_RESBIAS	0.019	0.051	0.033	0.008	0.186	0.077	0.012	0.625	0.256
MUON_SAGITTA_RHO	0.048	0.056	0.020	0.019	0.002	0.120	0.014	0.659	0.953
MuonID	0.006	0.000	0.030	0.005	0.083	0.033	0.060	0.381	0.488
MuonMS	0.035	0.013	0.038	0.065	0.107	0.058	0.294	0.248	0.110
MuonScale	0.055	0.011	0.063	0.027	0.064	0.202	0.067	0.270	0.471
Modeling Uncertainties									
AxisSmearing	0.051	0.029	0.174	0.038	0.127	0.274	0.443	1.100	2.925
FakeMuons	0.065	0.022	0.049	0.005	0.017	0.150	0.155	3.454	0.601
GluonSplitB	0.005	0.101	0.024	0.056	0.027	0.290	0.102	0.747	0.092
GluonSplitC	0.138	0.006	0.113	0.099	0.069	0.037	0.263	1.291	0.283
Extrapolation	0.923	0.923	0.923	0.923	0.923	0.923	0.923	0.923	0.923
MC Statistical Uncertainties									
SimulationStats	0.204	0.150	0.150	0.121	0.152	0.177	0.158	0.191	0.221
TemplateStats	0.762	0.630	0.702	0.537	1.167	1.994	6.088	1.635	3.160
Template Selection Uncertainties									
JVTEfficiency	0.035	0.012	0.010	0.009	0.007	0.061	0.050	0.787	0.467
DataStats	2.191	0.777	0.728	1.405	0.599	0.975	0.480	0.512	0.460
TotalSystematicErr	1.371	1.183	1.360	1.113	1.572	2.330	6.216	6.434	4.877

Table A.3: Systematic uncertainties for the $MV2c10$ tagging algorithm at 70% nominal b -tagging efficiency

Systematic Uncertainty Source	Systematic Uncertainty in $p_T^{\text{jet}} [GeV]$ Bins								
	[20, 30]	[30, 40]	[40, 50]	[50, 70]	[70, 90]	[90, 110]	[110, 140]	[140, 170]	[170, 200]
Detector and Calibration Uncertainties									
PileupOffsetMu	0.014	0.095	0.132	0.094	0.181	0.375	0.186	0.448	0.586
PileupOffsetNPV	0.011	0.170	0.581	0.034	0.130	0.461	0.121	0.349	0.248
PileupPtTerm	0.025	0.025	0.011	0.001	0.094	0.439	0.008	0.728	0.891
PileupRhoTopology	0.350	0.286	0.570	0.031	0.262	0.557	0.152	3.746	0.442
BJESResponse	0.401	0.403	0.472	0.205	0.322	0.394	0.022	0.282	0.534
FlavorComposition	0.200	0.021	0.304	0.320	0.136	0.418	0.023	0.167	0.236
FlavorResponse	0.020	0.040	0.208	0.131	0.061	0.060	0.134	0.202	0.264
EtaIntercalibrationModeling	0.165	0.109	0.242	0.043	0.013	0.131	0.207	0.461	0.321
EtaIntercalibrationTotalStat	0.048	0.101	0.125	0.042	0.017	0.003	0.077	0.244	0.155
EffectiveNP1	0.263	0.287	0.560	0.028	0.438	0.583	0.305	0.855	0.171
EffectiveNP2	0.050	0.110	0.160	0.040	0.070	0.037	0.060	0.151	0.179
EffectiveNP3	0.054	0.020	0.034	0.067	0.050	0.052	0.055	0.062	0.179
EffectiveNP4	0.048	0.072	0.047	0.126	0.028	0.198	0.117	0.036	0.121
EffectiveNP5	0.035	0.021	0.057	0.011	0.035	0.067	0.102	0.050	0.097
EffectiveNP6	0.008	0.063	0.034	0.039	0.058	0.105	0.046	0.168	0.084
EffectiveNP7	0.015	0.020	0.074	0.022	0.068	0.010	0.030	0.034	0.002
EffectiveNP8restTerm	0.045	0.012	0.002	0.010	0.059	0.112	0.106	0.274	0.258
JER_DataVsMC	0.071	0.082	0.001	0.022	0.026	0.058	0.095	0.091	0.043
JER_EffectiveNP_1	0.035	0.016	0.032	0.007	0.039	0.153	0.082	0.018	0.255
JER_EffectiveNP_2	0.090	0.017	0.002	0.011	0.003	0.089	0.005	0.253	0.073
JER_EffectiveNP_3	0.033	0.010	0.023	0.008	0.090	0.010	0.080	0.260	0.174
JER_EffectiveNP_4	0.014	0.039	0.014	0.044	0.074	0.119	0.072	0.002	0.516
JER_EffectiveNP_5	0.006	0.094	0.031	0.018	0.068	0.060	0.020	0.341	0.040
JER_EffectiveNP_6	0.002	0.021	0.017	0.013	0.067	0.071	0.121	0.425	0.027
JER_EffectiveNP_7restTerm	0.002	0.014	0.011	0.055	0.041	0.059	0.187	0.195	0.212
PunchThrough_MC16	0.037	0.011	0.009	0.034	0.012	0.342	0.230	0.760	0.548
MUON_SAGITTA_RESBIAS	0.010	0.046	0.021	0.031	0.132	0.005	0.096	0.452	0.144
MUON_SAGITTA_RHO	0.055	0.034	0.002	0.033	0.060	0.148	0.282	0.015	0.078
MuonID	0.025	0.023	0.011	0.058	0.010	0.052	0.168	0.634	0.418
MuonMS	0.033	0.027	0.032	0.133	0.103	0.016	0.150	0.206	0.484
MuonScale	0.062	0.019	0.085	0.098	0.217	0.233	0.197	1.318	0.895
Modeling Uncertainties									
AxisSmearing	0.278	0.001	0.147	0.158	0.053	0.073	0.494	2.046	0.373
FakeMuons	0.754	0.438	0.044	0.230	0.082	0.047	0.237	2.297	0.586
GluonSplitB	0.063	0.123	0.115	0.096	0.267	0.267	0.089	2.019	0.011
GluonSplitC	0.122	0.191	0.272	0.161	0.115	0.062	0.449	0.509	0.363
Extrapolation	1.096	1.096	1.096	1.096	1.096	1.096	1.096	1.096	1.096
MC Statistical Uncertainties									
SimulationStats	0.279	0.198	0.198	0.159	0.199	0.236	0.209	0.256	0.307
TemplateStats	0.969	0.765	0.889	0.805	1.541	2.464	6.349	2.086	3.120
Template Selection Uncertainties									
JVTEfficiency	0.023	0.006	0.031	0.017	0.097	0.143	0.167	0.343	0.282
DataStats	0.759	0.850	0.709	0.836	0.619	0.949	0.467	0.547	0.528
TotalSystematicErr	1.807	1.570	1.892	1.484	2.062	3.041	6.529	6.251	3.963

Table A.4: Systematic uncertainties for the $MV2c10$ tagging algorithm at 60% nominal b -tagging efficiency

Systematic Uncertainty Source	Systematic Uncertainty in $p_T^{\text{jet}} [GeV]$ Bins								
	[20, 30]	[30, 40]	[40, 50]	[50, 70]	[70, 90]	[90, 110]	[110, 140]	[140, 170]	[170, 200]
Detector and Calibration Uncertainties									
PileupOffsetMu	0.129	0.059	0.203	0.144	0.151	0.397	0.122	0.129	0.084
PileupOffsetNPV	0.073	0.096	0.761	0.111	0.069	0.350	0.193	1.721	0.728
PileupPtTerm	0.007	0.003	0.017	0.084	0.077	0.434	0.220	0.178	1.017
PileupRhoTopology	0.645	0.004	0.813	0.027	0.501	0.375	1.234	0.754	0.941
BJESResponse	0.765	0.051	0.673	0.172	0.132	0.064	0.809	0.243	0.193
FlavorComposition	0.308	0.147	0.396	0.550	0.270	0.638	0.073	0.344	0.006
FlavorResponse	0.159	0.122	0.290	0.300	0.103	0.541	0.024	0.301	0.637
EtaIntercalibrationModeling	0.164	0.033	0.338	0.049	0.072	0.272	0.134	0.506	0.375
EtaIntercalibrationTotalStat	0.157	0.046	0.141	0.057	0.103	0.197	0.096	0.636	0.193
EffectiveNP1	0.522	0.147	0.821	0.049	0.089	0.273	0.793	1.230	0.248
EffectiveNP2	0.168	0.064	0.182	0.208	0.092	0.323	0.117	0.265	0.441
EffectiveNP3	0.009	0.005	0.025	0.036	0.241	0.042	0.018	0.240	0.391
EffectiveNP4	0.046	0.006	0.064	0.084	0.171	0.016	0.275	0.242	0.285
EffectiveNP5	0.043	0.001	0.086	0.064	0.269	0.088	0.042	0.014	0.158
EffectiveNP6	0.020	0.027	0.079	0.022	0.057	0.001	0.161	0.149	0.395
EffectiveNP7	0.015	0.015	0.110	0.001	0.092	0.326	0.418	0.014	0.290
EffectiveNP8restTerm	0.008	0.019	0.009	0.066	0.019	0.255	0.273	0.007	0.209
JER_DataVsMC	0.060	0.018	0.002	0.020	0.012	0.355	0.229	0.000	0.148
JER_EffectiveNP_1	0.006	0.025	0.048	0.006	0.087	0.330	0.105	0.114	0.012
JER_EffectiveNP_2	0.011	0.004	0.021	0.070	0.088	0.294	0.140	0.063	0.344
JER_EffectiveNP_3	0.068	0.030	0.082	0.023	0.063	0.017	0.252	0.160	0.153
JER_EffectiveNP_4	0.034	0.023	0.009	0.003	0.012	0.201	0.168	0.164	0.470
JER_EffectiveNP_5	0.025	0.020	0.028	0.025	0.053	0.269	0.009	0.199	0.102
JER_EffectiveNP_6	0.023	0.002	0.021	0.040	0.066	0.095	0.245	0.094	0.099
JER_EffectiveNP_7restTerm	0.019	0.029	0.025	0.022	0.050	0.046	0.371	0.060	0.170
PunchThrough_MC16	0.100	0.039	0.075	0.000	0.147	0.513	0.544	0.055	1.169
MUON_SAGITTA_RESBIAS	0.058	0.030	0.038	0.025	0.028	0.227	0.426	0.832	0.562
MUON_SAGITTA_RHO	0.073	0.053	0.037	0.031	0.228	0.216	0.286	0.558	0.293
MuonID	0.078	0.042	0.003	0.035	0.083	0.426	0.241	0.203	0.565
MuonMS	0.061	0.014	0.134	0.107	0.492	0.169	0.045	1.124	0.925
MuonScale	0.086	0.027	0.123	0.030	0.120	0.130	0.098	0.231	0.062
Modeling Uncertainties									
AxisSmearing	0.218	0.020	0.204	0.373	0.096	2.073	0.139	2.977	1.453
FakeMuons	1.948	0.169	0.948	0.535	0.807	1.179	1.273	0.969	1.271
GluonSplitB	0.044	0.014	0.163	0.017	0.329	0.813	0.617	0.772	1.095
GluonSplitC	0.270	0.790	1.295	1.073	0.331	0.338	1.885	0.021	1.276
Extrapolation	1.351	1.351	1.351	1.351	1.351	1.351	1.351	1.351	1.351
MC Statistical Uncertainties									
SimulationStats	0.448	0.290	0.287	0.228	0.289	0.345	0.309	0.392	0.481
TemplateStats	0.830	0.972	0.970	0.926	1.975	2.751	6.036	2.617	4.421
Template Selection Uncertainties									
JVTEfficiency	0.032	0.032	0.026	0.035	0.213	0.137	0.237	0.081	0.573
DataStats	0.736	0.838	0.756	0.772	0.662	1.029	0.536	0.668	0.768
TotalSystematicErr	2.825	1.876	2.883	2.195	2.758	4.324	6.942	5.273	5.959

A.3 p_T^{rel} Fit Results

A.3.1 Post-fit p_T^{rel} Plots for 60% WP

The results for the $\varepsilon_b^{\text{nom}} = 60\%$ WP of the MV2c10 algorithm and all p_T^{jet} bins are shown in Figures A.2-A.4.

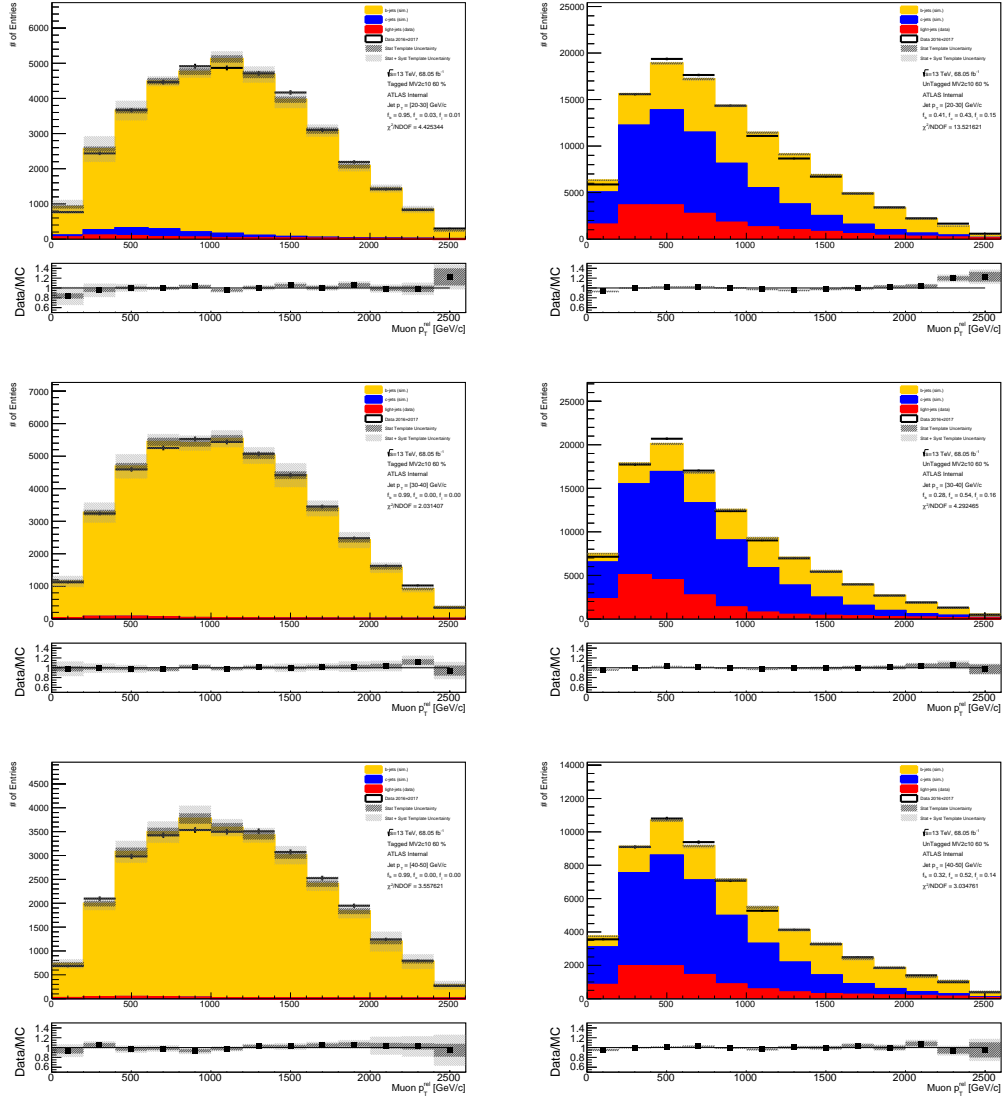


Figure A.2: Tagged (left) and untagged (right) p_T^{rel} distributions for 20-30 GeV (top), 30-40 GeV (middle), and 40-50 GeV (bottom) p_T^{jet} bins using flavor fractions obtained by the log-likelihood fit.

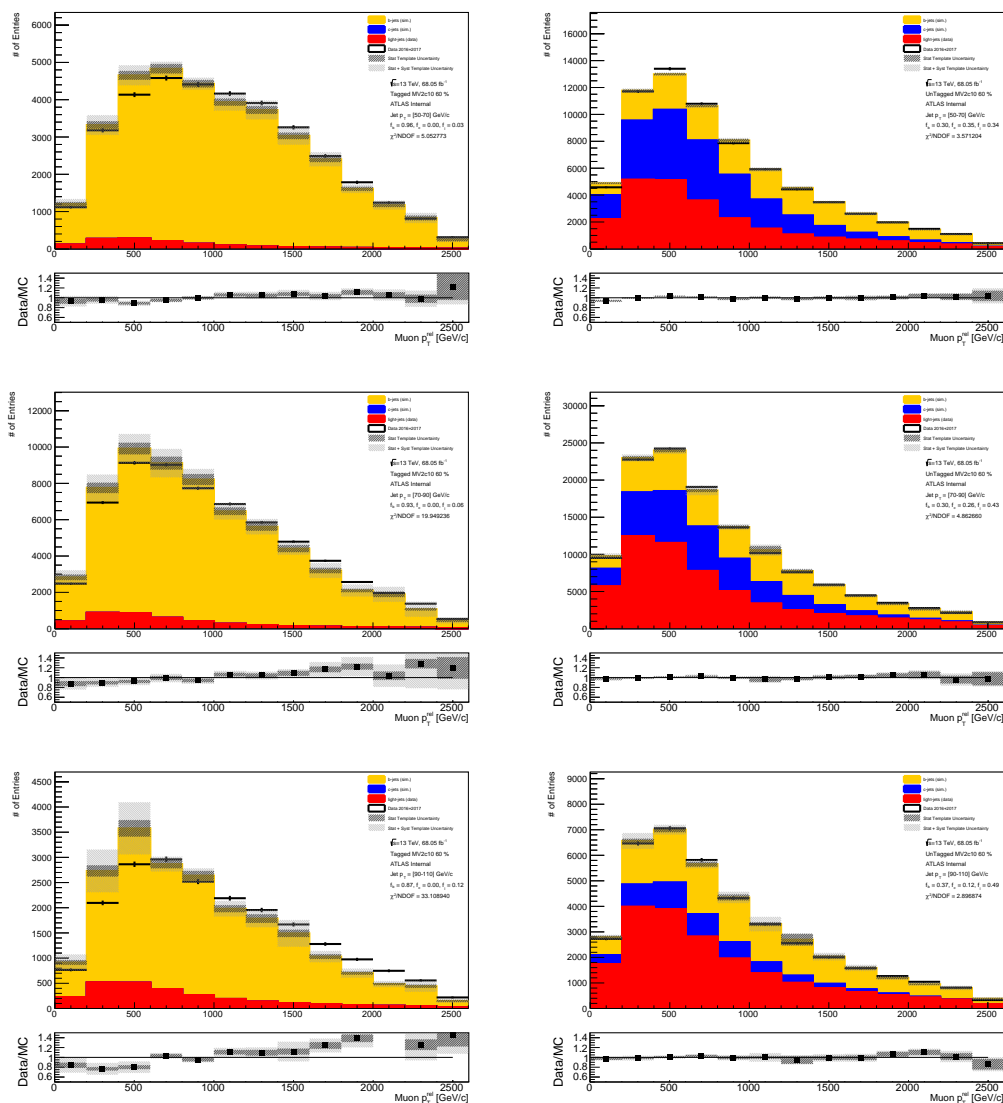


Figure A.3: Tagged (left) and untagged (right) p_T^{rel} distributions for 50-70 GeV (top), 70-90 GeV (middle), and 90-110 GeV (bottom) p_T^{jet} bins using flavor fractions obtained by the log-likelihood fit.

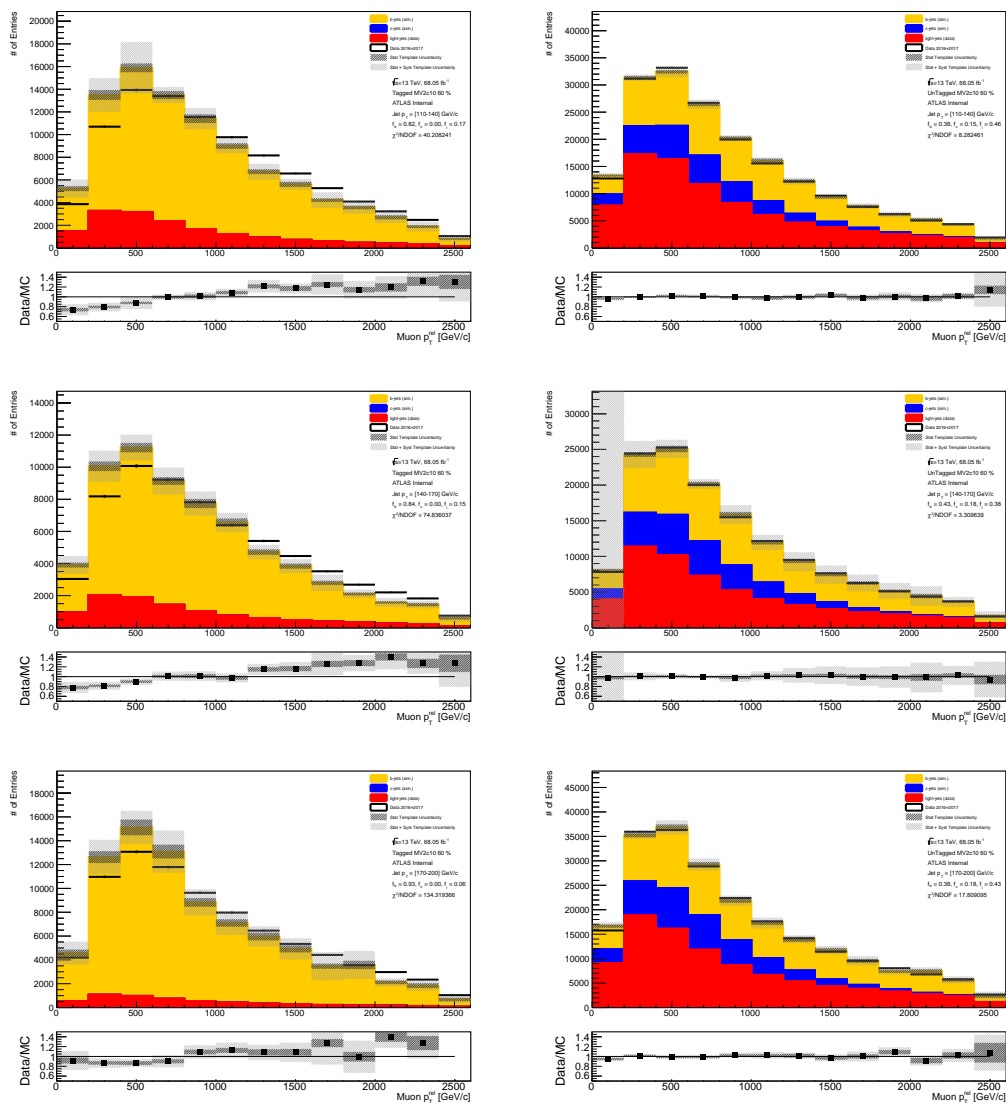


Figure A.4: Tagged (left) and untagged (right) p_T^{rel} distributions for 110-140 GeV (top), 140-170 GeV (middle), and 170-200 GeV (bottom) p_T^{jet} bins using flavor fractions obtained by the log-likelihood fit.

A.3.2 Post-fit p_T^{rel} plots for 70% WP

The results for the $\varepsilon_b^{\text{nom}} = 70\%$ WP of the MV2c10 algorithm and all p_T^{jet} bins are shown in Figures A.5-A.7.

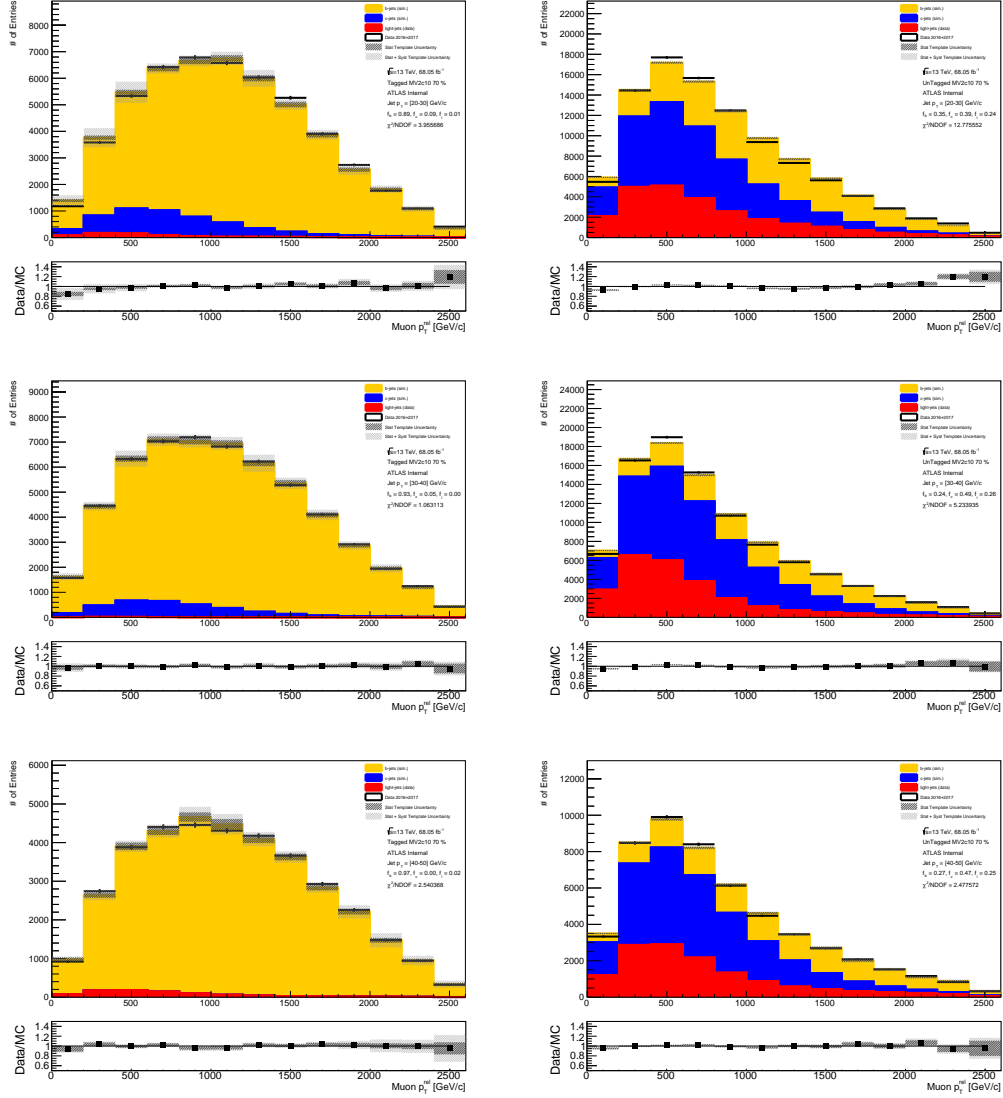


Figure A.5: Tagged (left) and untagged (right) p_T^{rel} distributions for 20-30 GeV (top), 30-40 GeV (middle), and 40-50 GeV (bottom) p_T^{jet} bins using flavor fractions obtained by the log-likelihood fit.

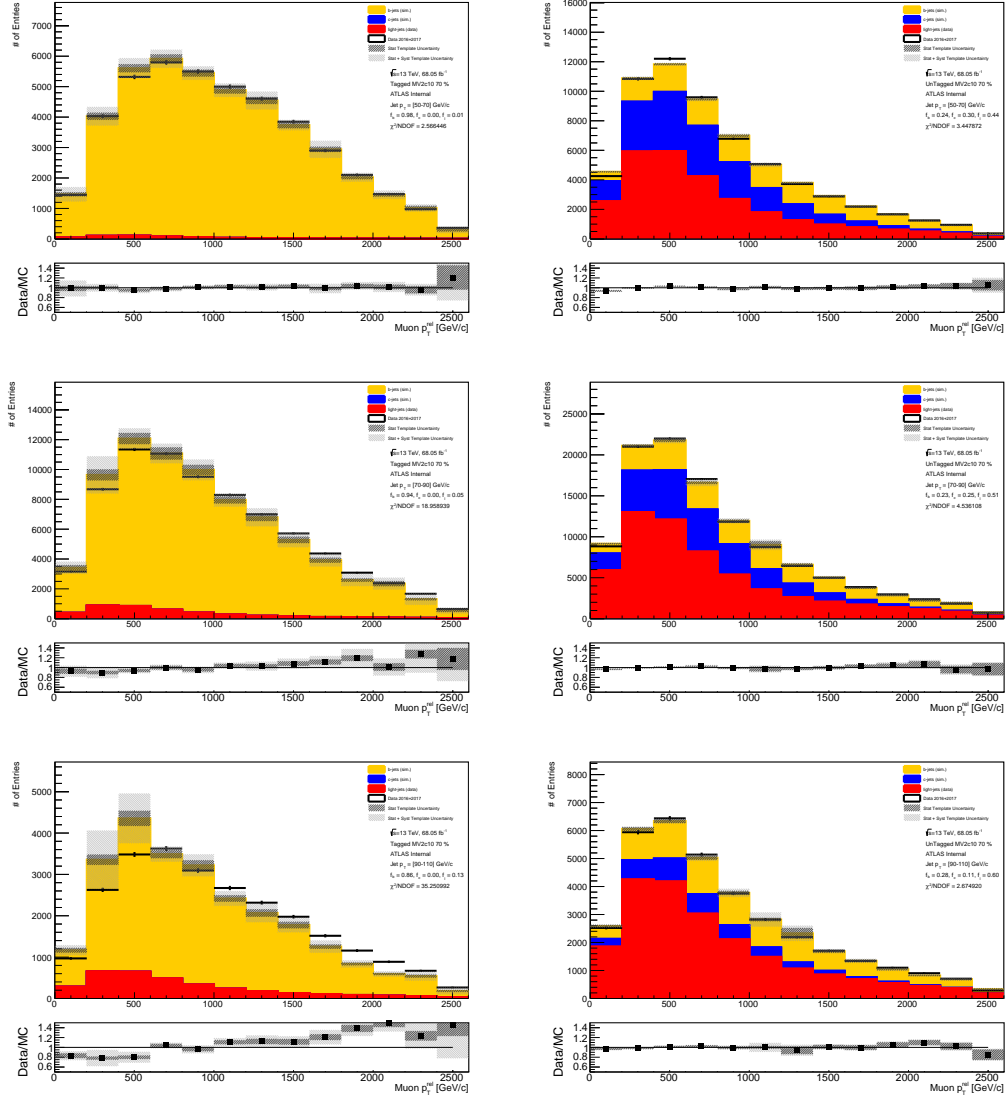


Figure A.6: Tagged (left) and untagged (right) p_T^{rel} distributions for 50-70 GeV (top), 70-90 GeV (middle), and 90-110 GeV (bottom) p_T^{jet} bins using flavor fractions obtained by the log-likelihood fit.

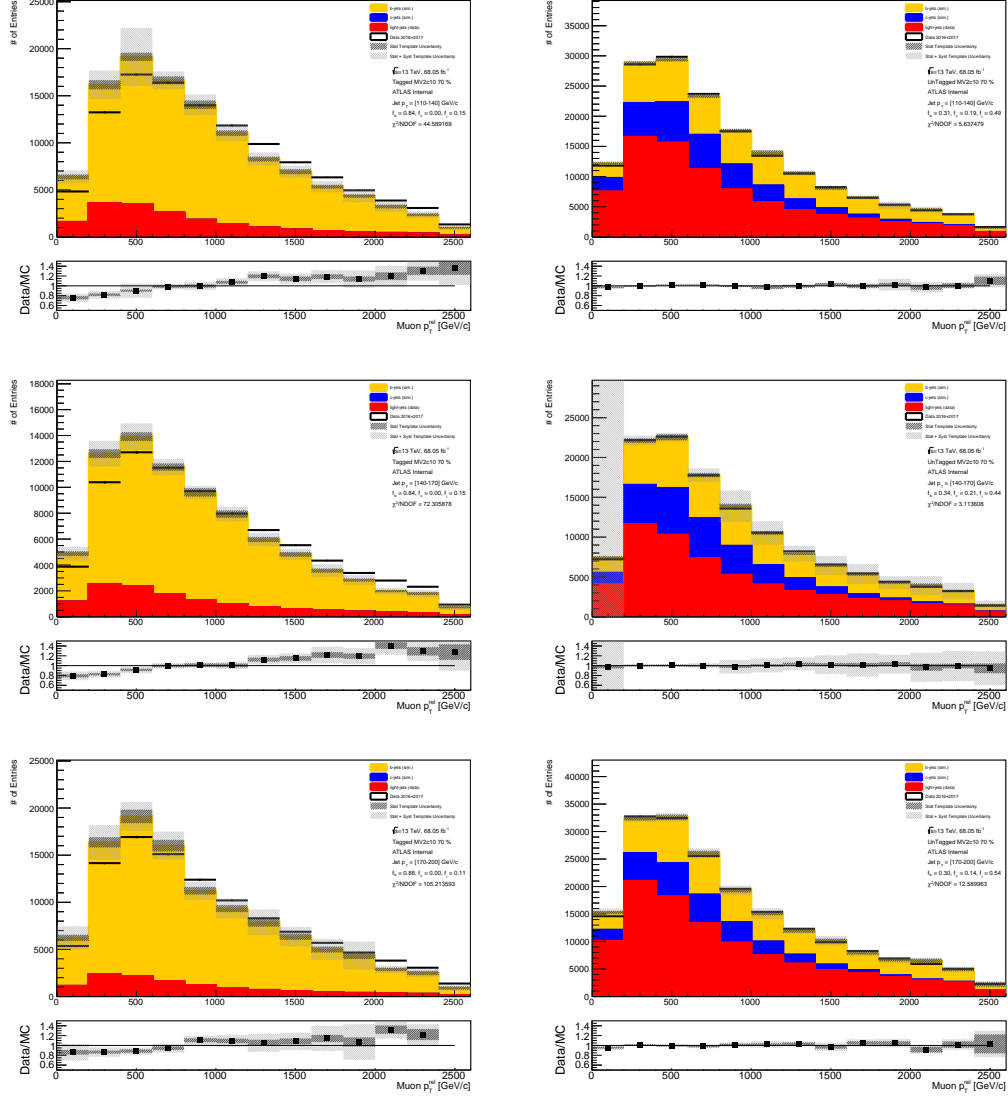


Figure A.7: Tagged (left) and untagged (right) p_T^{rel} distributions for 110-140 GeV (top), 140-170 GeV (middle), and 170-200 GeV (bottom) p_T^{jet} bins using flavor fractions obtained by the log-likelihood fit.

A.3.3 Post-fit p_T^{rel} plots for 77% WP

The results for the $\varepsilon_b^{\text{nom}} = 77\%$ WP of the MV2c10 algorithm and all p_T^{jet} bins are shown in Figures A.8-A.10.

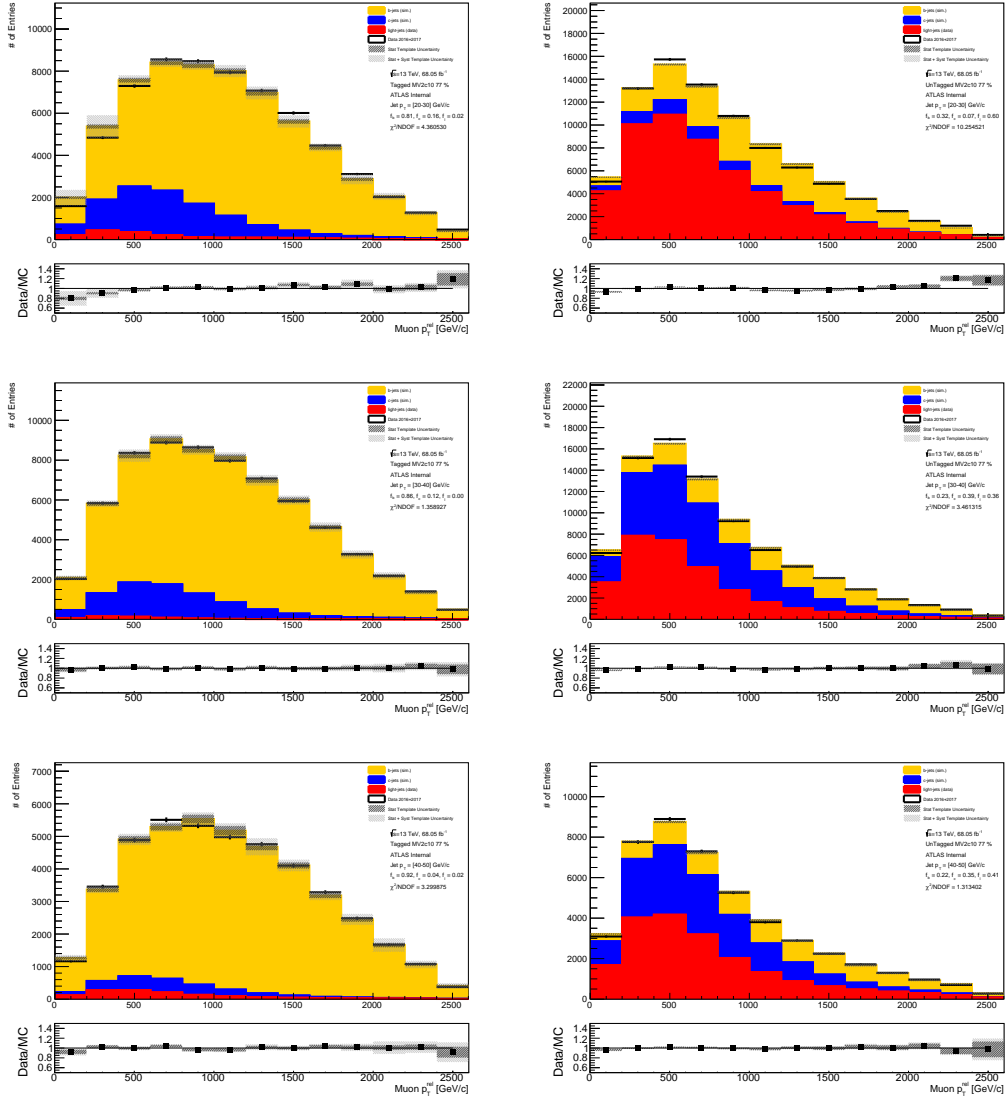


Figure A.8: Tagged (left) and untagged (right) p_T^{rel} distributions for 20-30 GeV (top), 30-40 GeV (middle), and 40-50 GeV (bottom) p_T^{jet} bins using flavor fractions obtained by the log-likelihood fit.

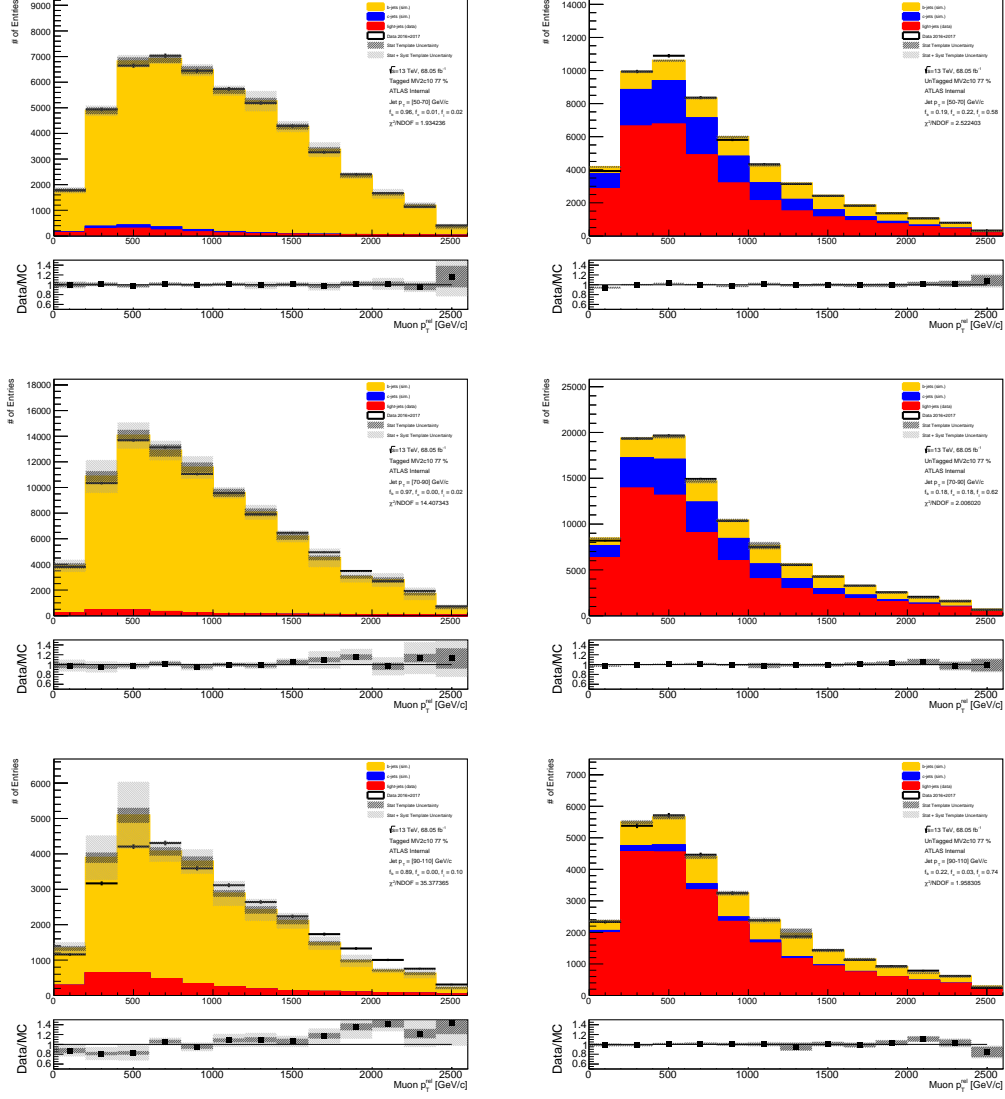


Figure A.9: Tagged (left) and untagged (right) p_T^{rel} distributions for 50-70 GeV (top), 70-90 GeV (middle), and 90-110 GeV (bottom) p_T^{jet} bins using flavor fractions obtained by the log-likelihood fit.

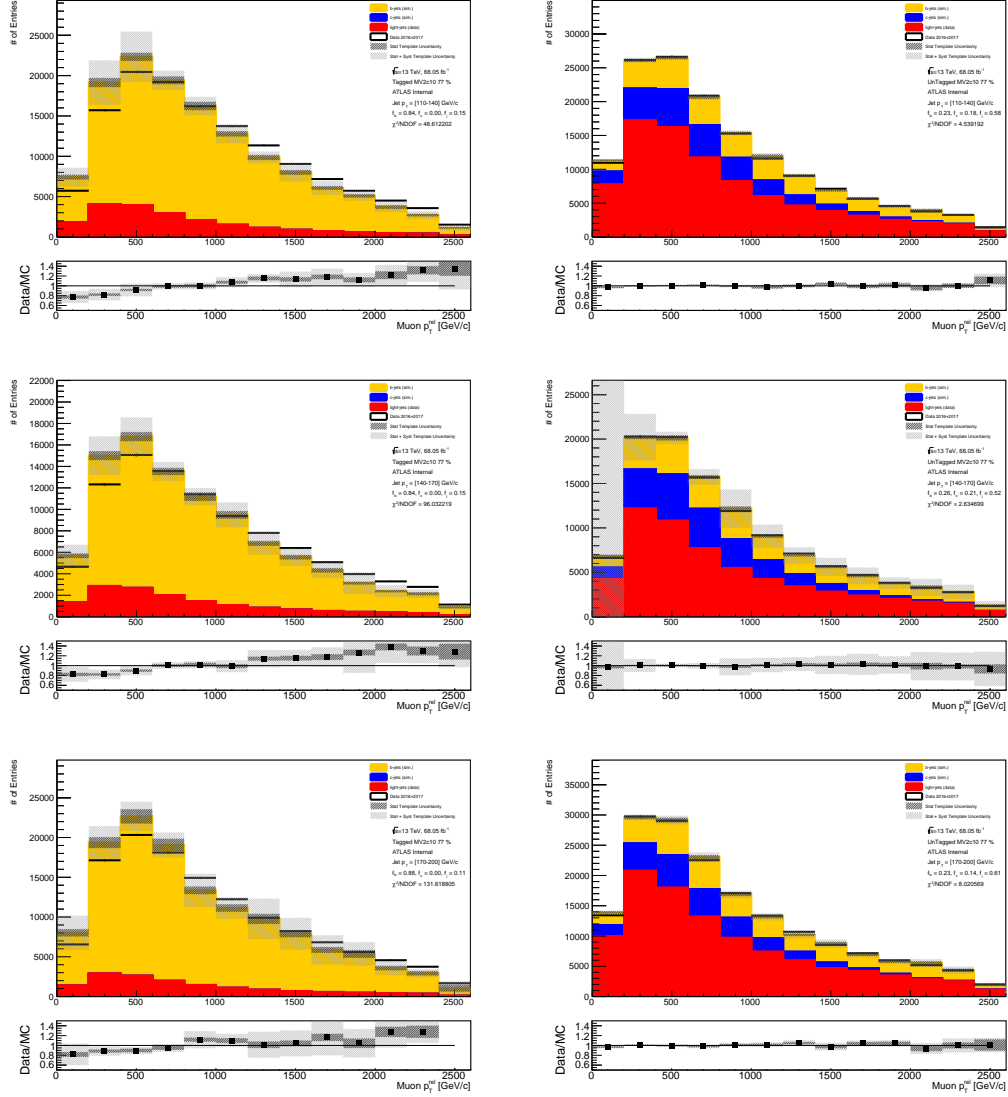


Figure A.10: Tagged (left) and untagged (right) p_T^{rel} distributions for 110-140 GeV (top), 140-170 GeV (middle), and 170-200 GeV (bottom) p_T^{jet} bins using flavor fractions obtained by the log-likelihood fit.

A.3.4 Post-fit p_T^{rel} plots for 85% WP

The results for the $\varepsilon_b^{\text{nom}} = 85\%$ WP of the MV2c10 algorithm and all p_T^{jet} bins are shown in Figures A.11-A.13.

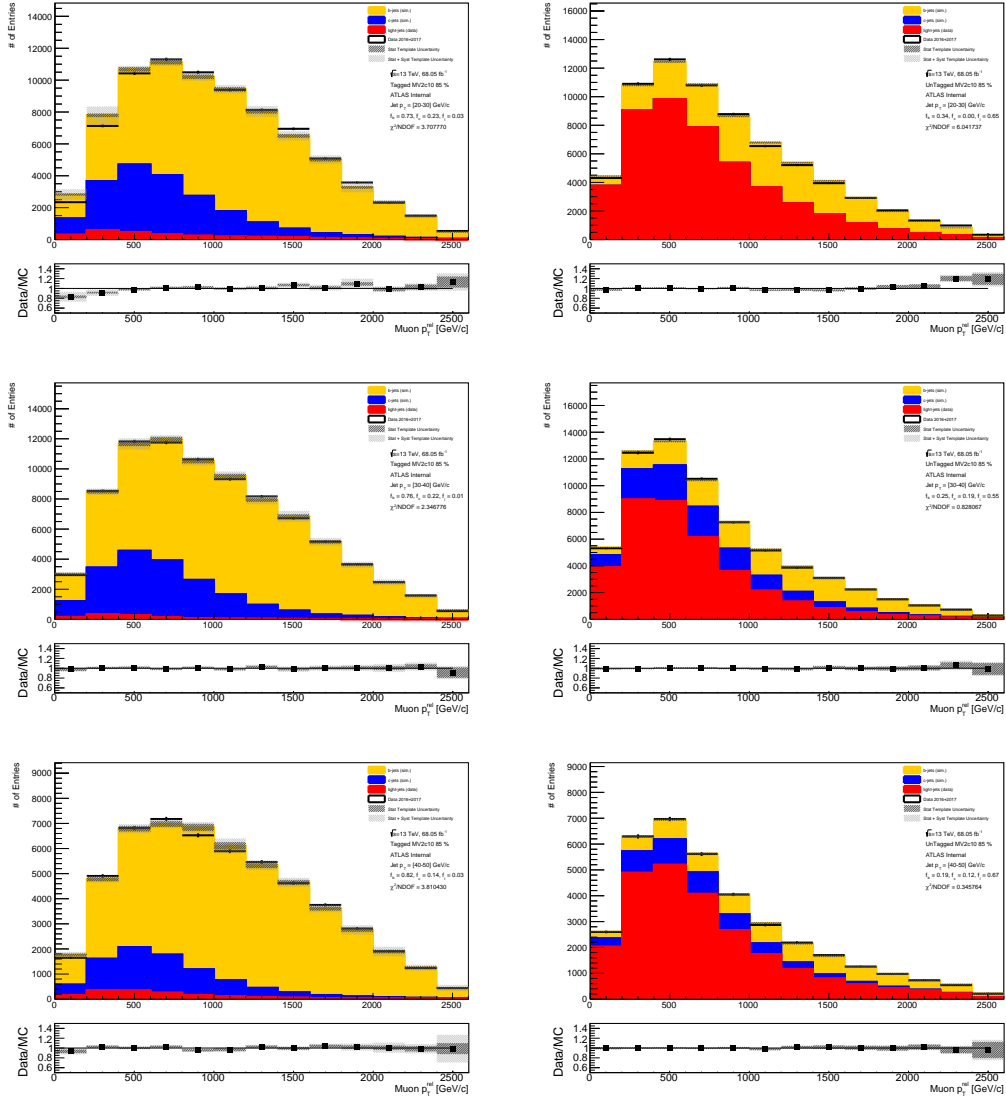


Figure A.11: Tagged (left) and untagged (right) p_T^{rel} distributions for 20-30 GeV (top), 30-40 GeV (middle), and 40-50 GeV (bottom) p_T^{jet} bins using flavor fractions obtained by the log-likelihood fit.

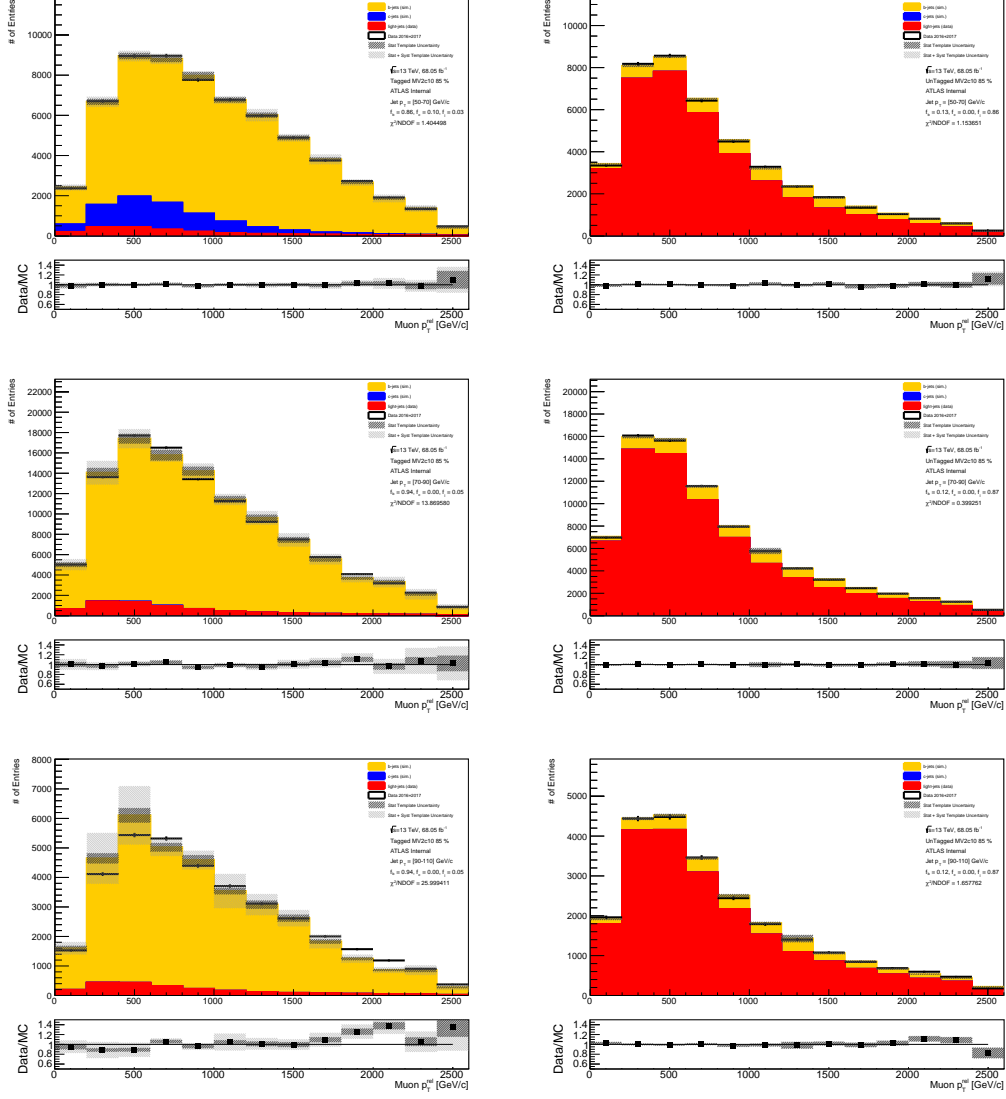


Figure A.12: Tagged (left) and untagged (right) p_T^{rel} distributions for 50-70 GeV (top), 70-90 GeV (middle), and 90-110 GeV (bottom) p_T^{jet} bins using flavor fractions obtained by the log-likelihood fit.

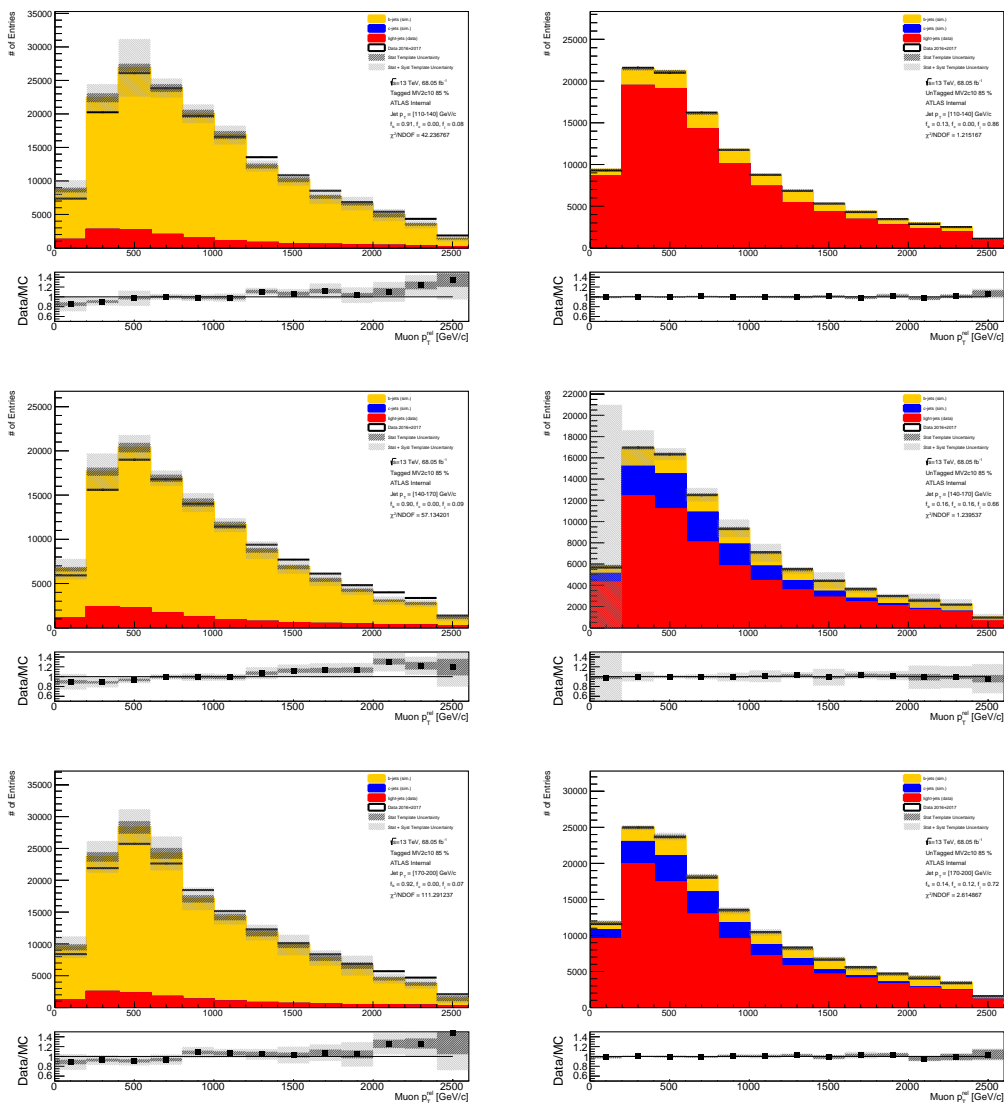


Figure A.13: Tagged (left) and untagged (right) p_T^{rel} distributions for 110-140 GeV (top), 140-170 GeV (middle), and 170-200 GeV (bottom) p_T^{jet} bins using flavor fractions obtained by the log-likelihood fit.

A.4 Correlation Study Plots for ABCD Method

This section presents plots documenting the correlation and distribution of signal and background samples for all signals and all regions in the ABCD method of background estimation for the boostedB2Q analysis. Plots are shown both without and with region-specific $\min \Delta\phi(j, E_T^{\text{miss}})$ cuts.

A.4.1 Wh Selection

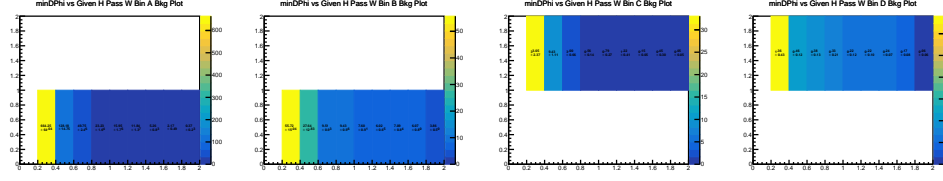


Figure A.14: Background distribution without $\min \Delta\phi(j, E_T^{\text{miss}})$ cuts for regions A, B, C, and D (from left to right) in $\min \Delta\phi(j, E_T^{\text{miss}})$ (x-axis) versus boson-tagging cut decision (y-axis)

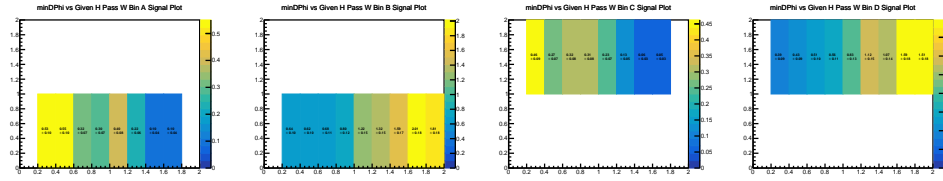


Figure A.15: Signal distribution without $\min \Delta\phi(j, E_T^{\text{miss}})$ cuts for regions A, B, C, and D (from left to right) in $\min \Delta\phi(j, E_T^{\text{miss}})$ (x-axis) versus boson-tagging cut decision (y-axis)

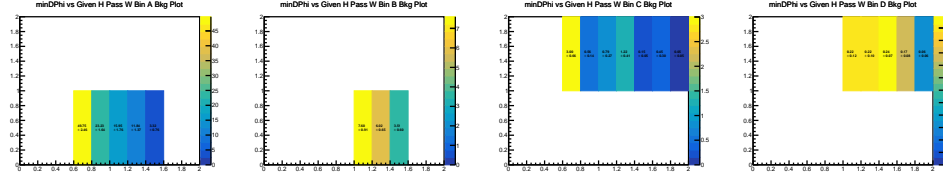


Figure A.16: Background distribution with $\min \Delta\phi(j, E_T^{\text{miss}})$ cuts for regions A, B, C, and D (from left to right) in $\min \Delta\phi(j, E_T^{\text{miss}})$ (x-axis) versus boson-tagging cut decision (y-axis)

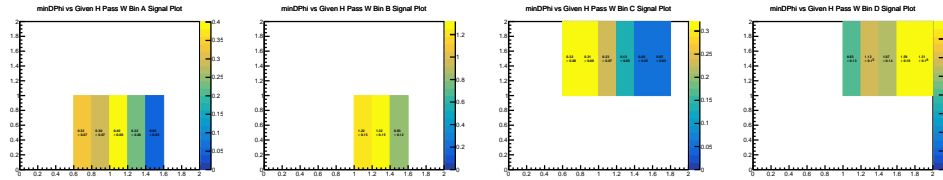


Figure A.17: Signal distribution with $\min \Delta\phi(j, E_T^{\text{miss}})$ cuts for regions A, B, C, and D (from left to right) in $\min \Delta\phi(j, E_T^{\text{miss}})$ (x-axis) versus boson-tagging cut decision (y-axis)

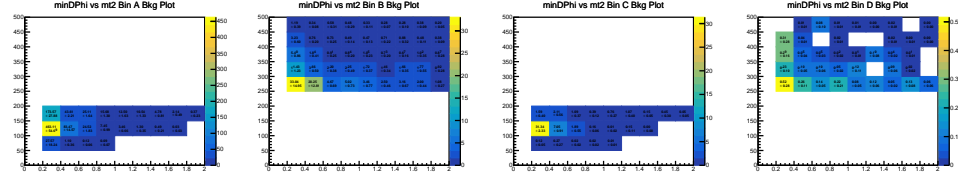


Figure A.18: Background distribution without $\min \Delta\phi(j, E_T^{\text{miss}})$ cuts for regions A, B, C, and D (from left to right) in $\min \Delta\phi(j, E_T^{\text{miss}})$ (x-axis) versus $m_{T2}^{100}(J_1, J_2)$ (y-axis)

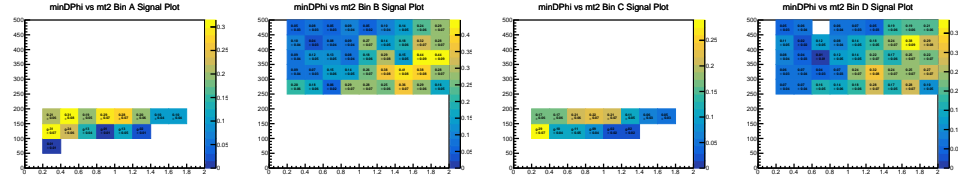


Figure A.19: Signal distribution without $\min \Delta\phi(j, E_T^{\text{miss}})$ cuts for regions A, B, C, and D (from left to right) in $\min \Delta\phi(j, E_T^{\text{miss}})$ (x-axis) versus $m_{T2}^{100}(J_1, J_2)$ (y-axis)

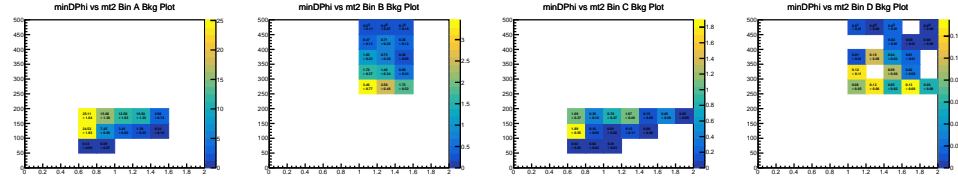


Figure A.20: Background distribution with $\min \Delta\phi(j, E_T^{\text{miss}})$ cuts for regions A, B, C, and D (from left to right) in $\min \Delta\phi(j, E_T^{\text{miss}})$ (x-axis) versus $m_{T2}^{100}(J_1, J_2)$ (y-axis)

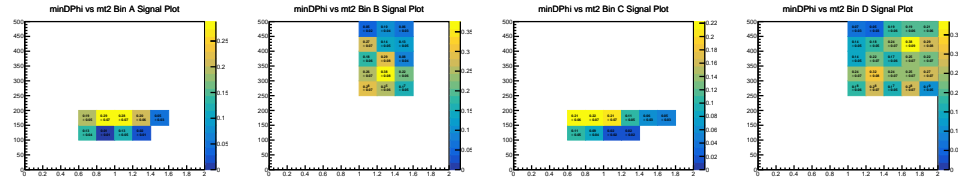


Figure A.21: Signal distribution with $\min \Delta\phi(j, E_T^{\text{miss}})$ cuts for regions A, B, C, and D (from left to right) in $\min \Delta\phi(j, E_T^{\text{miss}})$ (x-axis) versus $m_{T2}^{100}(J_1, J_2)$ (y-axis)

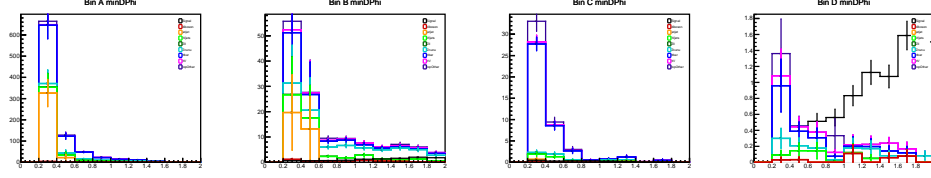


Figure A.22: Background (colors) and signal (black) $\min \Delta\phi(j, E_T^{\text{miss}})$ distributions without $\min \Delta\phi(j, E_T^{\text{miss}})$ cuts for regions A, B, C, and D (from left to right)

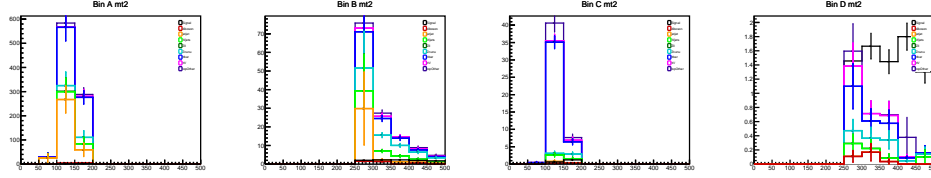


Figure A.23: Background (colors) and signal (black) $m_{T2}^{100}(J_1, J_2)$ distributions without $\min \Delta\phi(j, E_T^{\text{miss}})$ cuts for regions A, B, C, and D (from left to right)

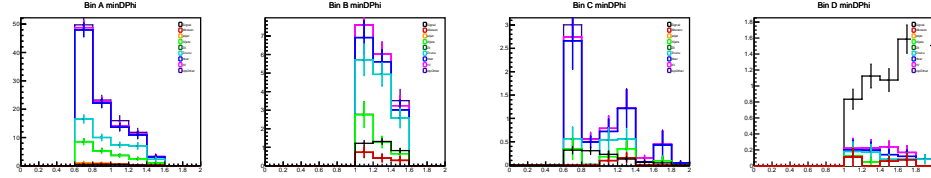


Figure A.24: Background (colors) and signal (black) $\min \Delta\phi(j, E_T^{\text{miss}})$ distributions with $\min \Delta\phi(j, E_T^{\text{miss}})$ cuts for regions A, B, C, and D (from left to right)

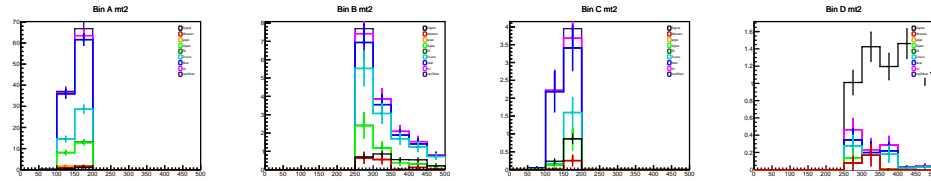


Figure A.25: Background (colors) and signal (black) $m_{T2}^{100}(J_1, J_2)$ distributions with $\min \Delta\phi(j, E_T^{\text{miss}})$ cuts for regions A, B, C, and D (from left to right)

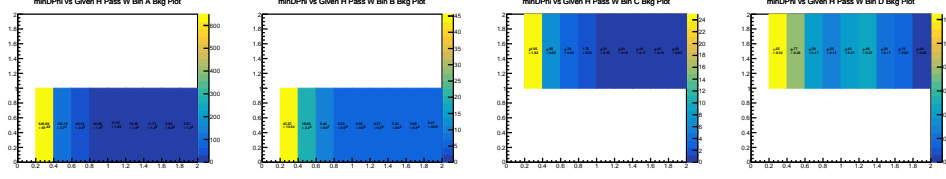
A.4.2 WZ Selection

Figure A.26: Background distribution without $\min \Delta\phi(j, E_T^{\text{miss}})$ cuts for regions A, B, C, and D (from left to right) in $\min \Delta\phi(j, E_T^{\text{miss}})$ (x-axis) versus boson-tagging cut decision (y-axis)

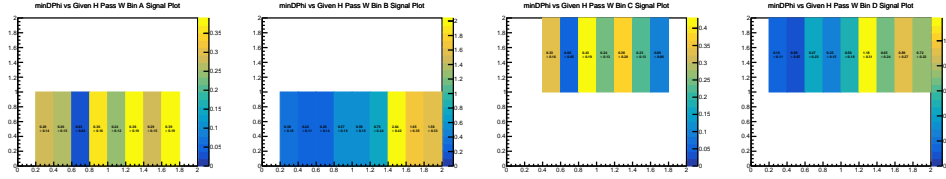


Figure A.27: Signal distribution without $\min \Delta\phi(j, E_T^{\text{miss}})$ cuts for regions A, B, C, and D (from left to right) in $\min \Delta\phi(j, E_T^{\text{miss}})$ (x-axis) versus boson-tagging cut decision (y-axis)

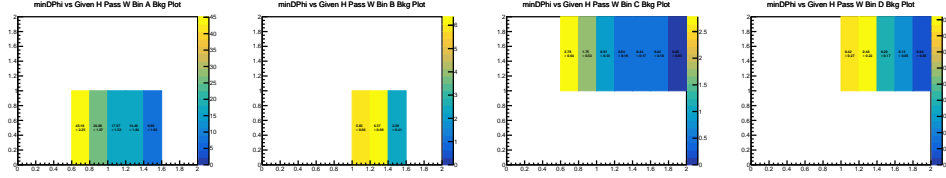


Figure A.28: Background distribution with $\min \Delta\phi(j, E_T^{\text{miss}})$ cuts for regions A, B, C, and D (from left to right) in $\min \Delta\phi(j, E_T^{\text{miss}})$ (x-axis) versus boson-tagging cut decision (y-axis)

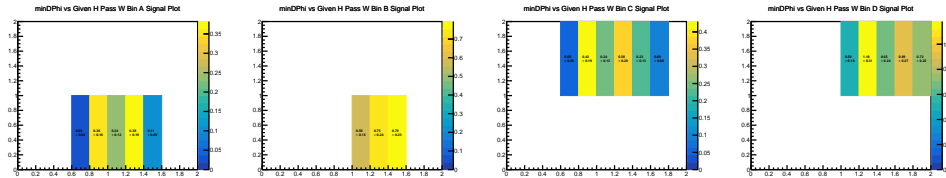


Figure A.29: Signal distribution with $\min \Delta\phi(j, E_T^{\text{miss}})$ cuts for regions A, B, C, and D (from left to right) in $\min \Delta\phi(j, E_T^{\text{miss}})$ (x-axis) versus boson-tagging cut decision (y-axis)

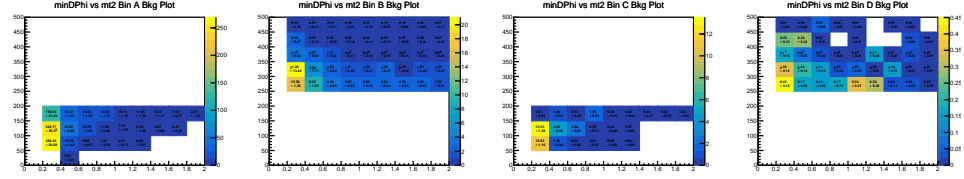


Figure A.30: Background distribution without $\min \Delta\phi(j, E_T^{\text{miss}})$ cuts for regions A, B, C, and D (from left to right) in $\min \Delta\phi(j, E_T^{\text{miss}})$ (x-axis) versus $m_{T2}^{100}(J_1, J_2)$ (y-axis)

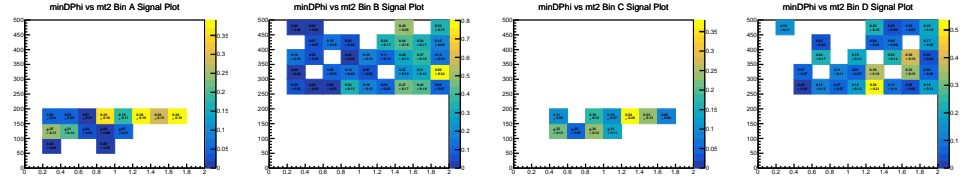


Figure A.31: Signal distribution without $\min \Delta\phi(j, E_T^{\text{miss}})$ cuts for regions A, B, C, and D (from left to right) in $\min \Delta\phi(j, E_T^{\text{miss}})$ (x-axis) versus $m_{T2}^{100}(J_1, J_2)$ (y-axis)

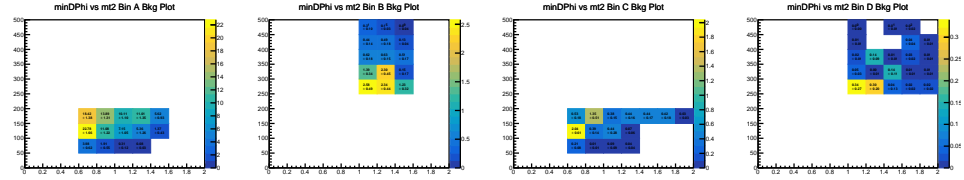


Figure A.32: Background distribution with $\min \Delta\phi(j, E_T^{\text{miss}})$ cuts for regions A, B, C, and D (from left to right) in $\min \Delta\phi(j, E_T^{\text{miss}})$ (x-axis) versus $m_{T2}^{100}(J_1, J_2)$ (y-axis)

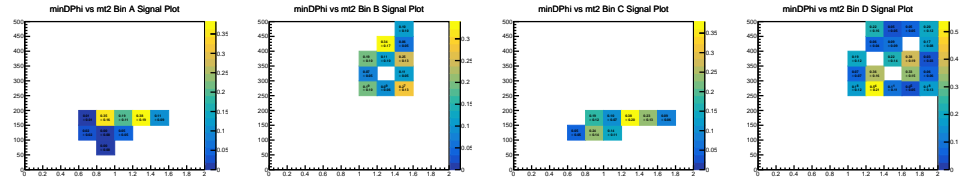


Figure A.33: Signal distribution with $\min \Delta\phi(j, E_T^{\text{miss}})$ cuts for regions A, B, C, and D (from left to right) in $\min \Delta\phi(j, E_T^{\text{miss}})$ (x-axis) versus $m_{T2}^{100}(J_1, J_2)$ (y-axis)

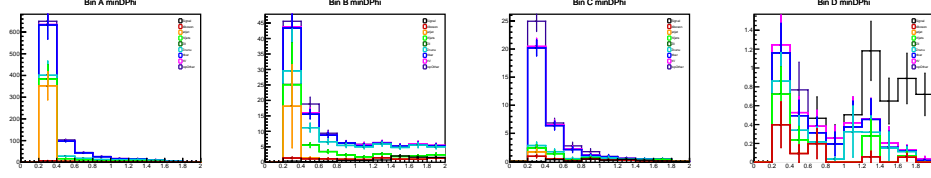


Figure A.34: Background (colors) and signal (black) $\min \Delta\phi(j, E_T^{\text{miss}})$ distributions without $\min \Delta\phi(j, E_T^{\text{miss}})$ cuts for regions A, B, C, and D (from left to right)

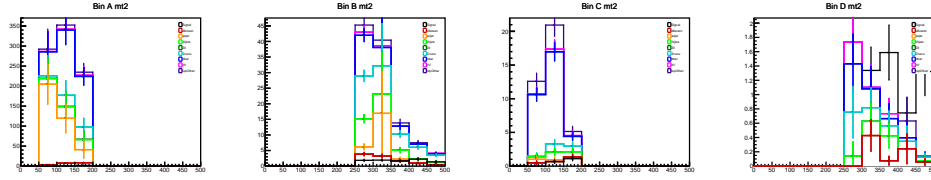


Figure A.35: Background (colors) and signal (black) $m_{T2}^{100}(J_1, J_2)$ distributions without $\min \Delta\phi(j, E_T^{\text{miss}})$ cuts for regions A, B, C, and D (from left to right)

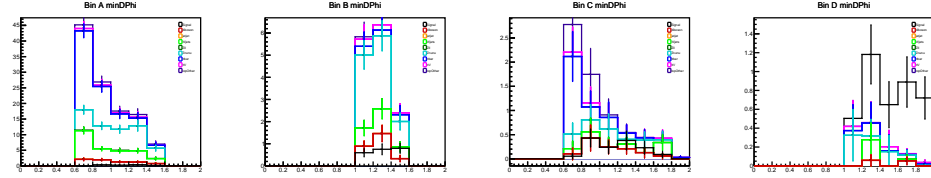


Figure A.36: Background (colors) and signal (black) $\min \Delta\phi(j, E_T^{\text{miss}})$ distributions with $\min \Delta\phi(j, E_T^{\text{miss}})$ cuts for regions A, B, C, and D (from left to right)

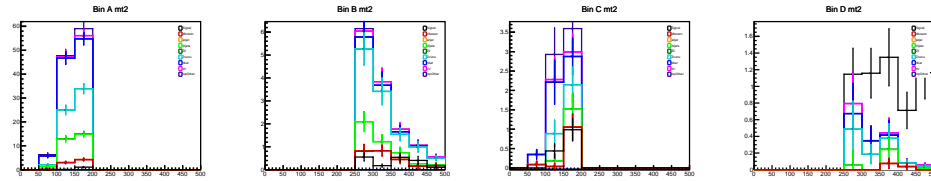


Figure A.37: Background (colors) and signal (black) $m_{T2}^{100}(J_1, J_2)$ distributions with $\min \Delta\phi(j, E_T^{\text{miss}})$ cuts for regions A, B, C, and D (from left to right)

A.4.3 Zh Selection

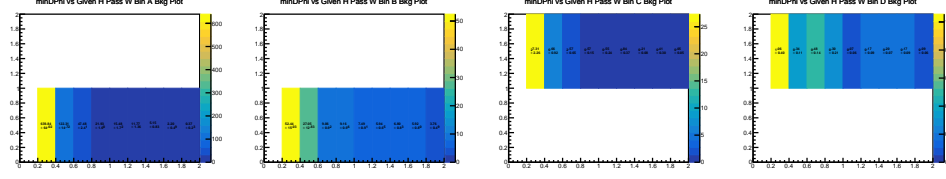


Figure A.38: Background distribution without $\min \Delta\phi(j, E_T^{\text{miss}})$ cuts for regions A, B, C, and D (from left to right) in $\min \Delta\phi(j, E_T^{\text{miss}})$ (x-axis) versus boson-tagging cut decision (y-axis)

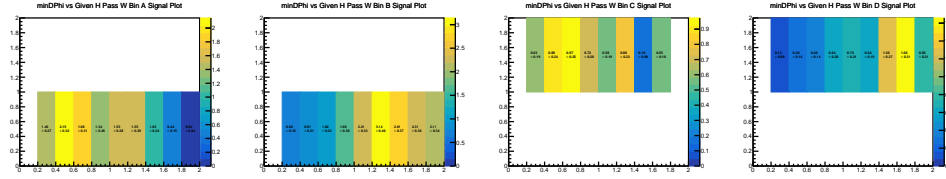


Figure A.39: Signal distribution without $\min \Delta\phi(j, E_T^{\text{miss}})$ cuts for regions A, B, C, and D (from left to right) in $\min \Delta\phi(j, E_T^{\text{miss}})$ (x-axis) versus boson-tagging cut decision (y-axis)

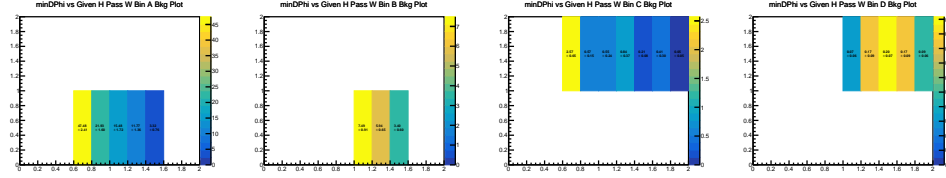


Figure A.40: Background distribution with $\min \Delta\phi(j, E_T^{\text{miss}})$ cuts for regions A, B, C, and D (from left to right) in $\min \Delta\phi(j, E_T^{\text{miss}})$ (x-axis) versus boson-tagging cut decision (y-axis)

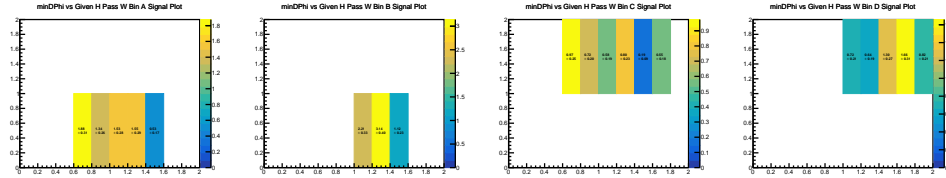


Figure A.41: Signal distribution with $\min \Delta\phi(j, E_T^{\text{miss}})$ cuts for regions A, B, C, and D (from left to right) in $\min \Delta\phi(j, E_T^{\text{miss}})$ (x-axis) versus boson-tagging cut decision (y-axis)

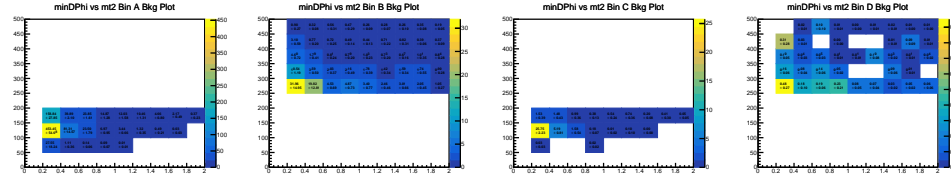


Figure A.42: Background distribution without $\min \Delta\phi(j, E_T^{\text{miss}})$ cuts for regions A, B, C, and D (from left to right) in $\min \Delta\phi(j, E_T^{\text{miss}})$ (x-axis) versus $m_{T2}^{100}(J_1, J_2)$ (y-axis)

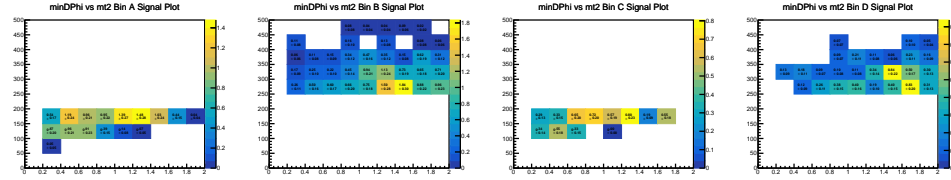


Figure A.43: Signal distribution without $\min \Delta\phi(j, E_T^{\text{miss}})$ cuts for regions A, B, C, and D (from left to right) in $\min \Delta\phi(j, E_T^{\text{miss}})$ (x-axis) versus $m_{T2}^{100}(J_1, J_2)$ (y-axis)

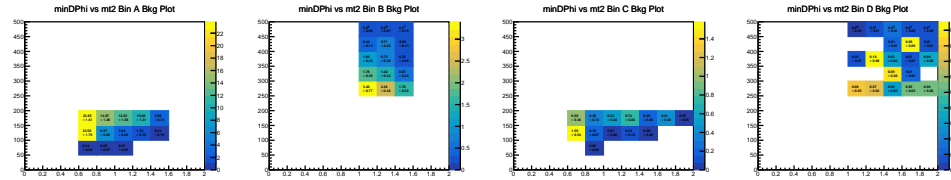


Figure A.44: Background distribution with $\min \Delta\phi(j, E_T^{\text{miss}})$ cuts for regions A, B, C, and D (from left to right) in $\min \Delta\phi(j, E_T^{\text{miss}})$ (x-axis) versus $m_{T2}^{100}(J_1, J_2)$ (y-axis)

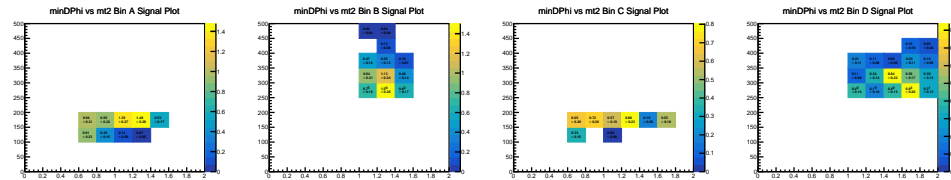


Figure A.45: Signal distribution with $\min \Delta\phi(j, E_T^{\text{miss}})$ cuts for regions A, B, C, and D (from left to right) in $\min \Delta\phi(j, E_T^{\text{miss}})$ (x-axis) versus $m_{T2}^{100}(J_1, J_2)$ (y-axis)

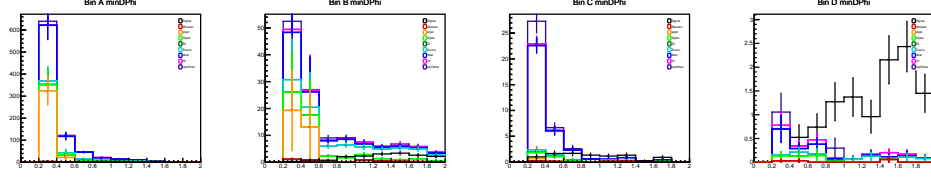


Figure A.46: Background (colors) and signal (black) $\min \Delta\phi(j, E_T^{\text{miss}})$ distributions without $\min \Delta\phi(j, E_T^{\text{miss}})$ cuts for regions A, B, C, and D (from left to right)

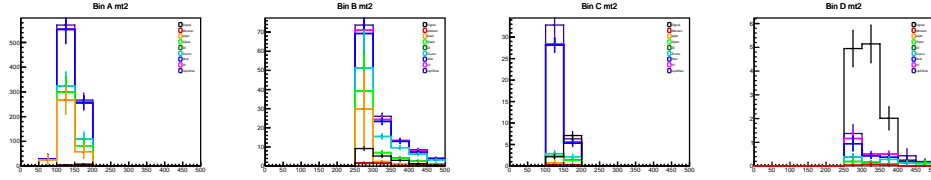


Figure A.47: Background (colors) and signal (black) $m_{T2}^{100}(J_1, J_2)$ distributions without $\min \Delta\phi(j, E_T^{\text{miss}})$ cuts for regions A, B, C, and D (from left to right)

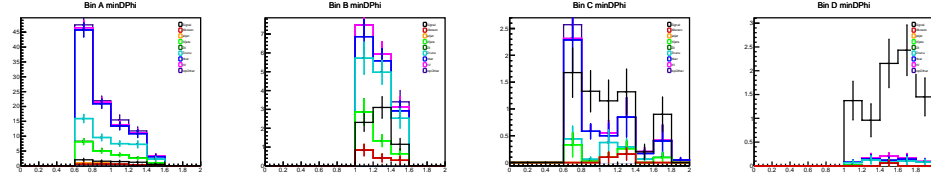


Figure A.48: Background (colors) and signal (black) $\min \Delta\phi(j, E_T^{\text{miss}})$ distributions with $\min \Delta\phi(j, E_T^{\text{miss}})$ cuts for regions A, B, C, and D (from left to right)

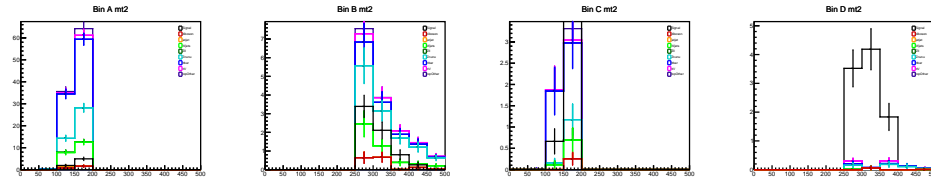


Figure A.49: Background (colors) and signal (black) $m_{T2}^{100}(J_1, J_2)$ distributions with $\min \Delta\phi(j, E_T^{\text{miss}})$ cuts for regions A, B, C, and D (from left to right)

A.4.4 ZZ Selection

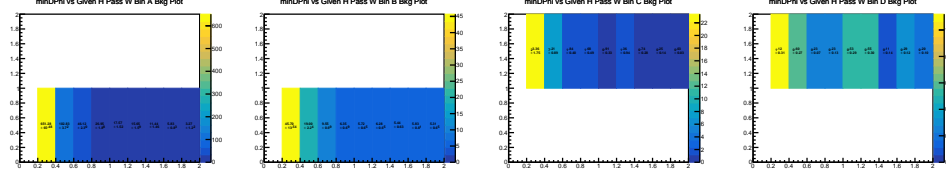


Figure A.50: Background distribution without $\min \Delta\phi(j, E_T^{\text{miss}})$ cuts for regions A, B, C, and D (from left to right) in $\min \Delta\phi(j, E_T^{\text{miss}})$ (x-axis) versus boson-tagging cut decision (y-axis)

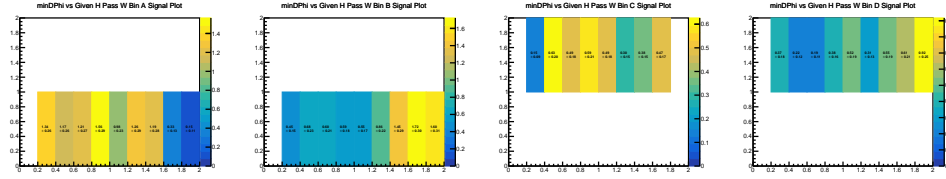


Figure A.51: Signal distribution without $\min \Delta\phi(j, E_T^{\text{miss}})$ cuts for regions A, B, C, and D (from left to right) in $\min \Delta\phi(j, E_T^{\text{miss}})$ (x-axis) versus boson-tagging cut decision (y-axis)

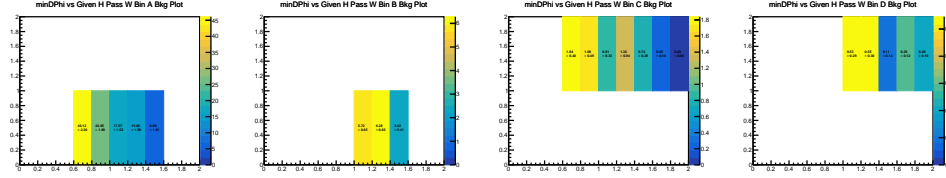


Figure A.52: Background distribution with $\min \Delta\phi(j, E_T^{\text{miss}})$ cuts for regions A, B, C, and D (from left to right) in $\min \Delta\phi(j, E_T^{\text{miss}})$ (x-axis) versus boson-tagging cut decision (y-axis)

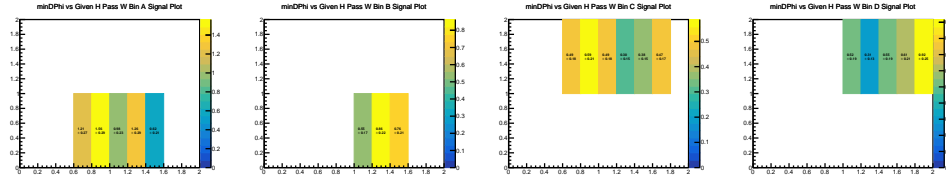


Figure A.53: Signal distribution with $\min \Delta\phi(j, E_T^{\text{miss}})$ cuts for regions A, B, C, and D (from left to right) in $\min \Delta\phi(j, E_T^{\text{miss}})$ (x-axis) versus boson-tagging cut decision (y-axis)

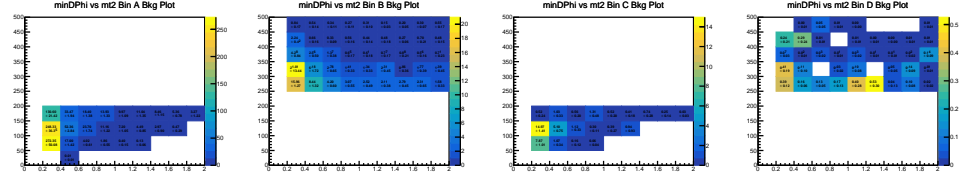


Figure A.54: Background distribution without $\min \Delta\phi(j, E_T^{\text{miss}})$ cuts for regions A, B, C, and D (from left to right) in $\min \Delta\phi(j, E_T^{\text{miss}})$ (x-axis) versus $m_{T2}^{100}(J_1, J_2)$ (y-axis)

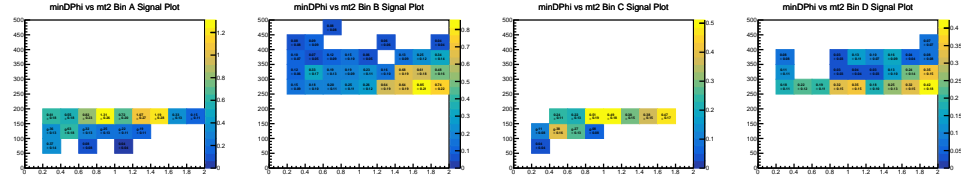


Figure A.55: Signal distribution without $\min \Delta\phi(j, E_T^{\text{miss}})$ cuts for regions A, B, C, and D (from left to right) in $\min \Delta\phi(j, E_T^{\text{miss}})$ (x-axis) versus $m_{T2}^{100}(J_1, J_2)$ (y-axis)

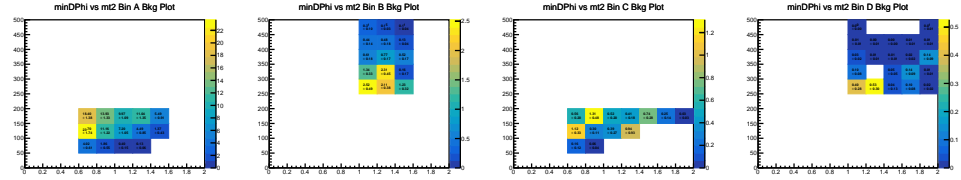


Figure A.56: Background distribution with $\min \Delta\phi(j, E_T^{\text{miss}})$ cuts for regions A, B, C, and D (from left to right) in $\min \Delta\phi(j, E_T^{\text{miss}})$ (x-axis) versus $m_{T2}^{100}(J_1, J_2)$ (y-axis)

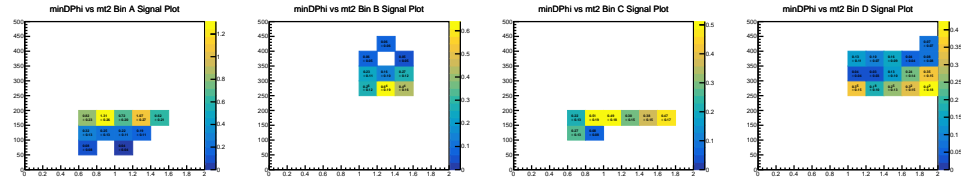


Figure A.57: Signal distribution with $\min \Delta\phi(j, E_T^{\text{miss}})$ cuts for regions A, B, C, and D (from left to right) in $\min \Delta\phi(j, E_T^{\text{miss}})$ (x-axis) versus $m_{T2}^{100}(J_1, J_2)$ (y-axis)

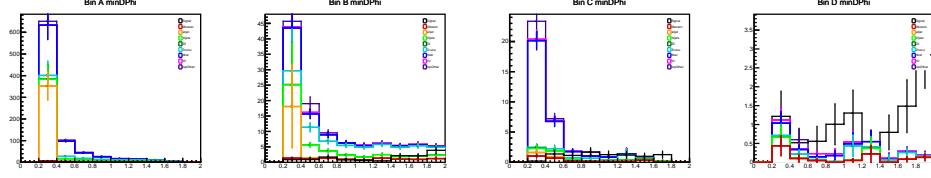


Figure A.58: Background (colors) and signal (black) $\min \Delta\phi(j, E_T^{\text{miss}})$ distributions without $\min \Delta\phi(j, E_T^{\text{miss}})$ cuts for regions A, B, C, and D (from left to right)

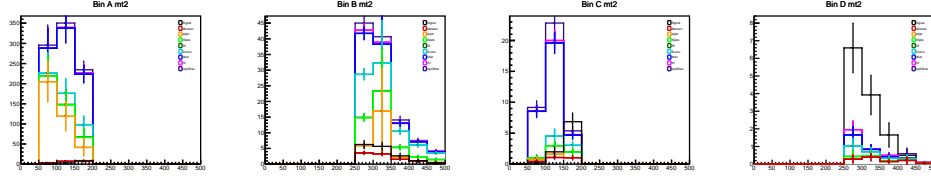


Figure A.59: Background (colors) and signal (black) $m_{T2}^{100}(J_1, J_2)$ distributions without $\min \Delta\phi(j, E_T^{\text{miss}})$ cuts for regions A, B, C, and D (from left to right)

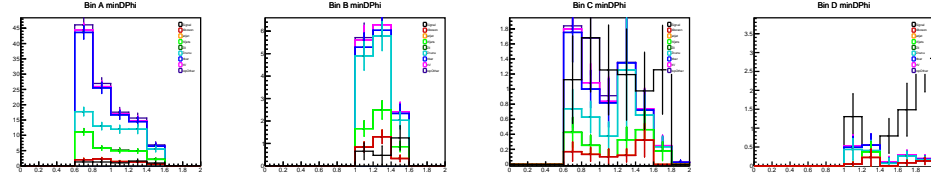


Figure A.60: Background (colors) and signal (black) $\min \Delta\phi(j, E_T^{\text{miss}})$ distributions with $\min \Delta\phi(j, E_T^{\text{miss}})$ cuts for regions A, B, C, and D (from left to right)

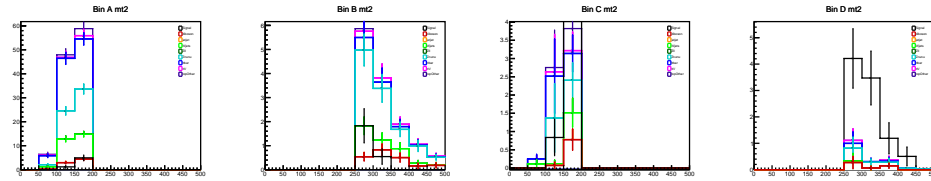


Figure A.61: Background (colors) and signal (black) $m_{T2}^{100}(J_1, J_2)$ distributions with $\min \Delta\phi(j, E_T^{\text{miss}})$ cuts for regions A, B, C, and D (from left to right)

Bibliography

- [1] N. Gaiman, *Good Omens: The Nice and Accurate Prophecies of Agnes Nutter, Witch*. William Morrow, Nov, 2006. <https://www.xarg.org/ref/a/0060853980/>. 1
- [2] ATLAS Collaboration Collaboration, M. Elsing, T. Eifert, G. Sabato, S. Kamioka, A. M. Nairz, E. Moyse, and C. Gumpert, *ATLAS Fast Physics Monitoring: TADA*, <https://cds.cern.ch/record/2218037>. 1
- [3] for the ATLAS collaboration Collaboration, P. Calafiura, C. Leggett, R. Seuster, V. Tsulaia, and P. van Gemmeren, *Running ATLAS workloads within massively parallel distributed applications using Athena Multi-Process framework (AthenaMP)*, Tech. Rep. ATL-SOFT-PROC-2015-020, CERN, Geneva, May, 2015. <https://cds.cern.ch/record/2015230>. 1, 3.6.7
- [4] Ovid, *Metamorphoses (Hackett Classics)*. Hackett Publishing Company, Inc., Sep, 2010. <https://www.xarg.org/ref/a/1603843078/>. 2
- [5] M. E. Peskin and D. V. Schroeder, *An Introduction To Quantum Field Theory (Frontiers in Physics)*. Westview Press, 1995. 2.1.1, 2.1.2
- [6] I. J. R. Aitchison and A. J. Hey, *Gauge Theories in Particle Physics: A Practical Introduction, Volume 1: From Relativistic Quantum Mechanics to QED, Fourth Edition*. CRC Press, 2012. 2.1.1, 2.1.2, 2.2.1.1
- [7] M. Thomson, *Modern particle physics*. Cambridge University Press, 2018. (document), 2.2, 2.2, 2.2.1, 2.2.1.2, 2.2.3, 2.2.3, 2.2.4.1, 2.2.5, 2.4, 2.3, 2.4, 3.3.3
- [8] V. D. Barger, *Collider Physics: Revised Edition (Frontiers in Physics)*. Westview Press, 1996. 2.2, 2.2.5
- [9] D. Griffiths, *Introduction to Elementary Particles*. John Wiley & Sons Inc, 1987. (document), 2.2, 2.2
- [10] Particle Data Group Collaboration, M. Tanabashi et al., *Review of Particle Physics*, *Phys. Rev. D* **98** (2018) 030001. (document), 2.1, 2.2.3, 2.2.4, 2.2.4.1, 2.2.4.1, 2.2.5, 2.2.5, 2.2.5, 2.5.2, 4.1, 4.7.2.1

- [11] A. Pich, *The Standard model of electroweak interactions*, pp. , 1–48. 2005.
[arXiv:hep-ph/0502010 \[hep-ph\]](#).
<http://doc.cern.ch/yellowrep/2006/2006-003/p1.pdf>. 2.2.1.1
- [12] J. Ellis, M. K. Gaillard, and D. V. Nanopoulos, *A Historical Profile of the Higgs Boson*, pp. , 255–274. 2016. [arXiv:1504.07217 \[hep-ph\]](#). 2.2.2
- [13] C. Quigg, *Gauge Theories Of The Strong, Weak, And Electromagnetic Interactions* (*Frontiers in Physics*). The Benjamin/Cummings Publishing Company, 1983. 10, A.1, A.1
- [14] J. Ellis, *Higgs Physics*, <https://cds.cern.ch/record/1638469>, 52 pages, 45 figures, Lectures presented at the ESHEP 2013 School of High-Energy Physics, to appear as part of the proceedings in a CERN Yellow Report. (document), 2.2.3, 2.2
- [15] ATLAS Collaboration, G. Aad et al., *Observation of a new particle in the search for the Standard Model Higgs boson with the ATLAS detector at the LHC*, *Phys. Lett.* **B716** (2012) 1–29, [arXiv:1207.7214 \[hep-ex\]](#). 2.2.3
- [16] *B Decays*. World Scientific Pub Co Inc, 1994. 2.2.4.1, 15
- [17] B. Grinstein, M. B. Wise, and N. Isgur, *Weak mixing angles from semileptonic decays in the quark model*, *Physical Review Letters* **56** (1986) 298–301,
<https://doi.org/10.1103/physrevlett.56.298>. 2.2.4.1
- [18] CMS Collaboration, A. M. Sirunyan et al., *Measurement of b hadron lifetimes in pp collisions at $\sqrt{s} = 8$ TeV*, *Eur. Phys. J.* **C78** (2018) 457, [arXiv:1710.08949 \[hep-ex\]](#),
[Erratum: *Eur. Phys. J.*C78,no.7,561(2018)]. 2.2.4.1
- [19] A. X. El-Khadra and M. Luke, *The mass of the b quark*, *Annual Review of Nuclear and Particle Science* **52** (2002) 201–251, [arXiv:hep-ph/0208114 \[hep-ph\]](#). 2.2.5
- [20] D. Dong, *Measurement of the b Quark Fragmentation Function in Z^0 Decays*. PhD thesis, MIT, 1999. <http://www-public.slac.stanford.edu/sciDoc/docMeta.aspx?slacPubNumber=slac-r-550>. 2.2.5
- [21] C. Peterson, D. Schlatter, I. Schmitt, and P. M. Zerwas, *Scaling violations in inclusive e^+e^- annihilation spectra*, *Phys. Rev. D* **27** (1983) 105–111,
<https://link.aps.org/doi/10.1103/PhysRevD.27.105>. (document), 2.2.5, 2.5
- [22] ATLAS Collaboration, *Optimisation of the ATLAS b -tagging performance for the 2016 LHC Run*, ATL-PHYS-PUB-2016-012, 2016, <https://cds.cern.ch/record/2160731>. 2.2.5, 4.1
- [23] CLEO Collaboration, G. Brandenburg et al., *Charged track multiplicity in B meson decay*, *Phys. Rev.* **D61** (2000) 072002, [arXiv:hep-ex/9907057 \[hep-ex\]](#). 2.2.5
- [24] D. Croon, T. E. Gonzalo, L. Graf, N. Košnik, and G. White, *GUT Physics in the era of the LHC*, *Front.in Phys.* **7** (2019) 76, [arXiv:1903.04977 \[hep-ph\]](#). 2.3
- [25] J. Primack.
<http://ircamera.as.arizona.edu/NatSci102/NatSci/images/extcosmo.htm>.
(document), 2.6, 2.3

- [26] E. Kolb, *Early Universe*. Addison-Wesley Publishing Company, Nov, 1990.
<https://www.xarg.org/ref/a/0201116030/>. 19, 2.4.1, 2.4.2, 2.4.3, 2.4.3
- [27] J. D. Kraus, *Radio Astronomy*. McGraw Hill Text, Jan, 1966.
<https://www.xarg.org/ref/a/0070353921/>. 2.4.1
- [28] K. Freese, *Status of Dark Matter in the Universe*, *Int. J. Mod. Phys. B* **1** (2017) 325–355, [arXiv:1701.01840](https://arxiv.org/abs/1701.01840) [astro-ph.CO]. (document), 2.4.1, 2.7
- [29] S. Dodelson, *Modern Cosmology*. Academic Press, Mar, 2003.
<https://www.xarg.org/ref/a/0122191412/>. 2.4.2
- [30] O. Piattella, *Lecture Notes in Cosmology (UNITEXT for Physics)*. Springer, 2018. 2.4.3
- [31] C. L. Bennett, D. Larson, J. L. Weiland, N. Jarosik, G. Hinshaw, N. Odegard, K. M. Smith, R. S. Hill, B. Gold, M. Halpern, E. Komatsu, M. R. Nolta, L. Page, D. N. Spergel, E. Wollack, J. Dunkley, A. Kogut, M. Limon, S. S. Meyer, G. S. Tucker, and E. L. Wright, *Nine-Year Wilkinson Microwave Anisotropy Probe (WMAP) Observations: Final Maps and Results*, [arXiv:1212.5225](https://arxiv.org/abs/1212.5225). (document), 2.8, 2.4.3
- [32] E. Fischer, *The properties of dark matter*, 2011. 2.4.4
- [33] D. G. Cerdeno, *Dark Matter 101*, Sep, 2016.
https://www.ippp.dur.ac.uk/~dcerdeno/Dark_Matter_Lab_files/DM.pdf. 2.4.4
- [34] C. L. Bennett, D. Larson, J. L. Weiland, N. Jarosik, G. Hinshaw, N. Odegard, K. M. Smith, R. S. Hill, B. Gold, M. Halpern, E. Komatsu, M. R. Nolta, L. Page, D. N. Spergel, E. Wollack, J. Dunkley, A. Kogut, M. Limon, S. S. Meyer, G. S. Tucker, and E. L. Wright, *Nine-Year Wilkinson Microwave Anisotropy Probe (WMAP) Observations: Final Maps and Results*, *The Astrophysical Journal Supplement Series* **208** (2012), [arXiv:1212.5225](https://arxiv.org/abs/1212.5225). 2.4.4
- [35] Planck Collaboration, *Astrophysics Special feature Planck 2015 results*, *Astronomy & Astrophysics* **594** (2016), [arXiv:1502.01589](https://arxiv.org/abs/1502.01589). 2.4.4
- [36] J. P. Dietrich, N. Werner, D. Clowe, A. Finoguenov, T. Kitching, L. Miller, and A. Simionescu, *A filament of dark matter between two clusters of galaxies*, [arXiv:1207.0809](https://arxiv.org/abs/1207.0809). 2.4.4
- [37] S. P. Martin, *A Supersymmetry primer*, [arXiv:hep-ph/9709356](https://arxiv.org/abs/hep-ph/9709356) [hep-ph], [Adv. Ser. Direct. High Energy Phys.18,1(1998)]. 2.5.1, 2.5.2, 25
- [38] D. A. Eliezer and R. P. Woodard, *The Problem of Nonlocality in String Theory*, *Nucl. Phys. B* **325** (1989) 389. 2.5.1
- [39] A. Bilal, *Introduction to supersymmetry*, [arXiv:hep-th/0101055](https://arxiv.org/abs/hep-th/0101055) [hep-th]. 2.5.2, 25
- [40] N. Shah, *Lecture Notes, Minimal Supersymmetric Standard Model (MSSM)*,. 2.5.2
- [41] R. N. Mohapatra, *Supersymmetry and R-parity: an Overview*, *Phys. Scripta* **90** (2015) 088004, [arXiv:1503.06478](https://arxiv.org/abs/1503.06478) [hep-ph]. 2.5.3
- [42] L. J. Hall, D. Pinner, and J. T. Ruderman, *A Natural SUSY Higgs Near 126 GeV*, *JHEP* **04** (2012) 131, [arXiv:1112.2703](https://arxiv.org/abs/1112.2703) [hep-ph]. 2.5.4

- [43] G. Belanger, C. Delaunay, and A. Goudelis, *The Dark Side of Electroweak Naturalness Beyond the MSSM*, *JHEP* **04** (2015) 149, [arXiv:1412.1833 \[hep-ph\]](#). 2.5.4
- [44] K. Hamaguchi and K. Ishikawa, *Prospects for Higgs- and Z-resonant Neutralino Dark Matter*, *Phys. Rev.* **D93** (2016) 055009, [arXiv:1510.05378 \[hep-ph\]](#). 2.5.4
- [45] S. Profumo and C. E. Yaguna, *Gluino coannihilations and heavy bino dark matter*, *Phys. Rev.* **D69** (2004) 115009, [arXiv:hep-ph/0402208 \[hep-ph\]](#). 2.5.4
- [46] J. R. Ellis, T. Falk, and K. A. Olive, *Neutralino - Stau coannihilation and the cosmological upper limit on the mass of the lightest supersymmetric particle*, *Phys. Lett.* **B444** (1998) 367–372, [arXiv:hep-ph/9810360 \[hep-ph\]](#). 2.5.4
- [47] C. Boehm, A. Djouadi, and M. Drees, *Light scalar top quarks and supersymmetric dark matter*, *Phys. Rev.* **D62** (2000) 035012, [arXiv:hep-ph/9911496 \[hep-ph\]](#). 2.5.4
- [48] H. Baer, T. Krupovnickas, A. Mustafayev, E.-K. Park, S. Profumo, and X. Tata, *Exploring the BWCA (bino-wino co-annihilation) scenario for neutralino dark matter*, *JHEP* **12** (2005) 011, [arXiv:hep-ph/0511034 \[hep-ph\]](#). 2.5.4
- [49] G. H. Duan, K.-I. Hikasa, J. Ren, L. Wu, and J. M. Yang, *Probing bino-wino coannihilation dark matter below the neutrino floor at the LHC*, *Phys. Rev.* **D98** (2018) 015010, [arXiv:1804.05238 \[hep-ph\]](#). 2.5.4
- [50] N. Arkani-Hamed, A. Delgado, and G. Giudice, *The Well-Tempered Neutralino*, *Nuclear Physics B* **741** (2006) 108–130, [arXiv:0601041 \[hep-ph\]](#). 2.5.4
- [51] A. C. Clarke, *Profiles of the Future: An Enquiry into the Limits of the Possible*. Victor Gollancz, Nov, 1982. <https://www.xarg.org/ref/a/0575032103/>. 3
- [52] M. D. Schwartz, *TASI Lectures on Collider Physics*, pp. , 65–100. 2018. [arXiv:1709.04533 \[hep-ph\]](#). 3.1.1
- [53] D. Overbye, *It's Intermission for the Large Hadron Collider*, The New York Times (2018), <https://www.nytimes.com/interactive/2018/12/21/science/cern-large-hadron-collider-ar-ul.html>. 3.2
- [54] L. R. Evans and P. Bryant, *LHC Machine*, *JINST* **3** (2008) S08001. 164 p, <https://cds.cern.ch/record/1129806>, This report is an abridged version of the LHC Design Report (CERN-2004-003). 3.2, 3.2.1
- [55] P. Mouche, *Overall view of the LHC. Vue d'ensemble du LHC*, <http://cds.cern.ch/record/1708847>, General Photo. (document), 3.1, 3.2
- [56] R. Steerenberg, *LHC report: full house for the LHC*, Jul, 2017. <https://home.cern/news/news/accelerators/lhc-report-full-house-lhc>. 3.2.1
- [57] CERN, *Experiments*, 2019. <https://home.cern/science/experiments>. 3.2.2
- [58] I. Aitchison, R. Cowan, and O. Long, *B-factories confirm matter-antimatter asymmetry; leads to 2008 Nobel Prize in Physics*, Dec, 2008. <https://www-public.slac.stanford.edu/babar/Nobel2008.aspx>. 3.2.2
- [59] J. Pequeno, *Computer generated image of the whole ATLAS detector*, Mar, 2008. (document), 3.2, 3.3

- [60] ATLAS Collaboration, G. Aad et al., *The ATLAS Experiment at the CERN Large Hadron Collider*, **JINST** **3** (2008) S08003. 3.3, 3.3.1, 3.3.3, 3.3.4
- [61] IOP, *Search and Discovery of the Higgs Boson*. IOP, 2016. (document), 3.3
- [62] J. Pequenaio, *Computer generated image of the ATLAS inner detector*, Mar, 2008. (document), 3.3.2, 3.4
- [63] A. La Rosa, *The ATLAS Insertable B-Layer: from construction to operation*, **JINST** **11** (2016) C12036, [arXiv:1610.01994](#) [physics.ins-det]. 3.3.2
- [64] J. Pequenaio, *Computer Generated image of the ATLAS calorimeter*, Mar, 2008. (document), 3.3.3, 3.5
- [65] J. Pequenaio, *Computer generated image of the ATLAS Muons subsystem*, Mar, 2008. (document), 3.6, 3.3.4
- [66] CMS Collaboration, D. d’Enterria, *CMS physics highlights in the LHC Run 1*, **PoS Bormio2015** (2015) 027, [arXiv:1504.06519](#) [hep-ex]. 3.4
- [67] A. Ruiz-Martinez and A. Collaboration, *The Run-2 ATLAS Trigger System*, Tech. Rep. ATL-DAQ-PROC-2016-003, CERN, Geneva, Feb, 2016. <http://cds.cern.ch/record/2133909>. 3.4.1
- [68] A. Collaboration, *Processing: What to record?*, 2019. <https://home.cern/science/computing/processing-what-record>. 3.4.1
- [69] R. Munroe, *Google’s Datacenters on Punch Cards*, <https://what-if.xkcd.com/63/>. 3.4.1
- [70] A. Collaboration, *LuminosityPublicResultsRun2*, https://twiki.cern.ch/twiki/bin/view/AtlasPublic/LuminosityPublicResultsRun2#2018_pp_Collisions. (document), 3.7
- [71] ATLAS Collaboration, W. Buttinger, *The ATLAS Level-1 Trigger system*, **J. Phys. Conf. Ser.** **396** (2012) 012010. 3.4.1.1
- [72] ATLAS Collaboration Collaboration, M. zur Nedden, *The Run-2 ATLAS Trigger System: Design, Performance and Plan*, Tech. Rep. ATL-DAQ-PROC-2016-039, CERN, Geneva, Dec, 2016. <https://cds.cern.ch/record/2238679>. 3.4.1.1, 3.4.1.2, 3.4.1.3
- [73] ATLAS Collaboration, G. Aad et al., *Expected Performance of the ATLAS Experiment - Detector, Trigger and Physics*, [arXiv:0901.0512](#) [hep-ex]. 3.5.1, 3.5.1, 3.5.1, 3.5.1
- [74] R. Fruehwirth, *Application of Kalman filtering to track and vertex fitting*, Nucl. Instrum. Methods Phys. Res., A **262** (1987) 444. 19 p, <https://cds.cern.ch/record/178627>. 3.5.1
- [75] T. G. Cornelissen, M. Elsing, I. Gavrilenko, J. F. Laporte, W. Liebig, M. Limper, K. Nikolopoulos, A. Poppleton, and A. Salzburger, *The global χ^2 track fitter in ATLAS*, **J. Phys. Conf. Ser.** **119** (2008) 032013. 3.5.1
- [76] W. Lampl, S. Laplace, D. Lelas, P. Loch, H. Ma, S. Menke, S. Rajagopalan, D. Rousseau, S. Snyder, and G. Unal, *Calorimeter Clustering Algorithms: Description and Performance*, Tech. Rep. ATL-LARG-PUB-2008-002. ATL-COM-LARG-2008-003, CERN, Geneva, Apr, 2008. <https://cds.cern.ch/record/1099735>. 3.5.1

- [77] ATLAS Collaboration, M. Aaboud et al., *Electron reconstruction and identification in the ATLAS experiment using the 2015 and 2016 LHC proton-proton collision data at $\sqrt{s} = 13$ TeV*, *Eur. Phys. J.* **C79** (2019) 639, [arXiv:1902.04655 \[physics.ins-det\]](#). 3.5.1
- [78] ATLAS Collaboration, M. Aaboud et al., *Measurement of the photon identification efficiencies with the ATLAS detector using LHC Run 2 data collected in 2015 and 2016*, *Eur. Phys. J.* **C79** (2019) 205, [arXiv:1810.05087 \[hep-ex\]](#). 3.5.1
- [79] ATLAS Collaboration, ATLAS Collaboration, *Muon reconstruction performance of the ATLAS detector in proton-proton collision data at $\sqrt{s} = 13$ TeV*, *Eur. Phys. J.* **C76** (2016) 292, [arXiv:1603.05598 \[hep-ex\]](#). 3.5.1, 4.3.2, 4.7.1
- [80] M. Cacciari, G. P. Salam, and G. Soyez, *The anti- k_t jet clustering algorithm*, *JHEP* **04** (2008) 063, [arXiv:0802.1189 \[hep-ph\]](#). 3.5.1
- [81] ATLAS Collaboration, M. Aaboud et al., *Measurements of b-jet tagging efficiency with the ATLAS detector using $t\bar{t}$ events at $\sqrt{s} = 13$ TeV*, *JHEP* **08** (2018) 089, [arXiv:1805.01845 \[hep-ex\]](#). (document), 3.5.1, 4.8, 4.26
- [82] on behalf of the ATLAS collaboration Collaboration, A. Coccaro, *Track Reconstruction and b-Jet Identification for the ATLAS Trigger System*, Tech. Rep. [arXiv:1112.0180](#). ATL-DAQ-PROC-2011-051, CERN, Geneva, Dec, 2011. <https://cds.cern.ch/record/1402986>. Comments: 7 pages, 10 figures, conference proceedings for ACAT 2011. (document), 3.5.1, 3.8
- [83] ATLAS Collaboration Collaboration, J. Taenzer, *Large R jet reconstruction and calibration at 13 TeV with the ATLAS detector*, <https://cds.cern.ch/record/2275665>. 3.5.1
- [84] ATLAS Collaboration, *Performance of large- R jets and substructure reconstruction with the ATLAS detector*, ATLAS-CONF-2012-065, 2012, <https://cds.cern.ch/record/1459530>. 3.5.1
- [85] E. N. Thompson, *Jet Grooming at ATLAS*, <http://cds.cern.ch/record/1491166>. 3.5.1
- [86] ATLAS Collaboration, M. Aaboud et al., *Performance of missing transverse momentum reconstruction with the ATLAS detector using proton-proton collisions at $\sqrt{s} = 13$ TeV*, *Eur. Phys. J.* **C78** (2018) 903, [arXiv:1802.08168 \[hep-ex\]](#). 3.5.1
- [87] ATLAS Collaboration, G. Aad et al., *The ATLAS Simulation Infrastructure*, *Eur. Phys. J.* **C70** (2010) 823–874, [arXiv:1005.4568 \[physics.ins-det\]](#). (document), 3.5.2, 3.9, 3.6.2
- [88] M. Dobbs and J. B. Hansen, *The HepMC C++ Monte Carlo event record for High Energy Physics*, *Comput. Phys. Commun.* **134** (2001) 41–46. 3.5.2
- [89] J. Allison, *Geant4 developments and applications*, *IEEE Trans. Nucl. Sci.* **53** (2006) 270, <https://cds.cern.ch/record/1035669>. 3.5.2
- [90] CERN, *The Worldwide LHC Computing Grid*, 2019. <https://home.cern/science/computing/worldwide-lhc-computing-grid>. 3.6.1
- [91] CERN, *Worldwide LHC Computing Grid*, 2019. <http://wlcg-public.web.cern.ch/>. 3.6.1
- [92] I. Bird, *Status of the WLCG Project, including Financial Status*, Tech. Rep. CERN-RRB-2018-081, CERN, Geneva, Sep, 2018. <http://cds.cern.ch/record/2638089>. (document), 3.10, 3.6.1, 3.6.2, 3.11

- [93] F. Fassi, *ATLAS Distributed Data Analysis: challenges and performance*, Tech. Rep. ATL-SOFT-PROC-2015-001, CERN, Geneva, Mar, 2015.
<https://cds.cern.ch/record/2004869>. 3.6.2
- [94] D. Barberis, *Distributed processing and analysis of ATLAS experimental data*, Tech. Rep. ATL-SOFT-PROC-2011-045, CERN, Geneva, Nov, 2011.
<http://cds.cern.ch/record/1397884>. 3.6.2
- [95] D. Golubkov, B. Kersevan, A. Klimentov, A. Minaenko, P. Nevski, A. Vaniachine, and R. Walker, *ATLAS Grid Data Processing: system evolution and scalability*,
<https://cds.cern.ch/record/1446195>. 3.6.2
- [96] A. Klimentov, M. Grigorieva, A. Kiryanov, and A. Zarochentsev, *Big Data and computing challenges in high energy and nuclear physics*, *Journal of Instrumentation* **12** (2017). 3.6.2
- [97] S. Kluth, *HS06 Benchmark for an ARM Server*, *J. Phys. Conf. Ser.* **513** (2014) 062025, [arXiv:1311.3928](https://arxiv.org/abs/1311.3928) [physics.comp-ph]. (document), 3.6.2, 3.11
- [98] ATLAS Collaboration Collaboration, *ATLAS Computing: technical design report*. Technical Design Report ATLAS. CERN, Geneva, 2005. <https://cds.cern.ch/record/837738>. 3.6.2
- [99] I. Antcheva et al., *ROOT: A C++ framework for petabyte data storage, statistical analysis and visualization*, *Comput. Phys. Commun.* **180** (2009) 2499–2512, [arXiv:1508.07749](https://arxiv.org/abs/1508.07749) [physics.data-an]. 3.6.3
- [100] V. Garonne, A. Graeme, M. Lassnig, A. Molfetas, M. Barisits, T. Beermann, A. Nairz, L. Goossens, F. Barreiro Megino, C. Serfon, D. Oleynik, and A. Petrosyan, *The ATLAS Distributed Data Management project: Past and Future*, Tech. Rep. ATL-SOFT-PROC-2012-049, CERN, Geneva, Jun, 2012.
<https://cds.cern.ch/record/1455298>. 3.6.3, 3.6.4
- [101] M. Barisits, T. Beermann, F. Berghaus, B. Bockelman, J. Bogado, D. Cameron, D. Christidis, D. Ciangottini, G. Dimitrov, M. Elsing, V. Garonne, A. D. Girolamo, L. Goossens, W. Guan, J. Guenther, T. Javurek, D. Kuhn, M. Lassnig, F. Lopez, N. Magini, A. Molfetas, A. Nairz, F. Ould-Saada, S. Prenner, C. Serfon, G. Stewart, E. Vaandering, P. Vasileva, R. Vigne, and T. Wegner, *Rucio - Scientific Data Management*, *CoRR abs/1902.09857* (2019), [arXiv:1902.09857](https://arxiv.org/abs/1902.09857), <http://arxiv.org/abs/1902.09857>. 3.6.4
- [102] J. Catmore, *A New Petabyte-scale Data Derivation Framework for ATLAS*,
<https://cds.cern.ch/record/2004909>. 3.6.6
- [103] J. P. Lash, *Helen and Teacher : The Story of Helen Keller and Anne Sullivan Macy*. Amer Foundation for the Blind, Aug, 1981. <https://www.xarg.org/ref/a/0891282343/>. 4
- [104] ATLAS Collaboration, M. Aaboud et al., *Performance of top-quark and W-boson tagging with ATLAS in Run 2 of the LHC*, *Eur. Phys. J.* **C79** (2019) 375, [arXiv:1808.07858](https://arxiv.org/abs/1808.07858) [hep-ex]. 4.1
- [105] A. Collaboration, *Measurement of the $t\bar{t}Z$ and $t\bar{t}W$ cross sections in proton-proton collisions at $\sqrt{s} = 13$ TeV with the ATLAS detector*, [arXiv:1901.03584](https://arxiv.org/abs/1901.03584). 4.1
- [106] ATLAS Collaboration, M. Aaboud et al., *Measurements of top-quark pair spin correlations in the $e\mu$ channel at $\sqrt{s} = 13$ TeV using pp collisions in the ATLAS detector*, Submitted to: *Eur. Phys. J.* (2019), [arXiv:1903.07570](https://arxiv.org/abs/1903.07570) [hep-ex]. 4.1

- [107] ATLAS Collaboration, G. Aad et al., *Search for flavour-changing neutral currents in processes with one top quark and a photon using 81 fb^{-1} of pp collisions at $\sqrt{s} = 13 \text{ TeV}$ with the ATLAS experiment*, [arXiv:1908.08461 \[hep-ex\]](#). 4.1
- [108] ATLAS Collaboration, M. Aaboud et al., *Observation of Higgs boson production in association with a top quark pair at the LHC with the ATLAS detector*, *Phys. Lett. B* **784** (2018) 173–191, [arXiv:1806.00425 \[hep-ex\]](#). 4.1
- [109] ATLAS Collaboration, M. Aaboud et al., *Observation of $H \rightarrow b\bar{b}$ decays and VH production with the ATLAS detector*, *Phys. Lett. B* **786** (2018) 59–86, [arXiv:1808.08238 \[hep-ex\]](#). 4.1
- [110] ATLAS Collaboration, M. Aaboud et al., *Search for pair production of Higgs bosons in the $b\bar{b}b\bar{b}$ final state using proton-proton collisions at $\sqrt{s} = 13 \text{ TeV}$ with the ATLAS detector*, *JHEP* **01** (2019) 030, [arXiv:1804.06174 \[hep-ex\]](#). 4.1
- [111] ATLAS Collaboration, ATLAS Collaboration, *Performance of b -Jet Identification in the ATLAS Experiment*, *JINST* **11** (2016) P04008, [arXiv:1512.01094 \[hep-ex\]](#). 62, 4.6.1, 4.7.2.1, 4.7.2.2
- [112] ATLAS Collaboration, *Measurement of the b -tag Efficiency in a Sample of Jets Containing Muons with 5 fb^{-1} of data from the ATLAS detector*, ATLAS-CONF-2012-043, 2012, <https://cds.cern.ch/record/1435197>. 4.1
- [113] T. Golling, H. S. Hayward, P. U. E. Onyisi, H. J. Stelzer, and P. Waller, *The ATLAS Data Quality Defect Database System*, [arXiv:1110.6119](#). 4.2, 5.2.2
- [114] A. Buckley, *ATLAS Pythia 8 tunes to 7 TeV data*, Tech. Rep. ATL-PHYS-PROC-2014-273, CERN, Geneva, Dec, 2014. <https://cds.cern.ch/record/1974411>. 4.2.2
- [115] R. D. Ball et al., *Parton distributions with LHC data*, *Nucl. Phys. B* **867** (2013) 244–289, [arXiv:1207.1303 \[hep-ph\]](#). 4.2.2, 5.2.3.2
- [116] D. J. Lange, *The EvtGen particle decay simulation package*, *Nucl. Instrum. Meth. A* **462** (2001) 152–155. 4.2.2, 5.2.3.2
- [117] GEANT4 Collaboration, S. Agostinelli et al., *GEANT4: A Simulation toolkit*, *Nucl. Instrum. Meth. A* **506** (2003) 250–303. 4.2.2
- [118] ATLAS Collaboration, *Properties of jets and inputs to jet reconstruction and calibration with the ATLAS detector using proton-proton collisions at $\sqrt{s} = 13 \text{ TeV}$* , ATL-PHYS-PUB-2015-036, 2015, <https://cds.cern.ch/record/2044564>. 4.3.1
- [119] ATLAS Collaboration, *Performance of pile-up mitigation techniques for jets in pp collisions at $\sqrt{s} = 8 \text{ TeV}$ using the ATLAS detector*, *Eur. Phys. J. C* **76** (2016) 581, [arXiv:1510.03823 \[hep-ex\]](#). 4.3.1
- [120] T. Sjostrand, S. Mrenna, and P. Skands, *A Brief Introduction to PYTHIA 8.1*, *Comput. Phys. Commun.* **178** (2008) 852–867, [arXiv:0710.3820 \[hep-ph\]](#). 4.5.1
- [121] ATLAS Collaboration, ATLAS Collaboration, *Performance of the ATLAS Trigger System in 2015*, *Eur. Phys. J. C* **77** (2017) 317, [arXiv:1611.09661 \[hep-ex\]](#). 4.5.2

- [122] ATLAS Collaboration, ATLAS Collaboration, *Jet energy scale measurements and their systematic uncertainties in proton-proton collisions at $\sqrt{s} = 13$ TeV with the ATLAS detector*, Tech. Rep. ATL-COM-PHYS-2016-213, CERN, Geneva, Mar, 2016.
<https://cds.cern.ch/record/2136864>. 4.7.1
- [123] ATLAS Collaboration, E. Diehl, *Calibration and Performance of the ATLAS Muon Spectrometer*, in *Particles and fields. Proceedings, Meeting of the Division of the American Physical Society, DPF 2011, Providence, USA, August 9-13, 2011*. 2011. [arXiv:1109.6933](https://arxiv.org/abs/1109.6933) [[physics.ins-det](#)]. 4.7.1
- [124] ATLAS Collaboration, *Tagging and suppression of pileup jets with the ATLAS detector*, ATLAS-CONF-2014-018, 2014, <https://cds.cern.ch/record/1700870>. 4.7.4, 5.3.1
- [125] BABAR Collaboration Collaboration, BABAR Collaboration, *Measurement of the electron energy spectrum and its moments in inclusive $B \rightarrow X e \nu$ decays*, *Phys. Rev. D* **69**.111104 (2004). 4.9
- [126] DELPHI Collaboration, DELPHI Collaboration, *Determination of heavy quark non-perturbative parameters from spectral moments in semileptonic B decays*, *Eur. Phys. J. C* **45** (2006) 35–59, [arXiv:hep-ex/0510024](https://arxiv.org/abs/hep-ex/0510024) [[hep-ex](#)]. 4.9
- [127] Heavy Flavor Averaging Group (HFAG) Collaboration, Y. Amhis et al., *Averages of b -hadron, c -hadron, and τ -lepton properties as of summer 2014*, [arXiv:1412.7515](https://arxiv.org/abs/1412.7515) [[hep-ex](#)]. (document), 4.9, 4.10
- [128] CDF Collaboration, CDF Collaboration, *Measurement of Ratios of Fragmentation Fractions for Bottom Hadrons in $p\bar{p}$ Collisions at $\sqrt{s} = 1.96$ -TeV*, *Phys. Rev. D* **77**.072003 (2008), [arXiv:0801.4375](https://arxiv.org/abs/0801.4375) [[hep-ex](#)]. (document), 4.9, 4.10
- [129] A. Collaboration, *LHC SUSY Cross Section Working Group*, <https://twiki.cern.ch/twiki/bin/view/LHCPhysics/SUSYCrossSections>. (document), 5.1.1, 5.1
- [130] C. Borschensky, M. Krämer, A. Kulesza, M. Mangano, S. Padhi, T. Plehn, and X. Portell, *Squark and gluino production cross sections in pp collisions at $\sqrt{s} = 13, 14, 33$ and 100 TeV*, *Eur. Phys. J. C* **74** (2014) 3174, [arXiv:1407.5066](https://arxiv.org/abs/1407.5066) [[hep-ph](#)]. 5.1.1
- [131] ATLAS Collaboration, G. Aad et al., *Search for squarks and gluinos in final states with same-sign leptons and jets using 139 fb^{-1} of data collected with the ATLAS detector*, [arXiv:1909.08457](https://arxiv.org/abs/1909.08457) [[hep-ex](#)]. 5.1.1
- [132] ATLAS Collaboration, G. Aad et al., *Search for displaced vertices of oppositely charged leptons from decays of long-lived particles in pp collisions at $\sqrt{s} = 13$ TeV with the ATLAS detector*, [arXiv:1907.10037](https://arxiv.org/abs/1907.10037) [[hep-ex](#)]. 5.1.1
- [133] ATLAS Collaboration, M. Aaboud et al., *Search for heavy charged long-lived particles in the ATLAS detector in 36.1 fb^{-1} of proton-proton collision data at $\sqrt{s} = 13$ TeV*, *Phys. Rev. D* **99** (2019) 092007, [arXiv:1902.01636](https://arxiv.org/abs/1902.01636) [[hep-ex](#)]. 5.1.1
- [134] ATLAS Collaboration, M. Aaboud et al., *Search for squarks and gluinos in final states with hadronically decaying τ -leptons, jets, and missing transverse momentum using pp collisions at $\sqrt{s} = 13$ TeV with the ATLAS detector*, *Phys. Rev. D* **99** (2019) 012009, [arXiv:1808.06358](https://arxiv.org/abs/1808.06358) [[hep-ex](#)]. 5.1.1

- [135] ATLAS Collaboration, M. Aaboud et al., *Search for heavy charged long-lived particles in proton-proton collisions at $\sqrt{s} = 13$ TeV using an ionisation measurement with the ATLAS detector*, *Phys. Lett.* **B788** (2019) 96–116, [arXiv:1808.04095 \[hep-ex\]](#). 5.1.1
- [136] ATLAS Collaboration, M. Aaboud et al., *Search for top-squark pair production in final states with one lepton, jets, and missing transverse momentum using 36 fb^{-1} of $\sqrt{s} = 13$ TeV pp collision data with the ATLAS detector*, *JHEP* **06** (2018) 108, [arXiv:1711.11520 \[hep-ex\]](#). 5.1.1
- [137] ATLAS Collaboration, M. Aaboud et al., *Search for top squarks decaying to tau sleptons in pp collisions at $\sqrt{s} = 13$ TeV with the ATLAS detector*, *Phys. Rev.* **D98** (2018) 032008, [arXiv:1803.10178 \[hep-ex\]](#). 5.1.1
- [138] ATLAS Collaboration, M. Aaboud et al., *Search for supersymmetry in final states with charm jets and missing transverse momentum in 13 TeV pp collisions with the ATLAS detector*, *JHEP* **09** (2018) 050, [arXiv:1805.01649 \[hep-ex\]](#). 5.1.1
- [139] A. Collaboration, *Supersymmetry searches*, <https://twiki.cern.ch/twiki/bin/view/AtlasPublic/SupersymmetryPublicResults>. (document), 5.1.1, 5.2, 5.3, 5.4, 5.5, 5.6, 5.7, 5.8
- [140] CMS Collaboration, T. Sakuma, *Squark/gluino searches in hadronic channels with CMS*, *PoS LHCP2016* (2017) 145, [arXiv:1609.07445 \[hep-ex\]](#). 5.1.1
- [141] CMS Collaboration, A. M. Sirunyan et al., *Search for the pair production of third-generation squarks with two-body decays to a bottom or charm quark and a neutralino in proton-proton collisions at $\sqrt{s} = 13$ TeV*, *Phys. Lett.* **B778** (2018) 263–291, [arXiv:1707.07274 \[hep-ex\]](#). 5.1.1
- [142] CMS Collaboration, A. M. Sirunyan et al., *Search for direct production of supersymmetric partners of the top quark in the all-jets final state in proton-proton collisions at $\sqrt{s} = 13$ TeV*, *JHEP* **10** (2017) 005, [arXiv:1707.03316 \[hep-ex\]](#). 5.1.1
- [143] CMS Collaboration, A. M. Sirunyan et al., *Search for top squark pair production in pp collisions at $\sqrt{s} = 13$ TeV using single lepton events*, *JHEP* **10** (2017) 019, [arXiv:1706.04402 \[hep-ex\]](#). 5.1.1
- [144] CMS Collaboration, A. M. Sirunyan et al., *Search for top squarks and dark matter particles in opposite-charge dilepton final states at $\sqrt{s} = 13$ TeV*, *Phys. Rev.* **D97** (2018) 032009, [arXiv:1711.00752 \[hep-ex\]](#). 5.1.1
- [145] P. Meade, M. Reece, and D. Shih, *Prompt Decays of General Neutralino NLSPs at the Tevatron*, *JHEP* **05** (2010) 105, [arXiv:0911.4130 \[hep-ph\]](#). 5.1.2
- [146] ATLAS Collaboration, M. Aaboud et al., *Search for chargino and neutralino production in final states with a Higgs boson and missing transverse momentum at $\sqrt{s} = 13$ TeV with the ATLAS detector*, *Phys. Rev.* **D100** (2019) 012006, [arXiv:1812.09432 \[hep-ex\]](#). 5.1.3, 5.4
- [147] ATLAS Collaboration, M. Aaboud et al., *Search for pair production of higgsinos in final states with at least three b -tagged jets in $\sqrt{s} = 13$ TeV pp collisions using the ATLAS detector*, *Phys. Rev.* **D98** (2018) 092002, [arXiv:1806.04030 \[hep-ex\]](#). 5.1.3

- [148] E. Bothmann, G. S. Chahal, S. Höche, J. Krause, F. Krauss, S. Kuttimalai, S. Liebschner, D. Napoletano, M. Schönherr, H. Schulz, S. Schumann, and F. Siegert, *Event Generation with Sherpa 2.2*, [arXiv:1905.09127](#). 5.2.3.1
- [149] ATLAS Collaboration, *Simulation of top-quark production for the ATLAS experiment at $\sqrt{s} = 13$ TeV*, ATL-PHYS-PUB-2016-004, 2016, <https://cds.cern.ch/record/2120417>. 5.2.3.1
- [150] T. Sjostrand, S. Ask, J. R. Christiansen, R. Corke, N. Desai, P. Ilten, S. Mrenna, S. Prestel, C. O. Rasmussen, and P. Z. Skands, *An Introduction to PYTHIA 8.2*, *Comput. Phys. Commun.* **191** (2015) 159–177, [arXiv:1410.3012](#) [[hep-ph](#)]. 5.2.3.1, 5.2.3.2
- [151] M. Cacciari, M. Czakon, M. Mangano, A. Mitov, and P. Nason, *Top-pair production at hadron colliders with next-to-next-to-leading logarithmic soft-gluon resummation*, *Phys. Lett. B* **710** (2012) 612–622, [arXiv:1111.5869](#) [[hep-ph](#)]. 5.2.3.1
- [152] P. Baernreuther, M. Czakon, and A. Mitov, *Percent Level Precision Physics at the Tevatron: First Genuine NNLO QCD Corrections to $q\bar{q} \rightarrow t\bar{t} + X$* , *Phys. Rev. Lett.* **109** (2012) 132001, [arXiv:1204.5201](#) [[hep-ph](#)]. 5.2.3.1
- [153] J. Alwall, M. Herquet, F. Maltoni, O. Mattelaer, and T. Stelzer, *MadGraph 5 : Going Beyond*, *JHEP* **06** (2011) 128, [arXiv:1106.0522](#) [[hep-ph](#)]. 5.2.3.2
- [154] ATLAS Collaboration, *ATLAS Pythia 8 tunes to 7 TeV data*, ATL-PHYS-PUB-2014-021, 2014, <https://cds.cern.ch/record/1966419>. 5.2.3.2
- [155] L. Lonnblad and S. Prestel, *Matching Tree-Level Matrix Elements with Interleaved Showers*, *JHEP* **03** (2012) 019, [arXiv:1109.4829](#) [[hep-ph](#)]. 5.2.3.2
- [156] J. Butterworth et al., *PDF4LHC recommendations for LHC Run II*, *J. Phys. G* **43** (2016) 023001, [arXiv:1510.03865](#) [[hep-ph](#)]. 5.2.3.2
- [157] W. Beenakker, C. Borschensky, M. Krämer, A. Kulesza, and E. Laenen, *NNLL-fast: predictions for coloured supersymmetric particle production at the LHC with threshold and Coulomb resummation*, *JHEP* **12** (2016) 133, [arXiv:1607.07741](#) [[hep-ph](#)]. 5.2.3.2
- [158] W. Beenakker, M. Krämer, T. Plehn, M. Spira, and P. M. Zerwas, *Stop production at hadron colliders*, *Nucl. Phys. B* **515** (1998) 3, [hep-ph/9710451](#). 5.2.3.2
- [159] W. Beenakker, S. Brensing, M. Krämer, A. Kulesza, E. Laenen, and I. Niessen, *Supersymmetric top and bottom squark production at hadron colliders*, *JHEP* **08** (2010) 098, [arXiv:1006.4771](#) [[hep-ph](#)]. 5.2.3.2
- [160] W. Beenakker, C. Borschensky, R. Heger, M. Krämer, A. Kulesza, and E. Laenen, *NNLL resummation for stop pair-production at the LHC*, *JHEP* **05** (2016) 153, [arXiv:1601.02954](#) [[hep-ph](#)]. 5.2.3.2
- [161] S. Marzani, G. Soyez, and M. Spannowsky, *Looking inside jets: an introduction to jet substructure and boosted-object phenomenology*, [arXiv:1901.10342](#). 5.2.3.2
- [162] ATLAS Collaboration, *Electron and photon reconstruction and performance in ATLAS using a dynamical, topological cell clustering-based approach*, ATL-PHYS-PUB-2017-022, 2017, <https://cds.cern.ch/record/2298955>. 5.3.1

- [163] ATLAS Collaboration, *Electron identification measurements in ATLAS using $\sqrt{s} = 13$ TeV data with 50 ns bunch spacing*, ATL-PHYS-PUB-2015-041, 2015, <https://cds.cern.ch/record/2048202>. 5.3.1
- [164] A. Collaboration, *Identification and rejection of pile-up jets at high pseudorapidity with the ATLAS detector*, [arXiv:1705.02211](https://arxiv.org/abs/1705.02211). 5.3.1
- [165] ATLAS Collaboration, G. Aad et al., *ATLAS data quality operations and performance for 2015-2018 data-taking*, [arXiv:1911.04632](https://arxiv.org/abs/1911.04632) [[physics.ins-det](#)]. 5.3.1
- [166] ATLAS Collaboration, *Identification of Boosted, Hadronically-Decaying W and Z Bosons in $\sqrt{s} = 13$ TeV Monte Carlo Simulations for ATLAS*, ATL-PHYS-PUB-2015-033, 2015, <https://cds.cern.ch/record/2041461>. 5.3.1
- [167] ATLAS Collaboration, *Jet mass reconstruction with the ATLAS Detector in early Run 2 data*, ATLAS-CONF-2016-035, 2016, <https://cds.cern.ch/record/2200211>. (document), 5.3.1, 5.3.1, 5.13
- [168] ATLAS Collaboration, *Flavor Tagging with Track-Jets in Boosted Topologies with the ATLAS Detector*, ATL-PHYS-PUB-2014-013, 2014, <https://atlas.web.cern.ch/Atlas/GROUPS/PHYSICS/PUBNOTES/ATL-PHYS-PUB-2014-013>. 5.3.1
- [169] M. Cacciari and G. P. Salam, *Pileup subtraction using jet areas*, *Phys. Lett.* **B659** (2008) 119–126, [arXiv:0707.1378](https://arxiv.org/abs/0707.1378) [[hep-ph](#)]. 5.3.1
- [170] S. Zenz, *Understanding Jet Structure and Constituents: Track Jets and Jet Shapes at ATLAS*, 2010. <https://cdsweb.cern.ch/record/1310336/files/ATL-PHYS-PROC-2010-126.pdf>. 5.3.1
- [171] P. Z. Skands, *A Quick guide to SUSY tools*, in *TeV4LHC Workshop: 2nd Meeting Brookhaven, Upton, New York, February 3-5, 2005*. 2006. [arXiv:hep-ph/0601103](https://arxiv.org/abs/hep-ph/0601103) [[hep-ph](#)]. http://lss.fnal.gov/cgi-bin/find_paper.pl?conf-06-004-T. 5.3.1
- [172] ATLAS Collaboration, *Performance of top-quark and W-boson tagging with ATLAS in Run 2 of the LHC*, [arXiv:1808.07858](https://arxiv.org/abs/1808.07858) [[hep-ex](#)]. (document), 5.3.1, 5.14
- [173] A. J. Larkoski, G. P. Salam, and J. Thaler, *Energy Correlation Functions for Jet Substructure*, *JHEP* **06** (2013) 108, [arXiv:1305.0007](https://arxiv.org/abs/1305.0007) [[hep-ph](#)]. 5.3.1
- [174] A. J. Larkoski, I. Moult, and D. Neill, *Power Counting to Better Jet Observables*, *JHEP* **12** (2014) 009, [arXiv:1409.6298](https://arxiv.org/abs/1409.6298) [[hep-ph](#)]. 5.3.1
- [175] C. G. Lester and D. J. Summers, *Measuring masses of semiinvisibly decaying particles pair produced at hadron colliders*, *Phys. Lett.* **B463** (1999) 99–103, [arXiv:hep-ph/9906349](https://arxiv.org/abs/hep-ph/9906349) [[hep-ph](#)]. 5.4.1.1
- [176] A. Barr, C. Lester, and P. Stephens, *$m(T2)$: The Truth behind the glamour*, *J. Phys.* **G29** (2003) 2343–2363, [arXiv:hep-ph/0304226](https://arxiv.org/abs/hep-ph/0304226) [[hep-ph](#)]. 5.4.1.1
- [177] *Missing Energy Trigger Public Results*, <https://twiki.cern.ch/twiki/bin/view/AtlasPublic/MissingEtTriggerPublicResults>. (document), 5.4.1.2, 5.15

-
- [178] ATLAS Collaboration, *Selection of jets produced in 13 TeV proton–proton collisions with the ATLAS detector*, ATLAS-CONF-2015-029, 2015, <https://cds.cern.ch/record/2037702>. 5.4.1.3
- [179] ATLAS Collaboration, *Non-collision backgrounds as measured by the ATLAS detector during the 2010 proton–proton run*, ATLAS-CONF-2011-137, 2011, <https://cds.cern.ch/record/1383840>. 5.4.1.4
- [180] G. Schott, *RooStats for Searches*, 2012. 5.4.3
- [181] J. T. Linnemann, *Measures of Significance in HEP and Astrophysics*, <https://cds.cern.ch/record/691153>, Comments: Talk from PhyStat2003, Stanford, Ca, USA, September 2003, 5 pages, LaTeX, 2 eps figures. MOBT001; typo fixed. 5.4.3
- [182] A. Loginov, *Strategies of data-driven estimations of $t\bar{t}$ backgrounds in ATLAS*, Tech. Rep. ATL-PHYS-PROC-2010-067, CERN, Geneva, Aug, 2010. <https://cds.cern.ch/record/1287126>. 5.5.1
- [183] ATLAS Collaboration, M. Aaboud et al., *Search for long-lived neutral particles in pp collisions at $\sqrt{s} = 13$ TeV that decay into displaced hadronic jets in the ATLAS calorimeter*, *Eur. Phys. J.* **C79** (2019) 481, [arXiv:1902.03094](https://arxiv.org/abs/1902.03094) [[hep-ex](#)]. 5.5.1

Glossary

***b*-jet** A jet originating from a *b*-quark. [49](#)

***b*-tagging** The identification of jets originating from *B*-hadron decays. Also called “flavor tagging”. [63](#)

p^* In hadronic decays, p^* is the momentum of final state particles in the hadron rest frame. [64](#)

$p_{\mathbf{T}}^{\text{rel}}$ In semileptonic *B*-hadron decays, $p_{\mathbf{T}}^{\text{rel}}$ is the transverse momentum of the lepton relative to the jet+lepton axis. [64](#)

action A functional whose input is an equation \mathbf{q} and which returns a scalar. The evolution $\mathbf{q}(t)$ of a physical system (e.g. how the system changes from time t_0 to t_1) corresponds to a stationary point (usually a minimum) of its action. [5](#)

AMI ATLAS Metadata Interface. [68](#)

antiparticle Each quark or lepton has a partnered antiparticle with the same mass but opposite charge. When a particle and its antiparticle meet, they annihilate each other and produce photons. [7](#)

Athena The ATLAS analysis software framework, designed to accommodate a wide range of physics data-processing applications. [56](#)

AthenaMP Athena Multi-Process. [3](#), [59](#)

barn The units of cross section, i.e. the probability of two particles interacting in a scattering event. 1 barn is equal to 10^{-28} m². [35](#)

baryon A composite particle consisting of three quarks held together by the strong force. In ground state, spin=1/2. [7](#)

baryon number A conserved SM quantum number, defined as $B = \frac{1}{3}(n_q - n_{\bar{q}})$, where n_q is the number of quarks and $n_{\bar{q}}$ is the number of antiquarks. $B = 1$ for baryons, $B = 0$ for meson, and $B = -1$ for antibaryons (i.e. baryons made only of antiquarks). [31](#)

- beam line** In accelerator physics, the beam line is the trajectory of the beam of accelerated particles. In the LHC, for example, the beam line consists of two rings around which protons are accelerated. [36](#)
- bootstrapping** A method for producing trigger turn-on curves where the efficiency of a higher trigger threshold is determined using events triggered by a lower threshold. [82](#)
- boson** An elementary particle with whole-integer spin. All force carriers and the Higgs particle are bosons. [7](#)
- branching** In version control, *branching* is the duplication of an object under version control (such as a source code file or a directory tree) so that modifications can occur in parallel along multiple branches. [60](#)
- branching ratio (BR)** The relative frequency of a particular decay mode of a particle. Also called branching fraction. [14](#)
- bremsstrahlung** Electromagnetic radiation produced when a charged particle decelerates. German for “braking radiation”. [41](#)
- BSM** Beyond the Standard Model. [14](#), [46](#)
- bunch** In a particle accelerator/collider, a bunch is a group of particles constrained into a single “blob”. The bunch is tightened using magnets to squeeze the particles closer together (assuming the particles are charged). If two bunches contain many particles packed very closely together, the particles are more likely to interact when the bunches pass through each other. [35](#)
- center-of-mass** The center-of-mass is the point representing the mean position of the mass in a body or system. The center-of-mass frame is an inertial frame in which the center of mass of a system is at rest with respect to the origin of the coordinate system. [37](#)
- CERN** European Organization for Nuclear Research (in French, Conseil européen pour la recherche nucléaire). [35](#)
- chemical equilibrium** An interaction $i + j \rightarrow k + l$ is at chemical equilibrium when the potential for the reaction to proceed forwards is identical to the potential to proceed backwards. [25](#)
- chiral** For massless particles, chirality is the same as helicity: if the spin points in the same direction as the particle’s motion, it’s right-handed, and if spin and motion point in opposite directions, it’s left-handed. For massive particles, these concepts are not the same: helicity can change based on the observer’s reference frame, but chirality will remain unchanged. Chirality for fermions is defined through a gamma matrix operator γ^5 . [11](#)
- CKM matrix** The “Cabibbo-Kobayashi-Maskawa” matrix, named for its creators. A unitary matrix which encodes the interaction strength between all flavors of quarks. [15](#)
- color charge** A property of quarks and gluons determining their possible strong force interactions. Consists of three conserved quantities: “red”, “green”, and “blue” charge. [8](#)
- color confinement** A property of quarks. A flavored particle cannot exist bare on its own; instead, quarks must be contained within a color-neutral hadron. [19](#)

Cosmic Microwave Background The CMB is the decoupled photons from the early universe era in which protons and neutrons were combined to form hydrogen. Prior to this, photons produced from such a reaction could scatter off free electrons; once there were no free electrons, however, the photons became the decoupled CMB. [26](#)

cosmic scale factor The cosmic scale factor is a dimensionless parameter governing the distance between points in the universe over time. [24](#)

Cosmological Principle The combined assumption that the universe is homogeneous and isotropic. Using these assumptions with the Friedmann equations produces the FLRW model of the universe. [23](#)

CP-even A process is CP-even if the process has a *positive* eigenvalue under the CP operation, i.e. simultaneous charge conjugation (particles \leftrightarrow antiparticles) and parity symmetry (flip the sign of one spatial coordinate, i.e. mirror image). [29](#)

CP-odd A process is CP-odd if the process has a *negative* eigenvalue under the CP operation, i.e. simultaneous charge conjugation (particles \leftrightarrow antiparticles) and parity symmetry (flip the sign of one spatial coordinate, i.e. mirror image). [29](#)

critical density The critical density ρ_{cr} of the universe is the mass-energy density which gives a perfectly flat (i.e. not expanding or contracting) universe. If the density is greater than ρ_{cr} , then the universe shall contract at infinite time; if the density is less than ρ_{cr} , the universe shall continue to expand. [24](#)

cross section When two particles interact, their cross section is the area transverse to their relative motion within which they must meet in order to scatter/interact. Depending on the interaction scale, this area may be larger than the particles themselves. More simply, cross section is a measure of the likelihood of a particle particle interaction occurring. Given in units of barns. [35](#)

cut In physics analysis, a “cut” is another word used for a selection requirement or criteria. For example, you could make a cut to select only jets above 100 GeV. [70](#)

cutflow In physics searches, a cutflow table is a way to understand the effect of selection criteria. The table (usually read left-to-right) shows the cumulative effect of each cut applied; the left side will have minimal cuts, and the right side will have all cuts applied. Cutflow tables are useful for understanding how each selection step changes the background composition and signal yield. [134](#)

DAOD Derived Analysis Object Data. [58](#)

dark matter Matter which cannot be directly detected. We observe the presence of dark matter in the universe indirectly through its gravitational effects, but we have not directly observed interactions between dark matter and SM matter. [23](#)

DDM Distributed Data Management. [57](#)

decay-in-flight A catch-all term referring to particles which decay after “flying” away from the primary vertex for a \sim long time (i.e. long enough to make it out of the inner detector). This usually refers to pions, which are commonly produced at the LHC and frequently decay in-flight. [71](#)

DID Dataset ID. [57](#)

DM Dark Matter. [26](#)

DSN Dataset Name. [57](#)

ECAL Electromagnetic Calorimeter. [40](#)

electromagnetic Electromagnetic force, also known as Lorentz force. One of the four fundamental forces of nature. Only affects particles with electromagnetic charge. [7](#)

electroweak symmetry breaking The mechanism which generates the masses of the W^\pm and Z bosons. The Higgs boson breaks electroweak symmetry spontaneously. [13](#)

electroweak unification A unified description of the electromagnetic and weak forces with gauge group $SU(2) \times U(1)$. [8](#)

electroweakino Also called “ewkinos”, this refers to the higgsino, wino, and bino. [31](#), [109](#)

elementary particle A subatomic particle with no substructure, i.e. it is not composed of smaller particles. [7](#)

event An event refers to the results that occur after a fundamental interaction takes place between subatomic particles in a collider experiment. For physics studies, the most interesting types of events are deep inelastic scattering events. [35](#)

fake In the context of object reconstruction, a “fake” is an incorrectly identified object. [118](#)

Fermi’s Golden Rule A formula describing the transition rate per unit time from an initial energy eigenstate i to final eigenstate(s) f . [16](#)

fermion An elementary particle with half-integer spin. All leptons and quarks are fermions. [7](#)

flat A dataset or data file is called *flat* if it contains no indexing or structure to relate objects in the file to one another. Another way to think of flat data files is that all the information within the file is expressed as histograms, not as relational objects. [58](#)

flavor Another way to refer to the different species of an elementary particle. There are six flavors of quarks and six flavors of leptons. In this thesis, “flavor” will always refer to *quark* flavors. plural. [15](#)

FLRW Friedmann-Lemaître-Robertson-Walker. [22](#)

four-vector A four-vector is a generalization of a three-vector. It usually defines the direction of an object’s velocity in 3-dimensional space as well as the magnitude of the momentum. [121](#)

fragmentation function A function describing the probability of a parton k producing a hadron h with energy fraction $z = \frac{E_h}{E_k}$. [19](#)

Friedmann equation The Friedmann equations are a set of equations governing the expansion of space in the FLRW model of the universe. They can be derived from the Einstein equations given the FLRW metric. [24](#)

gauge group A gauge group is the group of local transformation under which a system of fields is invariant. [6](#)

gaugino A gaugino is the superpartner of a SM gauge boson. [29](#)

ghost-association A technique for associating tracks to jets. First, start with the “ghosts”, the track jet 4-vectors in the event with track jet p_T set to ~ 0 . The ghosts are then reclustered using the usual jet techniques. [122](#), [123](#)

gravitino The superpartner of the hypothesized graviton, the quantum of gravity. [31](#)

grid search The “brute force” method of multivariate optimization. In a grid search, you selected several values to test for each parameter, then test every point on your cut “grid” to find the best combination. [134](#)

group A group is a finite or infinite set of elements together with a binary operation \cdot which respects four properties:

- Closure: if A and B are elements of a group G , then $A \cdot B$ is also an element of G
- Associativity: \cdot is associative, i.e. $\forall A, B, C \in G, (A \cdot B) \cdot C = A \cdot (B \cdot C)$
- Identity: there exists an identity element I such that $\forall A \in G, I \cdot A = A \cdot I = A$.
- Inverse: each element must have an inverse, i.e. $\forall A \in G, \exists B \in G$ such that $A \cdot B = B \cdot A = I$

A closed subset of a group which is itself a group is called a “subgroup”. [6](#)

GUT Grand Unification Theory. [21](#)

hadron A composite particle made of two or more quarks. Mesons and baryons are both hadrons. [7](#)

hadronic A hadronic decay of a particle is a decay producing only hadrons (quarks). [17](#)

hadronization The process by which hadrons are formed from quarks and gluons. When quarks are produced (e.g. in a particle collider), they cannot exist on their own due to color confinement. Hence, through the process of hadronization, additional quark-antiquark pairs are “pulled” from the vacuum to create hadrons. [19](#)

harder In the context of momentum in particle physics, a sample or object is “harder” than another if it has a high p_T than the “softer” object. In general, an object is described as “hard” if it has a high p_T . [74](#)

HCAL Hadronic Calorimeter. [40](#)

heavy-flavor Heavy-flavor jets are jets originating from b or c -quarks. [67](#)

HFAG Heavy Flavor Averaging Group. [106](#)

HLT High-Level Trigger. [44](#), [45](#)

homogeneous In cosmology, we assume that the universe is homogeneous, i.e. the metric R is the same at all points in space at a given time. [23](#)

Hubble constant The Hubble constant H_0 is the current value of the Hubble parameter. [24](#)

Hubble parameter The Hubble parameter $H(t)$ is the expansion rate of the universe at some time t . [24](#)

hydrogen-line profile A technique for measuring the rotational velocity of a galaxy as a function of radius. The hydrogen in the galaxy emits a well-known spectral line; shifts in the line's frequency are caused by the relative velocity of the hydrogen at that point in the galaxy. By measuring the shifts as a function of radius r , one can measure the rotational velocity of the galaxy as a function of r . [23](#)

hyperfine transition When the magnetic dipole of the hydrogen electron is parallel to that of the nucleus, the total energy of the hydrogen atom is slightly higher than if the dipoles were anti-parallel. Transitions between these two states are called “hyperfine transitions”. [23](#)

IBL Insertable b -Layer. [40](#)

ID Inner Detector. [40](#)

impact parameter The distance of closest approach between a track and the primary vertex of an event. [21](#)

instantaneous luminosity In collider physics, the instantaneous luminosity is the rate of particle collisions per second. This is determined by the number of bunches in a collider ring, the size of the bunches, and how many particles are packed into a bunch. Given in units of $\text{cm}^{-2} \text{s}^{-1}$. [35](#)

integrated luminosity In collider physics, the integrated luminosity is integral of the instantaneous luminosity over time. The integrated luminosity times the cross section equals the number of events expected over that period of time. Given in units of cm^{-2} . [35](#)

IP Impact Parameter. [49](#)

isotropic In cosmology, we assume that the universe is isotropic, i.e. the universe looks the same in all directions and matter is distributed evenly across space. [23](#)

ISR Initial-State Radiation. [136](#)

jet A collimated spray of hadrons and decay particles produced by the hadronization of a quark, gluon, or (possibly) a tau lepton. [49](#)

kinetic equilibrium A state in which the particles in a system can effectively exchange energy and momentum between them. The system must be dense enough for particles to regularly interact with each other. [25](#)

L1 Trigger Level-1 Hardware Trigger. [44](#)

Lagrangian A function (denoted L) of the coordinates q_i and their time derivatives \dot{q}_i which can be integrated over time (or time and space) to get the action of the system. The “Lagrangian density” (denoted \mathcal{L}), the volume density of the Lagrangian, is sometimes called the Lagrangian as well. [5](#)

lepton number A conserved SM quantum number, defined as $L = n_l - n_{\bar{l}}$, where n_l is the number of leptons and $n_{\bar{l}}$ is the number of antileptons. Total lepton number is always conserved; one can define a lepton number each for μ , τ and e , but they will not always be conserved (for example, during neutrino oscillations). [31](#)

leptonic A leptonic decay of a particle is a decay producing only leptons. [17](#)

LFN Logical File Name. [57](#)

LHC Large Hadron Collider. [35](#)

light-flavor Light-flavor jets are jets originating from u , d , or s -quarks. [49](#)

LO leading order. [117](#)

LSP Lightest Supersymmetric Particle. [31](#)

matter-antimatter asymmetry The observed imbalance in baryonic matter and antimatter in the universe. Currently the SM does not provide a full explanation for this observed asymmetry. [37](#)

MC Monte Carlo. [46](#)

ME-PS Matrix Element-Parton Shower. [117](#)

meson A composite particle consisting of two quarks held together by the strong force. In ground state, spin=1 or 0. [7](#)

MS Muon Spectrometer. [42](#)

MSSM Minimal Supersymmetric Standard Model. [29](#)

NLO next-to-leading order. [117](#)

NNLO next-to-next-to-leading order. [117](#)

nuclear interaction length The mean distance between hadronic interactions of relativistic hadrons. [41](#)

null pointer A null pointer is a pointer that does not point to any object or function. [85](#)

overflow bin In a histogram, the overflow bin is a bin at the right containing all events outside of the displayed x-axis range. [77](#)

PanDA Production and Distributed Analysis. [55](#)

particle shower A cascade of secondary particles produced as the result of a high-energy particle interacting with dense matter. [40](#)

parton The constituent quarks of a hadron. [8](#)

PDF parton distribution function. [117](#)

pileup The average number of particle interactions per bunch crossing. It is very rare for a bunch crossing to contain more than one deep inelastic scattering event per crossing (in fact, many contain no such events), so the majority of pileup events are “soft scattering” events, which are of no interest in high energy physics studies. [43](#)

prescale factor A scaling factor used to control the rate at which a trigger fires. If a trigger has prescale factor N , then it will only fire on one out of every N events passing its criteria. [46](#)

preselection In physics searches, “preselection” requirements are basic cuts used to make coarse signal-region-like cuts. The preselection sample is the starting point for further selections and is very useful for reducing sample sizes and event rates (much like a trigger selection). [125](#)

primary vertex The reconstructed position of the initial hard scattering interaction point in a particle collision. [47](#)

QED Quantum Electrodynamics. [11](#)

quark-gluon plasma A hypothetical, highly energized form of matter containing unbound quarks and gluon. Quark-gluon plasma is believed to have existed in the very early universe (post-Big Bang). [37](#)

R-parity A potentially conserved quantum number of SUSY models, defined as $(-1)^R = (-1)^{3B-L+2S} \equiv (-1)^{3(B-L)+2S}$ where B is baryon number, L is lepton number, and S is particle spin. If R-parity is conserved, then SUSY particles are always produced in pairs and the LSP is stable. [31](#)

radiation length The average distance over which the energy of an electron is reduced by bremsstrahlung by a factor of $\frac{1}{e}$. [41](#)

read out In the context of the ATLAS detector, “reading out” is the process by which information recorded by the detector is saved into a packet and that packet is pushed off the detector to a server farm. A read-out system helps coordinate the read-out process, making sure everything stays synchronized and that the various pieces of the detector receive their read-out signals correctly. The latency of the read-out packets traveling along wires to the server is nontrivial at ATLAS timescales. [45](#)

relic abundance In cosmology, the relic abundance of a particle is the present quantity of that particle remaining from the Big Bang era. [26](#)

RF Cavities Radiofrequency Cavities. [37](#)

RPC R-parity Conserving. [31](#)

RPV R-parity Violating. [31](#)

sagitta In geometry, the sagitta of a circular arc is the distance from the center of the arc to the center of its base. The sagitta of muon tracks are used to study muon reconstruction performance. [99](#)

scintillation A flash of light produced in a transparent material when a particle passes through it. The scintillating material absorbs some of particle’s energy then re-emits it as light. A detector which uses scintillation to absorb and measure a particle’s energy is called a scintillator. [41](#)

semileptonic A semileptonic decay of a particle is a decay caused by the weak interaction, producing a lepton, the corresponding neutrino, and another hadron. [17](#)

sfermion A sfermion is the superpartner of a SM fermion. [29](#)

slice In the context of kinematic distributions, a “slice” is a range of a particular kinematic distribution. Jet MC is divided into slices so that users may select the slices of interest to them and to speed up the simulation process. [74](#)

SM Standard Model of particle physics. [6](#), [7](#)

Spectator Model A model for understand B -hadron decays. It is assumed that the other quark(s) in the B -hadron has a negligible effect on the decay of the b -quark. This model works for a variety of reasons, the most important of which being the large b -quark mass. [16](#)

spin Intrinsic angular momentum carried by a particle. Typically given in terms of the spin quantum number, $s = \frac{b}{2}$, where b is a non-negative integer. Particles with whole-integer spin are called bosons, and those with half-integer spin are called fermions. [7](#)

SR Signal Region. [132](#)

strong Strong nuclear force. Bonds quarks into hadrons, protons and neutrons into atomic nuclei. [7](#)

superconducting Superconductivity is a property of certain physical material wherein the electrical resistance is reduced to ~ 0 , usually at low temperatures. When something has this property, we say it is “superconducting”. [37](#)

superfield A superfield is a single mathematical object containing all the bosonic, fermionic, and auxiliary fields within a corresponding supermultiplet. [30](#)

supermultiplet A supermultiplet is a representation of a SUSY algebra. It consists of a collection of particles, called superpartners. Each multiplet contains an equal number of fermionic and bosonic states. [29](#)

superpartner In SUSY, each particle has a “matching” supersymmetric particle called its superpartner. Fermions superpartners must be bosons, and each boson has a superpartner fermion plural. [29](#)

support trigger In the bootstrapping method of trigger turn-on curve production, the support trigger is the fully-efficiency lower-threshold trigger used to collect an inclusive sample of objects. [82](#)

SUSY supersymmetry. [27](#)

tag-and-probe A method for selecting a pure sample of objects by utilizing known physics two-object physics processes. One leg of the decay is identified as the “tag”, and the second leg is used to “probe” an independent system or reconstruction technique. [90](#)

TDAQ Trigger and Data Acquisition. [43](#)

The Grid The Worldwide LHC Computing Grid, a collaborative effort between facilities and universities collaborating on the LHC. The Grid is a distributed network of computing sites all over the globe designed to handle the massive computing challenges at the LHC. [53](#)

three-vector A vector describing a direction in 3-dimensional space. [65](#)

track-jet Jets formed using ID tracks instead of calorimeter clusters, often with $R = 0.2$ to identify small sub-jets. Further jet reconstruction techniques remain the same. [122](#), [123](#)

tracking As a charged particles moves through some medium, it leaves a trail of ionized atoms and freed electrons. By detecting these electrons and ions, one can reconstruct the trajectory of a charged particle. This reconstruction is called tracking. [40](#)

- train** In ATLAS derivation production, a “train” is a processing task for multiple derivation formats. Each format can run in its own process, sharing Athena software tools between them. This helps speed up production, especially for data processing. [60](#)
- trigger** A system (hardware, software, or both) used to decide quickly which events should be recorded to disk. [44](#)
- trigger chain** A unique combination of L1 and HLT trigger configurations. Each trigger chain corresponds to a particular event topology. [45](#)
- truth record** In ATLAS MC generator, the truth record details all promptly decaying and “stable” particles (i.e. particles stable enough to propagate through a part of the detector). In MC simulation, the truth record details the true trajectories and decays of particles in the simulated detector for comparison against the reconstructed values after digitization. [52](#)
- turn-on** In a plot of object identification or trigger efficiency, the “turn-on” region is the region in the distribution where the selection changes from low efficiency (i.e. few true positives pass the selection) to high efficiency (i.e. almost all true positives pass the selection). [81](#)
- turn-on curve** In a plot of object identification or trigger efficiency, a “turn-on curve” illustrates the efficiency crossing from a low efficiency to high efficiency region. This usually has an S-curve or step-function shape. [81](#)
- unblinded** In a particle physics search, physicists do not wish to bias themselves by looking at data too early. Therefore, all data (or just the data in the signal region) is kept “blinded”, i.e. covered up or hidden, until the scientists think they are ready to “unblind”. After unblinding, changes to the analysis are somewhat restricted. [144](#)
- unitarity** A *unitary* transformation is a transformation that preserves the inner product, i.e. the inner product of two vectors is the same before and after the transformation. Similarly, a square matrix \mathbf{U} is called *unitary* if $\mathbf{U}\mathbf{U}^\dagger = \mathbf{1}$, where $\mathbf{1}$ is the identity matrix. [10](#)
- untagged** In the context of b -tagging, an “untagged” jet is a jet which fails the b -tagging criteria. [66](#)
- vacuum expectation value** The lowest energy state of a field ϕ , equivalent to the minimum of the potential term of that field’s Lagrangian. The average expected value of the field in a vacuum. [13](#)
- vector boson** A vector boson is a boson with spin = 1, i.e. the gauge bosons γ , Z , W^\pm , and g . [117](#)
- weak** Weak nuclear force. One of the four fundamental forces of nature. Capable of changing a particle’s flavor. Violates parity symmetry. [7](#)
- weak isospin** A quantum number conserved by the weak interaction. [8](#)
- working point** In the context of b -tagging algorithms, a working point is a defined cut value (either fixed or varying across p_T^{jet}) which corresponds to a certain nominal b -tagging efficiency in $t\bar{t}$ MC. For example, a 77% working point algorithm cut will correctly identify 77% of the b -jets in the $t\bar{t}$ MC sample. Also called “operating point”. [65](#)
- xAOD** Analysis Object Data. [58](#)